

Modeling of Nonwoven Formation Processes

BY

Arkaprovo Ghosal

B.Ch.E., Jadavpur University, Kolkata, India, 2007

M.Sc., University of Stuttgart, Stuttgart, Germany, 2012

DOCTORAL THESIS

Submitted as a partial fulfillment of the requirements
for the degree of Doctor of Philosophy in Mechanical Engineering
in the Graduate College of the
University of Illinois at Chicago, 2019

Chicago, Illinois

Defense Committee

Professor Dr. Alexander L. Yarin,	Chair and Advisor
Professor Dr. Eduard Karpov,	Civil and Materials Engineering
Dr. Suman Sinha-Ray,	Mechanical and Industrial Engineering
Professor Jeremiah Abiade,	Mechanical and Industrial Engineering
Professor W.J. Minkowycz,	Mechanical and Industrial Engineering

Every moment I breathe, learn and progress in life, is offered at the feet of my Durga Mata. That being said, I dedicate my entire existence at her lotus feet.

As I offer my 'pronam' (a Bengali gesture of highest extent of respect), I dedicate this thesis to my father Mr. Alope Ghosal (Late), my mother Mrs. Indrani Ghosal, my childhood inspiration Ratan Kaku (Professor Dr. Ranjan Bhattacharyya, Mechanical Engineering department of Indian Institute of Technology, Kharagpur), my mentors Uma, Shyam and Swami Vivekananda, without whose fighting spirit, guidance and support it would never have been accomplished.

ACKNOWLEDGEMENTS

I would like to express my deepest gratitude to my “Doctoralvater”, the German synonym for “Doctoral Father”, Professor Alexander Yarin, who made me unlearn the misconceptions in physics of fluids and trained me to be a thinker. I will never be able to pay off my debt in learning that I owe to him. His teachings proved to be my keys to enjoy the beauty of mathematics in human life. I sincerely thank him for encouraging me to have the quest to discover and explore in scientific endeavors and to push forward despite all odds. I am also thankful for all those wonderful historical and scientific stories and discussions that he shared with me. I feel honored to be a disciple of my Professor whose academic genetics roots back to the “Landau School of thoughts”. Without his consistent help, push and insight this dissertation would not have been possible.

I would like to thank my thesis committee members for their suggestions, support and assistance, which helped me in achieving my goals.

I would like to emphasize my gratitude to Dr. Suman Sinha-Ray for his support and inspiration in my research. A brilliant mind as such has set examples to follow, which shaped up my thinking to a great extent and taught me to never quit. It is my honor to have found an honest friend, a sincere guide and a strict critique in the same person whom I admire for his sharpness and intellect despite having a lot of constructive arguments and difference in opinions. I learnt a lot.

I would like to appreciate my father for everything he taught me since childhood and my mother for the unceasing support and encouragement to leave a mark. I would like to thank my brother and fellow shoulder-sharer Arunodaya (Puchku) for his unconditional support and encouragement during all these years spent in fulfilling my dream. I thank my wife, Madhurima for having her unflinching trust on me. I thank Mithudada for showing me the difference between a good thinker and a great thinker. I am blessed to have them all in my life.

Portions of this thesis have been published in peer-reviewed journals. Chapter 4 has been published in *Polymer* by the Elsevier journals (Ghosal et al. (2016)). Chapter 5, has been also published in *Polymer* (Ghosal et al. (2016a)). Chapter 6 has been accepted for publication in *Industrial & Engineering Chemistry Research*. The copies of permissions for the published works as available and applicable, have been included in the Appendix.

CONTRIBUTION OF AUTHORS

The work on meltblowing in Chapter 4 represents a published manuscript [Ghosal et al. (2016)] for which I was the primary author and conducted all the simulations. Dr. Suman Sinha-Ray contributed in the design of the parametric study using the stand-alone numerical code for simulation. Dr. Sinha-Ray also assisted in writing of the manuscript. The work on solution blowing in Chapter 5 represents a published manuscript [Ghosal et al. (2016a)] for which Dr. Suman Sinha Ray and Dr. Sumit Sinha Ray were the designer of the apparatus and I am the primary author and conductor of experimental measurements. In all published works my advisor, Dr. Yarin, contributed to all aspects of the research. Dr. Pourdeyhimi also assisted in writing of the manuscript. Chapter 6 is the unpublished numerical simulation results directed at understanding the crystallization kinetics in meltblowing process. Ms. Kailin Chen had significant contribution in debugging the subroutines programs accounting for the crystallization kinetics of meltblowing which modified the numerical simulation results of chapter 6. All of the work has been done with an aim to predict physical properties of nonwoven fibers starting from the governing parameters of nonwoven formation processes. I anticipate Chapter 6 will be also published in a peer-reviewed journal in the future. Chapter 7 summarizes the overall conclusions of the research presented in the thesis.

TABLE OF CONTENTS

<u>CHAPTER</u>		<u>PAGE</u>
1.	ABSTRACT	1
1.1	Meltblowing.....	1
1.2	Solution blowing	2
1.3	Crystallization kinetics in meltblowing.....	3
2.	INTRODUCTION	6
2.1	History of nonwovens and nanotechnology.....	6
2.2	Manufacturing processes for micro- and nanofibers	8
2.3	Thesis objectives: significance of the work	23
2.4	Thesis structure	24
3.	BACKGROUND AND LITERATURE REVIEW	26
3.1	Meltblowing.....	26
3.2	Solution blowing	30
3.3	Crystallization in melt spinning processes	34
4.	NUMERICAL PREDICTION OF THE EFFECT OF UPTAKE VELOCITY ON THREE-DIMENSIONAL STRUCTURE, POROSITY AND PERMEABILITY OF MELTBLOWN NONWOVEN LAYDOWN	38
4.1	Introduction	38
4.2	Theoretical background	40
4.3	Results and discussion.....	45
4.4	Orientation probability density function of the ensemble of fiber filaments in the meltblown laydown:	60
4.5	Experimental measurements of meltblown laydown.....	61
4.5.1	Optical profilometry: Measurement of laydown thickness including individual nanofiber elevation.....	61
4.5.2	Vertical Scanning Interferometry measurement mode	61
4.5.3	High Definition Vertical-Scanning Interferometry measurement mode.....	62
4.5.4	Operating conditions in experiments.....	62
4.5.5	Overview of measured data processing from as-received meltblown fiber mats and numerical results.....	63
4.5.6	Comparison between numerical predictions and experimental data of laydown surface morphology and elevation.....	73

4.6	Conclusion	77
-----	------------------	----

TABLE OF CONTENTS (continued)

5.	NUMERICAL MODELING AND EXPERIMENTAL STUDY OF SOLUTION-BLOWN NONWOVENS FORMED ON A ROTATING DRUM.....	79
5.1	Introduction	79
5.2	Numerical model	82
5.3	Characteristic input parameters	87
5.4	Rotating drum collector	87
5.5	Results and discussion	91
5.6	Experiments of the present work versus the numerical predictions	99
5.7	Signal filtering using the Fourier and Gaussian smoothing.....	103
5.8	Conclusion	109
6.	MODELING POLYMER CRYSTALLIZATION KINETICS IN MELTBLOWING PROCESS.....	110
6.1	Introduction	111
6.2	Dynamics equations	113
6.3	Rate of crystallization and degree of crystallinity.....	117
6.4	Thermal balance equation.....	126
6.5	Results and discussion.....	129
6.5.1	Numerical simulations of meltblowing process accounting for crystallization.....	129
6.5.2	Comparison with experimental data.....	133
6.5.3	Numerical prediction of the laydown degree of crystallinity.....	137
6.5.3.1	Effect of temperature of the collector screen	137
6.5.3.2	Effect of DCD (Die-to-collector distance)	143
6.5.3.3	Crystallization in polymers with different activation energy of viscous flow	147
6.5.3.4	Effect of gas blowing velocity	150
6.6	Conclusion	152

TABLE OF CONTENTS (continued)

<u>CHAPTER</u>	<u>PAGE</u>
7. SUMMARY AND CONCLUSION	154
8. BIBLIOGRAPHY	161
9. APPENDIX A:	181
9. APPENDIX B:	182
10. CURRICULAM VITAE	183

LIST OF TABLES

<u>TABLE</u>	<u>PAGE</u>
4.1 Sample specifications and operating conditions as received for 4 different meltblown Polypropylene fibermats produced from the same batch of polymer granules. All sample were made with a polymer flow rate of 0.6 ghm (grams per hole per minute).....	64
5.1 Mean values and standard deviations of the numerically predicted solution-blown laydowns shown in Fig. 5.2.....	92
5.2 The mean values, the standard deviation and the coefficient of variation of mass distributed across laydown for different angular velocities of the collector.....	96
5.3 Comparison of the predicted and experimental volumetric porosity for two different polymer concentrations in solution and two different angular velocities of the rotating drum.	100
5.4 Tabulated operating conditions used to form 4 samples of the predicted and experimental volumetric porosity for two different polymer concentrations in solution and two different angular velocities of the rotating drum collector.....	105
6.1 Numerically predicted and experimentally measured degree of crystallinity for the four meltblown PP samples formed at different values of DCD and the uptake velocity. In particular, the last two columns with the values of the degree of crystallinity η_c are the average values predicted numerically and measured from the DSC thermograms.	134

LIST OF FIGURES

<u>FIGURE</u>	<u>PAGE</u>
2.1 Schematics for several polymer nonwoven manufacturing and bonding processes. Panel (a) shows as a setup for electrospinning [Sinha-Ray 2018, Zupančič et al. 2016] and panel (b) is a setup/schematic for a single-nozzle solution blowing to produce nanofibers [Sinha-Ray et al. 2015a]. In panel (c) schematic for manufacturing of polymer fibers from molten polymer is shown [Fedorova et al. 2017].....	13
2.2 Scanning electron micrographs of nano and micro fiber nonwoven are shown as examples. Panel (a) is the SEM image for electrospun nanofibers deposited on a substrate of wetlaid cellulose substrate for air filtration purposes [Grafe et al. 2003] and panel (b) is SEM image of composite spunbond-meltblown-spunbond nonwoven structure [Grafe et al. 2003] to elucidate relative fiber sizes as compared to nanofibers in panel (a).....	15
2.3 Measured observation on effect of polymer flow rate as an operating parameters on meltblown fibers (Hassan et al. 2013). Panel(a) and (b) are the corresponding SEM micrograph and fiber diameter distribution obtained thereof fibrous meltblown web developed at polymer melt throughput of 0.214 ghm (gms per hole per minute) with a collector screen velocity of 15.6 m/min. The basis weight reported for this nonwoven fabric was 20 g/m ² [Hassan et al. 2013]. Panels (c) and (d) are the SEM micrograph and the fiber diameter distribution for the meltblown laydown produced with polymer melt throughput of 0.0125 gms per nozzle/hole per minute with other parameters unchanged. The basis weight reported for this nonwoven fabric was reduced to 2.5 g/m ² [Hassan et al. 2013].....	21
2.4 Scanning electron micrograph of solution blown nanofibers and corresponding size distribution. Panels (a) and (c) are SEM image and radius distribution of subsonic solution blown fiberweb as reported in [Sinha-Ray et al. 2015a]. Panels (b) and (d) are the same for electrically charged supersonically blown fiberweb as reported in [Sinha-Ray et al. 2013a].	22
3.1 Images taken from experimental facility of meltblowing at Nonwovensinstitute [Fedorova 2017] is shown in panel (a) where the distinct straight and bent parts of a molten polymer jet is clearly visible. Panel (b) shows in two parts the snapshots taken from a non-stretchable and flexible threadline subjected to turbulent pulsations to determine flapping	

length and the envelope configuration [Sinha-Ray et al. 2010]. Panels(c) shows the two snapshots of the travelling wave form due to bending perturbations of polymer jet magnified by the distributed aerodynamic lift force [Sinha-Ray 2012]. Panel (d) shows the in-flight configuration of a single polymer jet and its evolution in non-isothermal planar blowing [Sinha-Ray 2012].....28

3.2 Schematic of solution blowing process and results from numerical and experimental investigation of the process using high-speed camera, as per [Sinha-Ray et al. 2015, Sinha-Ray 2016]. Panel (a) shows the image of a single nozzle polymer solution jet captured by the high speed camera and panel (b) is a schematic of electrically assisted supersonic blowing of polymer solutions that results in fibers less than 50 nm. [Sinha-Ray et al. 2016].32

3.3 Investigation into melt spinning process and simulated variation of degree of crystallization in viscoelastic fluid (Giesekus) jets, as reported in [Ziabicki et al. 2000.] Panel (a) shows a Schematic of modeling melt spinning crystallization process as modeled by [Ziabicki et al. 2000]. Panle (b) shows the variation of jet temperature profile with different mass throughput at constant take-up speed, as per [Ziabicki et al. 2000]. Panel (c) shows the contribution of the amorphous and the semi-crystalline phases to the tensile stress and resultant crystallinity of the fiber jet, as per [Ziabicki et al. 2000]. Panel (d) elucidates the profiles of strain rate, crystallinity, and semi-crystalline orientation factor in the jet in-flight, as per [Ziabicki et al. 2000].34

4.1 (a) Schematic of meltblowing process: the overall view. (b) Schematic of a single polymer jet and its interaction with the surrounding air jet.....41

4.2 Results of numerical simulations of the meltblowing process. (a) Predicted snapshot of the isometric projection of 65 polymer jets being collected on the collector screen moving at a velocity of 10 m/s in the Z-direction. (b) Predicted laydown pattern. All the parameters are rendered dimensionless. In both panels only the fiber axes are shown. The nosepiece corresponds to $\xi=0$, while the collector screen is located at $\xi=1$ (rendered dimensionless by the nosepiece-to-screen distance used as a length scale for all the coordinates)46

4.3 Left column: the collector screen velocity of 0.1 m/s; right column: the collector screen velocity of 10 m/s. (a) Isometric projections of the snapshots of melblown polymer jets for two different velocities of the collector screen (left panel: the dimensionless time $t=20000$, and right panel: the dimensionless time $t=10000$). (b) The three-dimensional structure of laydown over the moving collector screen; both panels at $t=20000$. (c) Configurations of a single fiber for the above-mentioned velocities of the collector screen; both panels at $t=20000$. In panels (a)-(c) only the fiber axes are shown. Also, in panels (b) and (c) the coordinate ξ is reckoned from the collector screen in the direction toward the nosepiece (opposite to Fig. 4.2 and panels (a) here) and is dimensional (in distinction from Fig. 4.2). (d) The cross-sectional fiber-radius distribution at $Z=1$ cm with the total number of loops crossed given in the panels; both panels at $t=20000$49

LIST OF FIGURES (continued)

<u>FIGURE</u>	<u>PAGE</u>
4.4 (a) Distribution of polymer mass in the predicted laydown over the moving collector screen. (b) Three-dimensional isometric projection of the laydown surface. (c) The altitude map of the laydown over the collector screen. The panels on the left correspond to the collector screen velocity of 0.1 m/s, whereas on the right - to 10 m/s.....	50
4.5 Cross-sections of fibers in two laydowns predicted at two different velocities of the collector screen: 0.1 m/s (the panels on the left), and 10 m/s are (the panels on the right). The zoomed-in views correspond to Z=10 cm at the dimensionless time moment of t=5000 (corresponding to 3.33 s).....	51
4.6 Variation of the cross-sectional porosity with the velocity of collector screen. (a) Cross-section Z=1 cm. (b) Cross-section Z=2 cm. (c) Cross-sectional porosity averaged over 50 cm of the collected laydown.	53
4.7 The average volumetric porosity versus velocity of the collector screen. The volumetric porosity was averaged over 50 cm of laydown.....	54
4.8 The predicted variation of the average dimensionless permeability with the velocity of the collector screen. The volumetric porosity used in Eq. (4.5) was averaged over 50 cm of laydown.....	55
4.9 Comparison of the dependence of the dimensionless permeability on the solid volume fraction (SVF) predicted in the present work with the data from the other sources. The present result corresponding to Eq. (4.5) (blue line) with the SVF predicted by our meltblowing model is shown by hollow blue squares. The empirical correlation of [Tomadakis et al. 2005] valid for SVF<0.3 is shown by the dashed red line. The empirical correlation of [Drummond et al. 1984] is shown by the dashed green line. The experimental data obtained for hydroentangled nonwoven fabric using Frazier air permeability tester is shown by the inverse grey triangles [Jaganathana et al. 2008]. The results of the direct numerical simulation of the dimensionless permeability of the experimentally reconstructed (DVI) hydroentangled nonwoven fabrics are shown by the purple upward triangles [Jaganathana et al. 2008]. The results for the 2D random model are shown as a brown dashed line [Chen et al. 2008]. The results for a layered structured fibrous medium	

are shown the red dashed-dotted line, while those for a randomized 3D model are shown by the black-dotted line [Spielman et al. 1968].....58

LIST OF FIGURES (continued)

<u>FIGURE</u>	<u>PAGE</u>
4.10	Panels (a) and (d) are SEM image of nanofiber mat meltblown from Polypropylene granules collected on a flate collector plate as per specifications of samples 1 and 2 in Table 4.1. Panels (b) and (c) are reconstructed 3-D images shown with arbitrary units of elevation when taken from sample 1 at two different locations of the sample. The optically reconstructed 3-D version of the images-processed version of several SEM image for sample 2 are shown in panels (e) and (f) respectively, for two different locations. The 3-D reconstructed images presented here show fibermat elevations by different colors and with same relative scaling.....64
4.11	Samples 3 and 4 from Table 4.1 have been produced with identical processing parameters except the collecting screen velocity. Panels (a) and (d) shows sample SEM image of meltblown fibermat accordingly for these samples. Panels (b) and (c) are reconstructed 3-D images shown with arbitrary units of elevation when taken from sample 3 at two different locations of the sample. The optically reconstructed 3-D version of the images-processed version of several SEM image relative scaling.....65
4.12	The original 3-D structure of fibermat captured with the optical profilometer Optical profilometer results are shown for samples 1 (Left panels) and 2 (Right Panels) from Table 4.1. The raw 2D images (top left and right panel) and 3D images in panels (e) and (f) respectively are obtained by optical profilometer for meltblown polypropylene laydowns. Surface elevation profiles are revealed by the optical profilometer in two perpendicular directions as shown to be blue and red graphs in panels (c) and (d).. Panels (e) and (f) show the same surface as in panel (a) and (b) at different relative heights to capture the fibrous structures in more detail.....67
4.13	Optical profilometer results for samples 3 (Left panels) and 4 (Right Panels). The raw 2D (top left and right panel) and 3D (top right panel) optical profilometer data for laydown corresponding to sample 2 from Table 4.1. Surface elevation distributions revealed by the optical profilometer in two perpendicular directions as shown to be blue and red graphs in panels (c) and (d).....68
4.14	Measured angular Orientation for samples 1 and 2 of Table 4.1, where sample 2 was produced with higher DCD as compared to the sample 1. Panels (a) and (b) tends to show

an effect on uptake collector distribution. A higher DCD leads to a wider orientation distribution pattern.....70

- 4.15 Measured angular Orientation for samples 3 and 4 of Table 4.1, which were produced with varying uptake velocity but all other processing parameters practically unchanged. Sample 3 has a represents a higher uptake velocity, and it clearly shows a higher velocity tends to orient the fibers on the mat more oriented to a specific direction, i.e, the uptake collector distribution gets narrowed..... 71

LIST OF FIGURES (continued)

<u>FIGURE</u>		<u>PAGE</u>
4.16	Experimentally measured morphology of the obtained samples 1-4 as panels a,b,c,d respectively using optical profilometer. A segment of each laydown is shown, and the elevation scale (shown in microns) across its thickness is exaggerated in the image to reveal the elevation contour in more detail. The negative value in the elevation scale bar signifies the distance between the arbitrary lower plane of the sample being viewed to the focal point. The comparison of different colors for different elevation also reveals the change in deposition pattern of fibers due to variation of the uptake velocity of the collector belt. For the higher velocity in panel (c) when compared to panel (d), the collected laydown reveals several distinguishable contour pattern suggesting a more uniform elevation distribution whereas in panel (d) shows sudden changes in elevation throughout the fibermat area and at the lower uptake collector velocity, the colors are blended suggesting a higher extent of fiber filament overlap and piling in this case.....	72
4.17	Simulated elevation of the meltblown polypropylene laydown samples collected on a flat collector plate with operating conditions according to samples 1-4 of Table 4.1. Deborah number $De_0 = 300$ was used in the simulation, which corresponds to the relaxation time of 0.1 s. The diameter of polymer jets at the nozzle exit was taken as 200 μm . The air blowing speed was 180 m/s (equivalent to 800 m^3/mhr), the die-to-collector distance was taken as 15 cm for panel (a), 30 cm for panel (b) and 22.5 cm for panels (c) and (d). Panels (a) and (b) re for uptake velocities of 13 m/min respectively. Panels (c) and (d) are for uptake velocities of 40 m/min and 13 m/min respectively. The mass flow rate was of the order of 0.6 grams per hole per minute.....	74
4.18	Comparison of simulated (according to operating conditions as specified for samples 1-4 in Table 4.1) and measured mass mapping of the meltblown polypropylene laydown collected on a flat collector plate. Numerical simulation with 100 polymer jets. The mass mapping is shown according to the color bars in gm/cm^2 . Top panels(a)and (b) are simulated mass maps of processing conditions similar to sample 3 and 4, where panel (a) is for higher uptake velocity of 40 m/min and panel (b) is for uptake velocity of 13 m/min. Measured mass for small components of the fibermat all over the received fibermats are shown in an interpolated form in panels (c) and (d) respectively for samples 3 and 4. Mass	

distribution in $\text{gm}/(\text{cm}^2)$ in the laydown on a flat collector plate predicted in the numerical simulations with 100 polymer jets.....75

LIST OF FIGURES (continued)

<u>FIGURE</u>	<u>PAGE</u>
5.1	(a) Schematic of solution blowing process. Polymer solution jets issued through concentric nozzles located along nosepiece are collected on a rotating drum and form a nonwoven laydown. Each oncoming polymer solution jet possess a short straight part (~1 mm) followed by a vigorously bending and flapping part. (b) Schematic of the different forces acting on a polymer solution jet undergoing vigorous flapping accompanied by solvent evaporation. (c) Snapshot of numerically simulated 60 polymer solution jets wound on a rotating drum. (d) Section of as deposited solution-blown laydown. (e) A drum used in the experiments to wind solution blown fiber laydown. (f) Schematic of the drum cross-section with coordinate system.....89
5.2	Predicted diameter distributions of solution-blown laydowns formed by 60 polymer jets at different angular velocities of the rotating drum. Panels (a)-(c) show the diameter distributions for $\varphi=0^\circ$, $\varphi=60^\circ$ and $\varphi=135^\circ$, respectively, for $\omega=10$ rpm. Panels (d)-(f) show the diameter distributions for $\varphi=0^\circ$, $\varphi=60^\circ$ and $\varphi=135^\circ$, respectively, for $\omega=50$ rpm. Panels (g)-(i) show the diameter distributions for $\varphi=0^\circ$, $\varphi=60^\circ$ and $\varphi=135^\circ$, respectively, for $\omega=100$ rpm. Panels (j)-(l) show the diameter distributions for $\varphi=0^\circ$, $\varphi=60^\circ$ and $\varphi=135^\circ$, respectively, for $\omega=200$ rpm.....91
5.3	Mass distribution in the numerically simulated solution-blown laydown. The values in g/cm^2 correspond to the color bars on the right. Different panels correspond to the mass distributions predicted for different values of the angular velocity, namely, panels (a), (b), (c) and (d) correspond to the angular velocities of the rotating drum of 10 rpm, 50 rpm, 100 rpm and 200 rpm, respectively. All the simulations were done for 60 polymer solution jets.....94
5.4	Predicted variation of the volumetric porosity (a), and the dimensionless permeability (b) with the angular velocity of the collector drum.96
5.5	Comparison of the dependence of the dimensionless permeability on the solid volume fraction (SVF) predicted in the present work (blue squares denoted Simulated permeability)

	with the other existing models and experimental data available in literature.....	98
5.6	Comparison of the measured laydown elevation (a)-(e) with the simulated average elevation (f) for a comparable laydown size.....	101
5.7	The raw 2D (top view) (panel (a)) and 3D (panel (b)) optical profilometer data for laydown corresponding to sample 1 from Table 5.4. Surface elevation distributions after noise removal is shown in panel (c). Span wise and cross-cut sectional profiles in two directions over the laydown are revealed in panel (d) as obtained by the optical profilometer corresponding to corresponding to sample 1 from Table 5.4.....	102

LIST OF FIGURES (continued)

<u>FIGURE</u>	<u>PAGE</u>	
5.8	The raw 2D (panel(a)) and 3D (panel (b)) optical profilometer data for laydown corresponding to row 2 from Table 5.4. Surface elevation distributions after noise removal is shown in panel(c) and spanwise and cross-cut sectional profiles in two directions over the laydown are revealed in panel (d) as obtained by the optical profilometer corresponding to sample 2 from Table 5.4.....	103
5.9	The comparison of the raw and smoothed elevation fields over the nanofiber sample obtained from solution-blowing of 15wt% polymer solution collected at an angular drum speed of 240 rpm as shown previously in Fig. 5.6(a). Panels (a), (c), and (e) represent the original dataset, the Fourier-filtered dataset and the Gaussian-filtered dataset, respectively. The right-hand-panels (b), (d) and (f) show the corresponding cross-sectional profiles measured along the axes shown in panels (a), (c) and (e).....	104
5.10	Smoothing of the data for sample 3 from Table 5.4. (a) Fourier- filtered surface elevation distribution of the uppermost layer of the laydown. (b) Gaussian-filtered surface elevation distribution. The elevations are measured by color scale bars. (c) The Fourier-smoothed result for the uppermost layer from the numerically simulated elevation profile with the input conditions corresponding to sample 3. (d) The Gaussian-smoothed numerically simulated elevation profile for the uppermost layer for sample 3. (e) The un-filtered original image from an arbitrary focus location from sample 3. Panels (f) and (g) show, respectively, the Fourier- and Gaussian-smoothed results obtained from panel (e). Panels (e)-(g) correspond to spunwise cross-sectional planes. Panel (h) represents a processed SEM image used for porosity calculation.....	106
6.1	Schematic of the spherical coordinate system used to describe crystal nuclei formation and growth.....	117

- 6.2 Schematic of the random process of crystallinity build-up at point P. The total number of the intervals is n120
- 6.3 Isometric view of the predicted meltblowing process accounting for crystallization. The coordinate across the laydown is denoted as H , and the coordinate spanning the nosepiece and the collector belt, and thus normal to the latter is denoted as ξ . The third Cartesian coordinate is Z . It is orthogonal to ξ and H , and thus, ξ , H , and Z form a Cartesian trihedron. Note that the auxiliary dimensionless axis $\xi' = 1 - \xi$ is used in the images, as a convenient representation for the laydown elevation. Panel (a) is the isometric view of predicted meltblown multiple polymer jets, panel (b) depicts a single jet with the degree of crystallinity increasing along it. Panel (c) shows the degree of crystallinity along multiple polymer jets in meltblowing process.....130

LIST OF FIGURES (continued)

<u>FIGURE</u>		<u>PAGE</u>
6.4	Effect of the polymer melt temperature at the die exit on the overall degree of crystallinity in the meltblown jets and laydown. Panels (a), (c) and (e) are isometric view of the thermal profile of 100 polymer jets, the degree of crystallinity along the jet path, and the resulting 2-D map of the degree of crystallinity of the nonwoven, respectively. The temperature of the molten polymer at the nozzle exit is 580 K. The right panels (b), (d) and (f) show the corresponding results for the initial polymer melt temperature of 550 K.....	131
6.5	DSC thermograms and thermogravimetric plots for samples 1-4 of Table 6.1. Panel (a) shows the first heating and cooling cycles for the four PP nonwoven samples listed in Table 6.1. Panel (b) shows the results of the thermogravimetric analysis of all four samples and suggests that there was no thermal degradation in the samples in the operating temperature range used in DSC. Panel (c) shows only the first heating curve for the nonwoven sample 1 heated at the rate of 10 °C/min. It shows that the melting temperature is approximately 151 °C. Integrating over the peak, the melting enthalpy was found as 88.15 J/g. The latter value corresponds to the degree of crystallinity of 0.425, or 42.5 %. Panel (d) show the 1 st heating/cooling cycle at the rate of 5 °C/min for the sample with a higher DCD (sample 2) with a zoomed-in view of the melting peak in the inset.....	135
6.6	The predicted 3D conformations of 100 polymer jets and the corresponding fields of the degree of crystallinity shown by color. (a) No localized cooling and enforcing of the laydown temperature to immediately become equal to the collection screen temperature. (b) The case with localized cooling at the touchdown point enforcing the laydown temperature to become that of the collection screen temperature and causing an enforced crystallization. The initial Deborah number at the nosepiece was $De_0=400$. The diameter of the polymer jets at the nozzle exit was taken as 500 μm . The air blowing speed was 200	

	m/s, the die-to-collector distance (DCD) was taken as 20 cm, the collector screen velocity was 1 m/s, and the mass flow rate was 0.3 g per hole per minute.....	137
6.7	Two cases with the enforced temperature of the laydown at the touchdown point. (a) $T_{\text{Screen}}=300$ K, (b) $T_{\text{Screen}}=280$ K. The isometric view of 100 meltblown polymer jets with the field of the degree of crystallinity shown in color. The initial polymer melt temperature at the nosepiece is $T_0 = 580$ K. DCD is 50 cm and the gas blowing velocity is 200 m/s; DCD=50 cm.....	138
6.8	The effect of the enforced touchdown temperatures on polymer jets in flight. (a) Temperature profiles along the jets. (b) The stretching ratio distribution. (c) The nucleation rate distribution. (d) Fiber-size distribution in the laydown with $T_{\text{Screen}}=300$ K. (e) Fiber-size distribution in the laydown with $T_{\text{Screen}}=280$ K.....	140

LIST OF FIGURES (continued)

<u>FIGURE</u>	<u>PAGE</u>	
6.9	Effect of DCD on the degree of crystallinity. The isometric views of 100 meltblown polymer jets. Panels (a) and (b) correspond to DCD of 20 cm. Panels (c) and (d) correspond to DCD of 50 cm. Panels (a) and (c) show the results with the touchdown temperature being enforced as 280 K. Panels (b) and (d) show the results with the touchdown temperature enforced as $T_{\text{Screen}}=300$ K.	143
6.10	Distribution of the degree of crystallinity in laydowns formed with different DCD values corresponding to the panels in Fig. 6.9. The initial melt temperature was kept at 580 K [Wehmann et al. 1999] for all cases. Panels (a) and (c) correspond to DCD of 20 cm and 50 cm, respectively, with the touchdown temperature being enforced as 280 K. Panels (b) and (d) correspond to the touchdown temperature enforced as $T_{\text{Screen}}=300$ K.	144
6.11	The effect of the activation energy of viscous flow on the degree of crystallinity in nonwoven laydown. The isometric view of the in-flight crystallization and the distribution of the overall degree of crystallinity corresponding to different values of the activation energy of viscous flow shown in panels. (a) $U_A=10$, (b) $U_A=20$. The corresponding distribution of the degree of crystallinity for the laydowns formed are shown in panels (c) and (d), respectively. The average degree of crystallinity in the fibrous laydown for panels (a) and (c) varies in the 0.539-0.58 range in multiple repeated simulations, and the average degree of crystallinity in the fibrous laydown for panels (b) and (d)- in the 0.597-0.612 range in multiple repeated simulations.....	146
6.12	Effect of gas blowing velocity U_{g0} on the degree of crystallinity. The isometric views of 100 meltblown polymer jets are shown. Panels (a) and (c) show the results with the gas blowing velocity $U_{g0} = 150$ m/s, and panels (b) and (d) show the results with $U_{g0} = 200$	

m/s. Panels (a) and (b) correspond to $U_A=10$. Panels (c) and (d) correspond to $U_A=20$. All panels show the results with the touchdown temperature being enforced as $T_{Screen}=280$ K, and $DCD=20$ cm. The average values of the degree of crystallinity of the laydown formed for panels (a), (b), (c) and (d) are 0.518, 0.609, 0.522748 and 0.6102, respectively.....148

6.13 The 2-D mapping of the degree of crystallinity in laydowns formed by 100 jets. The results illustrate the effect of the gas blowing velocity U_{g0} on the laydowns formed from polymers with different activation energies of viscous flow. Panels (a) and (c) show the results with the gas blowing velocity $U_{g0} = 150$ m/s, and panels (b) and (d) show the results with $U_{g0} = 200$ m/s. Panels (a) and (b) correspond to $U_A=10$. Panels (c) and (d) correspond to $U_A=20$. All panels show the results with the touchdown temperature being enforced as $T_{Screen}=280$ K and $DCD=20$ cm..... 149

Chapter 1: ABSTRACT

1.1: Meltblowing

The aim of this part of the thesis is to describe the development of a robust numerical user-friendly model for prediction of meltblowing in a wide range of the operational parameters, and in particular, to predict the thickness and porosity of laydown formed on a flat collector plate. The experimental work dealt with meltblowing and measurements of the thickness and porosity of the resulting micro- and nanofiber mats. The experimental results were used for validation of the numerical results, and a good agreement was found, even though no adjustable parameters were involved. In addition, such characteristics of meltblown laydowns as their three-dimensional morphology, mass distributions and fiber orientation distributions were predicted under different operational conditions. This work describes the first detailed model of meltblowing process which allows prediction of such integral laydown properties as thickness, porosity and permeability. Also, such laydown properties as the detailed three-dimensional micro-structure, fiber-size distribution and polymer mass distribution are predicted. The effects of the governing meltblowing parameters on the variation of all these laydown properties are accounted for, with the influence of the collector screen velocity being in focus. For this aim numerical solutions of the system of quasi-one-dimensional equations of the dynamics of free liquid polymer jets moving, cooling and solidifying when driven by the surrounding air jet are constructed for a non-isothermal process. Multiple polymer jets are considered simultaneously when they are deposited on a moving screen and forming nonwoven laydown. The results reveal the three-dimensional configuration of the laydown and, in particular, its porosity and permeability, as well as elucidate the dependence of the laydown structure on the forming conditions, in particular, on the velocity of the screen motion.

It is shown and explained how an increase in the velocity of the collector screen increases porosity and permeability of the meltblown nonwoven laydown.

1.2: Solution blowing

The numerical code developed during the primary work for simulation of meltblowing and the resulting laydown properties was modified and extended also for solution blowing to predict the laydown thickness and porosity, and compare them with the experimental data. The thickness and porosity of the laydown removed from the rotating collector drum was measured using optical profilometry and SEM imaging. Several additional features of solution-blown laydowns were predicted as well, including the three-dimensional morphology in a wide range of operational parameters. In this work the three-dimensional architecture and properties of solution-blown laydown formed on a rotating drum are studied using the system of quasi-one-dimensional equations of the dynamics of free liquid polymer viscoelastic jets moving, evaporating and solidifying, while being driven by the surrounding high-speed air jet. Solution blowing of multiple polymer jets simultaneously issued from a nosepiece and collected on a rotating drum is modelled numerically. The developments shown in this part of the thesis focus on the computational approach developed to calculate the three-dimensional architecture based on the complex dynamics of fiber formation from a polymer solution under isothermal conditions. Numerical modeling of nonwoven formation processes accounting for detailed dynamics of multiple polymer solution jets moving in air with high relative velocity is undertaken for the first time with the goal to predict the intrinsic parameters of the resulting three-dimensional laydown. In particular, the results predicted the three-dimensional architecture of the laydown, the surface and volumetric porosity and permeability. The effect of the viscoelasticity of polymeric liquids and the governing

parameters of the process, for example, of the velocity of the collector screen, are studied in such detail for the first time. The numerical results on the volumetric porosity of nonwoven laydown are compared with the experimental data of the present work. The numerical predictions are in good agreement with the experimental data and elucidate the effect of the angular drum velocity on the mass and angular fiber distribution, as well as the volumetric porosity and permeability of the solution-blown nonwovens. Polymer mass distribution in solution-blown nonwoven laydown, as well as their thicknesses are also elucidated. It was found that instead of doing any upstream modification of the solution blowing process, the easiest way to control the laydown structure (the mass and angular fiber distribution, as well as the volumetric porosity and permeability) is to vary the angular velocity of the collecting drum. The modeling and numerical approaches developed in this work, as well as the numerical code resulting from it are quite unique and can find wide applications in the nonwoven industry and facilitate optimization of fiber-forming processes, such as meltblowing, solution blowing, as well as in describing fiber behavior by modeling post-processing stages such as hydroentanglement using the same framework of the quasi-1-D formulations of free liquid jet dynamics.

1.3: Crystallization kinetics in meltblowing

In this part of the work, the theoretical model of crystallization kinetics in meltblowing process is developed. It was also incorporated in the numerical code describing polymer jet formation during meltblowing process and the corresponding laydown structure as mentioned above. This new approach towards accounting for crystallization has been attempted by predicting a distribution pattern and growth behavior of polymer crystal nuclei along the jet pathway. The

primary focus of this phase of work has been to determine the effects of the different operational parameters on the properties of the produced fibrous meltblown (nonwoven) laydown and establish a statistical correlation between the final product properties and the corresponding processing conditions. This part of the work also involves experimental validation of the numerically predicted processing parameter effects on the degree of crystallinity in meltblown fiber mats using the data obtained at the experimental facility of the Nonwovens Institute, NCSU.

The numerical simulation tool developed at this phase of the work is capable of predicting the degree of crystallinity along the jet spinline, as well as the distribution of the degree of crystallinity in the laydown collected on a flat moving collector belt. Since meltblowing is a highly non-isothermal process, the thermal profile along the polymer jet path not only affects the rheological parameters, but determines the rate of crystallization, which in turn affects the viscoelastic behavior of the polymer jets, in particular, their stretching and attenuation. The process of formation of polymer crystals in the polymer jets formed under the action of the surrounding high-speed hot air jets is described. The spinline crystallization is studied using numerical solutions of the system of coupled quasi-one-dimensional equations describing the dynamics of free liquid polymer jets moving, cooling and solidifying along the travel path when driven by the surrounding air jets, as well as the nucleation and crystallization kinetics are simultaneously addressed. The developed numerical code predicts the distribution of the degree of polymer crystallinity along the bending jet path in flight, as well as the resulting distribution of the degree of crystallinity in the three-dimensional laydown. Accordingly, the degree of crystallinity maps in the meltblown laydown are predicted. In the numerical solutions multiple polymer jets are considered simultaneously when they are moving toward the collector belt and form an entangled laydown on it. The numerical model is applied for a range of processing parameters, such as the

initial velocity and temperature of the surrounding air jets, the die-to-collector distance (DCD), the collector belt velocity, the Deborah number and the activation energy of viscous flow. The results reveal that the crystallization kinetics is sensitive to all the above-mentioned parameters. In addition, the results elucidate the correlation between the onset of the large-amplitude bending perturbations of polymer jets and fluctuations of the degree of crystallinity along the spinline.

Acknowledgement

The entire work presented here has been supported by the Nonwovens Cooperative Research Center (NCRC), grant no. 13-149.

Chapter 2: INTRODUCTION

2.1 History of nonwovens and nanotechnology

From the Ancient times of human civilization, fabrics played a dominant role. Most simple example of fabrics were hand-woven fabrics made from cotton, wool, or other natural fibrous materials. As industrial/mass-scale production of fabrics was developed, the word 'textile' was coined and eventually the textile industry gained an upsurge from the early 19th century onwards. The term "textile" is derived from Latin word "texere", which means "to weave". By conventional terminology, textile refers to a flexible material comprised of a network of natural or artificial fibres, known as yarn. (<https://www.textileschool.com/>). This definition was limited to 'woven' fabrics only.

In contrast to woven fabrics and textiles, the term 'nonwoven' was coined in the United States following the technology-driven production developments of the 1940s [Batra et al. 2012]. Although the definition of nonwoven means "something which is not woven or knit", the nonwoven fabrics stand for far more than that [Batra et al. 2012]. One of the definitions of nonwoven fabric is "a primarily fibrous assembly other than a traditional paper, woven, or knit fabrics , which has been engineered to some level of structural integrity by physical and/or chemical means" [INDA 2002]. An alternate definition suggests that a nonwoven fabric is a "sheet or web structures bonded together by entangling fiber or filaments (and by perforating films) mechanically, thermally or chemically. They are flat, porous sheets that are made directly from separate fibers or from molten plastic or plastic film. They are not made by weaving or knitting and do not require converting the fibers to yarn" [INDA 2002]. The nonwovens industry has an organizational structure which is distinctly different from that of textile, pulp and paper industries.

The nonwovens industry at its early stages of upsurge has adapted techniques and innovations from pulp and paper industries and polymer extrusion industries as well as classical textile industry [Batra et al. 2012, Formhals 1934]. Despite sharing some common history with the aforementioned industries, the nonwoven industry developed different integration techniques in the value-added/value-based cost-effective approach towards mass-scale high-speed production of engineered polymer-based fibers. Depending on market demands and adjustments allowed within available manufacturing framework components such as bonding techniques, upstream and downstream parametric variations, raw material selection and thermal, mechanical or chemical treatment of web can be aimed to achieve fabric characteristics and properties as per functional requirements. The integrated nature of nonwoven manufacturing allows the nonwoven fabrics industry to support and hold a wide range of markets starting from medical to armaments and protective gears, construction, geo-textiles as well as high-efficiency particle capture/ filtration applications. Nonwoven industry is a multi-billion USD market, for which the current forecast predicts steady growth [Gagliardi 2016, Grafe et al. 2003, Grafe et al. 2001, Graham et al. 2002].

Eventually, discovery of polymeric liquids and applicability of their rheological/viscoelastic properties made the production of continuous fibers possible from synthetic polymeric materials. That in turn led to an upsurge in the nonwoven production due to their manifold applications in a wide range of industries. The nonwoven industry is aimed at producing fabrics/laydowns/fibrous webs consisting of micro- and nanofibers which is an integral part of the nanotechnology applications. In a broader sense, the latter is already an USD 2 trillion industry by itself [Sinha-Ray 2012, <http://www.nanowerk.com/news/newsid=1140.php>]. Nonwovens are an integral part of nanotechnology as a scientific discipline where a very wide range of nanotechnological applications depends on nonwoven structures. As mentioned in [Sinha-Ray 2012], Richard

Feynman delivered a lecture titled “There's Plenty of Room at the Bottom: An Invitation to Enter a New Field of Physics” at the American Physical Society meeting at Caltech [Feynman 1960]. Richard Feynman insight and tapping of the immense potential of nanotechnology in modern era triggered multiple further developments. Despite his vision remaining practically unnoticed for some time, eventual discovery of several material characterization techniques such as, for example, Scanning and Transmission electron microscopy and contributions from the IBM Zurich Research Laboratory researchers and Nobel laureates Gerd Binnig and Heinrich Rohrer [Sinha-Ray 2012] played a significant role in turning the tide in favor of extensive research activities in the field of nanotechnology, both in academia and industry. The discovery of carbon nanotubes contributed to availability of a higher extent of industrial funding. However, nanotechnology itself being a multibillion dollar industry, has a lot of challenges of its own. The lack of fundamental understanding of application-oriented usage of nanotechnology, i.e, nanofibers, nano-particles and nano-materials creates a barrier. The expensive existing experimental methods and risk associated with high cost of modifications required to optimize scalability of setups diminish scalability and the way to market profitability. However, for the sake of brevity, we emphasize the nonwoven manufacturing and issues related to that as a partial part of nanotechnology, directly related to the scope of this thesis.

2.2 Manufacturing processes for micro- and nanofibers

Nonwoven fabrics are composed of micro- or nanofibers. Due to the small pore size, as well as high surface area, there is a very wide range of applications where nonwovens are absolutely essential. Applications related to filtration, thermal insulation, acoustic shielding, shock absorbance, durability and higher fluid retention capacity should be mentioned first. For example,

medical hygienic products are significantly dependent on nonwovens. In addition, products intended for liquid and aerosol filtration, composite materials for protective gear and clothing, and high performance wipes could benefit enormously from the introduction of such small fibers [Fedorova 2017, Formhals 1934]. Important applications of nanofibers are in medical scaffold manufacturing, cellular reaction control and tissue engineering. It also benefits the heat removal applications in microelectronics and in nano fluidic devices, in particular, for space exploration [Subbiah et al. 2005, Sun et al. 2003, Sinha-Ray et al. 2010]. Commercial air filtration applications [Okamoto et al. 1978, Baker et al. 1998, Cheng et al. 1998, Fedorova 2017, Grafe et al. 2001, Grafe et al. 2003, Gogins 1993] finds immense applications of nanofibers. In a sense, the modern civilization depends heavily on nonwovens and nanomaterials in multiple aspects of life. With new requirements to functional materials, the market for upsurge in nanomaterial production is expected.

The recent upsurge in the nonwoven industries intends making cheaper materials or reducing costs of production, which should be established on a scientifically solid foundation. Also, for quality material and sophisticated products in the application market, application-specific, high-end products are required. That dictates the requirement of investigation and research of the physical mechanism responsible for the polymer nonwoven production, with the aim to understand and optimize the industrial processes and facilitate needs of the application-based market. This thesis will explain the research goals, which are necessary to address to optimize the existing manufacturing processes of melt-and-solution blowing in order to develop a scientifically sound framework based on the applied hydrodynamics of rheologically complex liquid jets.

The advantage of the scientifically based approach attempted in this thesis is in that that the desired product properties can be predicted rather than found by trial and error. This also relates to such stages as fiber selection, web formation, bonding and post-processing and finishing techniques. Due to its assortment of achievable characteristics nonwoven fabrics penetrate a wide range of markets including medical, geo-textile or construction, apparels, HEPA or filtration applications, protective clothing, acoustics, armaments/defense related industries, as well as automotive industries. These fabrics composed of micro- and nanofibers typically provide a very high surface area to volume ratio, i.e., the pore size of the order of microns and a resulting large surface area. This characteristics is the most useful in the application where thermal insulation and acoustics, pressure-filtration performance and collective strength of fibrous laydown are of relevance and importance. Typically, nanofibers are broadly defined as fibers of diameter less than 1 micron [Schaefer et al.1998a ,Grafe et al.2001, Grafe et al.2003, Graham et al. 2002]. According to multiple source, nanofibers can be considered as fibers with the diameter ranging from 0.5 to 1 micron. On the other hand, fibers of diameter below 0.1 micron are more suitable in specific applications [Graham et al. 2002], which makes unavailable a standard definition of nanofibers in the nonwovens industry. At the same time, fibers with diameter varying between 0.5 to 10 microns are generally considered as standard microfibers [Fedorova 2017, Graham et al. 2004, Sun et al. 2003, McCann et al. 2005, Reneker et al. 1996]

In a broader sense, nanofibers are generally understood as a class of fibers with a diameter less than 1 micron. Examples of such fibers are glass fibers and electrospun fibers. Electrospinning has been the most widely known manufacturing process to produce electrospun nanofibers of diameter range on the scale of 500 nanometers. Such fibers have been manufactured and used commercially for air filtration applications for almost 3 decades [Grafe 2003]. On the other hand,

polymeric meltblown fibers are just beginning to break the micron barrier. Several value-added nonwoven applications, including filtration, barrier fabrics, wipes, personal care, medical and pharmaceutical applications may benefit from the interesting technical properties of commercially available microfiber and nanofiber webs. This thesis focuses on process optimization of meltblowing and solution blowing for the formation of micro- and nanofiber webs used in for industrial production of nonwovens from synthetic fiber-forming polymers. The thesis will also discuss crystallization phenomena in meltblowing process to predict the degree of crystallinity of fibrous webs and mats produced using the abovementioned process. The resulting physical characteristics of the nanofiber webs will be discussed. In order to provide a useful context for the nonwovens industry, physical properties and characteristics of fibers produced under different upstream and downstream operating conditions will be discussed via both numerical simulation results and the corresponding experimental validations. The description of the physical mechanisms responsible for the on-demand production of nonwoven webs will be given. The comparison of the predicted properties with the experimental data should provide the product designers in the nonwovens industry confidence in the tools developed in this thesis to optimize and control the operating conditions used to manufacture products according to the desirable properties of nonwovens in various applications.

There are several manufacturing processes of fiber webs from polymer melts and solutions and the products can be subjected to various bonding techniques. This is essential to categorize the nonwovens according to the manufacturing and treatment procedures. One of the major advantages of nonwoven manufacturing is the speed at which fabric can be produced, especially when compared to the production rates of knitted or woven fabrics. The effect of this is in the reduction in the cost of manufacturing.

Broadly, nonwovens can be broadly categorized in the following three groups: those manufactured with/by dry-laid methods, wet-laid methods, or spun-melt processes. The general information on manufacturing, properties and the end uses of these nonwovens is described below. In the case of dry-laid nonwovens, the staple fibers then processed to create fibrous webs of limited strength and mechanical integrity. There are two different methods of dry-laid web manufacturing. The air-laid is the process where the generated fibers are randomly oriented, whereas carded nonwovens contain oriented fibers. The method used depends on the desirable fiber orientation. The method of bonding can be used (note, that it is difficult to successfully mechanically bond short fibers). The air-laid technology produces a randomly orientated fibrous web where fibers of the size 1-15 mm are dispersed in air by various means. To name a few, are rotating blade used to generate “cloud” of fibers [<http://www.tikp.co.uk>] with the help of an air-lay chamber. The fibers are then transported through air toward a permeable conveyor belt under which suction is applied. This helps to gather the fibers onto the conveyor surface, where the web is formed.

Wet-laid nonwovens are produced in a manufacturing process similar to paper and pulp manufacturing. A dilute mixture or slurry of solvent and polymer nonwoven is deposited on a moving wire screen and drained to form a web with installed suction. Upon further dewatering, the web is consolidated with hot roller pressing, and dried afterwards.

Spunmelt nonwovens are the most widely used manufacturing process in the nonwoven industry. In these processes webs are made directly from filaments spun from polymeric liquids, either molten or in the form of solution obtained from the original solid polymer pellets. According to several sources, spunbond is the most favored and direct method of making a nonwoven.

Continuous filaments, not staple fibers, are spun (extruded) directly from polymer pellets through a nosepiece. Normally, polymers are melt-extruded in the spunbond process. The formation of a web of continuous filaments deposited on the conveyor belt is assisted by suction. The web is then bonded directly by various means, normally by thermal bonding.

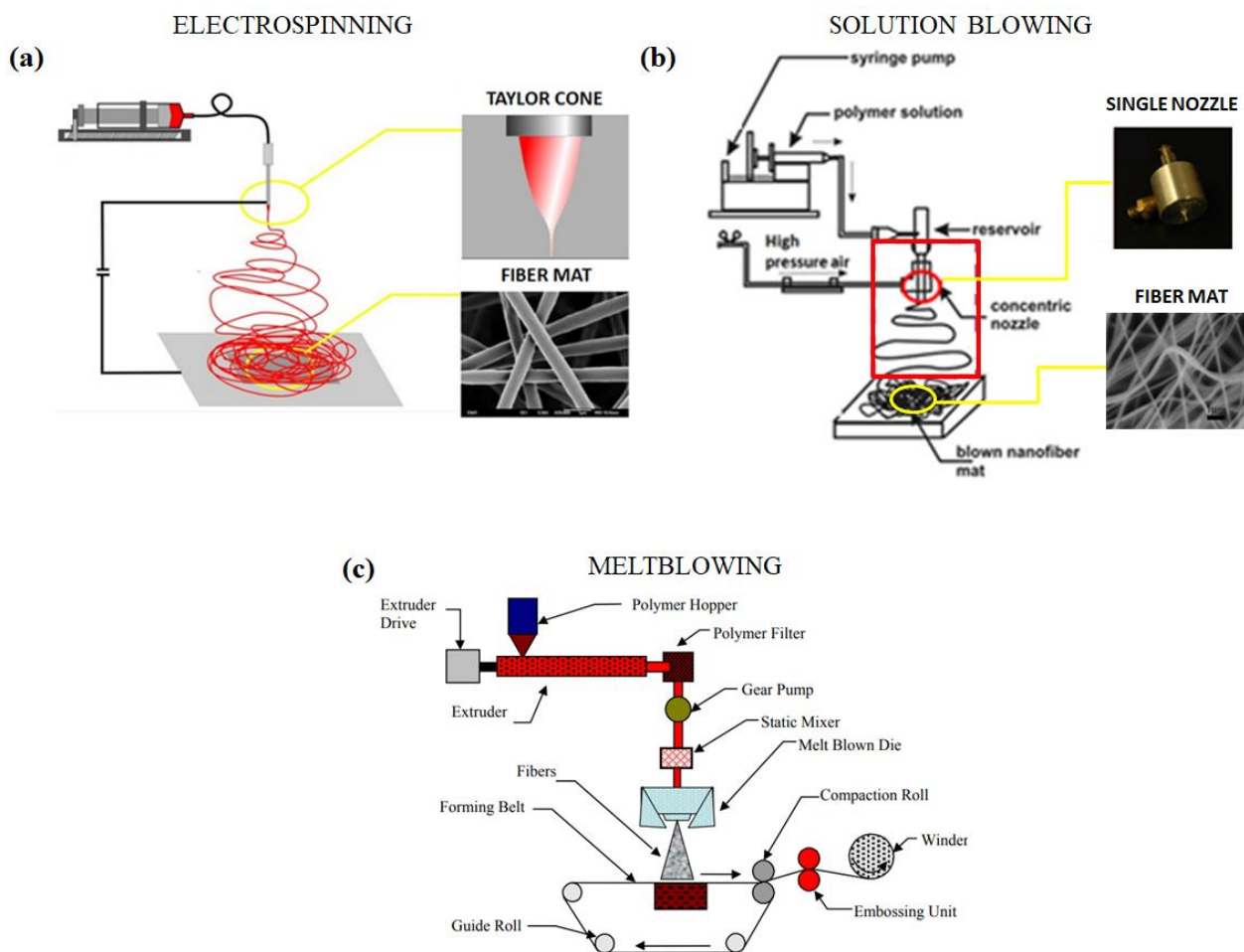


Figure 2.1: Schematics for several polymer nonwoven manufacturing and bonding processes. Panel (a) shows as a setup for electrospinning [Sinha-Ray 2018, Zupančič et al. 2016] and panel (b) is a setup/schematic of a single-nozzle solution blowing to produce nanofibers [Sinha-Ray et al. 2015a]. In panel (c) schematic of the manufacturing of polymer fibers from molten polymer is shown [Fedorova et al. 2017].

The existing literature reveals that polymer nanofibers can be formed using the electrospinning process [Filatov et al. 2007, Greiner et al. 2007, Lee et al. 2002, Kirichenko et al. 2010, Khansari et al. 2013, Noruzi et al. 2016, Ramakrishna 2005, Reneker et al. 1996, Reneker et al. 2002, Reneker et al. 2008, Stachewicz et al. 2014, Wendorff 2012, Wnek et al. 2003, Yarin et al. 2001, Tsai et al. 2004, Yarin et al. 2014]. Electrospinning is an electrohydrodynamic process [Sinha-Ray 2018], which has been discussed extensively in existing literature and patents [Doshi et al. 1995, Tsai et al. 2002, Grafe et al. 2001, Reneker et al. 1996,] Yarin et al. 2014. A basic schematic of an electrospinning apparatus is shown in Figure 1 (a) [Sinha-Ray 2018]. In electrospinning process, electric field of the order of 1-2 kV/cm is used to provide the electric force after drawing a polymer melt or polymer solution from the tip of a capillary to a grounded collector [Sinha-Ray 2018]. The fine jets dry to form polymeric fibers, which are collected as a nonwoven web with specific architecture. The electrospinning process has been applied to a variety of polymers selected as the spinnable materials, as well as the fibers were collected on different substrates [Reneker et al. 1996, Chun et al. 1999, Kalayci 2002, Schaefer 1998, Schaefer 1998a, Tsai et al. 2002, Tsai et al. 2004, Yarin et al. 2014).

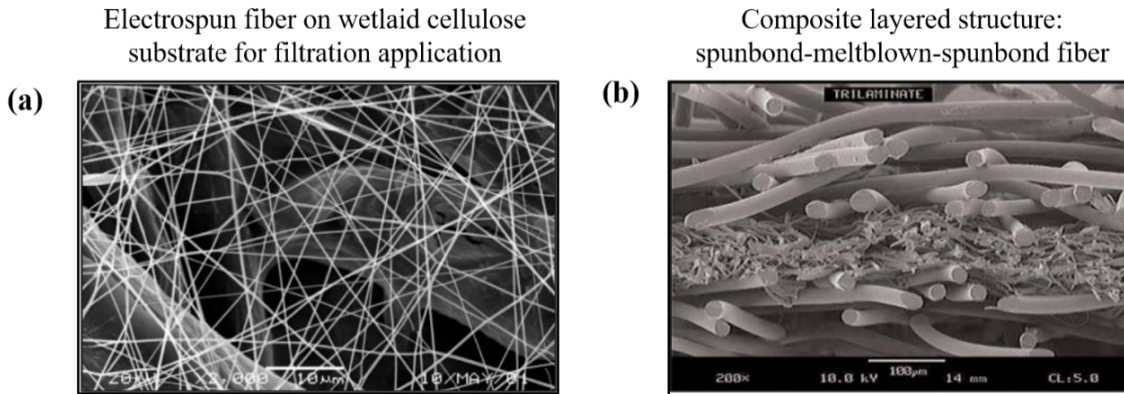


Figure 2.2: Scanning electron micrographs of nano- and micro fiber nonwovens. Panel (a) is the SEM image for electrospun nanofibers deposited on a wetlaid cellulose substrate for air filtration purposes [Grafe et al. 2003] and panel (b) is SEM image of composite spunbond-meltblown-spunbond nonwoven structure [Grafe et al. 2003] which allows one to elucidate relative fiber sizes as compared to nanofibers in panel (a).

Figure 2(a) shows a 10,000X magnification of scanning electron micrograph (SEM) of electrospun nanofibers of 250 nanometers in diameter [Grafe et al. 2003]. It shows the nanofibers collected on a substrate of cellulose which has diameters above 10 microns. The choice of the substrate depends on the requirements on mechanical properties, whereas the layering of nanofibers significantly controls the HEPA filtration efficiency and performance. Although the substrates provide appropriate functionality to the nanofiber webs, the parametric variation and control of operating conditions in the electrospinning allows the nanofiber generation with desirable filtration performances and characteristics due to the variation in fiber diameter. By choosing a suitable polymer and solvent system in electrospinning, nanofibers with diameters in the 50-2000 nm range can be formed. Fiber diameters can be varied and controlled. However, despite having unique advantages, electrospinning has few challenges from the viewpoint of

industrial production at a larger scale. It has very low productivity/output as reported in [Fedorova 2017, Luzhansky et al. 2003]. Also, unavailability of an effective system for solvent re-capture in electrospinning poses as a barrier to commercial profitability of its industrial upscaling. Limited availability of polymer-solvent combinations is also a factor from the industrial point of view as electrospinning is an solvent-mediated process [Sinha-Ray et al. 2018].

The limitations of electrospinning as described above make the meltblowing process a more suitable choice for mass-scale production of microfibers [Fedorova 2017], although there are few cases reported of producing nanofiber webs using meltblowing [Hassan et al. 2013]. Following Exxon corporation, the first company to commercially implement meltblowing in 1960, several other companies over the last few decades invested heavily in meltblowing process [Sinha-Ray 2012, Sinha-Ray et al. 2017], making it a market of the order of several billion US Dollars. The commercial viability and popularity of meltblowing stems from the low-cost mass-scale production with the advantage of the need-based operational tuning of parameters [Sinha-Ray et al. 2017]. Such important fiber web properties such as porosity, permeability, thickness, the degree of crystallinity and strength can be controlled comparatively easy in meltblowing comparing to electrospinning. Meltblown nonwoven fiber webs affect a wide range of applications and most of them are dependent on porosity and permeability of the fiber web [Li et al. 2001, Ellis et al. 1996, Schladitz et al. 2006, Wei et al. 2003, Mukhopadhyay et al. 2008, Jaganathana et al. 2008a, Jaganathan et al. 2008b, Hoferer et al. 2007, Lux et al. 2006, Koponen et al.. 1998]. The fiber web properties depend heavily on the operational conditions in the manufacturing process.

Although there are several other manufacturing processes available to make nonwoven webs, SEM images from two major manufacturing products, namely, [meltblown and spunbonded webs

shown in Fig. 2(b) to compare electrospun nanofiber webs and meltspun fiber webs [Grafe et al. 2003]. There are some similarities between electrospinning and the two meltspun processes. The processes begin with a liquid phase polymer and form fibers and webs directly in a one-step process, whereas the resulting products consist essentially of polymer fibers with no other binders, resins or additives [Luzhansky et al. 2003]. Additionally, other nonwoven processes generally employ subsequent mechanical or thermal binding processes, such as carding, hydroentanglement and needle punching, to name a few, to bond fibers within the web to each other. The variation of fiber diameter results in a significant variation of the basic web characteristics and properties of the nonwoven structure, such as thickness, surface-to-volume ratio, and basis weight. Later in this thesis, it will be described in detail how to estimate the effect of the operational conditions on such final product properties as the 3-D architecture, porosity, permeability, as well as the variation of the degree of crystallinity in the as-spun polymer fibers. Although electrospinning leads to an increase in the fiber surface area and a lower basis weight compared to the meltspun fibers, meltblowing has unique advantages of its own especially in the case of microfiber web production, as it is more suited for producing microfibers than to the nanofiber manufacturing [Fedorova 2017].

As the most popular and established method of nonwoven manufacturing for the last 50 years, meltblowing is similar to spunbond but produces finer filaments of smaller diameters. Although scarce, recently efforts have been made to produce meltblown nanofibers as well. A schematic of meltblowing process is shown in Fig. 2.1c. In this process an extruder forces a molten thermoplastic polymer through a row of fine orifices directly into two converging high velocity streams of heated air or other gas in order to form a stream continuous polymer jets. At the nozzle exit, the filament bundle attenuated by convergent streams of the high-velocity air is formed. Upon

attenuation, vigorous forward and backward movement happening due to the fiber stretching in the ambient air. The fibers are stretched and flapped throughout from the nozzle exit location up to the collection location on an uptake collector screen. The hot, high velocity air streams responsible for stretch the filaments. It subjects the filaments to drag and lift forces resulting in diameter attenuation. Meltblowing is a non-isothermal process. The polymer jets reveal two distinctive parts- a straight part of the initial jet up to 4 cm, and then a bending part due to onset of bending perturbation caused by turbulent eddies and the lift force [Sinha-Ray et al. 2010]. The filaments and air gradually cool as they move toward to the collector. The use of suction at the collector assists in web formation. The webs are then bonded by mechanical, thermal or chemical means at several stages, as per requirement of the end-product characteristics. Several mechanical bonding techniques, such as needle punching or hydroentanglement are used in the nonwovens industry. The fibers in the nonwoven web are thus entangled, twisted and upon rearrangement, create bonding and patterning required in the final product. Patterns and apertures in the collected fabric are produced by altering the design of the conveyor sleeve surface [Luzhansky et al. 2003]. However, in this thesis we consider only the fiber generation process from melt and solution blowing, whereas bonding techniques are not dealt.

Solution blowing, has unique advantages in the case of nanofiber and microfiber production depending on the choice of solvents and polymers. A schematic for subsonic single needle solution blowing is shown in Fig. 2.1b. It is one of newest techniques to produce polymer nanofibers on the industrial scale [Sinha-Ray et al. 2014, Sinha-Ray et al. 2014a, Kolbasov et al. 2016, Khansari et al. 2013]. Electrically-driven supersonic solution blowing has been proven to produce nanofiber webs less than 50 nm in diameter [Sinha-Ray et al. 2013a, Sinha-Ray et al. 2015a]. It facilitated the development of novel techniques for micro- and nanoparticle capture in the filtration

applications, which has immense potential for industrial production for high-value nonwoven fiber webs. Solution blowing can be considered as an offshoot of meltblowing due to its use of air blowing, but it also differs significantly from the latter. In solution blowing, polymer solution is fed through a die consisting of single or several orifices as a slow jet into a surrounding circular annular gas jet which may be subsonic, as well as supersonic. Solution blowing results in nanofibers as a contrast to meltblown fiber web which consists of microfibers. The subsonic solution blowing does not require any electrical voltage supply in distinction from electrospinning. The supersonic gas jet can be assisted with a high voltage supply applied at the nozzle exit similarly to electrospinning, whereas the Laval nozzle issuing the supersonic air jet and the collector screen are grounded. The annular air or gas jet stretches the polymer jet into continuous nanofibers. Similarly to meltblowing, the polymer jet is subjected to a vigorous stretching and bending instability, which dramatically attenuates the fiber size [Sinha-Ray et al. 2010, Yarin et al. 2014].

As the upsurge in nonwoven production in the last decade became prominent, so did the issues of the optimization of the operational parameters required for value-based production. Prior to that, nonwoven industry operated aiming at the manufacturing cost reduction to succeed in the competitive market of nonwoven products. However, high-value nonwoven products became important with the extensive expansion and applications of nanotechnology. The more sustainable model of business depends on the capacity to produce complex nonwoven products required for industrial applications. This is termed as business-on-demand. The necessary tool to achieve that is to acquire knowledge of the optimal control parameters of the manufacturing processes and understand the physical mechanisms responsible for the nonwoven formation. The current trial and error approach towards modifying nonwoven products using existing setups is extremely expensive. Thus, scientific prediction of the effect of the operational parameters on the

optimization of nonwoven manufacturing is in focus in the last decade in academia as well as industry. Accordingly, there might be several ways to approach the existing manufacturing optimization issues that can serve nonwovens industry. The goal would be to introduce a new functioning system which could be financially viable, or to establish an optimized production line in order to meet the business demands using the currently existing manufacturing systems. This thesis aims at the process parameters optimization.

Solution blowing was recently up-scaled [Kolbasov et al. 2016] from pilot-scale to mass-production industrial scale [Kolbasov et al. 2016]. The understanding of the physics responsible for the polymer nonwoven formation is necessary to meet the high-end product specifications, as well as satisfy and supply market demands according to the “on-demand-business” model [<https://www.reuters.com/brandfeatures/venture-capital/article?id=15814>, <https://www.marketwatch.com/press-release/global-spunbond-nonwoven-market-trends-demand-production-sales-supply-analysis-forecast-to-2023-2019-04-04>]. Nonwovens with a desirable range of physical properties, such as strength, stiffness, porosity, permeability, polydispersity, are required, which could be achieved by the operational parameter variation. As a result, earlier efforts have been made experimentally to observe the effect of several operating conditions in nonwoven manufacturing on the final product [Hassan et al. 2013, Chhabra et al. 1996, Tate et al. 1998, Barilovits 2018, Begenir et al. 2004, Uyttendaele et al. 1990, Xiang et al. 2009, Xiang 2007, Yarin et al. 2007]. An example is given in Fig. 2.3 which illustrates the effect of variation of the operating conditions on some of the fiber web properties resulting from the meltblowing process.

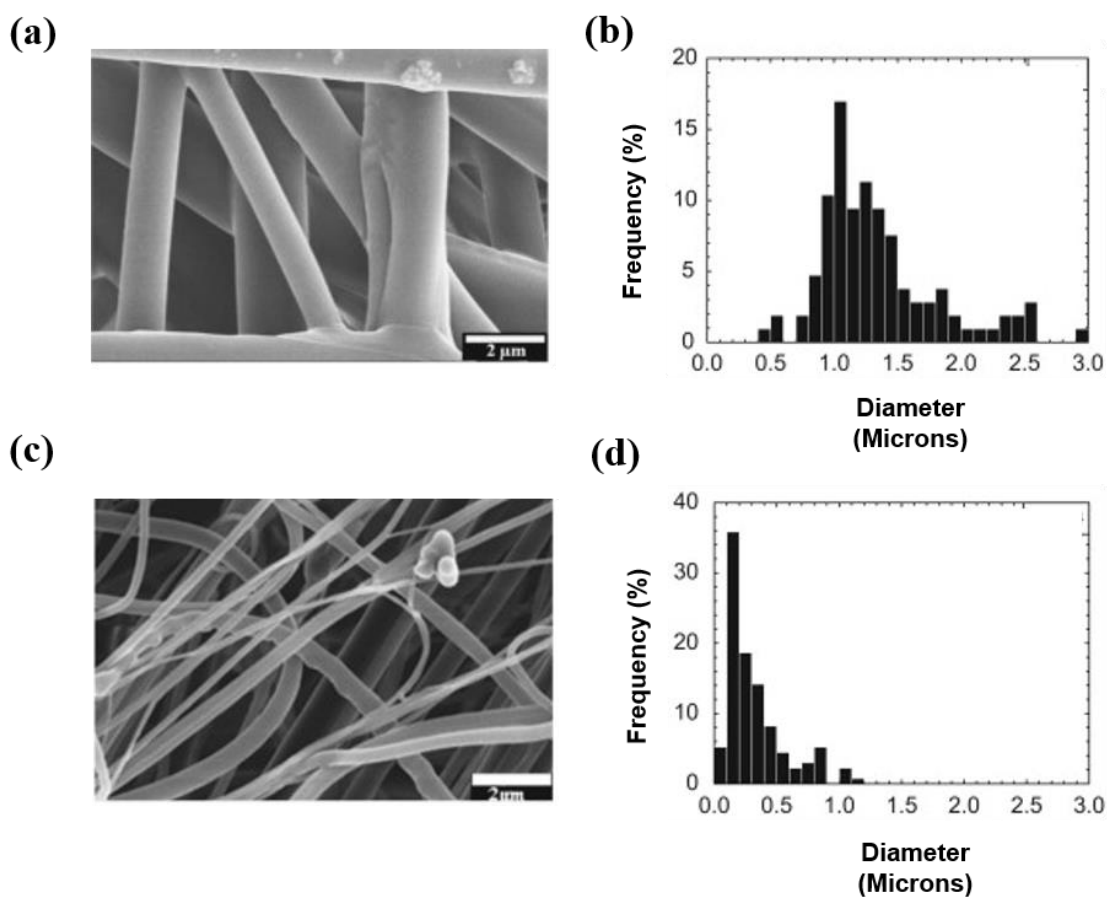


Figure 2.3: Observation of the effect of polymer flow rate on meltblown fibers (Hassan et al. 2013). Panel(a) and (b) are the corresponding SEM micrograph and fiber diameter distribution obtained using fibrous meltblown web formed at the polymer melt throughput of 0.214 ghm (gms per hole per minute) with a collector screen velocity of 15.6 m/min. The basis weight reported for this nonwoven fabric was 20 g/m² [Hassan et al. 2013]. Panels (c) and (d) are the SEM micrograph and the fiber diameter distribution for the meltblown laydown produced with polymer melt throughput of 0.0125 gms per nozzle/hole per minute with the other parameters practically unchanged. The basis weight reported for this nonwoven fabric was reduced to 2.5 g/m² [Hassan et al. 2013].

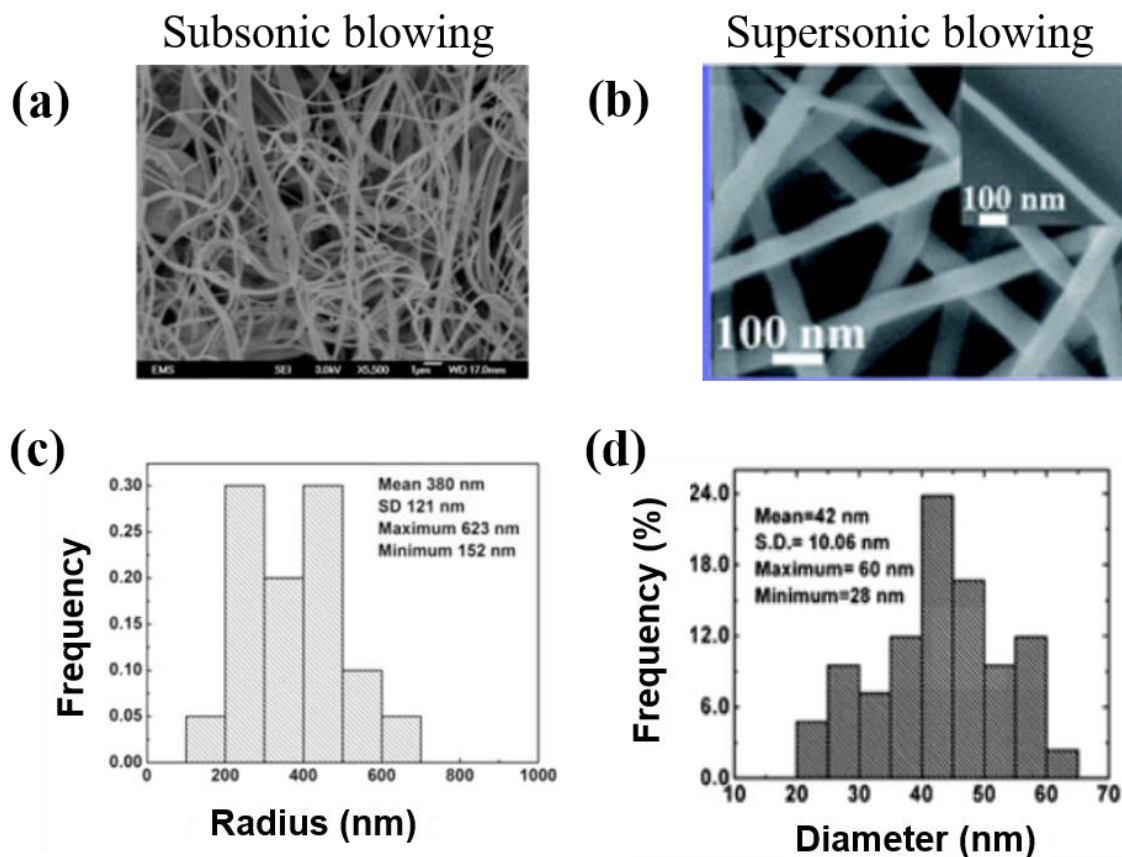


Figure 2.4: Scanning electron micrograph of solution-blown nanofibers and the corresponding size distribution. Panels (a) and (c) are SEM image and radius distribution of subsonic solution blown fiber web, respectively, as reported in [Sinha-Ray et al. 2015a]. Panels (b) and (d) are the same for the electrically-assisted supersonically blown fiber web as reported in [Sinha-Ray et al. 2013a].

Comparing Figs. 2.3 and 2.4, it can be visible that that solution-blown fibers are typically in the nanometer range in contrast to the meltblown fibers which are mostly of the order of several microns.

2.3 Thesis objectives: significance of the work

Most of the manufactured nonwoven products such as meltspun fabrics, are usually compacted before being used in applications, whereas solution-blown nonwovens are not. Nevertheless, the porosity and permeability of compacted nonwoven materials are still pre-determined by the three-dimensional structure and porosity of the original fibrous laydown. As to our knowledge, the three-dimensional structure, porosity, permeability and polydispersity of as-formed meltblown and solution nonwovens and their relation to the operational parameters have not been explored so far. Effects of these parameters on the degree of crystallization in polymer jets have been studied earlier, but a computationally easier and mathematically robust approach in the melt- and solution blowing modeling has not been implemented so far. Accordingly, the aims of this work are related to the above-mentioned factors. Viscoelastic behavior of thermoplastic or soluble polymeric liquid has a significant effect on jet dynamics and that directly affects the end result ,i.e., the fiber properties. There are several assumptions that were put forward in literature due to unavailability of conclusive data and the lack of sufficient understanding of the physical phenomena. Accordingly, this work aims at the elucidation and description of the underlying physical phenomena involved in nonwoven manufacturing. Although solution blowing is similar to meltblowing and both involve three-dimensional stretching and bending of viscoelastic polymer jets entrained by the surrounding high-speed air jet, the fundamental difference is that meltblowing is a non-isothermal process, whereas the solution blowing is the isothermal one. In meltblowing polymer jet and hot air are gradually cooled down by the surrounding air. Accordingly, in meltblowing polymer jet solidifies, whereas in solution blowing solvent evaporates and polymer jet precipitates. These two processes form solid polymer micro- or nanofibers, respectively. Therefore, the motivation of the present work also includes modeling of solution blowing and

subsequent experimental investigation under controlled conditions for verification. The numerical code employed in the present work is an extension of the previously developed code by Professor Yarin's group. Moreover, here using the newly developed post-processing tools, the three-dimensional structure of collected fibrous laydown, its fiber size and mass distributions, as well as the corresponding porosity and permeability are predicted. A realistic description of the dynamics of bending perturbations should account for the interplay of jet formation and diameter attenuation in both meltblowing and solution blowing, which determine the pattern of bending perturbation propagation over polymer jets. The present work aims all these physical aspects, as well as add the new one – the prediction of the degree of crystallinity in the final fiber web product.

2.4 Thesis structure

The thesis is structured as follows. Chapter 1 is the abstract and includes a brief overview of the work related to nonwoven generation. Chapter 2 is the introduction to several nonwoven manufacturing processes and depicts the requirement and the potential of predictive process optimization of several physical processes of micro- and nanofiber formation, as well as the post-processing aspects. Chapter 3 includes a detailed literature survey to describe the state-of-the-art in the technological research and development used to facilitate the nonwoven manufacturing. Chapter 4 includes the algorithms and numerical simulation methods that are proposed for nonwoven production processes in meltblowing. Because meltblowing is the process where rheology and thermal regimes are inter-dependent the mathematical model developed it incorporates all these aspects. A novel technique to predict the 3-D architecture and thus porosity and permeability of meltblown fiber mats and their dependence on sensitive operational

parameters is also included in Chapter 4. Chapter 5 deals with solution blowing process and elucidates the dependence of the abovementioned laydown properties on sensitive operational parameters. It also contains comparison with experimental data. Chapter 6 includes a novel theory of thermally-induced and flow-induced polymer crystallization in meltblowing process and predicts the dependence of the degree of crystallinity and its distribution in fibrous aydown for several processing conditions. Finally, conclusions are drawn in Chapter 7.

Chapter 3: BACKGROUND AND LITERATURE REVIEW

3.1 Meltblowing.

As mentioned in the introductory chapter, in meltblowing the issued slow-moving jet of molten polymer is subjected to direct stretching by a coaxial high-speed air jet. Bending instability of thin polymer jets is a source of further additional stretching, as is evident from the works discussed below.

One of the first seminal works on studying behavior of a high-velocity viscous liquid jet moving in gas suggested that the jet experiences a distributed lateral force which in turn increases the bending perturbation [Weber et al. 1931] resulting in bending and flapping of the jet and eventual capillary break-up. The important developments in understanding the meltblowing process were achieved by Exxon Corporation, following the initial experimental observations by V.A. Wentz [Wentz 1954, Wentz et al. 1956]. Experimental investigations intended to address the polymer jet behavior in conjunction to turbulence and rheology were attempted by [Breese et al. 2003, Pinchuk 2012]. The behavior of the polymer jet in meltblowing has been demonstrated to be transient and there is a clear transition from an initial straight segment to a non-straight/bent segment within 4-5 centimeters [Breese et al. 2003, Sinha-Ray 2012] from the nozzle exits of the polymer die nosepiece. This suggested that despite a strong turbulent pulsations in the surrounding gas flow, there is an initial straight part of the jet which is caused by the high bending stiffness. This is where polymer rheology plays a significant role. The jet-jet interactions and merging of jets occur at different instances and were studied by [Marla et al. 2003, Marla et al. 2004]. One of the significant effects on the polymer jet behavior is caused by the interaction with the turbulent eddies formed due the strong high-speed gas flow. Initially, a series of publications suggested the stretching and bending of liquid polymeric jets were only due to the turbulent pulsations [Gotz et

al. 2007, Marheineke et al. 2006]. The effect of the drag force fluctuations resulting from the turbulent pulsation on the polymer jet was discussed and developed using a similar approach [Bonilla et al. 2007]. However, the experimental investigations by [Marla et al. 2003, Uyttendaele et al. 1990, Sinha-Ray et al. 2011, Marla et al. 2004, Sinha-Ray 2012], suggested that the cause of the polymer jet behavior could not be reduced only to the interaction with turbulent eddies and the interaction with the mean flow is also significant. Additionally, the thermal regime of the jet dictates the change in the rheological properties of polymer melt in-flight and that in turn affects several characteristics of the collected nonwoven laydowns as was studied by [Uyttendaele et al., 1990, Marla et al. 2003, Marla et al. 2004]. Thus, several studies were made to provide ground for a realistic description of the process that can account for the propagation of bending perturbations in the high-speed polymer jets. One of the first attempt to include basic rheological behavior in the description of the thermal regime was done by [Uyttendaele et al. 1990] considering a simple model of a single straight jet. Some preliminary attempts to include effects due to turbulence were done by [Chhabra et al. 2004].

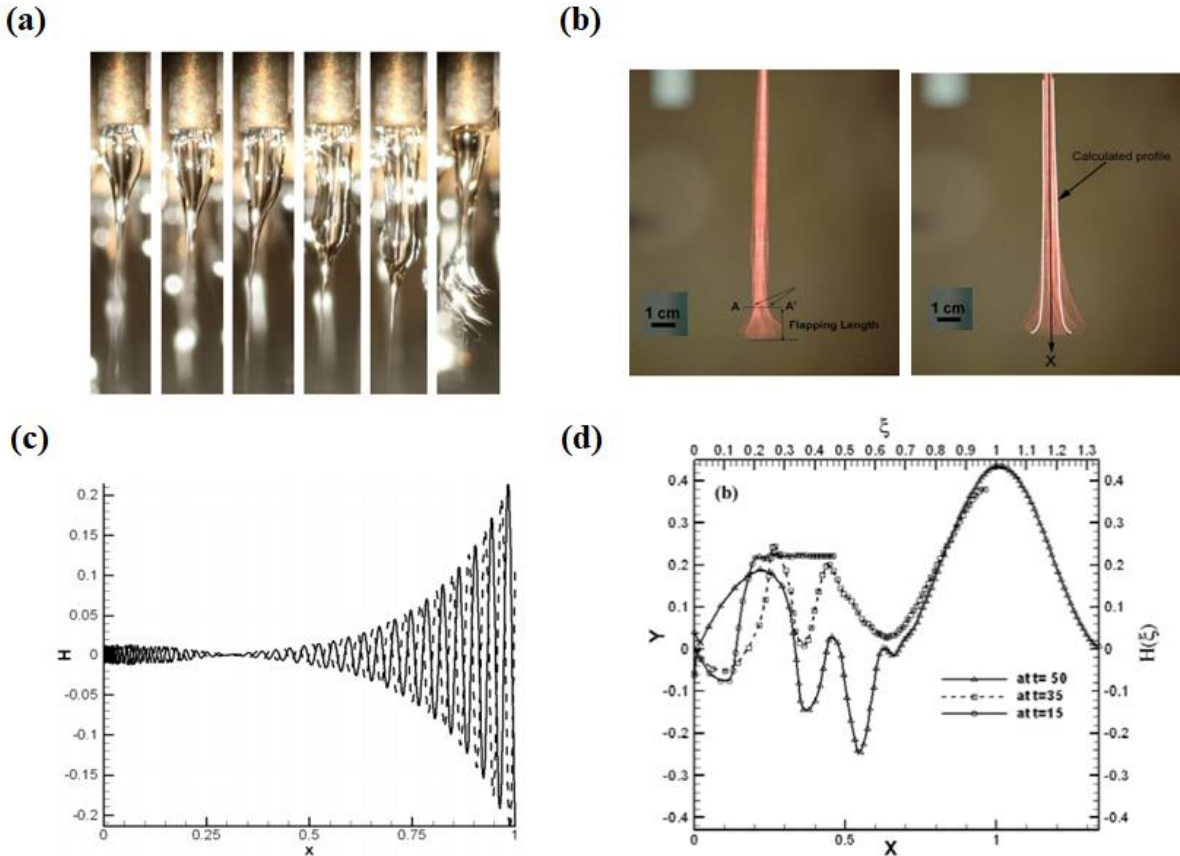


Figure 3.1. Images of meltblowing taken at the experimental facility at the Nonwovens Institute [Fedorova 2017] are shown in panel (a) where the distinct straight and bent parts of a molten polymer jet are clearly visible. Panel (b) shows in two parts the snapshots taken from a non-stretchable and flexible threadline subjected to turbulent pulsations to determine flapping length and the envelope configuration [Sinha-Ray et al. 2010]. Panel (c) shows the two snapshots of the travelling wave formed due to bending perturbations of polymer jet magnified by the distributed aerodynamic lift force [Sinha-Ray 2012]. Panel (d) shows the in-flight configuration of a single polymer jet and its evolution in non-isothermal planar blowing [Sinha-Ray 2012].

However, the dynamics of a liquid thin jet moving in air or gas is much more complex than only in-flight thinning and attenuation of the jet diameter [Sinha-Ray et al. 2015a]. Two of the early significant works were done by Weber and Debye [Weber et al. 1931, Debye et al. 1959] where a linearized problem of coupled evolution of the three-dimensional shape of a jet due to interactions with the surrounding gas was addressed. Stability analysis carried in these works suggested that the bending instability actually happens in a specific frequency range of the perturbations. It was proposed that for a comparatively high-velocity inviscid jet, the bending instability reveals exponential growth [Debye et al. 1959, Sinha-Ray 2015a]. This was understood as the variation of gas pressure on convex and concave parts of the jet resulting in a distributed lift force causing the bending phenomena [Yarin 1993] and [Entov et al. 1984]. The latter two works also accounted for the viscoelastic rheological behavior of liquid jets and introduced quasi-one-dimensional models of the jet dynamics, which significantly simplifies the dynamics equations. This approach is applicable to bending, rather than only to straight jets attempted by [Marla et al. 2003, Marla et al. 2004]. Based on the quasi-one-dimensional models of the jet dynamics derived by [Yarin 1993] and [Entov et al. 1984], a series of publications appeared which address the viscoelastic wave propagation on meltblowing jets [Sinha-Ray et al. 2010, Yarin et al. 2010, Yarin et al. 2011, Yarin et al. 2013]. In these works the transition from a straight to a non-straight part of the jet was also addressed in order to describe the effect of the bending instability on the jet behavior in flight. In addition these works also accounted for the drag force, the Bernoulli lift force and the net hydrodynamic forces in full detail. This series of works developed the model that accounts for the viscoelasticity of polymer melts, predicts thermal profile along the jet and accounts for polymer jet interaction with the surrounding high-speed hot air flow, and polymer solidification. The results revealed the polymer jet configurations in flight, as well the overall

patterns of laydowns deposited on the moving screen. Figure 3.1 shows some of the experimental and numerical results obtained by [Fedorova 2007, Sinha-Ray et al. 2010] where a visible bending perturbations and a blow-up flapping region due to turbulent fluctuations transmitted to the threadline was recorded experimentally and compared with the predicted three-dimensional jet conformation. It was also shown that the description of the initial part of the jet is in the framework of the hyperbolic partial differential equation and at the threshold to the onset of bending perturbation, the equations become an elliptic. Meltblowing was essentially reduced to a problem of “elastic sound” propagation through the jet and the onset of the growing bending perturbations was pinned to the transition in the governing equation type [Sinha-Ray 2012, Yarin et al. 2011].

An additional process which was modeled in the framework of the quasi-one-dimensional equations of the dynamics of thin viscoelastic liquid jets is electrospinning of polymer nanofibers, where in contrast to meltblowing, the electric Coulombic repulsion force was the factor responsible for jet the bending instability, as shown in [Reneker et al. 2002, Reneker et al. 2007, Yarin et al. 2001]. It is emphasized that in the case of electrospinning jets, the repulsion force was shown to be proportional to the local curvature of the polymer jet axis and this is similar to the distributed aerodynamic lift force in melt- and solution blowing as suggested by [Yarin 1993; Entov et al., 1984].

3.2 Solution blowing

Blowing of polymer solutions has been proven to hold immense potential for its wide-scale applicability and scalability to the large-scale industrial production of nanofibers [Kolbasov et al. 2016, Sinha-Ray et al. 2015, Khansari et al. 2013]. It was extensively studied experimentally [Medeiros et al., 2009, Sinha-Ray et al. 2010a]. Although solution blowing could be considered as an offshoot of the meltblowing process, it is an isothermal process and results in nanofiber

formation in distinction from microfibers produced by meltblowing process [Sinha-Ray et al. 2010, Yarin 2014]. Solution blowing was used for manufacturing of nanofibers for a wide range of applications such as microfiltration [Zhang et al. 2003] and biomedical applications [Khansari et al. 2013]. Additionally, production of nanotubes stems from the coaxial nanofibers produced by solution blowing as shown by [Oliveira et al. 2012, Sinha-Ray et al. 2010]. Realizing the importance of this process, several groups attempted to formulate the physical mechanism responsible for the solution blowing using experimental and numerical investigations [Triantafyllou et al. 1992, Connel et al. 2007, Shelley et al. 2005], as mentioned in [Sinha-Ray 2011].

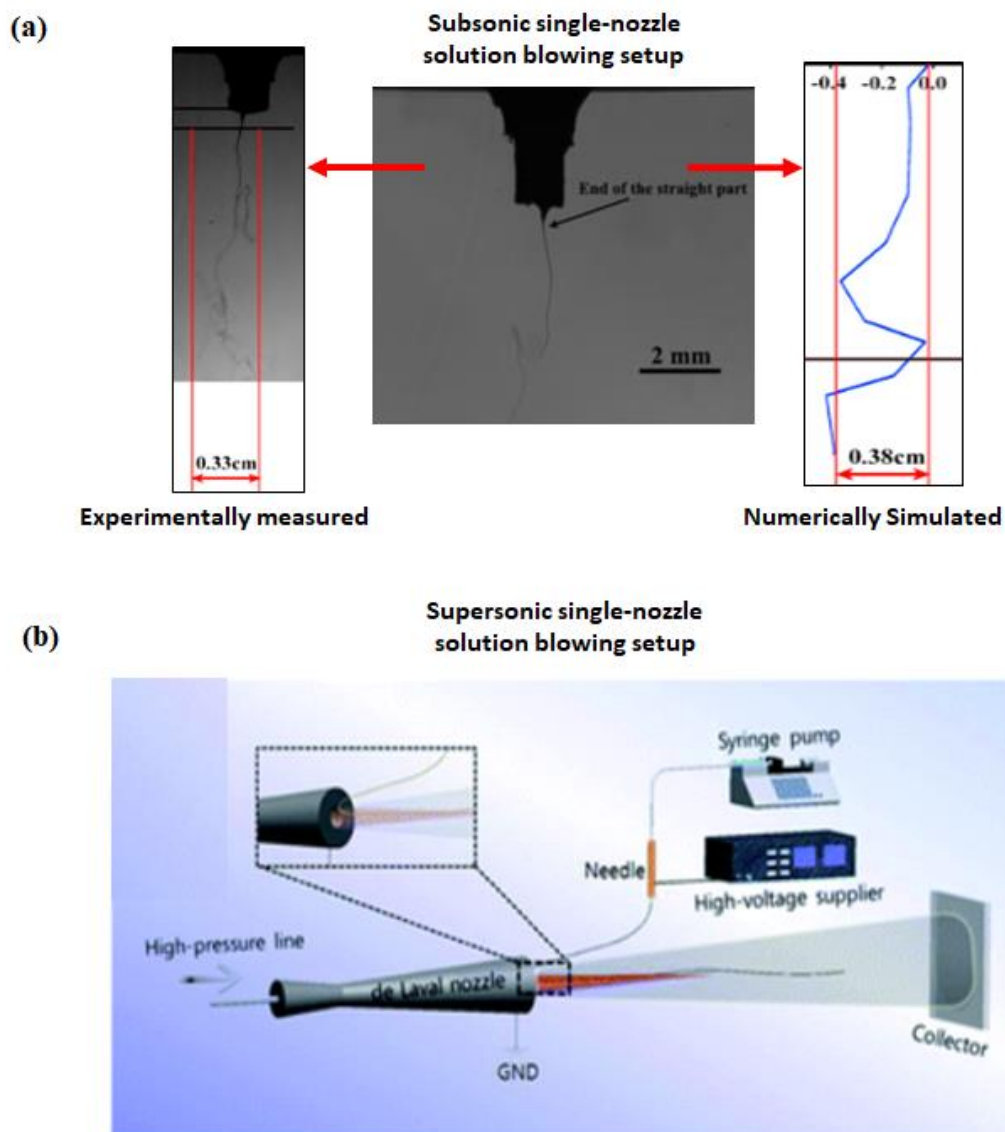


Figure 3.2. Schematic of solution blowing process and results from numerical and experimental investigation of the process using high-speed camera, as per [Sinha-Ray et al. 2015, Sinha-Ray 2016]. Panel (a) shows the image of a single-nozzle polymer solution jet captured by the high-speed camera, and panel (b) is a schematic of electrically-assisted supersonic blowing of polymer solutions that results in fibers less than 50 nm. [Sinha-Ray et al. 2016].

Similarly to meltblowing, the flag flapping phenomena in gas flow was investigated as a deterministic problem of flow-induced vibrations [Argentina et al. 2005, Paidoussis et al. 1966] of non-turbulent nature [Williamson et al. 2004]. Some of these works accounted for bending stiffness of flexible flag to describe the flapping mechanism and proposed the von-Karman vortex shedding to result in lateral forces responsible for the bending even if later experimental measurements suggested a relatively small vortex-shedding effect in reality. The description of the flapping dynamics was reduced a PDE of the fourth order which fails to describe flapping phenomena due to truncation of the higher order terms responsible for the obstruction effect.

Turbulent high-speed liquid jets moving through gas were studied by several groups [Ziabicki et al. 1976, Yarin 1993, Ziabicki et al. 1985]. The description of the pulling drag and lift forces using both theoretical and empirical formulations was included. These works resulted in threadline models using the framework of the boundary layer theory, and experimental investigations revealed good comparison with predicted characteristics of the liquid jet behavior [Ziabicki et al. 1976, Yarin 1993, Ziabicki et al. 1985, Loitsyanskiy 1966]. That was the first set of works that provided the tool to calculate drag force on liquid jets moving in gas which were relevant to all three types of nonwoven manufacturing, such as melt spinning, dry spinning or wet spinning processes. The breakthrough in the describing of the bending jet mechanism happened when the theoretical foundation was laid down as the seminal quasi-one-dimensional approach for thin liquid jets by [Entov et al. 1984, Yarin 1993]. This approach was later used by [Sinha-Ray et al. 2015] and the theoretical formulation also incorporated the viscoelastic behavior of polymer solution jets subjected to turbulent co-axial gas stream. The proposed mechanisms were investigated both numerically and experimentally by [Sinha-Ray et al. 2015, Yarin 2014], which established a realistic comparison between the predicted and observed characteristics of the

process with a very high degree of accuracy, as seen in Fig. 3.2a. Also, for high-efficiency filtration applications of nanofibers it was proposed by [Sinha-Ray et al. 2015, Sinha-Ray et al. 2016] to manufacture nanofibers of the order of 50 nm using electrically assisted supersonic blowing of polymer solutions as shown in Fig. 3.2b.

3.3 Crystallization in melt spinning processes

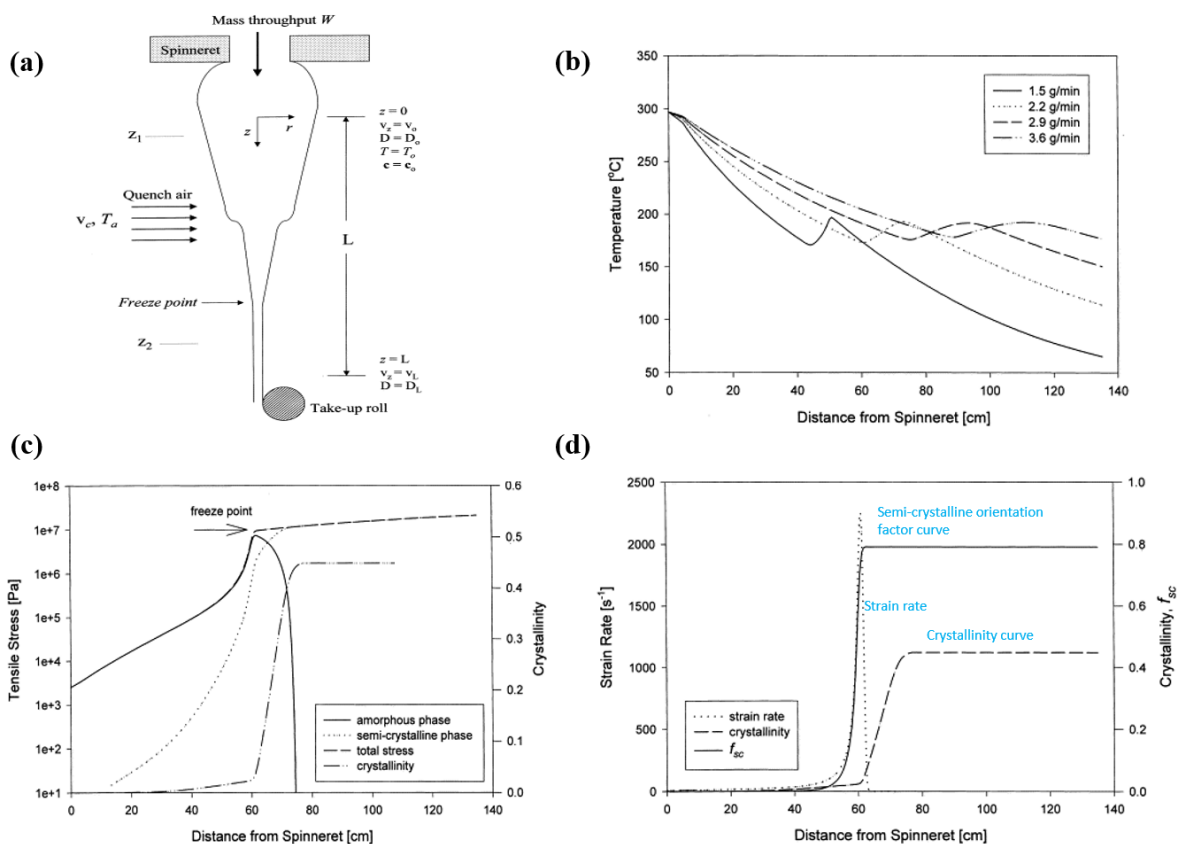


Figure 3.3. Investigation of melt spinning process and predicted degree of crystallization in viscoelastic fluid (the Giesekus fluid) jets, as reported in [Ziabicki et al. 2000.] Panel (a) shows a schematic of modeling of melt spinning crystallization process in [Ziabicki et al. 2000]. Panel (b) shows the jet temperature profile with different mass throughputs at a constant take-up speed, as per [Ziabicki et al. 2000]. Panel (c) shows the contribution of the amorphous and the semi-

crystalline phases to the tensile stress and the resultant degree of crystallinity of the fiber, as per [Ziabicki et al. 2000]. Panel (d) elucidates the profiles of strain rate, the degree of crystallinity, and semi-crystalline orientation factor in the jet in-flight, as per [Ziabicki et al. 2000].

The process of crystallization in meltblowing directly affects the laydown characteristics and has been a subject of experimental and theoretical studies carried out in the last few decades. Several experimental observations and data are available from [Moharir et al. 1982, Talbot et al. 1987, Okuno et al. 1992, Liu et al. 2013, Lau et al. 2013]. Especially in the applications related to filtration and fluid transport, a strong effect on gas permeability due to variation in the degree of crystallinity in fibers was reported in [Liu et al. 2013]. The mechanical properties such as tensile, compressive and shear properties, as well as fracture energy and fracture toughness of thermoplastic polymers such as PEEK 150p and APC-2 [Liu et al. 2013] were observed to depend on the degree of crystallinity. The strong dependence of plasma susceptibility and dyeability characteristics of PET and Nylon-66 fibers as a function of the degree of crystallinity in fibers were observed to be decreasing with the increasing degree of crystallinity up to a threshold value, and then an increase was reported in [Okuno et al. 1992]. From the standpoint of material design and fabrication, membranes with comparatively high degree of crystallinity and sufficient mechanical properties are required to withstand harsh operating conditions of commercial gas separation processes, as reported in [Lau et al. 2013]. The degree of crystallinity in polymer fibers also strongly affects the performance characteristics of the fiber-reinforced concrete and was investigated in details by [Morozova et al. 1998]. Due to the wide range of applications involving fibrous structures, several attempts were made to estimate and theoretically predict the degree of crystallinity in fibers by developing dynamic models of the on-line crystallization process in

industrial fiber production setups. The coupled problems on threadline dynamics and flow-induced crystallization associated with melt spinning were studied in the early experimental and theoretical works [Yarin et al. 1992, Yarin 1993, Ziabicki et al. 2010, Ziabicki 1976, Ziabicki et al. 1988a]. Numerical modeling of pneumatic melt spinning process was conducted by applying the $k-\epsilon$ turbulence model to the gas blowing, and initial attempts to account for non-linear viscoelasticity are available in [Jarecki et al. 2012]. An on-line crystallization theory was developed by [Ziabicki et al. 1988, Ziabicki et al. 1988a, Ziabicki 1976] for high-speed fiber spinning processes where the rheological framework behavior was modelled by means of the Giesekus fluids subjected to shear-induced crystallization in melt spinning processes. Later, the concentrated ('neck-like') deformation during the high-speed melt spinning was theoretically studied by [Ziabicki et al. 2001] where it was shown that the gradient of the elongational viscosity along the spinline was the most significant factor responsible for the deformation. It was proposed by [Ziabicki et al. 2001] that stress-induced polymer crystallization acts as a potential source of the rapid viscosity increase in melt spinning processes and also the on-line polymer jet temperature was shown to be affected by the occurrence of the stress-induced crystallization. Theoretical models for melt spinning were proposed by [Meerveld et al. 2007] to describe the quiescent nucleation and growth in the case of spherulitic crystal structure, as well as the flow-induced nucleation and longitudinal growth kinetics for crystals of fibrillary structure. A viscous stress profile was used to investigate the influence of crystallization, as well as of the glass transition characteristics on the rheological properties of the polymer jet in flight [Meerveld et al. 2007]. A continuum model for the flow-induced crystallization in injection molding of polymers was proposed by [Kim et al. 2005] where the degree of crystallinity and skin-layer thickness of the microstructure in semi-crystalline polymer were numerically simulated. A nonlinear rheological constitutive equation was used by

[Kim et al. 2005] to quantify the entropy reduction in the oriented melt and the resulting elevated equilibrium melting temperature. The elevated equilibrium melting temperature was used to determine the extent of the flow-induced crystallization occurring in the injection molding process.

Chapter 4: NUMERICAL PREDICTION OF THE EFFECT OF UPTAKE VELOCITY ON THREE-DIMENSIONAL STRUCTURE, POROSITY AND PERMEABILITY OF NMELTBLOWN NONWOVEN LAYDOWN

(Previously published as Ghosal, A., Sinha-Ray, S., Yarin, A. L., and Pourdeyhimi, B. (2016)

Numerical prediction of the effect of uptake velocity on three-dimensional structure, porosity and permeability of meltblown nonwoven laydown. *Polymer*, 85: 19-27.)

Abstract

This work describes the first detailed model of meltblowing process which allows prediction of such integral laydown properties as thickness, porosity and permeability. Also, such laydown properties as the detailed three-dimensional micro-structure, fiber-size distribution and polymer mass distribution are predicted. The effects of the governing meltblowing parameters on the variation of all these laydown properties are accounted for, with the influence of the collector screen velocity being in focus. For this aim numerical solutions of the system of quasi-one-dimensional equations of the dynamics of free liquid polymer jets moving, cooling and solidifying when driven by surrounding air jet are constructed. Multiple polymer jets are considered simultaneously when they are deposited on a moving screen and forming a nonwoven laydown. The results reveal the three-dimensional configuration of the laydown and, in particular, its porosity and permeability, as well as elucidate the dependence of the laydown structure on the forming conditions, in particular, on the velocity of the screen motion. It is shown and explained how an increase in the velocity of the collector screen increases porosity and permeability of the meltblown nonwoven laydown.

4.1. Introduction

Nonwoven industry is expected to reach \$7.1 billion by 2016 with meltblowing being the most important process employed [[Gangloff 2013; http://www.nonwovens-industry.com/issues/2013-03/view_features/reportus-nonwovens-fabric-demand/](http://www.nonwovens-industry.com/issues/2013-03/view_features/reportus-nonwovens-fabric-demand/)]. In meltblowing process polymer melt is issued through multiple specially designed dies in a nosepiece and hot air is supplied coaxially at a very high velocity ($\sim 150\text{--}200$ m/s) [Bresee et al. 2003, Pinchuk 2012, Uyttendaele et al. 1990, Marla et al. 2003, Marla et al. 2004]. The hot air jets pull the polymer jets. In addition, the latter undergo a vigorous bending instability, which results in flapping and looping and continues to elongate the polymer jets. In parallel, cooling and solidification proceed resulting in microscopic solidified polymer fibers being collected on a screen as a nonwoven laydown. Although meltblowing is more than 60 years old, an in-depth research of the physical mechanisms of the process started only in the 1980s. Threadline dynamics associated with meltblowing were studied in the early experimental and theoretical works [Ziabicki 1976], [Ziabicki 1985]. Several empirical correlations were developed to calculate the drag force and the heat transfer coefficients at the surface of molten polymer jets moving with high speed relative to gas. Different studies revealed several important aspects of meltblowing [Bresee et al. 2003, Pinchuk 2012, Uyttendaele et al. 1990, Marla et al. 2003, Marla et al. 2004, Chhabra et al. 1996, Xin et al. 2012, Xin et al. 2012a]. The physical mechanism of meltblowing was studied in the previous works of this group and a detailed model was proposed with an ultimate goal to predict properties of the resulting laydown [Sinha-Ray et al. 2010, Yarin et al. 2010, Sinha-Ray et al. 2011, Sinha-Ray et al. 2013, Sinha-Ray et al. 2014]. Solution blowing, the process in which polymer solutions are blown by surrounding high-speed air jets, which results in pulling, bending, solvent evaporation,

solidification and formation of nanofibrous nonwoven laydown, was also studied recently [Sinha-Ray et al. 2015].

Meltblown nonwoven materials find several important applications, and most of them are dependent on porosity and permeability. In Ref. [Li et al. 2001] nonwoven PET matrices were used as tissue engineering scaffolds. It was shown that smaller pores in the matrix allowed faster and better proliferation of ED₂₇ and NIH 3T3 cells, while larger pores resulted in poor proliferation and agglomeration of cells. Porosity and permeability of nonwoven mats also determine nonwoven performance in the personal care [Ellis 1996], the acoustic-protection [Schladitz et al. 2006], oil-absorbent [Wei et al. 2003], and breathable fabric [Mukhopadhyay et al. 2008] applications. Accordingly, several methods were developed to determine permeability and porosity of meltblown nonwoven materials, in particular, digital volumetric imaging [Jaganathana et al. 2008, Jaganathana et al. 2008a], MRI [Hoferer et al. 2007], and X-ray tomography [Lux et al. 2006]. In Ref. [Koponen et al. 1998] permeability of nonwoven materials was found using ab initio calculation.

It should be emphasized that meltblown nonwovens are usually compacted before being used in applications. Nevertheless, the porosity and permeability of compacted nonwoven materials are still pre-determined by the three-dimensional structure and porosity of the original laydown. As to our knowledge, the three-dimensional structure, porosity and permeability of as-formed meltblown nonwovens and their relation to the processing conditions have not been explored so far. In the present work a systematic study of porosity and permeability of meltblown nonwoven laydown formed on a moving collector screen is undertaken to relate them to the governing parameters of the process. The theoretical background is introduced first. Then, the results of the numerical solution are presented and discussed. Finally, conclusions are drawn.

4.2.Theoretical background:

The theoretical background of the present work is described in detail in the previous works of this group [Sinha-Ray et al. 2010, Yarin et al. 2010, Sinha-Ray et al. 2011, Sinha-Ray et al. 2013, Sinha-Ray et al. 2014]. The schematic which visualizes the meltblowing process in the context of the model developed in the present work is shown in Fig. 4.1a. In addition, the schematic which illustrates the polymer jet/air jet interaction is shown in Fig. 4.1b. In brief, a polymer jet in

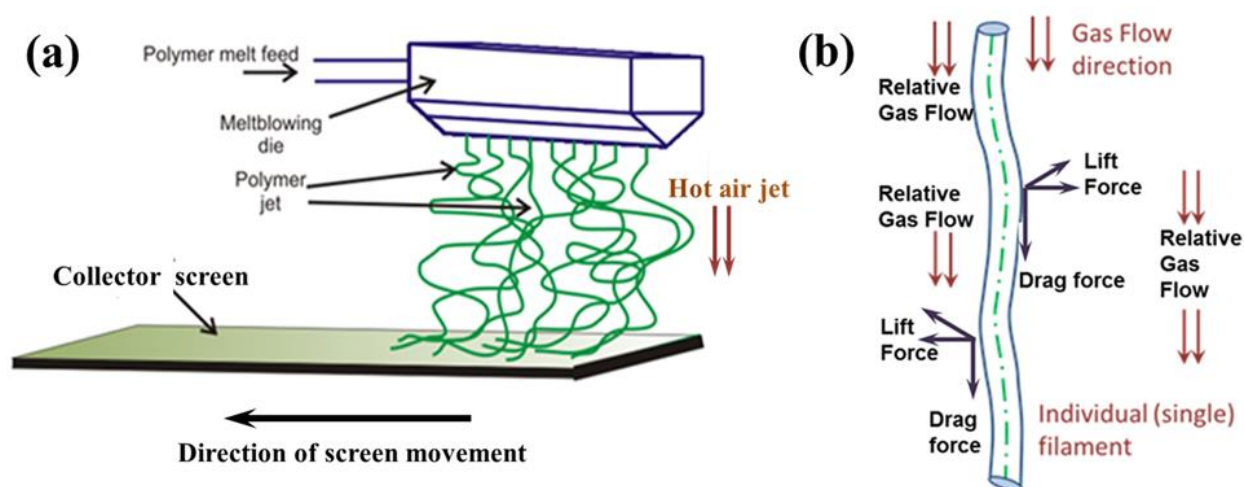


Fig. 4.1. (a) Schematic of meltblowing process: the overall view. (b) Schematic of a single polymer jet and its interaction with the surrounding air jet.

meltblowing process possesses a short straight part near the die and a much longer bending part up to the collector screen. In the straight part (~ 1 mm long) polymer jets are still too thick to bend, since their bending stiffness is still high. So, the straight parts of polymer jets are stretched by the surrounding high-speed air jets. Accordingly, the polymer jets undergo strong elongational flow and their diameters are reduced from about $100 \mu\text{m}$ to $8 \mu\text{m}$ [Sinha-Ray et al. 2013]. Right after the straight part of the polymer jet becomes thin, its bending stiffness (depending on the cross-sectional jet radius a as the fourth power, i.e. a^4) decreases dramatically, and a vigorous bending

driven by the aerodynamic forces begins. Both straight and bending parts of polymer jets are described in the framework of the quasi-one-dimensional equations of the dynamics of free liquid jets moving in air, with the continuity and momentum balance equations for an individual three-dimensional polymer jet being as follows [Sinha-Ray et al. 2010, Yarin et al. 2010, Sinha-Ray et al. 2011, Sinha-Ray et al. 2013, Sinha-Ray et al. 2014, Yarin 1993, Yarin 2014].

$$\frac{\partial \lambda f}{\partial t} + \frac{\partial f W}{\partial s} = 0 \quad (4.1)$$

$$\frac{\partial \lambda f \mathbf{V}}{\partial t} + \frac{\partial f W \mathbf{V}}{\partial s} = \frac{1}{\rho} \frac{\partial P \boldsymbol{\tau}}{\partial s} + \lambda f \mathbf{g} + \frac{\lambda}{\rho} \mathbf{q}_{\text{total}} \quad (4.2)$$

In Eqs. (4.1) and (4.2) t is time, s is an arbitrary parameter (coordinate) reckoned along the jet axis, $f(s,t)=\pi a^2$ is the cross-sectional area (the cross-section is assumed to stay circular even in bending jets, as shown in [Yarin 1993]), W is the velocity of polymer melt along the jet relative to a cross-section with a certain value of s , the stretching factor $\lambda = |\partial \mathbf{R} / \partial s|$, with $\mathbf{R}(s,t)$ being the position vector of the jet axis, $\mathbf{V}(s,t)$ is the absolute velocity of polymer melt in the jet, ρ is the polymer melt density, $P(s,t)$ the magnitude of the longitudinal internal viscoelastic force in the jet cross-section, $\boldsymbol{\tau}$ is the unit tangent vector of the jet axis, \mathbf{g} is gravity acceleration, and $\mathbf{q}_{\text{total}}$ is the overall aerodynamic force applied by the surrounding gas on a unit jet length. Here and hereinafter boldfaced characters denote vectors. The longitudinal force in the jet cross-section $P(s,t) = f(\tau_{\tau\tau} - \tau_{nn})$, where $\tau_{\tau\tau}$ and τ_{nn} are the longitudinal and normal deviatoric stresses in the jet cross-section, respectively. It should be emphasized that any individual element of a polymer jet marked by its Lagrangian parameter s reckoned over the jet axis undergoes strong local uniaxial (in the direction of the local unit tangent $\boldsymbol{\tau}$ to the bending jet axis) elongational flow. This means that the axial

deviatoric stress $\tau_{\tau\tau}$ is significantly larger than any radial stress in the cross-section, which are τ_{nn} and τ_{bb} (the latter being equal to τ_{nn} due to the local axial symmetry, with \mathbf{n} and \mathbf{b} being the unit normal and binormal vectors to the bending jet axis). Thus, in meltblowing, since stretching (or elongation due to bending) are strong, the inequality $\tau_{\tau\tau} \gg \tau_{nn}$, holds. Thus, $P = f\tau_{\tau\tau}$. The deviatoric stresses are calculated using an appropriate rheological constitutive equation, for example, the upper-convected Maxwell model, cf. Eq. (A16) in [Sinha-Ray et al. 2011]. Note also, that traditionally both the deviatoric stress tensor and the unit tangent vector are denoted as $\boldsymbol{\tau}$. There should be no confusion in the notation $\tau_{\tau\tau}$, which (according to the standard hydrodynamic notations) denotes the component of the deviatoric stress tensor acting at a surface normal to the unit tangent vector $\boldsymbol{\tau}$ (i.e. at a jet cross-section) in the direction of the unit tangent vector $\boldsymbol{\tau}$.

It should be emphasized that Eqs. (4.1) and (4.2) are also used to describe electrospinning of nanofibers, with the only difference that $\mathbf{q}_{\text{total}}$ in that case is the overall electric force applied by the electrodes and the other parts of a jet on a unit jet length under consideration [Yarin 2014]. The similarity between the aerodynamic and electric forces stems from the fact that their normal components are proportional to local curvature of the jet axis, which triggers bending instability in both cases. A detailed description of electrospinning modeling based on the quasi-one-dimensional equations (4.1) and (4.2) is available in [Yarin 2014].

Note also, that there is no “preferable” rheological constitutive equation for description of strong elongational flows with the strain rates comparable to those in meltblowing ($\sim 10^4 \text{ s}^{-1}$), since none of them was tested in rheometric flows under comparable conditions. Since the upper-convected Maxwell model has solid micro-mechanical foundations for strong uniaxial elongational flows, as discussed in Appendix 3 in [Yarin 1993], this model is used in the present and preceding works on meltblowing [Sinha-Ray et al. 2011]. The changes of the parameters of this model (the viscosity

and relaxation time) with temperature are accounted for according to Eqs. (A17) in [Sinha-Ray et al. 2011] with the energy balance equation (A18) in [Sinha-Ray et al. 2011] solved simultaneously with Eqs. (4.1) and (4.2), which allows calculation of polymer jet solidification during cooling in flight.

The governing equations of the problem are supplemented with the vectorial kinematic equation, which allows prediction of the evolution of the jet axis in time and space [Sinha-Ray et al. 2011, Yarin 1993]. The polymer jets are subjected to the aerodynamic stretching and bending force (cf. Fig. 4.1b), as well as loose heat to the surrounding air jet. The flow and temperature fields in the surrounding air jet are calculated using the well-known self-similar solutions for the axisymmetric turbulent jets [Sinha-Ray et al. 2011, Yarin et al. 2007], in particular, cf. Eqs. (A14)-(A23) in [Sinha-Ray et al. 2011]. Note that the aerodynamic jet-jet interactions are typically negligibly small for such tiny objects and are neglected [Sinha-Ray et al. 2011].

The results of the numerical simulations reveal the exact time when a certain element of a polymer jet touches the moving screen and adheres to it [Sinha-Ray et al. 2011]. Using the predicted touchdown times of the individual material elements of all polymer jets, it is possible to establish which one of them (being deposited later) is superimposed on another one (being deposited earlier), and thus reconstruct the three-dimensional structure of the predicted laydown. That is the novel method used to predict the three-dimensional structure, and thus, porosity, of the numerically simulated laydowns introduced in the present work and discussed below.

For the numerical simulations based on Eqs. (4.1) and (4.2), the governing equations are rendered dimensionless and dimensionless groups, in particular, the Deborah number De_0 appear [Sinha-Ray et al. 2010, Yarin et al. 2010, Sinha-Ray et al. 2011, Sinha-Ray et al. 2013, Sinha-Ray et al.

2014]. In the present simulations the Deborah number De_0 was varied in the 50-400 range. In particular, $De_0 = 400$ corresponds to the relaxation time of 0.1 s. Also, in the simulations the following parameters were used: the diameter of polymer jet at the nozzle exit was taken as 200 μm as in the commercially available meltblowing dies, the air blowing speed was 150 m/s, the zero-shear viscosity of polymer melt was 15 $\text{g}/(\text{cm} \times \text{s})$, its density was about 1 g/cm^3 , the die-to-collector distance was 10 cm, and the activation energy of viscous flow or solidification was 33 kJ/mol. The velocity of the collector screen was varied in the 0-10 m/s range to explore the currently used and potentially important future values.

In the numerical results discussed below the lengths were rendered dimensionless by the die-to-collector distance (L), velocities - by the air velocity at the die exit (U_{g0}), and time- by L/ U_{g0} . In a standard meltblowing process $L \sim 10\text{-}15$ cm and $U_{g0} \sim 150$ m/s. It should be emphasized our group developed in the past a custom-written code which was used to predict different aspects of meltblowing in [Sinha-Ray et al. 2010, Yarin et al. 2010, Sinha-Ray et al. 2011, Sinha-Ray et al. 2013, Sinha-Ray et al. 2014] and underwent multiple convergence tests. In addition, in the present work this code is extended to predict detailed three-dimensional structures of meltblown laydown. Therefore, additional convergence tests were conducted to determine whether the time stepping interval chosen could guarantee reproducibility of the predicted laydown thickness and porosity when time stepping was varied. The convergence for the entire range of parameters used was proven to be very good, and all the results for the laydown thickness and porosity were highly reproducible.

4.3. Results and discussion:

The overall view of the predicted deposition of meltblown polymer jets on a moving collector screen is shown in Fig. 4.2 (only the fiber axes are shown). In Fig. 4.2a the predicted three-dimensional pattern of meltblowing process is shown, where 65 polymer jets vigorously bend and flap due to the action of the aerodynamic force (the schematics corresponding to that of Fig. 4.1b is shown as the inset in Fig. 4.2a). The polymer jets are collected on a collector screen moving normally to the blowing direction at a velocity in the 0-10 m/s range. In Fig. 4.2 and hereinafter, the ξ coordinate is reckoned in the direction of blowing, the H coordinate is reckoned in the direction of the nosepiece row, and the Z coordinate is reckoned in the direction of the collector screen motion. It should be emphasized that air suction is applied through the collector screen to guarantee the adherence of polymer jets. Figure 4.2b shows the predicted top view of the laydown on the moving collector screen.

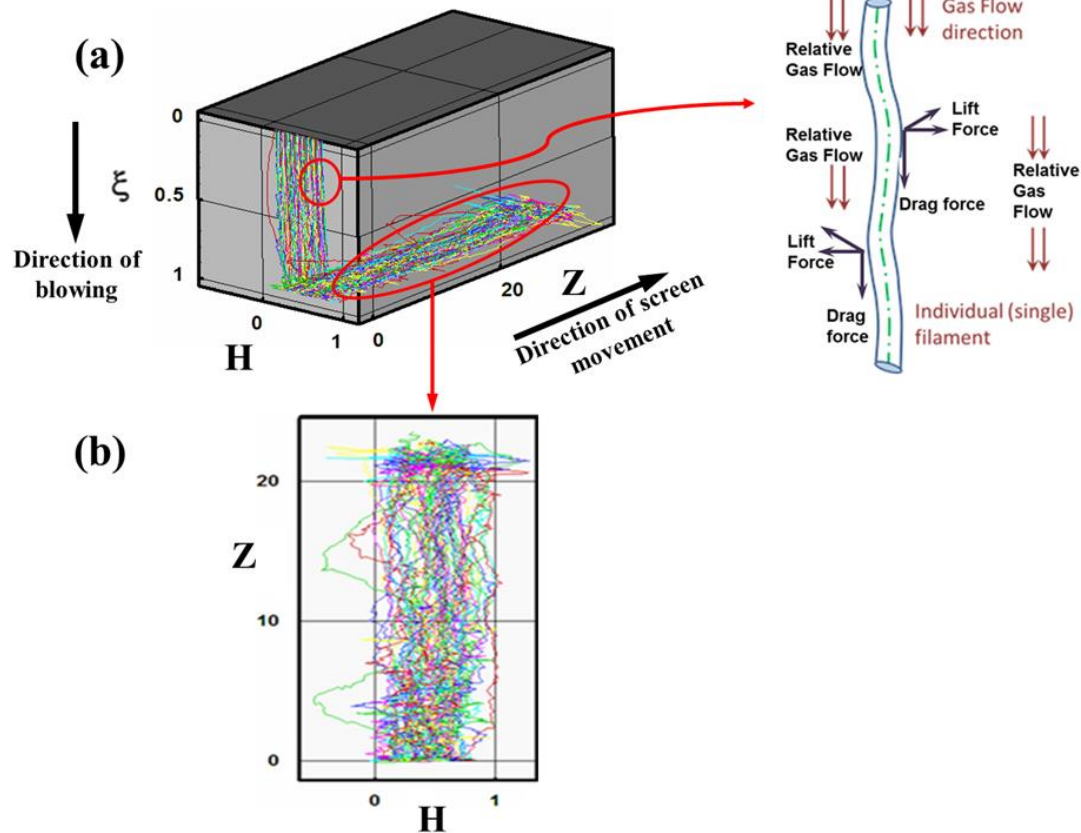


Fig. 4.2. Results of numerical simulations of the meltblowing process. (a) Predicted snapshot of the isometric projection of 65 polymer jets being collected on the collector screen moving at a velocity of 10 m/s in the Z-direction. (b) Predicted laydown pattern. All the parameters are rendered dimensionless. In both panels only the fiber axes are shown. The nosepiece corresponds to $\xi=0$, while the collector screen is located at $\xi=1$ (rendered dimensionless by the nosepiece-to-screen distance used as a length scale for all the coordinates).

Note also that in the simulations the initial perturbations of the polymer jets are imposed by random turbulent fluctuations of the surrounding gas (cf. Eqs. (A34) in [Sinha-Ray et al. 2011]). This strongly affects the subsequent bending instability and causes some fluctuations in the number of fiber loops crisscrossing the laydown at different locations Z along the collector screen as is seen in Fig. 4.2b (only the fiber axes are shown). Note also that fiber deposition on the screen is strongly

dependent on the velocity of the screen motion: the slower it is, the more fiber overlapping is observed. Indeed, the results shown in Fig. 4.3d reveal the number of the overlapping loops at the location $Z=1$ cm on the screen being 241 for the screen velocity of 0.1 m/s, and only 78 for the screen velocity of 10 m/s.

The number of the fiber loop axes crisscrossing a certain location on the collector screen seen in Figs. 4.2b and 4.3a is not a direct indication of the local thickness of the corresponding laydown. The latter can be established only by reconstructing the three-dimensional laydown structure, which reveals the effect of the fiber size and mutual location and thus, porosity. Figure 4.3a contrasts the isometric projections of the snapshots of 65 meltblown polymer jets predicted for two different collector screen velocities of 0.1 and 10 m/s. The Deborah number was chosen to be 100, which corresponds to the range explored in [Sinha-Ray et al. 2011, Sinha-Ray et al. 2013, [Sinha-Ray et al. 2014](#)]. Figure 4.3b shows the detailed dimensional isometric projection of the predicted three-dimensional structure of the corresponding laydowns collected on the moving screens in these two cases. Note, that any configuration of a section of a polymer jet stays unchanged after its both ends touched the collector screen or a fiber attached to it. Figure 4.3c shows the conformation and the cross-sectional diameter distribution predicted for a single polymer fiber on the collector screen for the two different velocities mentioned above. To elucidate the effect of the collector screen velocity on the cross-sectional fiber-radius distribution in laydown, the predicted distributions at $Z=1$ cm at the dimensionless time moment $t=20000$ are shown in Fig. 4.3d. It can be seen that for the collector screen velocity of 10 m/s, the radius distribution reveals two distinct peaks at around 3 and 5 μm , whereas for the velocity of 0.1 m/s the radius is distributed more uniformly. It can be also seen that for the collector velocity of 0.1 m/s, the total number of fiber loops passing through the cross-section $Z=1$ cm at the dimensionless time moment $t=20000$ in the

predicted laydown is 241, whereas for collector velocity of 10 m/s it is only 78. This stems from the fact that at higher velocities of the collector screen stretching is transmitted by the internal viscoelastic stresses to the oncoming material elements of polymer jets, which results in their straightening as they approach the screen. This trend was observed in the entire range of the collector screen velocities studied in the preset work.

The algorithm which allows finding the polymer mass distribution in the predicted laydown was developed and described in our previous paper [Sinha-Ray et al. 2013]. The mass distributions over the collector plate shown in Fig. 4.4a for the two collector screen velocities of 0.1 and 10 m/s were predicted using this algorithm. It can be seen that at the higher collector screen velocity, the polymer mass is more evenly distributed across the collector plate in comparison to the case of the lower collector screen velocity. This is similar to the predictions [Sinha-Ray et al. 2013]. In Fig. 4.4b the landscapes of the upper surfaces of the predicted laydowns for two different velocities of the collector screen are shown. It is seen that for the lower velocity of the collector screen the envelope surface is more undulated, whereas for the high collector one it is smoother. The altitude map in Fig. 4c corroborates this conclusion. It can be seen that at the screen velocity of 0.1 m/s, the altitude of the envelope surface varies in the 0-180 μ m range, whereas at 10 m/s it varies only in the 0-60 μ m range. It can be also seen that at the collector screen velocity of 0.1 m/s the altitude of the predicted laydown surface is non-uniformly distributed over the screen in comparison to the case corresponding to the collector screen velocity of 10 m/s.

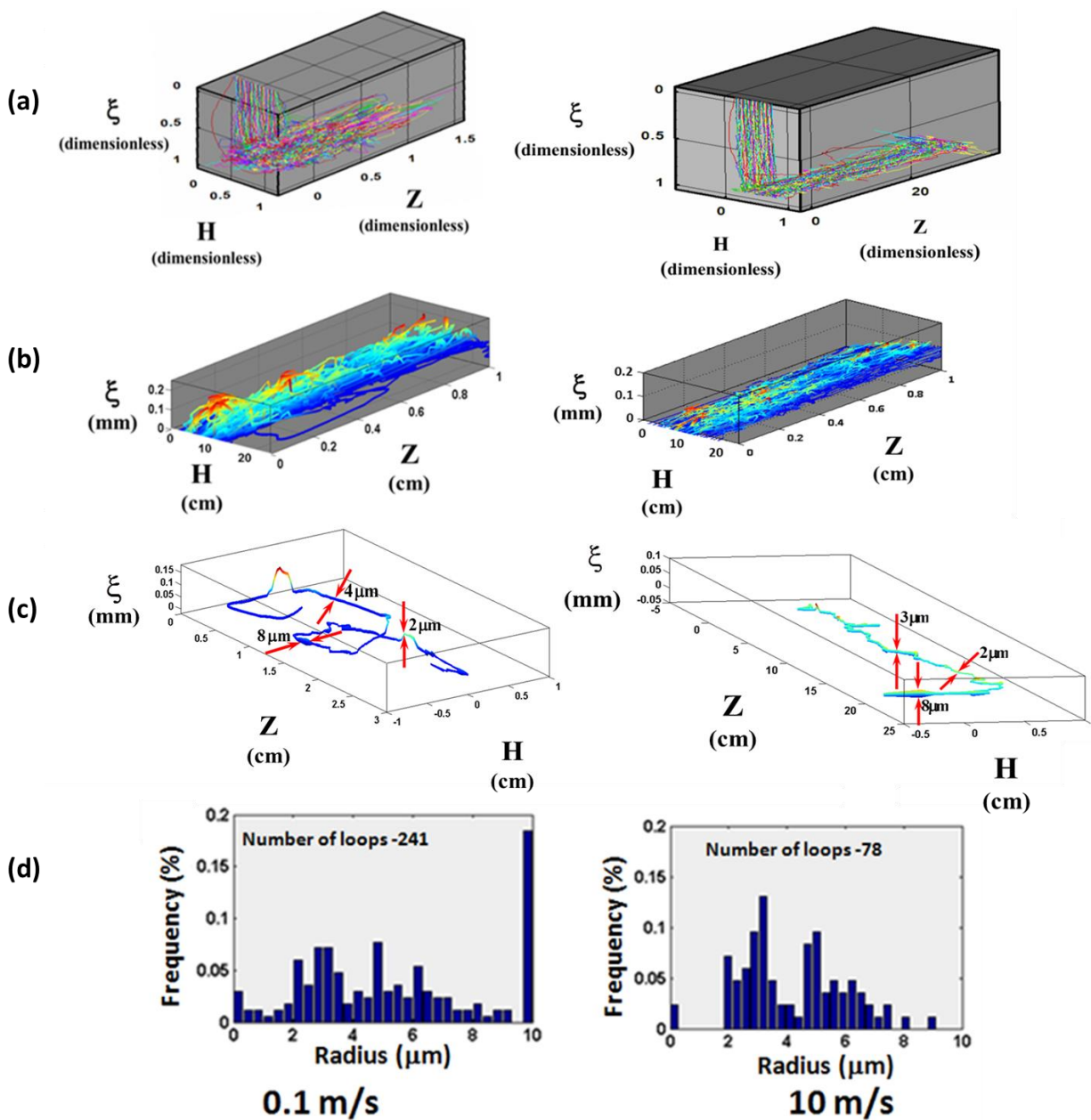


Fig. 4.3. Left column: the collector screen velocity of 0.1 m/s; right column: the collector screen velocity of 10 m/s. (a) Isometric projections of the snapshots of melblown polymer jets for two different velocities of the collector screen (left panel: the dimensionless time $t=20000$, and right panel: the dimensionless time $t=10000$). (b) The three-dimensional structure of laydown over the moving collector screen; both panels at $t=20000$. (c) Configurations of a single fiber for the above-

mentioned velocities of the collector screen; both panels at $t=20000$. In panels (a)-(c) only the fiber axes are shown. Also, in panels (b) and (c) the coordinate ξ is reckoned from the collector screen in the direction toward the nosepiece (opposite to Fig. 4.2 and panels (a) here) and is dimensional (in distinction from Fig. 4.2). (d) The cross-sectional fiber-radius distribution at $Z=1$ cm with the total number of loops crossed given in the panels; both panels at $t=20000$.

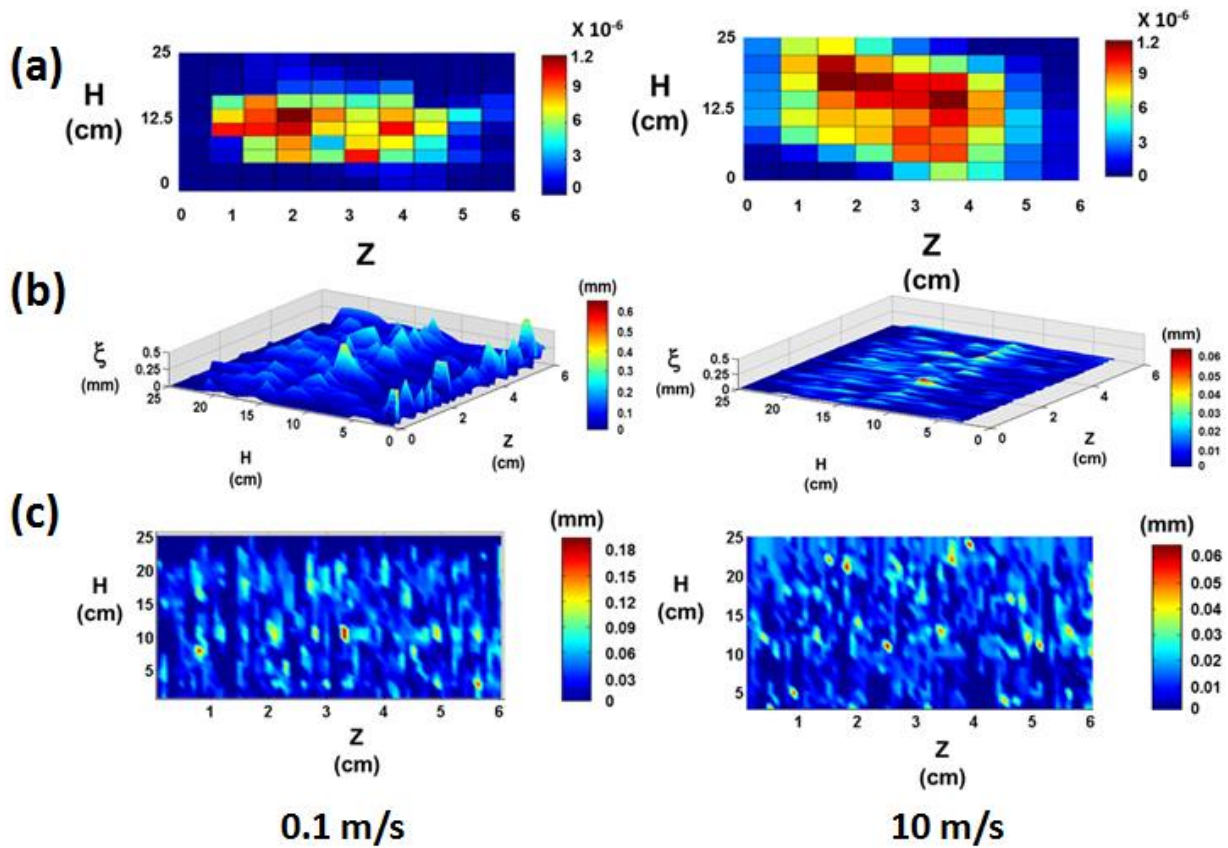


Fig. 4.4. (a) Distribution of polymer mass in the predicted laydown over the moving collector screen. (b) Three-dimensional isometric projection of the laydown surface. (c) The altitude map of the laydown over the collector screen. The panels on the left correspond to the collector screen velocity of 0.1 m/s, whereas on the right - to 10 m/s.

After the reconstruction of the three-dimensional structure of meltblown laydown on a moving collector screen, its different cross-sections can be visualized. For example, in Fig. 4.5 the

ξ - H cross-sections are selected from the deposited laydowns. The fiber cross-sections which appear as a result of the ξ - H cuts are shown by color-filled circular/oval shapes, with the differences between the shapes resulting from the fiber orientation relative to the ξ - H cut. It is seen that at the lower velocity of 0.1 m/s of the collector screen, the number of fibers cut in the ξ - H cross-section is higher than in the case of 10 m/s, which corresponds to the higher number of loops revealed in Fig. 4.3d-left compared to Fig. 4.3d-right. Figure 5 also shows that fibers in the laydown corresponding to 0.1 m/s are thicker than those corresponding to 10 m/s.

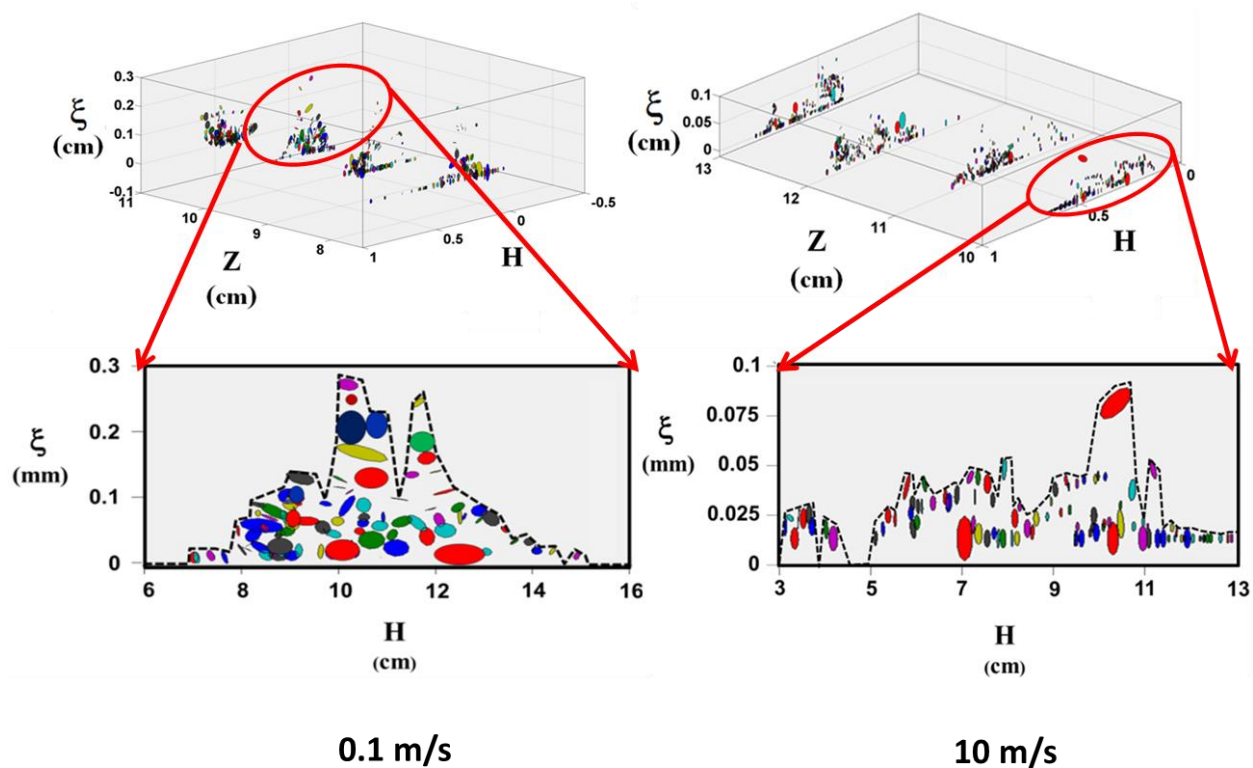


Fig. 4.5. Cross-sections of fibers in two laydowns predicted at two different velocities of the collector screen: 0.1 m/s (the panels on the left), and 10 m/s are (the panels on the right). The zoomed-in views correspond to $Z=10$ cm at the dimensionless time moment of $t=5000$ (corresponding to 3.33 s).

Two important parameters of interest in relation to meltblown nonwovens are the porosity and permeability. After the three-dimensional reconstruction of the laydown structure is completed, porosity can be found in two different ways, namely, as cross-sectional and volumetric porosity. The cross-sectional porosity can be introduced as following. At any location Z along the collector screen, a vertical cut of the laydown is made in the ξ - H plane, as in Fig. 4.5. Then, the area under the resulting cross-sectional envelope S_0 is calculated numerically. Also, the cumulative cross-sectional area of all polymer fibers in this cross-section $S_{\xi-H}$ is calculated numerically, and the cross-sectional porosity $p_{\text{cross-sectional}}$ is defined using the ratio of the two areas as

$$p_{\text{cross-sectional}} = \left(1 - \frac{S_{\xi-H}}{S_0} \right) \times 100\% \quad (4.3)$$

In Figs. 4.6a and 4.6b the predicted cross-sectional porosity for different velocities of the collector screen is shown at the laydown cross-sections of $Z=1$ cm and 2 cm, respectively, whereas in Fig. 4.6c the average cross-sectional porosity is shown. It can be seen in Fig. 4.6c that the cross-sectional porosity increases with velocity of the collector screen. It should be emphasized that the positions $Z=1$ cm and 2 cm are located almost at the plane which starts at the nosepiece and is normal to the collector screen (this plane is oriented in the blowing direction). Polymer jets in flight experience significant looping due to the bending instability and their frequency of “visiting” and touching the screen at the positions $Z=1$ cm and 2 cm is mostly dominated by this factor, rather than by the screen velocity. That is the reason of an independence of the local porosity on the screen velocity visible in two ranges of the latter, while only about 5-6 m/s a sharp transition to a higher porosity level happens. However, the effect of such local porosity fluctuations is smoothed when porosity is averaged over 50 cm of the collected laydown, as in Fig. 4.6c, which shows that the averaged porosity gradually increases with the collector velocity. Note also that at the nosepiece-to-collector distances practically used and considered here ($L \sim 10$ -15 cm), fibers are

already practically solidified [Yarin et al. 2010] and thus hold the collector by adhesive forces due to their relatively high adhesive energy [Stachewicz et al. 2014, Lee et al. 2015].

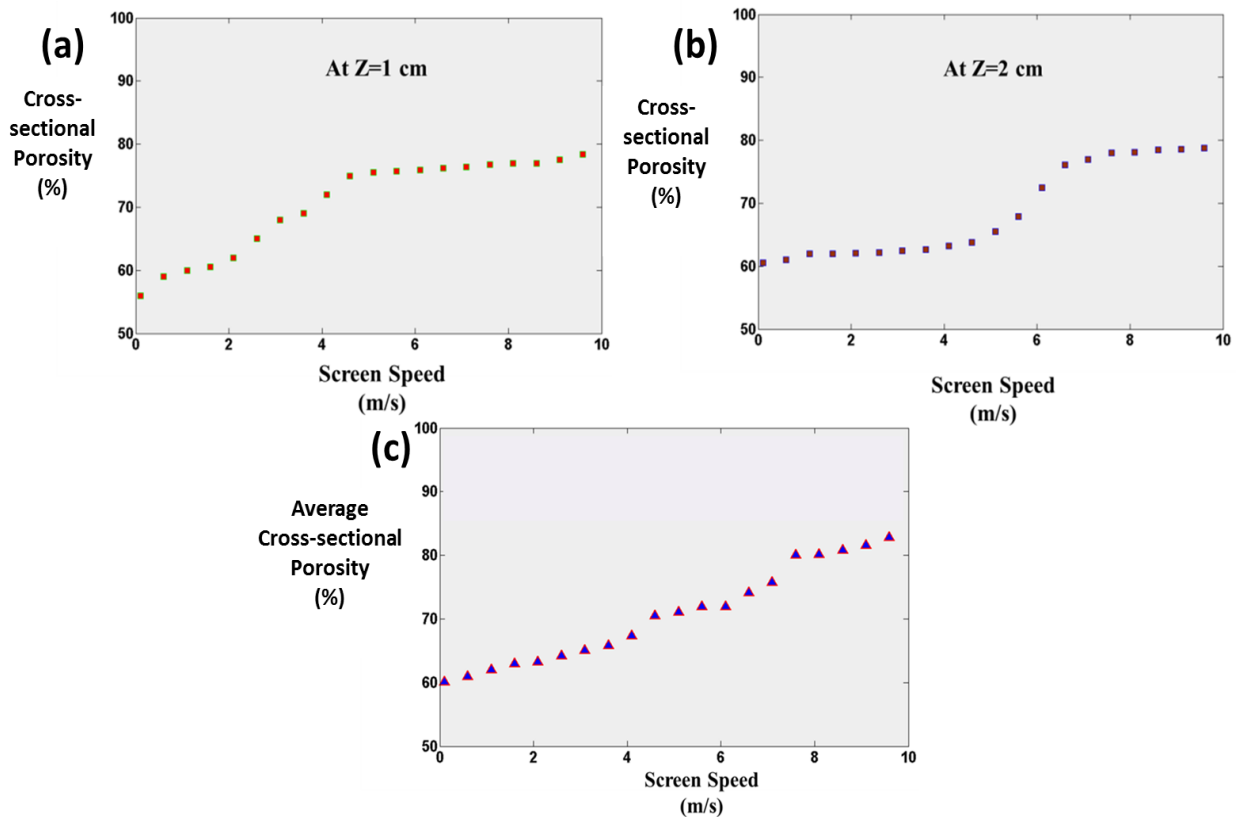


Fig. 4.6. Variation of the cross-sectional porosity with the velocity of collector screen. (a) Cross-section $Z=1$ cm. (b) Cross-section $Z=2$ cm. (c) Cross-sectional porosity averaged over 50 cm of the collected laydown.

The volumetric porosity is defined based on the predicted volume of the laydown envelope V_0 and the corresponding volume of the polymer filaments in the laydown V_f over the collector screen. Accordingly, the volumetric porosity p_{vol} is introduced as

$$p_{vol} = \left(1 - \frac{V_f}{V_0}\right) \times 100\% \quad (4.4)$$

The results for the average volumetric porosity predicted for different velocities of the collector screen are shown in Fig. 4.7, which reveals how the former increases with the latter.

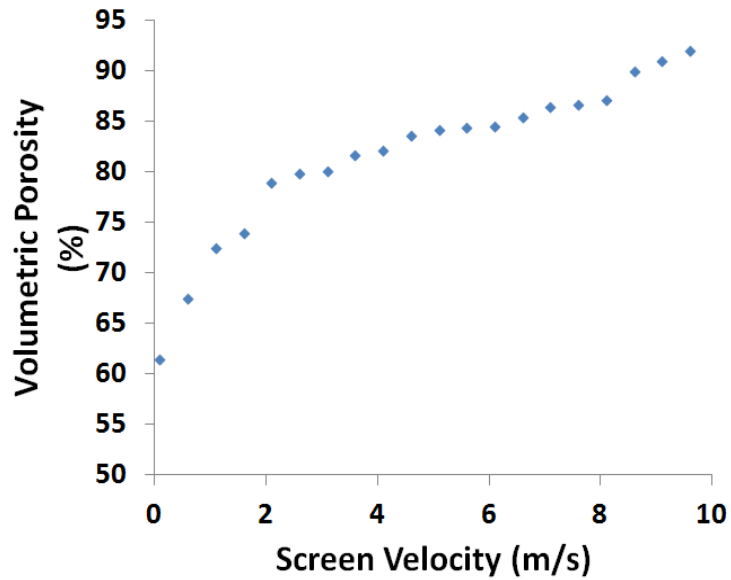


Fig. 4.7. The average volumetric porosity versus velocity of the collector screen. The volumetric porosity was averaged over 50 cm of laydown.

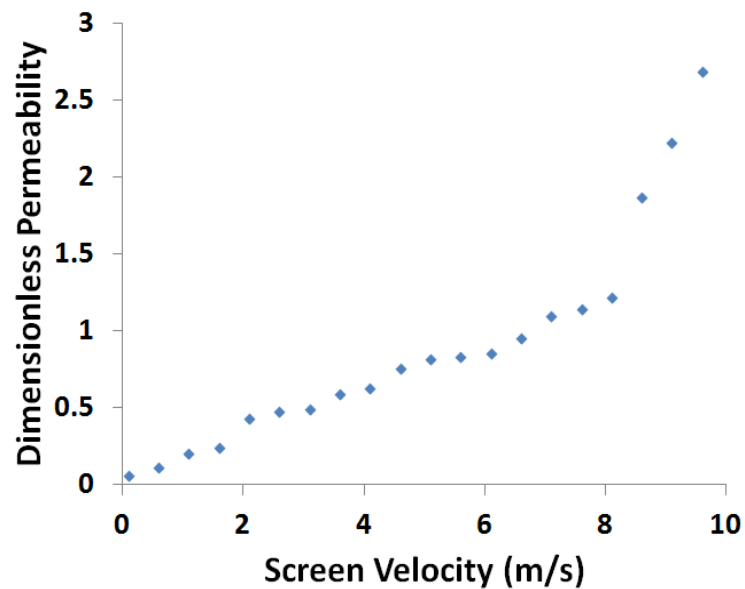


Fig. 4.8. The predicted variation of the average dimensionless permeability with the velocity of the collector screen. The volumetric porosity used in Eq. (4.5) was averaged over 50 cm of laydown.

The relation between the collector screen velocity and the corresponding laydown porosity and permeability is elucidated by the following facts. Figure 4.3d reveals that at the lower screen velocity, the fiber-size distribution is wider than at the higher one. A wider fiber-size distribution facilitates a better packing and thus, a lower porosity, which is indeed corroborated by the results shown in Figs. 4.4, 4.6 and 4.7. At the lower screen velocity subsequent fiber loops still can have a significant overlap with the previously deposited part of laydown, filling the gaps and decreasing porosity. This is not the case at the higher screen velocity, where the newly arriving fiber loops miss the previously deposited ones, since the latter were already moved away by a rapidly moving collector screen. As a result, porosity is higher at the higher screen velocity. Since permeability is closely related to the porosity, it is lower at the lower screen velocity and higher at the higher one (cf. Fig. 4.8).

Permeability of nonwoven and fibrous media was in focus in several works in the past [Davies et al. 1952, Tomadakis et al. 2005, Tomadakis et al. 2005a, Zhu et al. 1995, Hosseini et al. 2010, Han et al. 2013, Spielman et al. 1968, Drummond et al. 1984, Tahir et al. 2009, Pradhan et al. 2009, Chen et al. 2008].

A detailed discussion of the applicability of different models developed in these works to the evaluation of permeability of fibrous media can be found in [Jaganathana et al. 2008, Jaganathana et al. 2008a]. In [Jaganathana et al. 2008, Jaganathana et al. 2008a] the predictions of various analytical models and empirical correlations are compared to the results of direct numerical simulations for several hydroentangled laydown geometries produced by Digital Volumetric Imaging (DVI). The following empirical correlation proposed in [Davies et al. 1952] showed the best match to all the data,

$$\frac{k}{r_0^2} = \left[16(1-\phi)^{1.5} \left\{ 1 + 56(1-\phi)^3 \right\} \right]^{-1} \quad (4.5)$$

where k/r_0^2 is the dimensionless permeability, r_0 is the average fiber radius, and ϕ is the solid volume fraction in the fibrous media.

Equation (4.5) was used to evaluate permeability of meltblown laydowns generated numerically in the present work. The solid volume fraction was found as $\phi = 1 - p_{\text{vol}}$ using the predictions shown in Fig. 4.7. The resulting dimensionless permeability is depicted in Fig. 4.8. It is seen that laydowns formed at higher screen speeds are more permeable.

It should be emphasized that the volumetric porosity increases more steeply when the screen velocity surpasses 8 m/s (cf. Fig. 4.7). Therefore, according to Eq. (4.5) the increase in the dimensionless permeability with the screen velocity appears to be more steeply after the screen velocity surpasses 8 m/s (cf. Fig. 4.8). This stems from the fact that Eq. (4.5) strongly nonlinearly amplifies the effect of the increased volumetric porosity as $\phi \rightarrow 1$, since $k/r_0^2 \sim (1-\phi)^{-1.5}$, which tends to infinity as $\phi \rightarrow 1$.

The increase in the porosity and permeability with the collector screen velocity stems from the fact that the distance between material elements touching the screen increases with its velocity. The laydown structure becomes sparser, which is also accompanied by thinner fibers formed at a higher collector velocity. Both factors increase porosity and permeability.

The numerical approach proposed in the present work has been also validated by the comparison with the available data on the dependence of the dimensionless permeability on solid volume fraction of different fibrous media. The previous works either provided the experimental data, or numerically “constructed” artificial two-dimensional porous media consisting of regular arrays of circular cylinder [Drummond et al. 1984], as well as randomly distributed them on a plane or in

space [Tomadakis et al. 2005a, Chen et al. 2008]. Some porous media used for the permeability simulations possessed structures of real hydroentangled fibrous fabrics obtained using Digital Volumetric Imaging (DVI) [Jaganathana et al. 2008, Jaganathana et al. 2008a]. Also, a mean-field matching of Darcy's law with predictions of Brinkman's equation for several model obstacle distributions was used to determine the effective permeability [Spielman et al. 1968]. In all these works, after a geometry of fibrous matrix had been established, as described above, a solution for a creeping flow through it was constructed analytically, or by means of modeling, typically numerical, using such commercial codes as, for example, Fluent. In distinction from all the above-mentioned works, in the present case the three-dimensional laydown structure was not generated artificially or obtained experimentally using DVI, but rather it was predicted as a result of the numerical simulation of the meltblowing process. In particular, the solid volume fraction (SVF) predicted by our meltblowing model as $\phi = 1 - p_{vol}$ was found first, and then, the dimensionless permeability was established using Eq. (4.5). The results of the analytical and direct numerical simulations, which revealed the dimensionless permeability of the artificially constructed or experimentally determined (using DVI) fibrous media were summarized in Fig. 4.6 in [Jaganathana et al. 2008]. Here, the dimensionless permeability predicted for the simulated meltblown laydowns is compared to those results in Fig. 4.9. The comparison shows that the present results are in good agreement with the most accurate previous data in the entire range of their validity. Also, the present results significantly widen the solid volume fraction range covered so far.

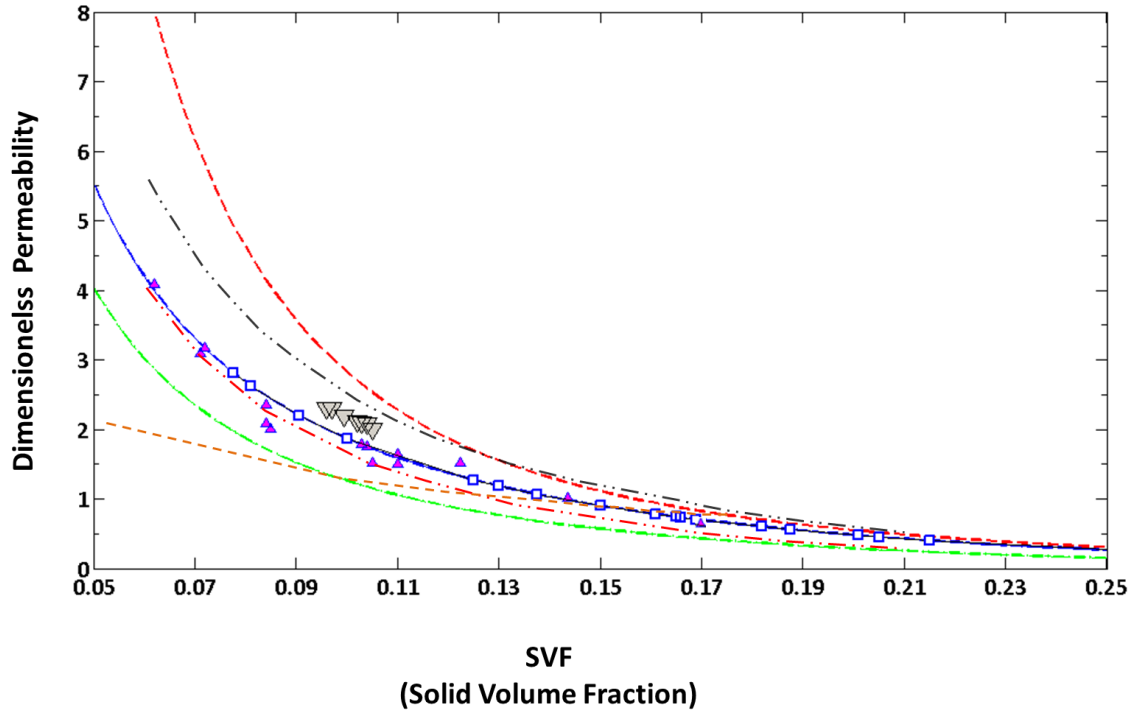


Fig. 4.9. Comparison of the dependence of the dimensionless permeability on the solid volume fraction (SVF) predicted in the present work with the data from the other sources. The present result corresponding to Eq. (4.5) (blue line) with the SVF predicted by our meltblowing model is shown by hollow blue squares. The empirical correlation of [Tomadakis et al. 2005a] valid for $SVF < 0.3$ is shown by the dashed red line. The empirical correlation of [Drummond et al. 1984] is shown by the dashed green line. The experimental data obtained for hydroentangled nonwoven fabric using Frazier air permeability tester is shown by the inverse grey triangles [Jaganathana et al. 2008]. The results of the direct numerical simulation of the dimensionless permeability of the experimentally reconstructed (DVI) hydroentangled nonwoven fabrics are shown by the purple upward triangles [Jaganathana et al. 2008]. The results for the 2D random model are shown as a brown dashed line [Chen et al. 2008]. The results for a layered structured fibrous medium are shown the red dashed-dotted line, while those for a randomized 3D model are shown by the black-dotted line [Spielman et al. 1968].

4.4. Orientation probability density function of the ensemble of fiber filaments in the meltblown laydown:

If $W(h,u)$ is the orientation probability density function for a fiber ensemble, then it can be derived from Fokker-Plank equation for an ensemble as [Yarin 1993]

$$W = \frac{\lambda^3}{4\pi(\lambda^3 \sin^2 \alpha + \cos^2 \alpha)^{3/2}} \quad (4.6)$$

$$\text{and } 2\pi \int_0^{\pi} W(\alpha, t) \sin \alpha d\alpha = 1$$

where α is the angle between a chain vector and the direction of interest (in particular case, the uniaxial stretching direction as shown here in Fig. 4.1(a))

Understanding variation of density is useful to understand multi-phase materials, either in macroscopic scale or in the nanoscale, and orientation distribution for semi-crystalline polymers can be a measure of the variation of densities in the crystalline and amorphous parts of the polymer material. Thus, a probability distribution of fiber orientation along axis of interest such as the axial stretching in case of meltblowing process is of importance to predict structural orientation of polymer crystals. In addition to density distribution of crystal nuclei concentrations, the orientation of local chain vectors and their ordering can have a correlation with the degree of crystallinity in a fibrous laydown. As a popular tool in describing both general and local polymer chain orientations, the Hermans' orientation factor F [Wang et al. 2014] is defined as

$$F = \frac{3}{2} \langle \cos^2 \alpha \rangle - \frac{1}{2} \quad (4.7)$$

Herman's orientation factor can be calculated by capturing the local ordering in the subdomains of the representative volume with different crystal orientations. Rather than using a specified direction, each chain vector in that domain is used as the reference direction, and thus the Herman's orientation factor of a domain is calculated by averaging the orientations of all other segments with respect to the chosen reference segment.

4.5. Experimental measurements of meltblown laydown

4.5.1. Optical profilometry: Measurement of laydown thickness including individual nanofiber

elevation- To measure deposit thickness including nanofiber elevation an optical metrology module (OMM) was used. It included a camera, LEDs that provided green and white illumination, a scanner assembly, and a measurement objective. The interference pattern used to calculate a local surface elevation was formed inside the measurement objective by splitting light into reference and measurement beams. The reference beam is reflected off an optically-flat reference mirror inside the objective, while the measurement beam is reflected off the sample. The reference mirror inside the objective was positioned so that it was in the same focal plane as the sample. In this configuration, the two light beams recombined and formed an interference pattern of light and dark bands, i.e. fringes. The number of the fringes and their spacing depends on the sample shape and the relative tilt between the sample and the reference mirror. Fringes are typically flat in case of a flat sample. The optical profilometry measurements are detailed in sections 4.5.5 and 4.5.6.

4.5.2. Vertical Scanning Interferometry measurement mode-

Vertical Scanning Interferometry (VSI) uses a broadband (normally white) light source. It is effective for measuring objects with rough surfaces, as well as those with adjacent pixel-height differences greater than 135 nm. VSI yields precision in the nanometer range. During a VSI measurement, the internal translator moves

the objective while the camera periodically records frames. As each point where the surface comes into focus, the modulation on that point reaches a maximum, then tapers off as the objective passes through focus. By recording the height of the translator at maximum modulation, the system can determine the height corresponding to each pixel. The maximum scan length for a VSI scan is 10 mm.

4.5.3. High Definition Vertical-Scanning Interferometry measurement mode- The High Definition Vertical-Scanning Interferometry (HDVSI) measurement mode offers very high vertical resolution combined with large vertical scan range. This makes it ideal for measuring smooth but stepped or highly sloped surfaces. Such surfaces often have sub-nanometer micro-roughness but may contain steps of >300 nm. In case of highly sloped samples, the fringes are not all located within the depth of focus for PSI. The VSI measurement method as discussed earlier can be used, but its approximately 3 nm noise floor may sometimes exaggerate the roughness of the sample. In such cases, HDVSI is an ideal choice of measurement mode.

4.5.4. Operating conditions in experiments- In the present work both VSI and HDVSI methods (described in sub-sections 5.2 and 5.3, respectively) were implemented. As discussed below, in addition to the optical profilometry, further image processing techniques were used to understand and visualize the difference in surface properties, mostly undulations patterns as well as standard deviation of the nanofiber mat thickness. In the cases when measurement results were affected by random noise, filtering was applied. Both Gaussian and Fourier filtering of images was done at times, depending on the noise level, as detailed in section 5.5. This helps in comparing the results on surface morphology and reveals otherwise non-recognizable fiber positioning.

4.5.5. Overview of measured data processing from as-received meltblown fiber mats and numerical results-

The following Table. 4.1 lists the operating conditions of 4 different fibermats as received from a pilot scale testing facility at Nonwovensinstitute, where the meltblown fibermats are derived from Ultra-pure Polypropylene granules of a specific gravity of 0.91, under fully controlled conditions. These samples as numbered, shows the variation of fibermat properties from measured data as well as simulated elevation, porosity and degree of crystallinity obtained with similar range of processing conditions.

Samp le Nr.	DCD (mm)	Vscreen (m/min)	Basis weight (g/m²)	Temperature of melt at die tip (° C)	Air temperature (° C)	Air flow rate (m³/hr)
1	150	13.2	60	246-258	260.1	800
2	300	13.2	60	247-259	261.4	800
3	225	39.8	20	245-258	255.8	800
4	225	13.2	60.1	246-258	261.5	800

Table 4.1: Sample specifications and operating conditions as received for 4 different meltblown Polypropylene fibermats produced from the same batch of polymer granules. All sample were made with a polymer flow rate of 0.6 ghm (grams per hole per minute).

The overall view of the sample collected on a flat collector plate reveals a typical sample structure used for the further analysis. Figs. 4.10(a) and 4.10(d) are SEM image of meltblown laydowns of sample 1 and 2 from Table 4.1. Figs. 4.10(a) and 4.10(d) are SEM images of samples 3 and 4 from Table 4.1. The cross-sectional porosity was found from the SEM images in Figs. 4.10(a) and 4.10(d) using a MATLAB code, which allows the image analysis of nanofiber mats according to the greyness scale generated by contrast sharpening. Namely, depending on the darker and lighter parts of the images, corresponding pixels were accounted for and thus the porosity of the upper layer was found. Figs. 4.10 and 4.11 (panels b,c,e,f) shows images-processed 3-D versions of the SEM images and reveals nanofiber elevations expressed by different colors using a 3-D reconstruction from several 2-D slices created based on processed grey-scaled SEM images from a single sample at different depths of vision. The image in Fig. 4.10 (panels b,c,e,f) and Fig 4.11 (panels b,c,e,f) can be used to estimate volumetric porosity of the sample by measuring the empty volume in the 3-D structure and the net volume occupied by an imaginary cuboid covering the topmost layer of the tomographic representative space. The 3-D reconstructed images presented in Figs 4.10 and 4.11 show fiber mat elevations by different colors and with relative scaling and arbitrary units of elevation, with a standard colorbar where blue being lowest and red becomes highest. The arbitrary units of the elevation colorbar has been excluded from the graph because that doesn't signify any exacting value.

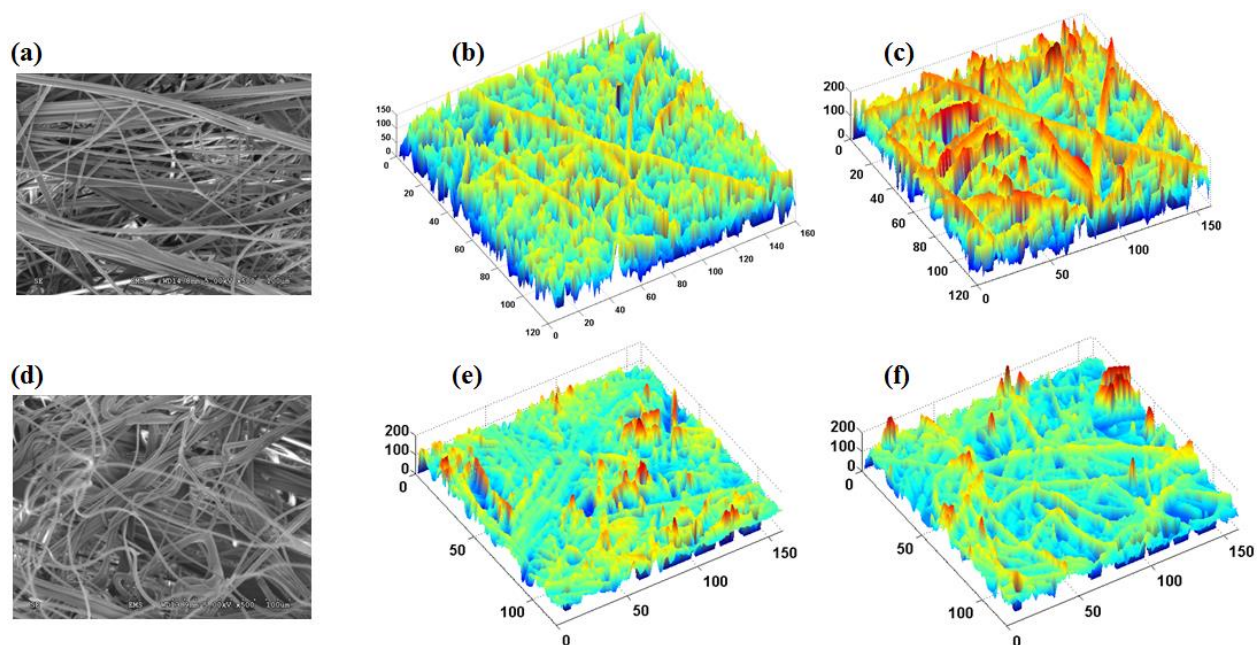


Figure 4.10: Panels (a) and (d) are SEM image of nanofiber mat meltblown from Polypropylene granules collected on a flate collector plate as per specifications of samples 1 and 2 in Table 4.1. Panels (b) and (c) are reconstructed 3-D images shown with arbitrary units of elevation when taken from sample 1 at two different locations of the sample. The optically reconstructed 3-D version of the images-processed version of several SEM image for sample 2 are shown in panels (e) and (f) respectively, for two different locations. The 3-D reconstructed images presented here show fibermat elevations by different colors and with same relative scaling. This information helps to calculated the volumetric porosity and observe the effects of the DCD on volumetric porosity.

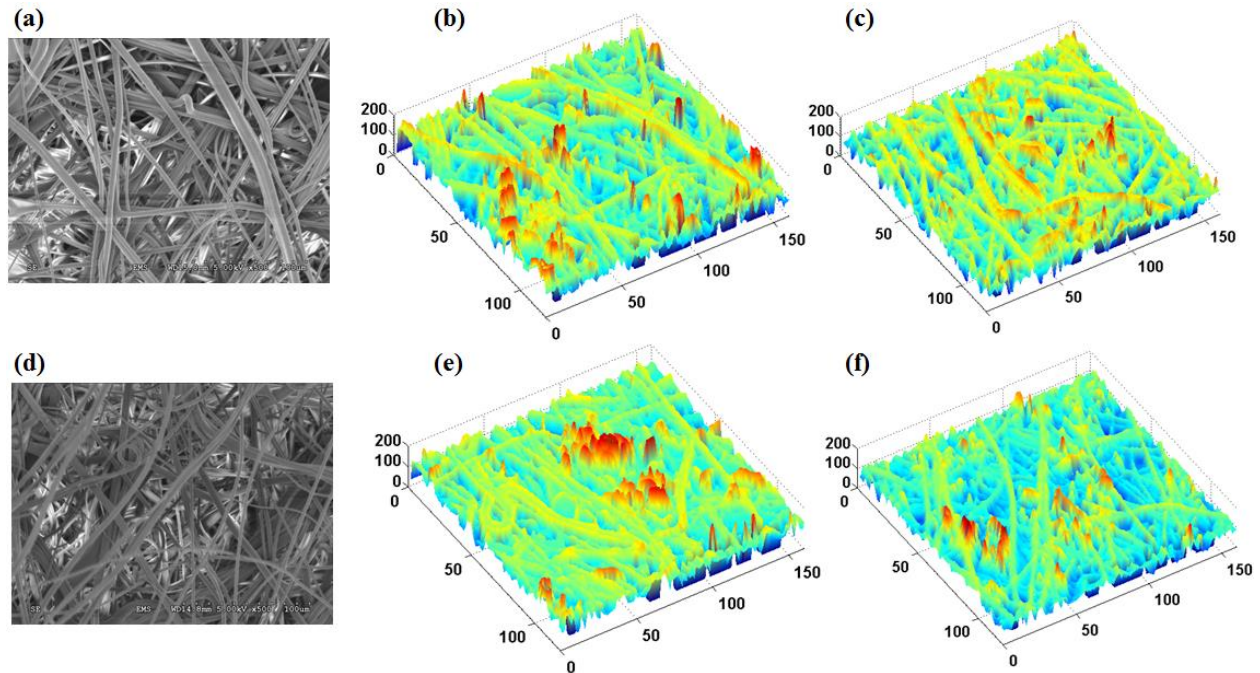


Figure 4.11: Samples 3 and 4 from Table 4.1 have been produced with identical processing parameters except the collecting screen velocity. Panels (a) and (d) show sample SEM images of meltblown fiber mats accordingly for these samples. Panels (b) and (c) are reconstructed 3-D images shown with arbitrary units of elevation when taken from sample 3 at two different locations of the sample. The optically reconstructed 3-D version of the images-processed version of several SEM images relative scaling. This information helps to calculate the volumetric porosity and observe the effects of the DCD on volumetric porosity.

The volumetric analysis of the profilometer results computes the void volume based on pixel measurements for sample 1 and 2 in Table 4.1 as shown in Fig. 4.12. The same analysis for samples 3 and 4 in Table 4.1 are shown in Fig. 4.13. The result reveals the entire three-dimensional morphology of the laydown which seems to be sensitive towards processing parameters like DCD and uptake velocity as specified in the pilot-scale meltblown samples. In these particular cases, the SEM-based cross-sectional and volumetric porosity values of these

two porosities are respectively 0.48 and 0.71, profilometer-based measured volumetric porosity for Fourier-filtered image is 0.8 and for Gaussian-filtered it is 0.71. Simulation results for the entire mat is already mentioned in Table 4.1, and that shows a very good agreement/matching in volumetric porosity values at least. Concerning only the uppermost layer of the surface additional comparisons were done by calculating the Gaussian and Fourier-smoothed volumetric porosities. As an example, the simulated Fourier-image shows a volumetric porosity of 0.88 compared to the Gaussian-image porosity of 0.75 for Fig. 4.13(b).

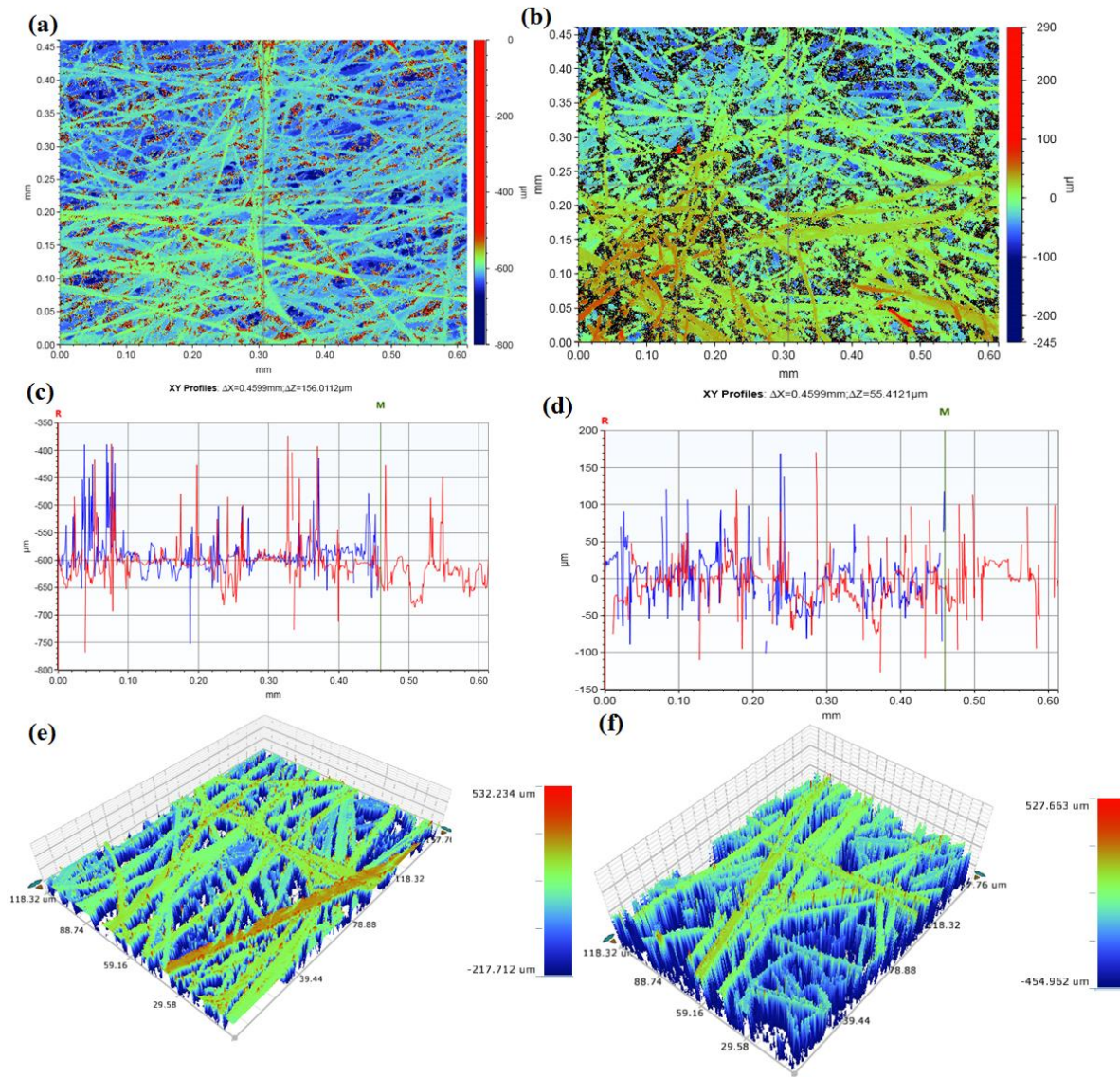


Figure 4.12: The original 3-D structure of fiber mat captured with the optical profilometer. Optical profilometer results are shown for samples 1 (Left panels) and 2 (Right Panels) from Table 4.1. The raw 2D images (top left and right panel) and 3D images in panels (e) and (f) respectively are obtained by optical profilometer for meltblown polypropylene laydowns. Surface elevation profiles are revealed by the optical profilometer in two perpendicular directions as shown to be blue and red graphs in panels (c) and (d). Panels (e) and (f) show the same surface as in panel (a) and (b) at different relative heights to capture the fibrous structures in more detail.

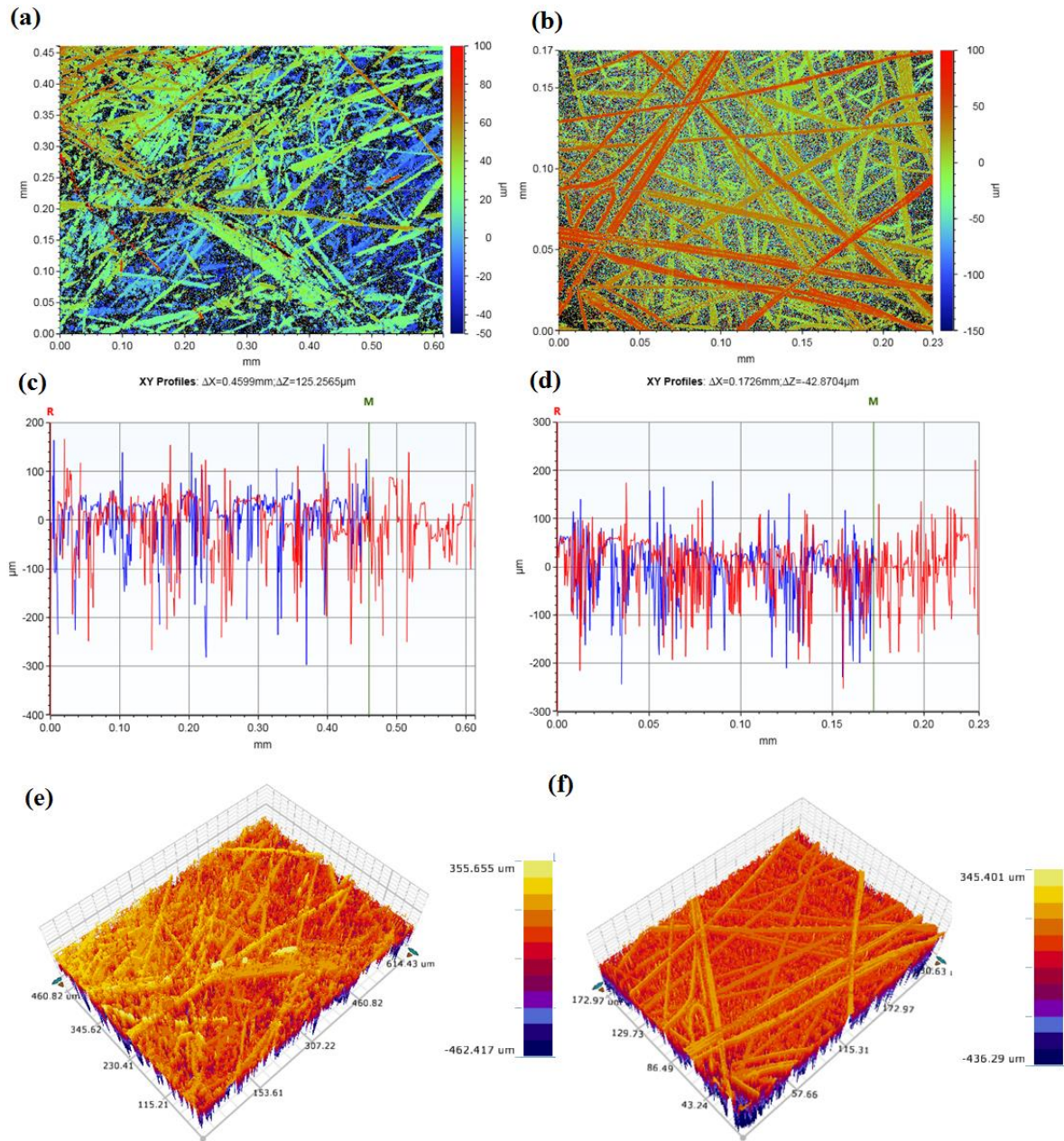


Figure 4.13: Optical profilometer results for samples 3 (Left panels) and 4 (Right Panels). The raw 2D (top left and right panel) and 3D (top right panel) optical profilometer data for laydown corresponding to sample 2 from Table 4.1. Surface elevation distributions revealed by the optical profilometer in two perpendicular directions as shown to be blue and red graphs in panels (c) and (d).

The uptake collector orientation can be calculated from SEM images as well, with a distribution of the same is given in Figs 4.14 and 4.15 by using 'OrientationJ' plugin of IMAGEJ Software. The 2-D planar structure in the form of the orientation angle mapping reproduces the same SEM images with every filament is tagged along its length according to the colorbar representing the angle formed with the principal axis of orientation. Looking at the color scale for comparison, it can be easily seen in Fig 4.14 that with a higher DCD, fibers orientation shows multiple peaks, suggesting the angular orientation to be very widely distributed. Figure 4.15 suggests that obviously, a higher uptake velocity results in fiber angular orientation to mostly have a single peak and the fiber alignment is visibly prominent as well in comparison to a laydown produced with lower uptake velocity.

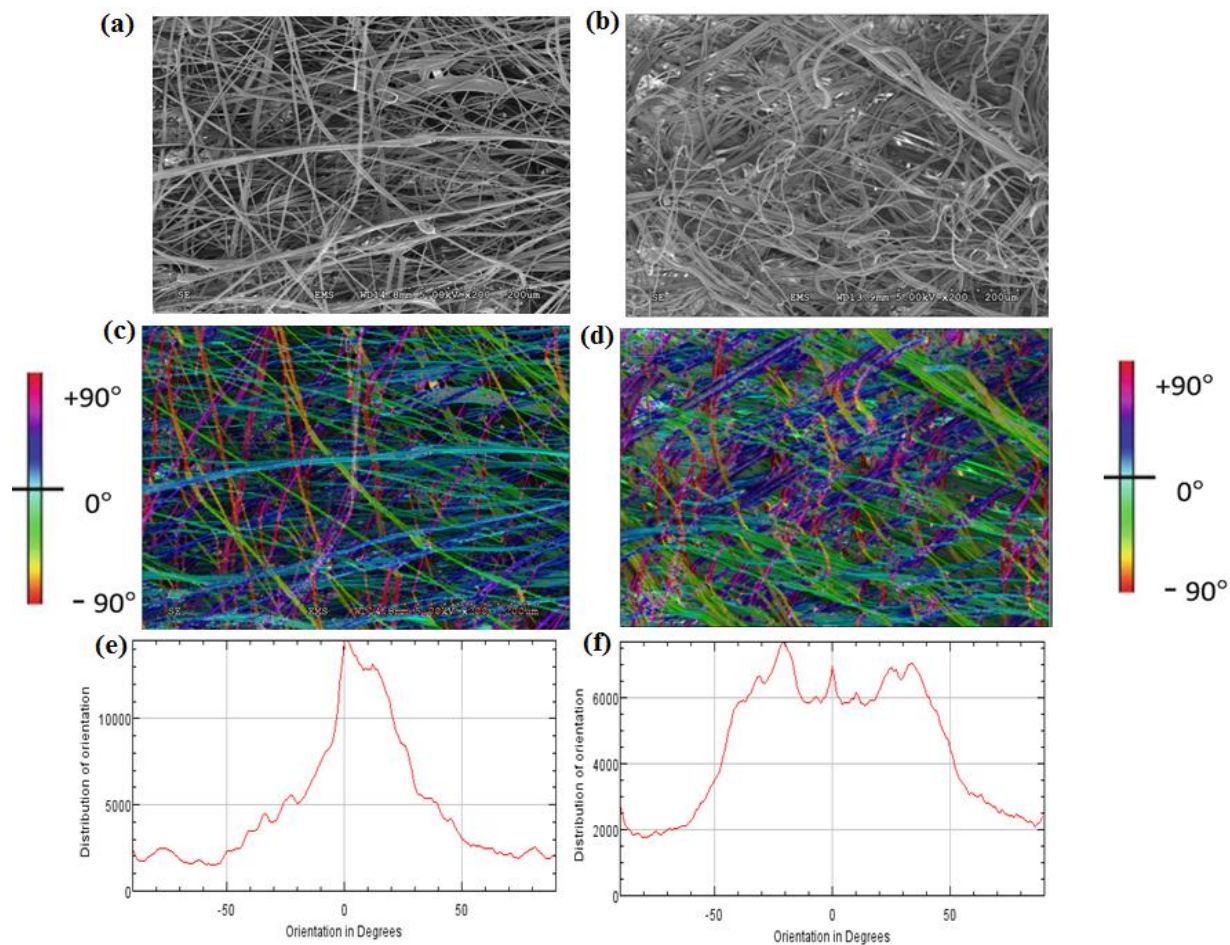


Figure 4.14: Measured angular Orientation for samples 1 and 2 of Table 4.1, where sample 2 was produced with higher DCD as compared to the sample 1. Panels (a) and (b) tends to show an effect on uptake collector distribution. A higher DCD leads to a wider orientation distribution pattern.

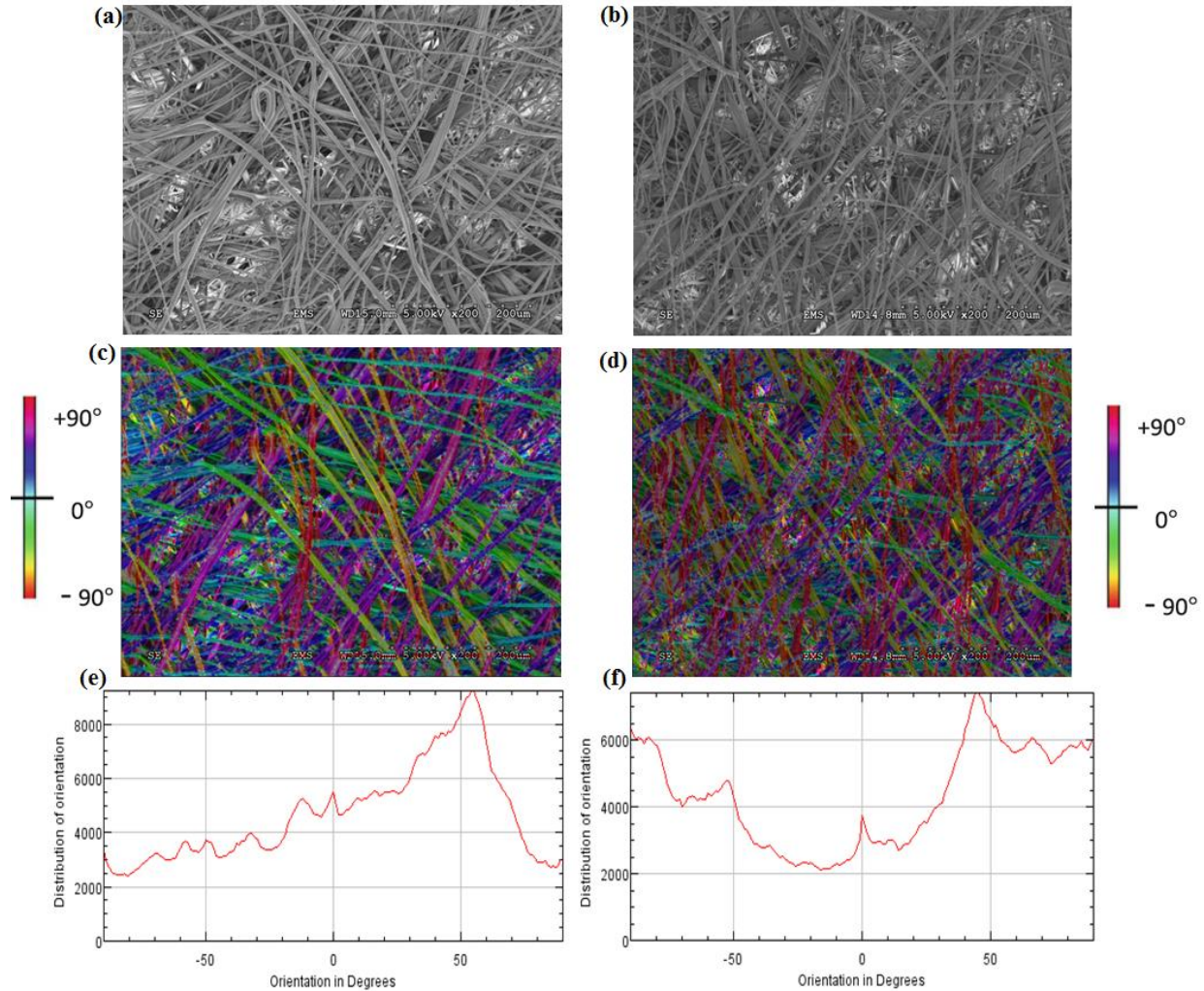


Figure 4.15: Measured angular Orientation for samples 3 and 4 of Table 4.1, which were produced with varying uptake velocity but all other processing parameters practically unchanged. Sample 3 has a represents a higher uptake velocity, and it clearly shows a higher velocity tends to orient the fibers on the mat more oriented to a specific direction, i.e, the uptake collector distribution gets narrowed.

4.5.6. Comparison between numerical predictions and experimental data of laydown surface morphology and elevation.

An example of the experimentally measured top view of the laydowns collected on a flat collector plate are shown in Figs. 4.16 and 4.17. The result reveals the surface morphology of the laydown is sensitive towards processing parameters like DCD and uptake velocity as specified in the pilot-scale meltblown samples in Table 4.1. Also, the predicted and measured mass distribution are shown in Fig. 4.18. As expected, a higher laydown density corresponds to the collector at lower uptake velocity.

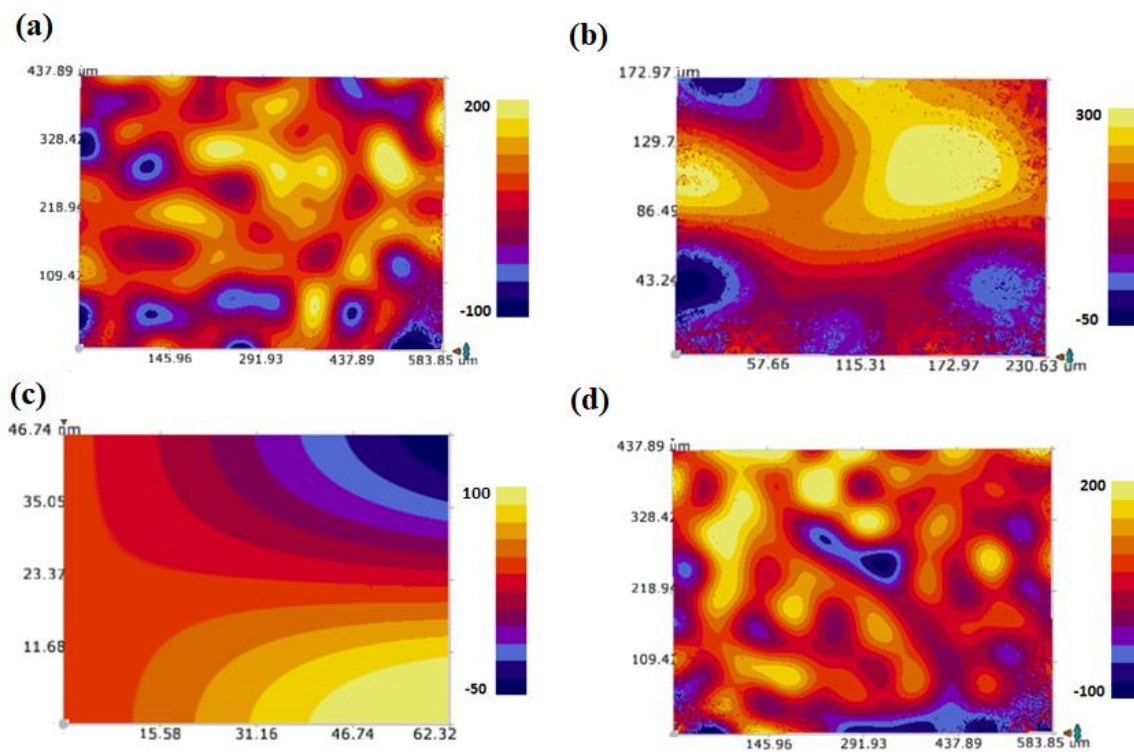


Figure 4.16: Experimentally measured morphology of the obtained samples 1-4 as panels a,b,c,d respectively using optical profilometer. A segment of each laydown is shown, and the elevation scale (shown in microns) across its thickness is exaggerated in the image to reveal the elevation

contour in more detail. The negative value in the elevation scale bar signifies the distance between the arbitrary lower plane of the sample being viewed to the focal point. The comparison of different colors for different elevation also reveals the change in deposition pattern of fibers due to variation of the uptake velocity of the collector belt. For the higher velocity in panel (c) when compared to panel (d), the collected laydown reveals several distinguishable contour pattern suggesting a more uniform elevation distribution whereas in panel (d) shows sudden changes in elevation throughout the fibermat area and at the lower uptake collector velocity, the colors are blended suggesting a higher extent of fiber filament overlap and piling in this case.

Also, comparing contour plots in Panels 4.16 (a) and 4.16(b) suggests that a higher DCD (in Panel b) may result in a tendency of fiber piling leading to prominent zones of varying thickness, whereas smaller DCD doesn't not allow the fibers to travel longer path and maybe formation of loops is considerably affected by changing DCD. Although the highest elevation in case of the laydown collected with higher uptake velocity is more than that in the lower speed laydown, it happens only at a few points and that doesn't represent the average thickness of the mat. This may be attributed to a momentary higher deposition along the entire breadth of the fibermat.

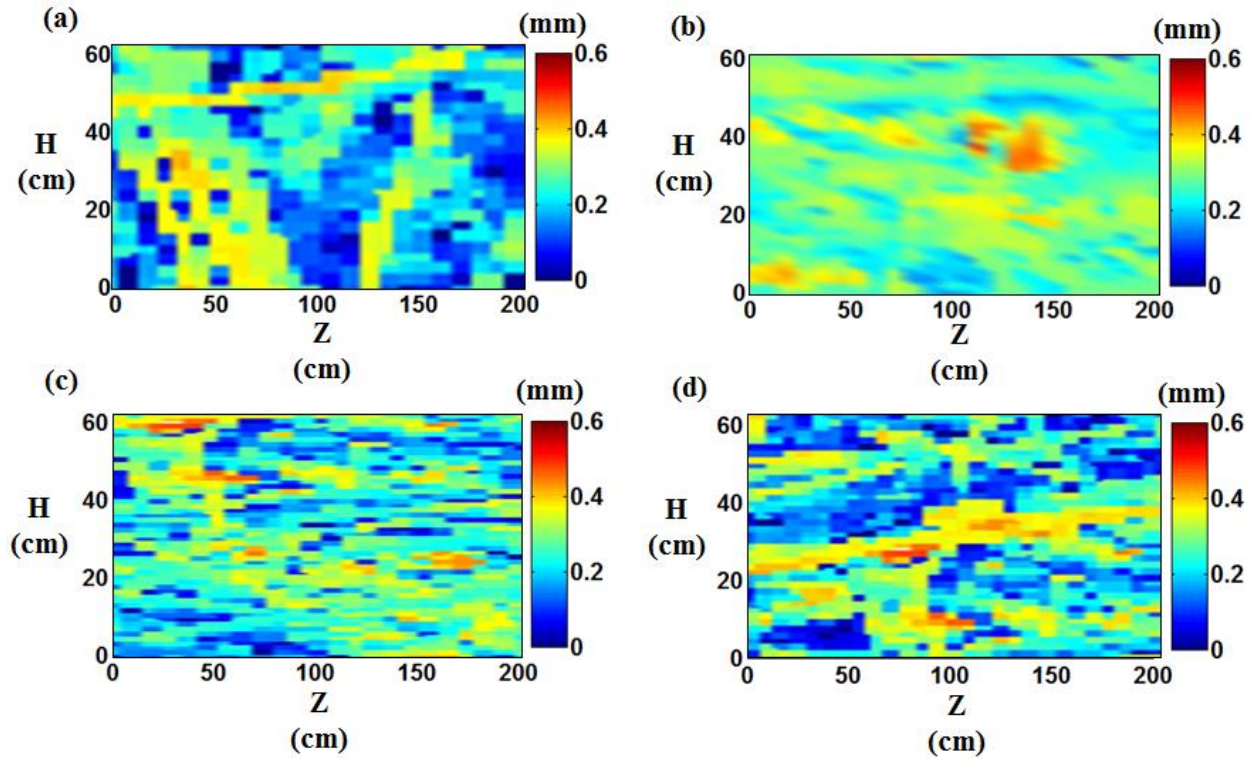


Figure 4.17: Simulated elevation of the meltblown polypropylene laydown samples collected on a flat collector plate with operating conditions according to samples 1-4 of Table 4.1. Deborah number $De_0 = 300$ was used in the simulation, which corresponds to the relaxation time of 0.1 s. The diameter of polymer jets at the nozzle exit was taken as $200 \mu\text{m}$. The air blowing speed was 180 m/s (equivalent to $800 \text{ m}^3/\text{mhr}$), the die-to-collector distance was taken as 15 cm for panel (a), 30 cm for panel (b) and 22.5 cm for panels (c) and (d). Panels (a) and (b) are for uptake velocities of 13 m/min respectively. Panels (c) and (d) are for uptake velocities of 40 m/min and 13 m/min respectively. The mass flow rate was of the order of 0.6 grams per hole per minute.

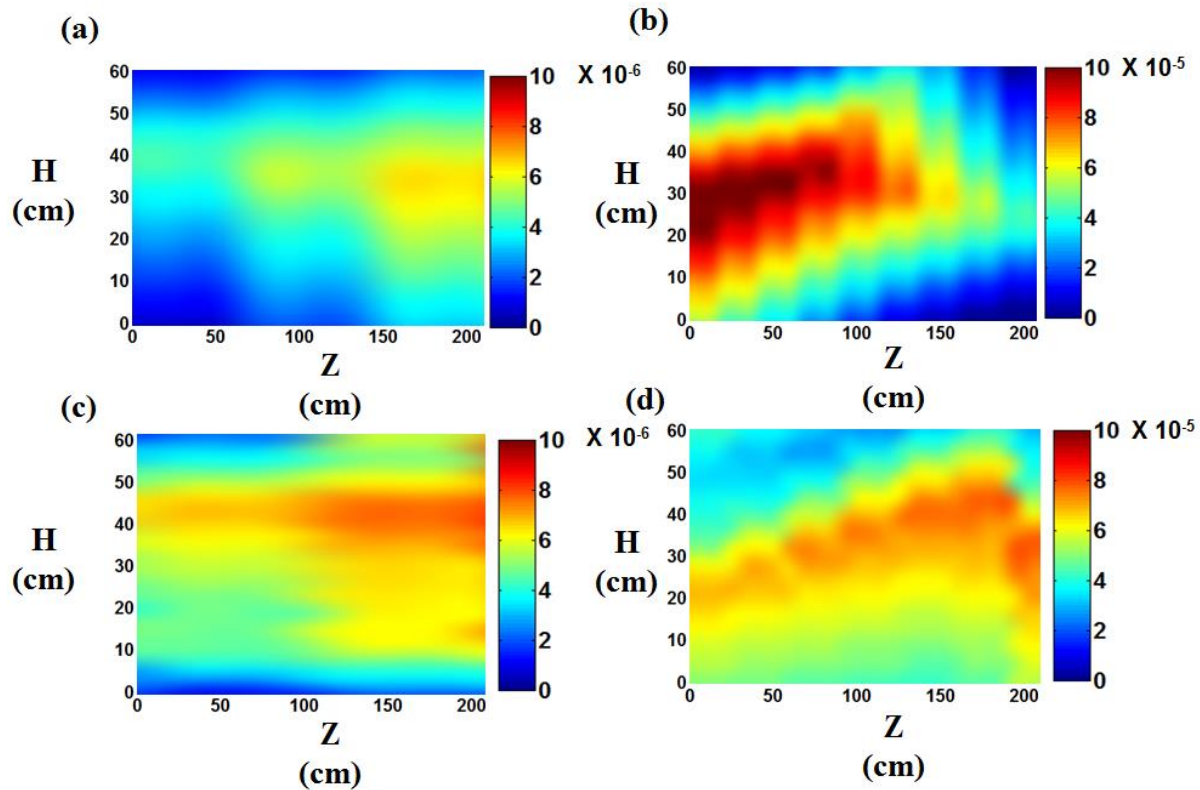


Figure 4.18: Comparison of simulated (according to operating conditions as specified for samples 1-4 in Table 4.1) and measured mass mapping of the meltblown polypropylene laydown collected on a flat collector plate. Numerical simulation with 100 polymer jets. The mass mapping is shown according to the color bars in gm/cm^2 . Top panels (a) and (b) are simulated mass maps of processing conditions similar to sample 3 and 4, where panel (a) is for higher uptake velocity of 40 m/min and panel (b) is for uptake velocity of 13 m/min. Measured mass for small components of the fibermat all over the received fibermats are shown in an interpolated form in panels (c) and (d) respectively for samples 3 and 4. Mass distribution in $\text{gm}/(\text{cm}^2)$ in the laydown on a flat collector plate predicted in the numerical simulations with 100 polymer jets.

The Deborah number $De_0=300$ used in all the simulations corresponds to the relaxation time of 0.1 s, diameter of polymer jet at the nozzle exit was taken as 200 μm . At the end of the straight

part of the jet the diameter was predicted as $10\ \mu\text{m}$. The air blowing speed was The air blowing speed was $180\ \text{m/s}$ according to the specified air flow rate of $800\ \text{m}^3/\text{hr}$, the die-to-collector distance was varied between $15\text{-}30\ \text{cm}$, as per fibermat sample specifications. The collection times in this simulation are varied between 4 seconds for samples collected with lower uptake velocity in comparison to 10 seconds for samples collected at higher uptake velocity to produce comparable length of the fibermats in both the case scenarios.

The fact that horizontal tangent to the direction of screen movement in the Z axis suggest that a higher elevation of roughly 100 microns is observed in middle region of the fibermat as compared to both the sides and the zone separation based on varying thickness is prominent at the lower collector uptake velocity. Comparing the scenario with Figs. 4.17 and 4.18, a higher extent of uniformity in elevation pattern is noted and it's unlikely to find a prominent zone of a higher range of thickness along the direction of collector movement relative to the rest of the high uptake velocity laydown. Moreover, most of the laydown shows a thickness range of $50\text{-}350$ microns.

4.6. Conclusion

The uniqueness of the present work is in the fact that the three-dimensional structure, thickness, porosity and permeability of meltblown nonwoven microfiber laydowns are predicted in the framework of the quasi-one-dimensional equations of the dynamics of viscoelastic polymer jets. This is the first micro-mechanical model, as to our knowledge, capable of predicting the detailed structure and properties of meltblown laydown starting from the governing parameters of the process. Conformations of the individual fibers in the laydown, as well as their mutual arrangement are found using the predicted touch-down times as markers of the individual elements of the fibers, which is a novel algorithm introduced to the theory in the present work. In addition,

fiber-size distributions, and polymer mass distributions are predicted. It is shown how the cross-sectional and volumetric porosities, as well the corresponding dimensionless permeability are affected by the processing parameters, especially by the collector screen velocity. The numerical results revealed how porosity and permeability increase with the collector velocity, which is explained by the fact that the material elements touching down at the screen form sparser laydown structures consisting of thinner fibers. The present results for the dependence of the dimensionless permeability on the solid volume fraction of the predicted meltblown laydown are in good agreement with the experimental data and analytical and direct numerical simulations of the predetermined structures available in the literature. It should be emphasized that the present results point at the change in the collector velocity as a convenient way of changing the laydown porosity, a conclusion, which aims at guiding practical implementations of the meltblowing process. The results for the two velocities of the collector screen (0.1 m/s and 10 m/s) are discussed in detail in the manuscript, albeit the simulations were conducted for the entire range in between. Typically, the meltblowing process is conducted with screen velocities of the order of 1 m/s, while velocities of the order of 0.1 m/s are still quite frequent. An increase in the production rate should be accompanied by an increase in the collector velocity. In some other processes collector velocities of the order of 10 m/s are not unusual. One of the goals of the present work is to provide a guideline for the optimization of the collector screen velocity using the predicted trend in the changes in the relevant laydown properties.

Chapter 5. NUMERICAL MODELING AND EXPERIMENTAL STUDY OF SOLUTION-BLOWN NONWOVENS FORMED ON A ROTATING DRUM

(Previously published as Ghosal, A., Sinha-Ray, S., Sinha-Ray, S., Yarin, A. L., and Pourdeyhimi, B. (2016) Numerical modeling and experimental study of solution-blown nonwovens formed on a rotating drum. *Polymer*, 105: 255-263.)

Abstract

In this work the three-dimensional architecture and properties of solution-blown laydown formed on a rotating drum are studied using the system of quasi-one-dimensional equations of the dynamics of free liquid polymer viscoelastic jets moving, evaporating and solidifying, while being driven by a surrounding high-speed air jet. Solution blowing of multiple polymer jets simultaneously issued from a nosepiece and collected on a rotating drum is modelled numerically. The numerical results on the volumetric porosity of nonwoven laydown are compared with the experimental data of the present work. The numerical predictions are in good agreement with the experimental data and elucidate the effect of the angular drum velocity on the mass and angular fiber distribution, as well as the volumetric porosity and permeability of the solution-blown nonwovens. It was found that instead of doing any upstream modification of the solution blowing process, the easiest way to control the laydown structure (the mass and angular fiber distribution, as well as the volumetric porosity and permeability) is to vary the angular velocity of the collecting drum.

5.1. Introduction

In the previous works of this group a comprehensive theory of solution blowing was developed with a goal to predict properties of nonwoven laydowns formed by this method [Sinha-Ray et al. 2015 a]. Solution blowing is an attractive novel method of formation of polymer micro-fibers and nanofibers from polymer solutions, while nanofibers belong to a wide class of nano-scaled or micro- and nano-textured materials expected to be delivered by nanotechnology. Over the last two decades, nanotechnology has become a household name. According to a recent survey by The National Science Foundation (NSF) and The National Nanotechnology Coordination Office (NNCO) the global market size of nanotechnology in 2013 was of the order of \$1 trillion [NSF 2014 https://www.nsf.gov/news/news_summ.jsp?cntn_id=130586], with micro- and nanofibers becoming an integral part of the nanotechnology deliverables. According to the recent Market Research Reports, the market size of nanofibers in 2009 was \$80.7M, which is forecasted to grow to a staggering \$2.2B by 2020 [BCC Research 2019, NAN043E; <https://www.bccresearch.com/market-research/nanotechnology/nanofiltration.html>; <https://www.bccresearch.com/market-research/nanotechnology/global-markets-and-technologies-for-nanofibers.html>]. Micro- and nanofibers have already revealed a multitude of applications in micro- and nano-fluidics [Sinha-Ray et al. 2009, Srikar et al. 2009], [Bazilevsky et al. 2008] controlled drug delivery [Srikar et al. 2008, Zupančič et al. 2015], [Zupančič et al. 2016, Khansari et al. 2013], agriculture and food science [Noruzi et al. 2016], microelectronics cooling [Sinha-Ray et al. 2010, Sinha-Ray et al. 2014 a, Sinha-Ray et al. 2014], etc. (see the recent comprehensive monograph [Yarin et al. 2014], as well as several preceding reviews in [Wnek et al. 2003, Reneker et al. 2008]. A significant widening of micro- and nanofiber application in general, and of solution-blown micro- and nanofibers, in particular, requires a thorough

understanding of the physical foundations of the process, its optimization and scaling up to the industrial level.

One of the most popular method of forming nanofibers is electrospinning [Yarin et al. 2014, Wnek et al. 2003, Renekar et al. 2008, Wendorff 2012, Filatov 2007, Reneker et al. 2007, Renekar et al. 1996, Renekar 2002, Greiner et al. 2007, Ramakrishna 2005]. However, electrospinning suffers from two significant drawbacks: (i) because of the poor scalability, electrospinning is a slow process and electrospun fiber production en masse is time consuming and relatively expensive; (ii) high voltage required for electrospinning makes it rather incompatible for utilization in a large-scale industrial facility. In recent years solution blowing of polymer micro- and nanofibers has been developed to overcome some of these difficulties [Medeiros et al. 2009, Sinha-Ray et al. 2010, Sinha-Ray et al. 2011]. In solution blowing process polymer solution is issued into a coaxial high-speed air jet which stretches the polymer jet directly, and triggers additional stretching due to the onset of bending instability [Sinha-Ray et al. 2015a, Yarin et al. 2014]. Solution blowing results in formation of polymer micro- and nanofibers and the fiber production rate is an order of magnitude higher than in the case of electrospinning. When the air jet is supersonic, solution blowing is capable of producing nanofibers in the 20-50 nm range [Sinha-Ray et al. 2013]. A few layers of such tiny nanofibers deposited on a commercial filter have already been used as very effective van der Waals collectors of ~10 nm nanoparticles from dilute aqueous suspensions practically without affecting pressure head [Sinha-Ray et al. 2015]. Recently, solution blowing was scaled up and implemented using an industrial nosepiece [Kolbasov et al. 2016].

It should be emphasized that solution blowing is an offshoot of meltblowing process, where a molten polymer jet is issued into a high speed air jet resulting in microscopic polymer fibers

[Bansal et al. 1998, Kwok 1999, Bresee et al. 2003, Pinchuk 2012, Uyttendaele et al. 1990, Marla et al. 2003, Marla et al. 2004, Yarin et al. 2011, Ghosal et al. 2016, Sinha-Ray et al. 2013]. Therefore, both processes involve three-dimensional stretching and bending of viscoelastic polymer entrained by the surrounding high-speed air jet. The difference between the two processes stems from the fact that in meltblowing polymer jet is cooled down by the surrounding air and thus, solidifies, whereas in solution blowing solvent evaporates and polymer in the jet precipitates and forms a solid polymer micro- or nanofiber.

Accordingly, the numerical model of polymer solution jet dynamics in solution blowing in [Sinha-Ray et al. 2015a]. significantly benefited from the previously developed numerical models of polymer jets in meltblowing [Yarin et al. 2011]. [Ghosal et al. 2016a],[Sinha-Ray et al. 2013]. the detailed three-dimensional architecture of solution-blown laydown and its dependence on the governing parameters of the process has never been attempted, as to our knowledge. Numerical efforts on modeling of solution blowing are also significantly hindered by the lack of the experimental data on solution-blown nonwovens with sufficient information on the values of the governing parameters in the experiment. Therefore, the motivation of the present work is in concerted modeling of solution blowing and its experimental investigation under controlled conditions. The numerical code employed in the present work stems from our previously developed code [Sinha-Ray et al. 2015a], albeit extends it to accommodate fiber collection on a rotating vacuumized drum, as well as provides it with post-processing tools, which allow one to restore the three-dimensional structure of collected fibrous laydown, its fiber size and mass distributions, as well as the corresponding porosity and permeability.

5.2. Numerical model

As in [Sinha-Ray et al. 2015a], modeling of solution-blown polymer jets employs the quasi-one-dimensional equations of the dynamics of thin liquid jets in the momentless approximation (cf. the details in [Yarin 1993, Yarin 2014]). Namely, the model implies the existence of an about 1 mm-long straight section of polymer jet near the die exit, where its bending stiffness is too high to let it bend, and a much longer bending part of the jet up to the collector (cf. Fig. 5.1a). In solution blowing the cross-sectional diameter of polymer jets diminish from about 1.2 mm to about 12 μm over the straight part due to the jet stretching by the surrounding high-speed air and solvent evaporation [Sinha-Ray et al. 2015a] At the end of the straight part polymer jets possess a very low bending stiffness (diminishing with the cross-sectional jet radius a as a^4), and begins to experience a vigorous bending driven by the aerodynamic distributed lift forces. The jet is also subjected to the aerodynamic drag force, turbulent pulsations, as well as solvent evaporation (cf. Fig. 5.1b). All the above-mentioned processes are described using the following quasi-one-dimensional mass and momentum balance equations [Yarin 1993, Yarin 2014, Yarin et al. 2001].

$$\frac{\partial \lambda f}{\partial t} + \frac{\partial f W}{\partial s} = -D_a b \pi \lambda \quad (5.1)$$

$$\frac{\partial \lambda f \mathbf{V}}{\partial t} + \frac{\partial f W \mathbf{V}}{\partial s} = \frac{1}{\rho} \frac{\partial P \boldsymbol{\tau}}{\partial s} + \lambda f \mathbf{g} + \frac{\lambda}{\rho} \mathbf{q}_{\text{total}} \quad (5.2)$$

In Eqs. (5.1) and (5.2) t is time, s is an arbitrary coordinate reckoned along the jet axis, $f(s,t)=\pi a^2$ is the cross-sectional area (the cross-section is assumed to stay circular even in bending jets, which is a plausible approximation according to [Yarin 1993]), W is the velocity of polymer

melt along the jet relative to a cross-section with a certain value of s , the stretching factor $\lambda = |\partial \mathbf{R} / \partial s|$, with $\mathbf{R}(s,t)$ being the position vector of the jet axis, $\mathbf{V}(s,t)$ is the absolute velocity of polymer solution in the jet, ρ is the polymer solution density, $P(s,t)$ the magnitude of the longitudinal internal viscoelastic force in the jet cross-section, $\boldsymbol{\tau}$ is the unit tangent vector of the jet axis, \mathbf{g} gravity acceleration, and $\mathbf{q}_{\text{total}}$ is the overall aerodynamic force applied by the surrounding gas on a unit jet length.

The projections of the momentum balance equation onto the accompanying trihedron of the jet axis, namely, the unit tangent vector $\boldsymbol{\tau}$, the unit principal normal vector \mathbf{n} , and the unit binormal vector \mathbf{b} , are kindred to the hyperbolic wave equation, as described in detail in our previous works [Yarin et al. 2011, Sinha-Ray et al. 2013, Yarin et al. 2010]. Accordingly, they are solved numerically using the implicit numerical scheme of the generalized Crank-Nicolson type with the central difference spatial discretisation at three time levels used in [Yarin et al. 2011, Sinha-Ray et al. 2013, Yarin et al. 2010]. and described in detail in [Mattheij et al. 2005]. Our previous works [Yarin et al. 2011, Sinha-Ray et al. 2013], also discuss in full detail the implementation of the initial and boundary conditions, whereas our previous work [Ghosal et al. 2016] specifies the post-processing procedure which allows one to reconstruct the three-dimensional architecture of the predicted laydown using the predicted touch-down times of the individual jet elements, their locations on the collecting screen and the cross-sectional radii of the as-deposited filaments.

The term on the right-hand side in the continuity equation (5.1) describes solvent evaporation. The factor b involved in this term reads [Yarin et al. 2001].

$$b = 0.495 \text{Re}_a^{1/3} \text{Sc}^{1/2} [C_{s,\text{eq}}(T) - C_{s,\infty}] \quad (5.3)$$

where D_a is the vapor diffusion coefficient in air, Re_a is corresponding Reynolds number, Sc is the Schmidt number and C_s is solvent concentration. Subscript eq corresponds to the equilibrium vapor pressure over the polymer solution surface determined by temperature T , while subscript ∞ corresponds to the vapor content far away from the jet surface in the surrounding air. Equations (5.1) and (5.3) show that solvent evaporation rate is dependent on temperature T through the dependence of the equilibrium solvent concentration over the polymer jet surface on temperature $C_{s,eq}(T)$. This dependence is typically derived from the Antoine equation, or similar equations available for different solvents [Reid 1987],[Seaver et al. 1989], [Yarin et al. 1999]. Since solution blowing is an isothermal process, temperature T is known as a room temperature. This temperature is typically above the theta-temperature, and thus the solvents are initially good. However, when the solvent concentration in the polymer jet decreases and, accordingly, polymer concentration C_p increases, the strongly nonlinear dependences of the zero-shear viscosity and the relaxation time on C_p given by Eqs. (5.4) practically arrest the polymer solution deformation, and effectively mean polymer precipitation due to a high concentration when the polymer-polymer self-interactions prevail.

In the notation used the boldfaced characters denote vectors. Also, the longitudinal force in the jet cross-section $P(s,t) = f(\tau_{\tau\tau} - \tau_{nn})$, with $\tau_{\tau\tau}$ and τ_{nn} being the longitudinal and normal deviatoric stresses in the jet cross-section, respectively. As usual, $\tau_{\tau\tau} \gg \tau_{nn}$, and accordingly, $P = f\tau_{\tau\tau}$. The deviatoric stresses are calculated using an appropriate rheological constitutive equation, for example, the Upper-Convected Maxwell model (UCM), as in [Sinha-Ray et al. 2015a], [Yarin 2014],[Yarin et al. 2001]. This means that the rheological behavior of polymer solutions is described using the phenomenological constitutive equation which does not utilize directly any physical information related to macromolecular chains and their conformations. However, the link

between UCM and micromechanical models of polymer solutions and jets has been established [Yarin et al. 2011], which shows that in strong stretching of polymer jets the higher value of the longitudinal deviatoric stress $\tau_{\tau\tau}$ corresponds to chain stretching and orientation in the axial stretching direction. Jet stretching in flight was studied in detail in the framework of meltblowing (cf. Figs. 7 in [Yarin et al. 2010]).

The rheological parameters involved in the UCM, namely, the viscosity and relaxation time of polymer solution vary with polymer concentration C_p as [Sinha-Ray et al. 2015a, Yarin 2014], [Yarin et al.2001].

$$\frac{\mu}{\mu_0} = 10^{B(C_p^m - C_{p0}^m)}, \quad \frac{\theta}{\theta_0} = \frac{C_{p0}}{C_p} \quad (5.4)$$

where μ_0 and θ_0 are the initial values of the viscosity and relaxation time, and B and m are known material constants.

If s is understood as a Lagrangian coordinate marking material elements along the jet axis, the local polymer concentration is found as in [Yarin 2014, Yarin et al.2001].

$$C_p = C_{p0} \frac{f_0 \lambda_0}{f \lambda} \quad (5.5)$$

where subscript 0 denotes the values at the initial cross-section of the bending part.

The aerodynamic forces $\mathbf{q}_{\text{total}}$ acting of polymer jet are calculated as given in [Sinha-Ray et al. 2015a, Yarin 2014, Yarin et al. 2001].

Note also that quasi-one-dimensional equations are widely used in many other problems related to the processes of fiber forming [Yarin 2014, Marheineke et al.2006, Ziabicki 1985, Hlod et al. 2007, Hlod et al. 2012].

5.3. Characteristic input parameters

In the simulations of solution blowing, the polymer concentration in solution was taken as 15 wt%, i.e. $C_{p0} = 0.15$. The values of B and m were chosen as in [Sinha-Ray et al. 2015a] as 7 and 0.1, respectively. The air velocity at the nozzle exit was taken as 180 m/s and the die-to-the collector top distance was chosen as 20 cm. The polymer solution jet diameter at the die exit was chosen as 1 mm. The solution feeding rate was chosen as 10 mL/h per jet corresponds to the polymer solution exit velocity of $V_0 = 1.38$ cm/s. The length of the straight part was taken as 1 mm, and at the end of the straight part of the jet, the jet diameter was predicted as 7 μ m. For the straight part, the relaxation time of the polymer solution jet was chosen as 0.01 s [Sinha-Ray et al. 2015a]. This corresponds to the Deborah number of 0.15 in the straight part of the jet. The polymer solution density was chosen as 1 g/cm³. The Deborah number at the beginning of the bending part of the jet, De_0 , was equal 10 [Sinha-Ray et al. 2015a]. The rotational speed of the collector drum varied between 10-200 rpm.

5.4. Rotating drum collector

In the experiments and numerical simulations of this work the oncoming polymer jets were collected on a rotating drum. The direction of the blowing is defined as ξ , whereas the die nosepiece is aligned along H (normal to ξ), while the third perpendicular direction is denoted as Z . Figure 5.1c shows these Cartesian coordinates along with a snapshot of 60 numerically simulated polymer solution jets wound on the collecting drum. Figure 5.1d shows a cut portion of the

numerically simulated laydown on the drum, whereas Fig. 5.1e shows the rotating drum used as a collector of solution-blown micro- and nanofiber laydown in the experiments of the present work.

The drum is assumed rotating with the angular velocity ω and has the cross-sectional radius R . The angular coordinate about the drum axis is denoted as φ . Accordingly, the angular coordinate of a material element after its touch-down at the drum (or at the preceding fiber laydown on the drum) is found as

$$\varphi = \varphi_{\text{touch}} + \omega(t - t_{\text{touch}}) \quad (5.6)$$

where the touch-down is implied to happen at the angle φ_{touch} at the moment $t_{\text{touch}} < t$.

The circumferential coordinate of a material element of a polymer filament on the drum axis denotes as Ψ and is found as

$$\Psi = \Psi_{\text{touch}} + \omega(t - t_{\text{touch}})R \quad (5.7)$$

where $\Psi_{\text{touch}} = \varphi_{\text{touch}} R$.

The drum axis is assumed to be parallel to the nosepiece. Therefore, the H coordinate of a material element of a polymer filament on the drum does not change after touch-down. On the other hand, its ξ coordinate varies as (cf. Fig. 5.1f).

$$\xi = \xi_{\text{touch}} + R \cos(\pi - \varphi) = \xi_{\text{touch}} - R \cos \varphi \quad (5.8)$$

which means that

$$\xi = \xi_{\text{touch}} - R \cos[\varphi_{\text{touch}} + \omega(t - t_{\text{touch}})] \quad (5.9)$$

where ξ_{touch} corresponds to the touch-down position.

It should be emphasized that Eq. (5.6) allows the angle φ to grow beyond $\varphi_{\text{touch}}+2\pi$, which means the deposited fibers have made a full rotation with the drum and are being covered by a newly deposited fiber layer. The previously and newly deposited layer could have the same value of the coordinate ξ as per Eq. (5.9), albeit they are distinguished by their coordinates Ψ , as per Eq. (5.7), which is the longitudinal coordinate along an unrolled laydown. Note also that Eqs. (5.6)-(5.10) allow one to pose the boundary conditions at the end of a free polymer jet already deposited on the rotating cylindrical collector screen, similarly to the boundary conditions used in [Sinha-Ray et al. 2015a], [Sinha-Ray et al. 2011],[Ghosal et al. 2016] on planar collector screens. These boundary conditions affect backward the oncoming part of the polymer jet/filament through the corresponding viscoelastic force acting along the jet/filament and predicted by the model (cf. [Sinha-Ray et al. 2015a]).

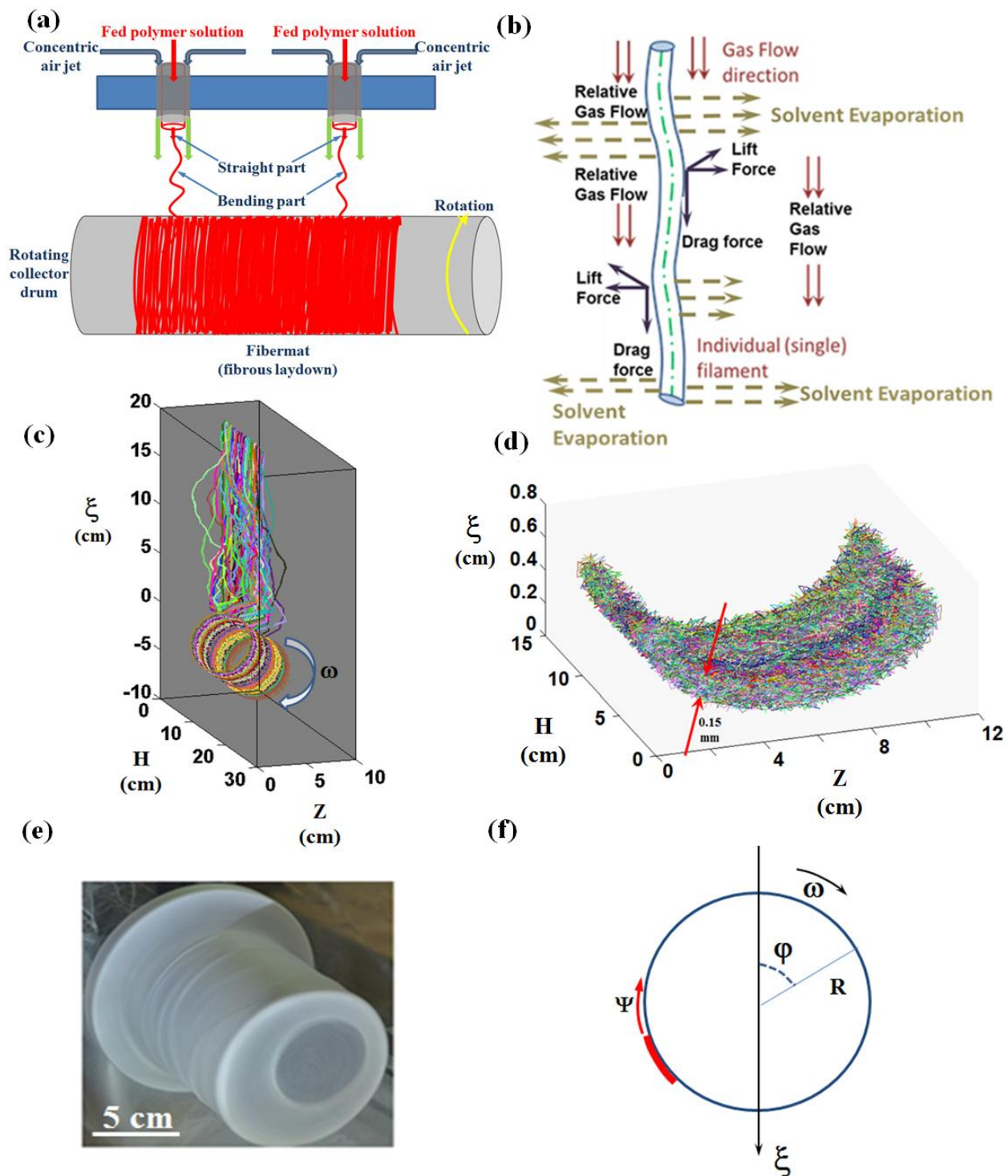


Fig. 5.1. (a) Schematic of solution blowing process. Polymer solution jets issued through concentric nozzles located along nosepiece are collected on a rotating drum and form a nonwoven laydown. Each oncoming polymer solution jet possess a short straight part (~ 1 mm) followed by

a vigorously bending and flapping part. (b) Schematic of the different forces acting on a polymer solution jet undergoing vigorous flapping accompanied by solvent evaporation. (c) Snapshot of numerically simulated 60 polymer solution jets wound on a rotating drum. (d) Section of as deposited solution-blown laydown. (e) A drum used in the experiments to wind solution blown fiber laydown. (f) Schematic of the drum cross-section with coordinate system.

5.5. Results and discussion

The overall view of the predicted solution blowing process is shown in Figs. 5.1c and 5.1d which depict sections of the predicted solution-blown laydown. The thickness of the numerically predicted laydown varied between 0.1-0.2 mm. Normally the collector drum is permeable and vacuumized from inside to facilitate the oncoming fibers to immediately stick upon touch-down, which was enforced by the touch-down conditions described above. The effect of the drum angular velocity on diameter distribution in the predicted solution-blown laydown is illustrated in Fig. 5.2 for the angular velocity values of 10, 50, 100 and 200 rpm. The diameter distributions are directly predicted by the solutions of Eqs. (5.1)-(5.3) (cf. [Yarin et al. 2011]) and are shown at three different values of $\varphi = 0^{\circ}$, 60° and 135° , each one at time $(t-t_{\text{touch}})=1$ min and $\varphi_{\text{touch}}=1.24^{\circ}$, 5.84° , 2.09° , 3.72° , respectively, for the above-mentioned angular velocities. The φ_{touch} value varies for every single jet and thus, the averaged value of φ_{touch} for 60 jets is shown for the different angular velocities. Figs. 5.2a-c, 5.2d-f, 5.2g-i and 5.2j-l correspond to $\omega=10$, 50, 100 and 200 rpm, respectively. Since the results in Fig. 5.2 correspond to the same time period, they correspond to the same polymer mass deposited at different angular velocities of the collecting drum. The mean values and the corresponding standard deviations of the predicted diameter distributions are listed in Table 5.1.

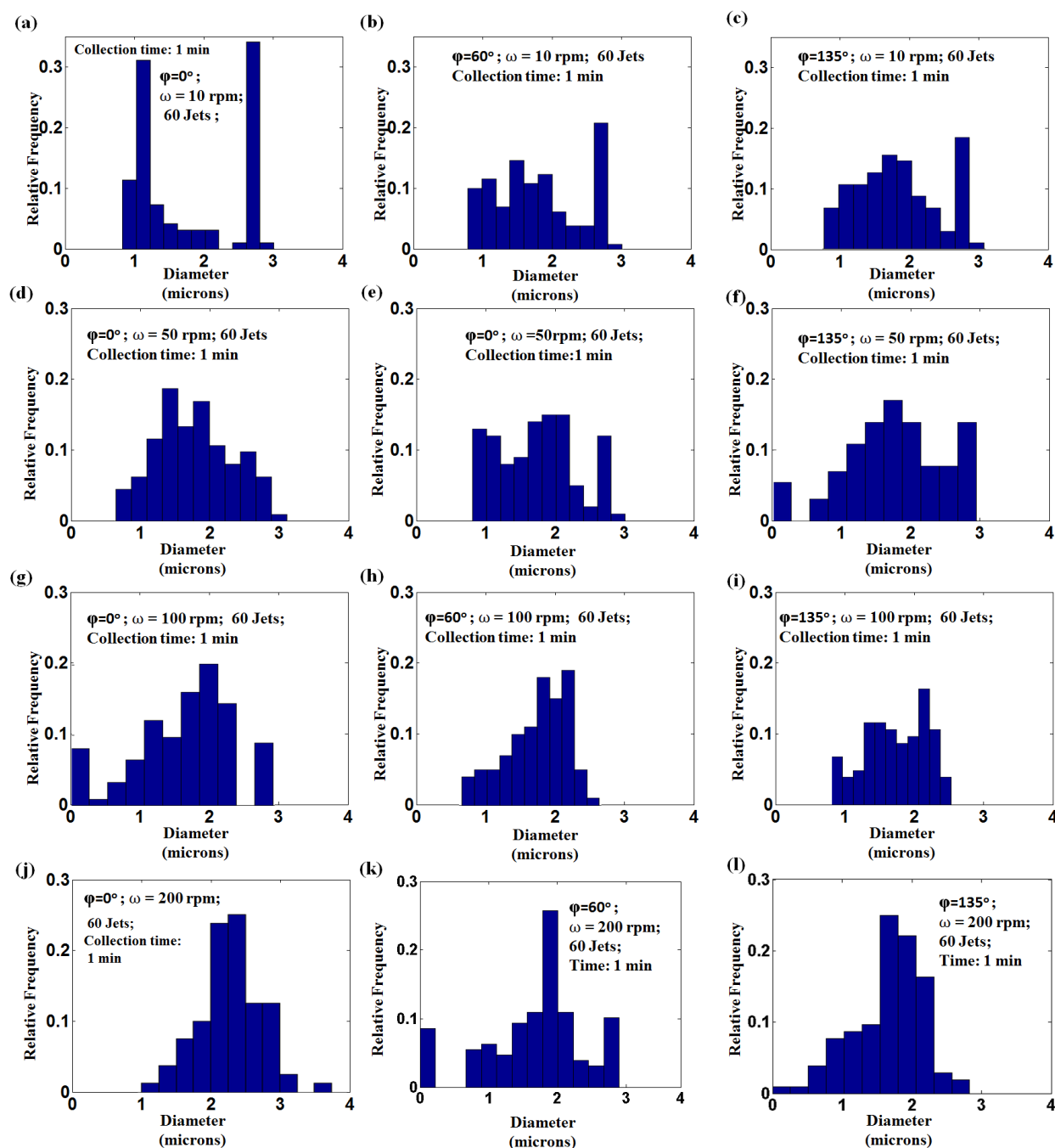


Fig. 5.2. Predicted diameter distributions of solution-blown laydowns formed by 60 polymer jets at different angular velocities of the rotating drum. Panels (a)-(c) show the diameter distributions for $\phi=0^\circ$, $\phi=60^\circ$ and $\phi=135^\circ$, respectively, for $\omega=10$ rpm. Panels (d)-(f) show the diameter distributions for $\phi=0^\circ$, $\phi=60^\circ$ and $\phi=135^\circ$, respectively, for $\omega=50$ rpm. Panels (g)-(i) show the

diameter distributions for $\varphi=0^\circ$, $\varphi=60^\circ$ and $\varphi=135^\circ$, respectively, for $\omega=100$ rpm. Panels (j)-(l) show the diameter distributions for $\varphi=0^\circ$, $\varphi=60^\circ$ and $\varphi=135^\circ$, respectively, for $\omega=200$ rpm.

Angular velocity (ω) (rpm)	$\varphi=0^\circ$		$\varphi=60^\circ$		$\varphi=135^\circ$	
	Mean (μm)	SD (μm)	Mean (μm)	SD (μm)	Mean (μm)	SD (μm)
10	1.87	0.64	1.90	0.61	1.96	0.58
50	1.89	0.62	1.81	0.64	1.91	0.66
100	1.71	0.52	1.75	0.46	1.65	0.51
200	1.71	0.48	1.71	0.59	1.61	0.52

Table 5.1. Mean values and standard deviations of the numerically predicted solution-blown laydowns shown in Fig. 5.2.

Figure 5.2 and Table 5.1 show that for every angular velocity the mean value and standard deviation of the diameter distribution do not vary significantly along the predicted laydowns, with the angle φ (the mean values and standard deviations are not shown in the panels). Figure 5.2 reveals that as the angular velocity of the collector drum ω increases, the fiber size distribution shifts from a bimodal to a more Gaussian-like, single-modal distribution. It is seen that for the

angular velocity of 10 rpm irrespective of the angular position, there are two peaks around 1-2 and 3 μm [cf. Figs. 5.2(a)- 5.2(c)]. On the contrary, as the angular velocity of the collector increases, the peak at $\sim 3 \mu\text{m}$ decreases. Moreover, at 200 rpm the peak at $\sim 3 \mu\text{m}$ practically disappeared, while a fully pronounced peak appeared between 1-2 μm . This pattern physically stems from the following. As the oncoming polymer jets touch the collector, they attain the velocity of the collector. A higher angular velocity of the collector, transmits a higher stretching back to the polymer jet in flight via the viscoelastic stresses acting along the jet. This stretching suppresses lateral excursions of the polymer jet and thus facilitates fiber orientation in the laydown in the machine direction. The mechanically transmitted stretching also facilitates diminishing the cross-sectional fiber diameter, which causes the disappearance of the peak $\sim 3 \mu\text{m}$ in Fig. 5.2 at higher angular velocities.

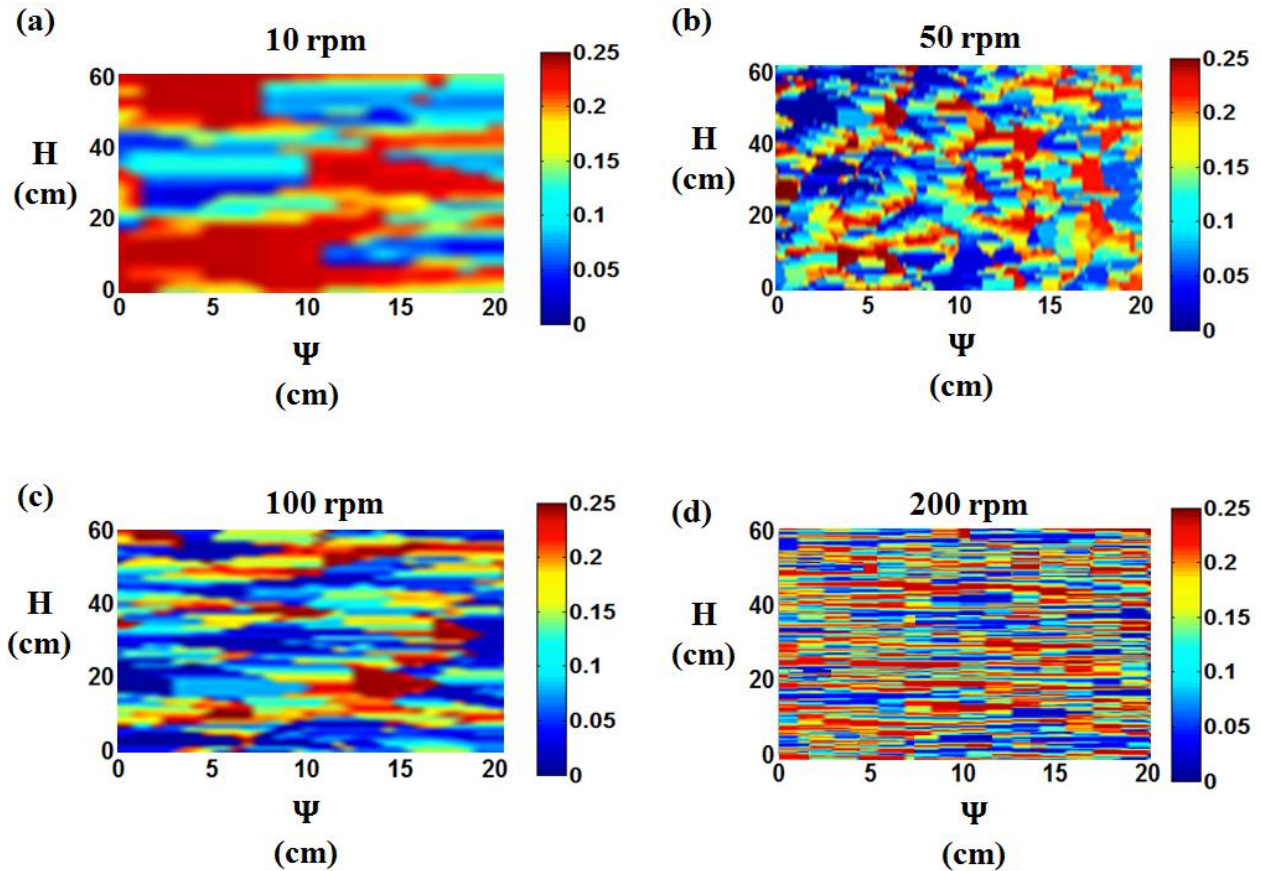


Fig. 5.3. Mass distribution in the numerically simulated solution-blown laydown. The values in g/cm^2 correspond to the color bars on the right. Different panels correspond to the mass distributions predicted for different values of the angular velocity, namely, panels (a), (b), (c) and (d) correspond to the angular velocities of the rotating drum of 10 rpm, 50 rpm, 100 rpm and 200 rpm, respectively. All the simulations were done for 60 polymer solution jets.

The deposited mass distribution in nonwoven laydown is an important characteristics of the process [Sinha-Ray et al. 2011, Sinha-Ray et al. 2013]. The process conditions should be optimized to achieve a uniform mass distribution over the laydown, improve the production output and minimize ‘rejects’. The present numerical simulations can provide intend to guide the industrial implementation of solution blowing process. For that purpose, the predicted mass

distribution across in the laydown unrolled from the collector drum is shown in Fig. 5.3. The mass distribution was established using the algorithm first proposed for the meltblowing process in [Sinha-Ray et al. 2013]. For the sake of comparison all the simulations were done under similar upstream conditions, namely, the solution-blown mats were generated for the 1 minute-long operation with 60 polymer jets resulting in the identical polymer mass deposited on the rotating drum in each case. Figures 5.3a- 5.3d depict the predicted mass distributions for the four angular velocities of the rotating drum listed in the caption. In addition, using the data of Fig. 5.3, the mean values (μ) and the standard deviations (σ) of the mass distribution were calculated, as well as the coefficient of variation (σ/μ) was found. It can be seen that as the angular collector velocity increased from 10 to 200 rpm, μ and σ/μ decreased from 0.1013 g/cm² and 0.9033, respectively, to 0.0907 g/cm² and 0.0706, respectively. These results show that the uniformity of laydown increases as the angular velocity of the collector increases. Also, as the angular velocity of the rotating drum increases, the non-uniform features in the deposited solution-blown laydown diminish in size, since a faster drum rotation facilitates filling the gaps in the laydown architecture. A similar phenomenon was revealed in the numerical simulations of meltblowing in [Sinha-Ray et al. 2011, Sinha-Ray et al. 2013], where it was found that for the higher the collector screen velocities the mass distribution in the laydown was more uniform. Therefore, an economically viable solution blowing process employing a high throughput with a high angular velocity of the collector drum simultaneously results in a more uniform laydown.

Angular Velocity (rpm)	Mean Value (g/cm ²)	Standard Deviation (g/cm ²)	Coefficient of Variation
10	0.1013	0.0915	0.9033
50	0.101	0.0524	0.5188
100	0.0928	0.0115	0.1239
200	0.0907	0.0064	0.0706

Table 5.2. The mean values, the standard deviation and the coefficient of variation of mass distributed across laydown for different angular velocities of the collector.

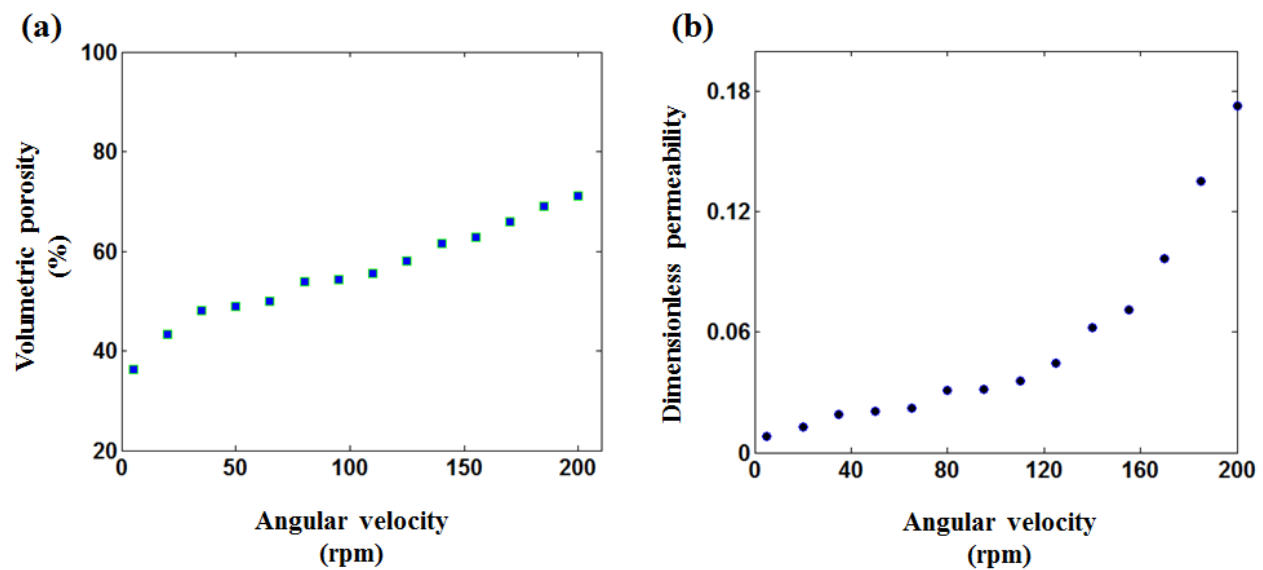


Fig. 5.4. Predicted variation of the volumetric porosity (a), and the dimensionless permeability (b) with the angular velocity of the collector drum.

Two additional characteristics of solution-blown nonwoven laydowns are the volumetric porosity and permeability. In the post-processing of the numerically simulated laydowns, the volumetric porosity p_{vol} was defined based on the predicted volume of the laydown envelope V_0 and volume V_f of the polymer fibers encompassed by this envelope, as per

$$p_{vol} = \left(1 - \frac{V_f}{V_0}\right) \times 100\% \quad (5.10)$$

Volumetric porosity values under different conditions were found by post-processing the simulated nonwoven laydowns formed by 60 polymer solution jets for 1 min, similarly to our previous work [Ghosal et al. 2016]. The laydown thicknesses were about 0.15 mm thick (cf. Fig. 5.1d).

The calculated volumetric porosity dependence of the angular speed of rotating drum is shown in Fig. 4a. As the drum angular increases, the volumetric porosity increases. This is reminiscent of the case of meltblowing on a moving collector screen studied in [Sinha-Ray et al. 2011]. Figure 5.2 and Table 5.1 show that the mean fiber size is not changing significantly with the drum speed. In the present case Fig. 5.3 shows that as the angular drum velocity increases, the mass distribution becomes more uniform in the sense that the “hills” are distributed more evenly over the laydown, i.e. fiber clustering at certain places becomes less probable, which increases the inter-fiber distances and thus the porosity.

In a number of works available in literature permeability of nonwoven and fibrous media was linked to the solid volume fraction in the framework of the following empirical correlation [Davies et al. 1952, Tomadakis et al. 2005a, Han et al. 2013, Zhu et al. 1995, Hosseini et al. 2010, Spielman et al. 1968, Drummond 1984, Tahir et al. 2009, Pradhan 2012, Chen 2008, Jackson 1986]

$$\frac{k}{r_0^2} = \left[16(1-\phi)^{1.5} \left\{ 1 + 56(1-\phi)^3 \right\} \right]^{-1} \quad (5.11)$$

where k/r_0^2 is the dimensionless permeability, r_0 is the average fiber radius, and ϕ is the solid volume fraction in the fibrous media.

Accordingly, the solid volume fraction ϕ is found from the numerically predicted porosity values shown in Fig. 5.4a as $\phi = 1 - p_{vol}$, and the dimensionless crystallinity predicted using Eq. (5.11) is plotted in Fig. 5.4b. Naturally, as the volumetric porosity increases, the dimensionless

permeability increases as well, or in the other word, as the angular velocity of the rotating drum increases, the dimensionless permeability increases too.

The predicted dimensionless permeability is compared in Fig. 5.5 with the experimental data from the literature.

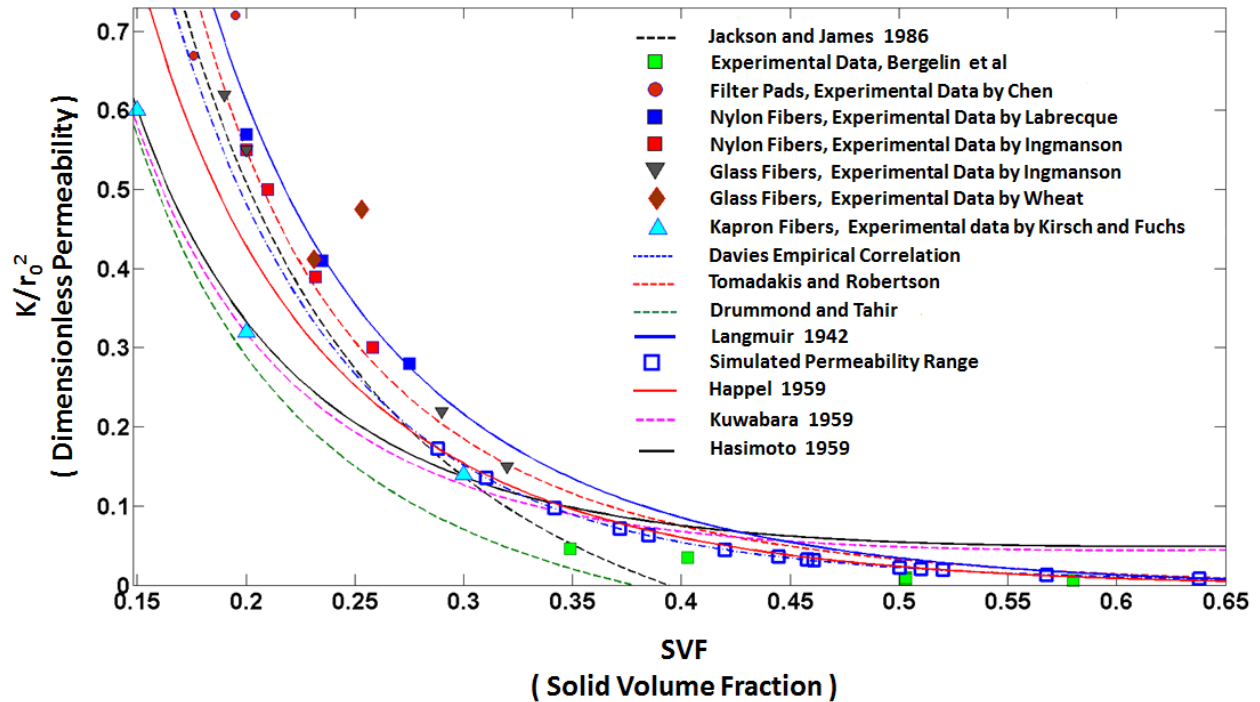


Fig. 5.5. Comparison of the dependence of the dimensionless permeability on the solid volume fraction (SVF) predicted in the present work (blue squares denoted Simulated permeability) with the other existing models and experimental data available in literature.

5.6. Experiments of the present work versus the numerical predictions

The numerical predictions were also compared with the experimental data of the present work. The experimental setup used in the present work had several limitations in comparison with the numerical model. Namely, (i) there were only two solution blowing nozzles (cf. Fig. 5.1a), (5.b) the rotating drum (Fig. 5.1e) was not vacuumized resulting in a partial bouncing of the

oncoming polymer solution jets, (iii) only two angular velocities of the rotating drum of 130 rpm and 240 rpm were available. Therefore, for the sake of comparison, in the numerical simulations in the present section only two polymer solution jets were generated. The simulations continued until the average simulated laydown thickness reached about 0.1-0.2 mm. Similarly, the collected nonwoven laydown thickness was about 0.1-0.2 mm. All the simulations were conducted for the two angular velocities of 130 and 240 rpm, for two different initial polymer (nylon-6 in formic acid) concentrations in solution of 15 and 18 wt%. The laydown characterization in the experiments were done using Vertical Scanning Profilometry with Bruker “Contour GT-K” optical profilometer model and the resulting images were processed with Vision 64 Software to calculate the laydown thickness and volumetric porosity.

The measurements of the sample elevation/thickness with the optical profilometer using laydown areas of the order of $100\ \mu\text{m} \times 100\ \mu\text{m}$ is illustrated in Fig. 5.6. Panels 5.6a and 5.6b show the two-dimensional (top view) images obtained by Bruker optical profilometer for a sample solution-blown from the 15wt% polymer solution an the angular drum speed of 240 rpm, taken at two different locations of the sample. Panels 5.6c and 5.6d show the corresponding three-dimensional images. Panel 5.6e shows the average elevation obtained from several locations of the sample. To obtain a statistically sound comparison between the simulated and measured thicknesses, the simulated laydown area ($20\ \text{cm} \times 10\ \text{cm}$) was subdivided into several smaller areas of $250\ \mu\text{m} \times 250\ \mu\text{m}$. Averaging the simulated mean elevation over those smaller areas, the average elevation distribution in panel 5.6f was found.

The optical profilometer estimates the pore volume in the following way. For a sample under observation, based on pixel count, the volume of water required to fill up to the topmost surface layer, is measured. That is the pore volume of the sample. Similarly, the total pixel count of the

raw sample stands for the volume of non-porous part, and adding these two, the net volume under the surface can be estimated. Then, the ratio of the pore volume and the total volume is calculated to estimate porosity.

All the experimental and numerical results are listed in Table 5.3. The comparison shows that for similar thicknesses of the numerically simulated and experimentally generated laydowns, the predicted and measured porosity values were quite close, and revealed a similar trend with the angular velocity and polymer concentration. Also, the comparison of the experimentally measured (Fig. 5.6e) and the numerically simulated (Fig. 5.6f) laydown landscapes is quite favorable in the sense that they both revealed a similar altitude variation, albeit the experimental one appeared to be more “hilly” than the numerically simulated one.

Polymer Concentration (%)	Collector Angular Velocity (rpm)	Numerical Prediction		Experimental Measurement (Optical Profilometry)	
		Average Thickness (μm)	Volumetric Porosity (%)	Average Thickness (μm)	Volumetric Porosity (%)
15	130	198.51	53.33	266.934	64.14
	240	158.84	88	163.752	87.59
18	130	167.26	84	173.54	76.50
	240	112.38	93	114.45	90.97

Table 5.3. Comparison of the predicted and experimental volumetric porosity for two different polymer concentrations in solution and two different angular velocities of the rotating drum.

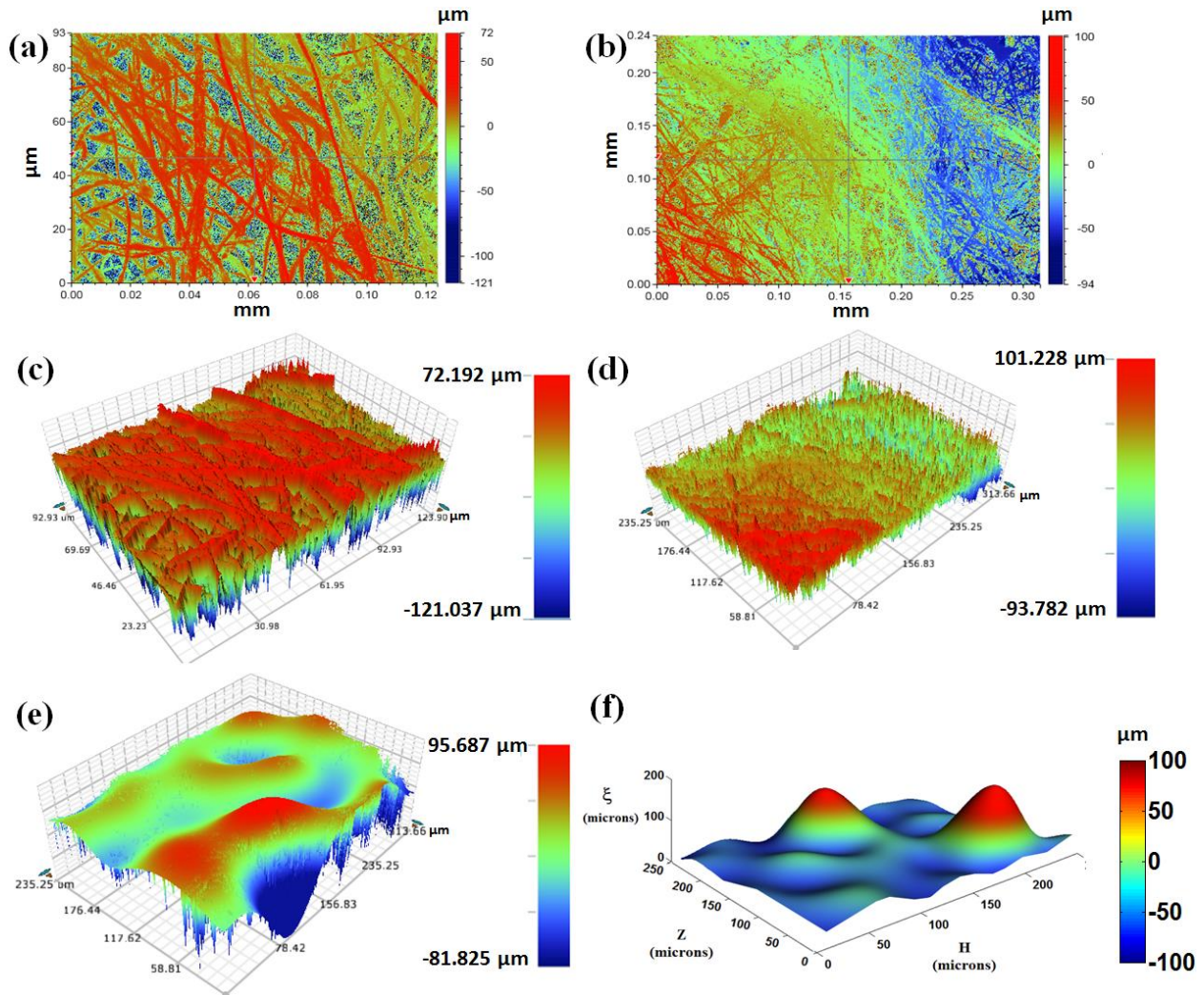


Fig. 5.6. Comparison of the measured laydown elevation (a)-(e) with the simulated average elevation (f) for a comparable laydown size.

The signal filtering procedure and images of solution blown naofibers from samples are given below in section 5.7.

5.7. Signal filtering using the Fourier and Gaussian smoothing

To obtain smoothed distributions of surface elevations, two types of smoothing were tested and compared, namely, the Fourier and Gaussian smoothing. The raw 3D and 2D (top view) data on the surface elevation distributions for a laydown of sample 1 from Table 5.4 are shown in Fig. 5.7 and for sample 2 from Table 5.4, the raw 3D, 2D (top view) data on the surface elevation distributions and the spanwise cut cross-sectional profiles are shown in Fig. 5.8.

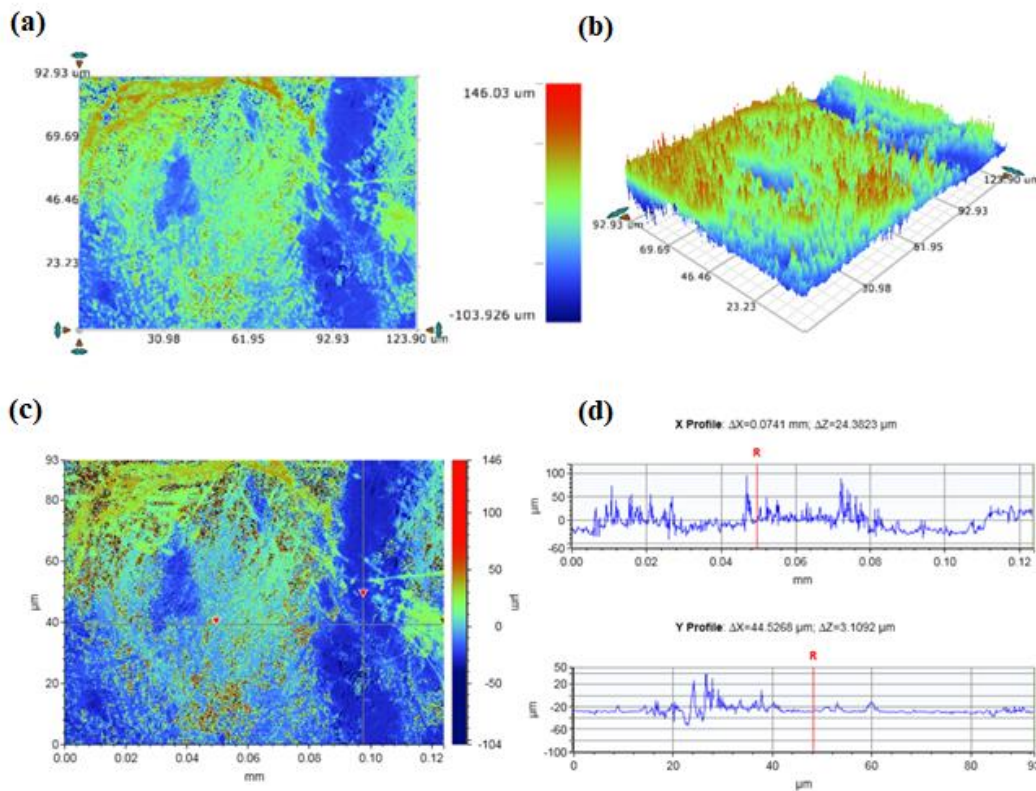


Figure 5.7: The raw 2D (top view) (panel (a)) and 3D (panel (b)) optical profilometer data for laydown corresponding to sample 1 from Table 5.4. Surface elevation distributions after noise removal is shown in panel (c). Span wise and cross-cut sectional profiles in two directions over the laydown are revealed in panel (d) as obtained by the optical profilometer corresponding to corresponding to sample 1 from Table 5.4.

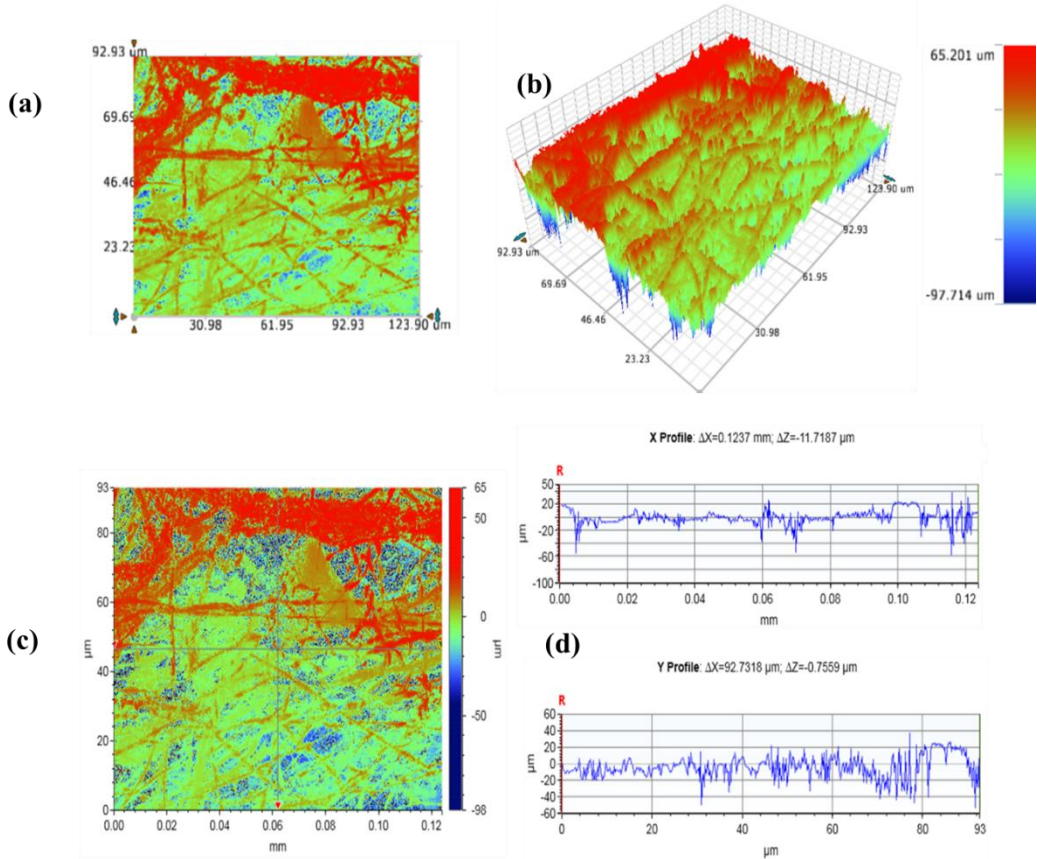


Figure 5.8: The raw 2D (panel(a)) and 3D (panel (b)) optical profilometer data for laydown corresponding to row 2 from Table 5.4. Surface elevation distributions after noise removal is shown in panel(c) and spanwise and cross-cut sectional profiles in two directions over the laydown are revealed in panel (d) as obtained by the optical profilometer corresponding to sample 2 from Table 5.4.

The smoothed data for sample of Fig. 5.6(a) is depicted in Fig. 5.9. The Fourier and Gaussian filtering produce qualitatively similar transformations of the raw optical profilometer data, albeit the values of the elevations after smoothing can significantly disagree. The raw and smoothed elevation fields over the same sample are compared in Fig. 5.9. Fourier smoothing of images is useful for understand and analysis of surface properties of experimental images.

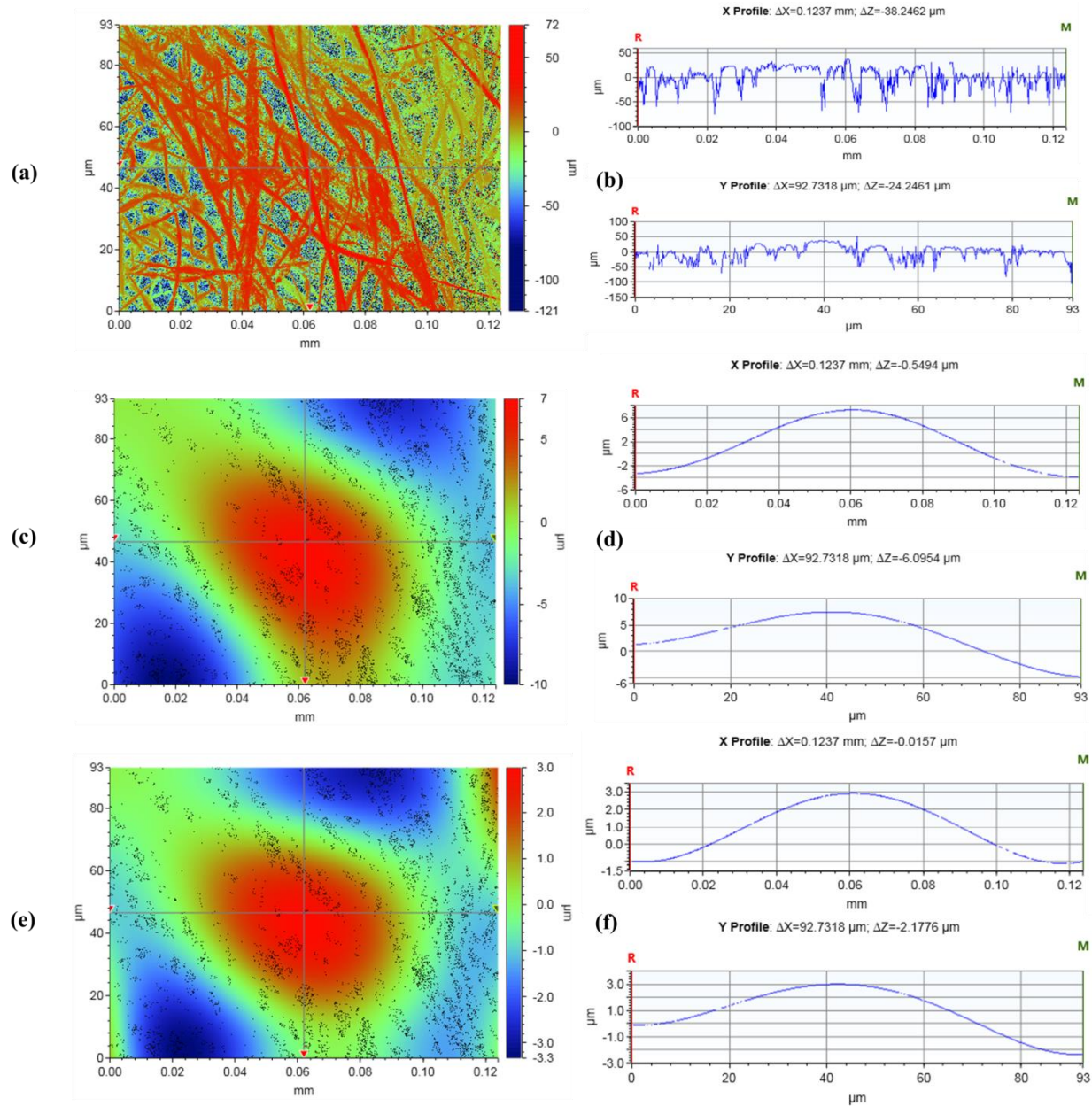


Figure 5.9: The comparison of the raw and smoothed elevation fields over the nanofiber sample obtained from solution-blowing of 15wt% polymer solution collected at an angular drum speed of 240 rpm as shown previously in Fig. 5.6(a). Panels (a), (c), and (e) represent the original dataset, the Fourier-filtered dataset and the Gaussian-filtered dataset, respectively. The right-hand-panels (b), (d) and (f) show the corresponding cross-sectional profiles measured along the axes shown in panels (a), (c) and (e).

Sample Number	Polymer	Rotation Speed (rpm)	Collection Time (mins)	Initial Polymer Concentration (wt%)
1	Nylon-6	134	10	15
2	Nylon-6	240	10	15
3	Nylon-6	137	10	18
4	Nylon-6	240	10	18

Table 5.4. Tabulated operating conditions used to form 4 samples of the predicted and experimental volumetric porosity for two different polymer concentrations in solution and two different angular velocities of the rotating drum collector.

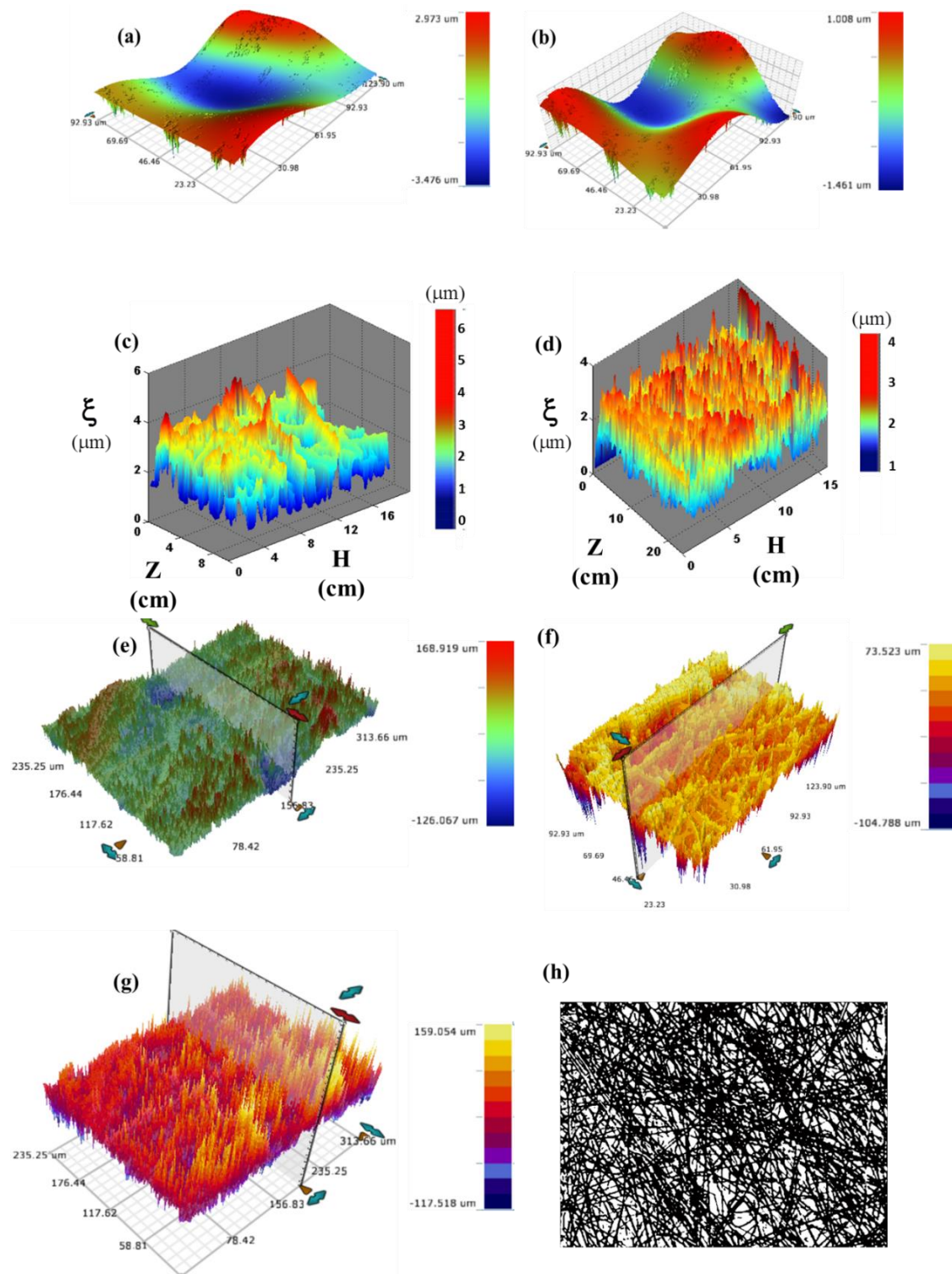


Figure 5.10: Smoothing of the data for sample 3 from Table 5.4. (a) Fourier- filtered surface elevation distribution of the uppermost layer of the laydown. (b) Gaussian-filtered surface elevation distribution. The elevations are measured by color scale bars. (c) The Fourier-smoothed

result for the uppermost layer from the numerically simulated elevation profile with the input conditions corresponding to sample 3. (d) The Gaussian-smoothed numerically simulated elevation profile for the uppermost layer for sample 3. (e) The un-filtered original image from an arbitrary focus location from sample 3. Panels (f) and (g) show, respectively, the Fourier- and Gaussian-smoothed results obtained from panel (e). Panels (e)-(g) correspond to spunwise cross-sectional planes. Panel (h) represents a processed SEM image used for porosity calculation.

Fig. 5.10 shows that the Gaussian filter usually produces a lower thickness as compared to the Fourier-smoothed image for both experimentally measured samples, as well as the numerically simulated thickness results, cf. panels (a)-(d) and (e)-(g). Moreover, the fibrous structure of the 3-D conformation domain is retained and expressed better in case of the Fourier filter.

The volumetric analysis of the profilometer results computes the void volume based on pixel measurements. In this particular case, the SEM-based cross-sectional and volumetric porosity values corresponding to Fig. 5.10(h) are, respectively 0.48 and 0.71, the profilometer-based measured volumetric porosity for the Fourier-filtered image in Fig. 5.10(f) is 0.8 and for the Gaussian-filtered image in Fig. 5.10(g) it is 0.71. For the uppermost layer of the laydown, the numerically simulated Fourier-image shown in Fig. 5.10(c) revealed the volumetric porosity of 0.88 compared to the Gaussian-image shown in Fig. 10(b) with the volumetric porosity of 0.75. The simulation results for the entire fibermat produced under similar conditions have already been mentioned in Table 5.3. They revealed a very good agreement between the measured and predicted values of the volumetric porosity.

5.8. Conclusion

Solution blowing has high potential for industrial production of nanofibers en masse. The experiments with solution blowing were conducted and samples of nanofiber laydowns were collected on a rotating drum under fully controlled conditions. The numerical code for prediction of solution blowing was modified to accommodate the rotating drum collector. The numerical predictions revealed the surface and volumetric porosities of the solution blown laydowns, and in particular that they differ from each other, which signifies a non-isotropic nature of such laydowns. The surface elevations and porosities were measured using the experimentally formed samples and compared with the numerical predictions. The first comparisons revealed a reasonable agreement between the experimental data and the predicted values. Variation of downstream parameters in the manufacturing process is always more cost-effective than changing upstream processes. Also, to change and control physical properties of solution blown product, one of the sensitive and effective parameter is the uptake angular velocity of the collector. It has been found in this current work that a higher uptake velocity in solution blowing process prepares nano-fibrous webs of higher porosity and permeability which is a desired property in several applications of the nonwoven industry.

Chapter 6: Modeling Polymer Crystallization Kinetics in Meltblowing Process

(Accepted for publication in Industrial & Engineering Chemistry Research as Ghosal, A., Chen, K., Sinha-Ray, S., Yarin, A.L. and Pourdeyhimi, B. (2019) Modeling Polymer Crystallization Kinetics in Meltblowing Process.)

Abstract

A novel model of crystallization process in meltblowing process is proposed and implemented in numerical simulations. The spinline crystallization is studied using numerical solutions of the system of coupled quasi-one-dimensional equations describing the dynamics of multiple polymer jets moving in the surrounding high-speed air. Cooling, crystallization and solidification accompany three-dimensional motion of polymer jets resulting in their vigorous stretching by the air flux including the aerodynamically-driven bending/flapping. The numerical solutions predict distribution of the degree of crystallinity in polymer jets in flight, as well as in the laydown formed on the collecting screen, with the three-dimensional structure of the laydown being fully reconstructed. The effect of collector screen temperature, die-to-collector distance, (DCD), gas blowing velocity and the activation energy of viscous flow in polymer melt on the laydown features is studied in detail.

6.1. Introduction

Meltblowing is one of the most widely used methods for nonwoven manufacturing. The global market of meltblowing is of the order of billions of dollars. The process of meltblowing dates back to the 1950s, when the US Naval Research Laboratory developed meltblowing as a means of formation of microfilters capable of collecting radioactive particles from the upper

atmosphere. This was later commercialized by Exxon as meltblowing process [Shambaugh et al. 1988, Wehmann et al. 1999]. The most attractive part of this process is in its ease and the rate of formation of micron-sized polymer fibers [Shambaugh et al. 1988, Wehmann et al. 1999, Uyttendaele et al. 1990]. In meltblowing process low-speed polymer melt is issued through multiple dies located along a nosepiece into a high-temperature high-velocity coaxial air flow, which then stretches, vigorously bends (still stretching) and attenuates polymer jets to smaller-sized fibers [Shambaugh et al. 1988, Wehmann et al. 1999, Uyttendaele et al. 1990, Yarin 2014, Yarin 1993, Sinha-Ray et al. 2010, Bresse et al. 2003, Hassan 2016, Lalagiri 2013]. The present group recently modelled meltblowing and the related solution blowing processes in detail accounting for the physical mechanisms involved [Yarin 2014, Sinha-Ray et al. 2010, Yarin et al. 2010, Yarin et al. 2011, Sinha-Ray et al. 2011, Sinha-Ray et al. 2013, Ghosal et al. 2016]. In particular, the entire three-dimensional structure of the laydown including fiber sizes, orientation, porosity and permeability was predicted in [Yarin et al. 2011, Sinha-Ray et al. 2013, Ghosal et al. 2016, Ghosal et al. 2016a]. However, the crystallization process and the degree of crystallinity were not included yet.

Crystallization of meltblown polymer fibers has a significant effect on physical properties of the resulting laydown. It was found that mechanical properties of thermoplastic polymers depend significantly on the degree of crystallinity [Talbot et al. 1987]. The effect of crystallinity of polyethylene terephthalate (PET) and nylon 66 fibers on susceptibility to plasma etching and dyeability was revealed in [Okuno et al. 1992]. It was also found that crystallinity of poly(ethylene oxide) (PEO) has a significant effect on gas transport, namely, that the higher the crystallinity of PEO is, the lower is the gas permeability [Liu et al. 2013]. A detailed literature survey of the effect of polymer crystallinity on gas or vapor separation is given in [Lau et al. 2013]. The effect of

polymer crystallinity on fiber-reinforced composites is discussed in detail in [Morozova et al. 1998]. Since crystallinity of meltblown polymer fibers affects significantly several practical applications, multiple efforts were directed at the research of crystallization kinetics in fiber forming [Jarecki et al. 2012, Ziabicki 1976, Ziabicki et al. 1988, Ziabicki et al. 1988a, Yarin et al. 1992, Grady et al. 2002, Bansal et al. 1996, Meerveld et al. 2008, Kim et al. 2005, Doufas et al. 2000, Doufas et al. 2000a, Cho et al. 1999, Entov et al. 1984, Schneider et al. 1988]. Several theoretical approaches for description of spinline crystallization were developed for the case of high-speed melt spinning processes [Yarin 1993, Jarecki et al. 2012, Ziabicki 1976, Ziabicki et al. 1988, Ziabicki et al. 1988a, Yarin et al. 1992, Grady et al. 2002], while the experimental investigations of the degree of crystallinity are available in [Okuno et al. 1992, Liu et al. 2013, Lau et al. 2013]. A continuum model of flow-induced crystallization in melt spinning and injection moulding of polymers was proposed in [Yarin 1993, Yarin et al. 1992, Kim et al. 2005]. Also, rheological aspects related to the shear-induced crystallization in melt spinning processes were discussed in [Doufas et al. 2000, Doufas et al. 2000a, Cho et al. 1999, Entov et al. 1984]. However, to the best of our knowledge, there is still no meltblowing model capable of predictions of crystallization kinetics and the degree of crystallinity under realistic conditions.

The present work aims at extending the spinline crystallization model of [Yarin 1993, Yarin et al. 1992] for the case of meltblowing, where in distinction from melt spinning, polymer jets acquire transient three-dimensional configurations due to the aerodynamically-driven bending instability. This model predicts nucleation rate and the crystal-growth kinetics. The model also accounts for the effect of the degree of crystallinity on the rheological behavior of polymer melt, and thus on the jet evolution and stretching. Ultimately, the model also predicts the degree of crystallinity and its distribution in the laydown.

6.2. Dynamics equations

The governing equations of the dynamics of free liquids jets implemented in the present work to describe the evolution of polymer jets were proposed in [Yarin 2014, Yarin 1993, Sinha-Ray et al. 2010, Yarin et al. 2010, Yarin et al. 2011, Sinha-Ray et al. 2013, Ghosal et al. 2016]

$$\frac{\partial \lambda f}{\partial t} + \frac{\partial f W}{\partial s} = 0 \quad (6.1)$$

$$\frac{\partial \lambda f \mathbf{V}}{\partial t} + \frac{\partial f W \mathbf{V}}{\partial s} = \frac{1}{\rho} \frac{\partial P \boldsymbol{\tau}}{\partial s} + \lambda f \mathbf{g} + \frac{\lambda}{\rho} \mathbf{q}_{\text{total}} \quad (6.2)$$

Equations (6.1) and (6.2) correspond to the mass and momentum balance in the jet written in the so-called momentless approximation, i.e. neglecting the effect of the shearing force in the jet cross-section and, accordingly, the moment-of-momentum equation [Yarin 1993, Entov et al. 1984]. The following notations are used: t is time, s is an arbitrary parameter (coordinate) reckoned along the jet axis (may be a Lagrangian coordinate), $f(s,t) = \pi a^2$ is the cross-sectional area, with the cross-section being assumed circular in spite of the jet bending (which is a legitimate approximation, as shown in [Yarin 1993, Entov et al. 1984]); the cross-sectional radius is denoted as $a(s,t)$, and W denotes the liquid velocity along the jet relative to a cross-section with a certain value of s , $\lambda = |\partial \mathbf{R} / \partial s|$ denotes the stretching factor, with $\mathbf{R}(s,t)$ being the position vector of the jet axis. Also, $\mathbf{V}(s,t)$ is the absolute liquid velocity in the jet, ρ is the liquid density, $P(s,t)$ is the magnitude of the internal force, of the rheological, e.g., viscoelastic origin, in the jet cross-section directed along the jet axis. The unit tangent vector to the jet axis is denoted by $\boldsymbol{\tau}$, the gravity acceleration – by \mathbf{g} , and the overall aerodynamic force acting on a unit jet length from the

surrounding air – by $\mathbf{q}_{\text{total}}$. It should be emphasized that here and hereinafter boldfaced characters denote vectors.

The longitudinal force in the jet cross-section $P(s,t) = f(\tau_{\tau\tau} - \tau_{nn}) \approx f\tau_{\tau\tau}$ where $\tau_{\tau\tau}$ and τ_{nn} are the longitudinal and normal deviatoric stresses in the jet cross-section, respectively. The deviatoric stresses are related to the kinematic parameters using an appropriate rheological constitutive equation, in the present case the upper-convected Maxwell model (UCM). Such rheological parameters of the model as the zero-shear viscosity and the viscoelastic relaxation time are described as temperature-dependent, as well as dependent of the degree of crystallinity as described below. This also allows for the prediction of the jet solidification as it undergoes cooling in flight, while also undergoing the aerodynamic stretching and bending.

The projections of the momentum balance equation (6.2) onto normal, tangent and binormal directions (the local unit tangent $\boldsymbol{\tau}$, normal \mathbf{n} , and binormal \mathbf{b}) of the jet axis in meltblowing can be reduced to the following form [Shambaugh et al. 1988, Yarin 2014, Yarin 1993, Sinha-Ray et al. 2010]

$$\frac{\partial V_{\tau}}{\partial t} = V_n \left(\frac{1}{\lambda} \frac{\partial V_n}{\partial s} + k V_{\tau} \right) + \frac{1}{\rho f \lambda} \frac{\partial P}{\partial s} + g_{\tau} + \frac{q_{\text{total},\tau}}{\rho f} \quad (6.3)$$

$$\frac{\partial V_n}{\partial t} = -V_{\tau} \left(\frac{1}{\lambda} \frac{\partial V_n}{\partial s} + k V_{\tau} \right) + \frac{Pk}{\rho f} + g_n + \frac{q_{\text{total},n}}{\rho f} \quad (6.4)$$

$$\frac{\partial V_b}{\partial t} = -V_b \left(\frac{1}{\lambda} \frac{\partial V_n}{\partial s} + k V_{\tau} \right) + \frac{Pk}{\rho f} + g_b + \frac{q_{\text{total},b}}{\rho f} \quad (6.5)$$

Here k is the local curvature of the jet axis, and subscripts τ , n and b designate the vector projections onto the local tangent, normal and binormal to the jet axis.

The projections of the momentum balance equations (6.3)-(6.5) are reduced further to the following dimensionless system of equations [Yarin 2014, Yarin 1993, Sinha-Ray et al. 2010]

$$\frac{\partial^2 \xi}{\partial t^2} = \frac{2}{\text{Re}} \Phi \frac{\partial^2 \xi}{\partial s^2} + \frac{\tau_\xi}{\text{Fr}^2} + \ell J \frac{q_{\text{total},\tau}}{f} \quad (6.6)$$

$$\frac{\partial^2 H}{\partial t^2} = \left[\frac{\tau_{\tau\tau}}{\text{Re}} - J\varphi^2(\xi, H, Z) \right] \left| b_\zeta \right| \frac{1}{\lambda^2} \frac{\partial^2 H}{\partial s^2} - \frac{\tau_\eta}{\text{Fr}^2} + b_\zeta \ell J \frac{\varphi^2(\xi, H, Z)}{\pi a} n_\xi^2 \text{sign}(n_\xi) \quad (6.7)$$

$$\frac{\partial^2 Z}{\partial t^2} = \left[\frac{\tau_{\tau\tau}}{\text{Re}} - J\varphi^2(\xi, H, Z) \right] \left| b_\eta \right| \frac{1}{\lambda^2} \frac{\partial^2 Z}{\partial s^2} + \frac{(b_\eta \tau_\eta + b_\xi)}{b_\eta \text{Fr}^2} - b_\eta \ell J \frac{\varphi^2(\xi, H, Z)}{\pi a} n_\xi^2 \text{sign}(n_\xi) \quad (6.8)$$

The scales used to render equations (6.6)-(6.8) dimensionless are mentioned [Yarin 2014, Sinha-Ray 2012] as follows. DCD (Die-to-c ollector distance) is used for all lengths except diameter of polymer jet . Cross-sectional radius at the end of the straight part of the jet $a_{0,\text{straight}}$ is used for jet radius whereas $a_{0,\text{straight}}^2$ is used for the cross-sectional area of the polymer jet. Initial velocity of gas blowing U_{g0} is used for all velocities. L/U_{g0} is used for time t and all stress terms are rendered dimensionless by $\mu_0 U_{g0}/L$, where μ_0 denotes the zero-shear viscosity of the polymer melt at the nozzle exit. The distributed aerodynamic force $q_{\text{total},\tau}$ and $q_{\text{total},n}$ are rendered dimensionless with $\rho_g U_{g0}^2 a_{0,\text{straight}}$ where ρ_g is the gas density.

The position vector of the jet axis in the Cartesian laboratory coordinate axes is presented as

$$\mathbf{R} = \mathbf{i}\xi(s, t) + \mathbf{j}H(s, t) + \mathbf{k}Z(s, t) \quad (6.9)$$

with \mathbf{i} , \mathbf{j} and \mathbf{k} being the unit vectors in the directions of blowing and two normals to it, respectively.

Also, such geometric parameters as the stretching ratio and curvature, λ and k , respectively, in Eqs.

(6.3)-(6.5) are found as

$$\lambda = \left(\xi_{,s}^2 + H_{,s}^2 + Z_{,s}^2 \right)^{1/2} \quad (6.10)$$

$$k = \frac{\sqrt{(Z_{,ss} H_{,s} - H_{,ss} Z_{,s})^2 + (\xi_{,ss} Z_{,s} - Z_{,ss} \xi_{,s})^2 + (H_{,ss} \xi_{,s} - \xi_{,ss} H_{,s})^2}}{\lambda^3} \quad (6.11)$$

The net aerodynamic force has three components: the distributed longitudinal lift force, the distributed drag force resulting from air flow across the jet, as well the pulling drag force due to the longitudinal air flow [Shambaugh et al. 1988, Yarin 2014, Yarin 1993, Sinha-Ray et al. 2010, Yarin et al. 2010]

$$\begin{aligned} \mathbf{q}_{\text{total}} = & \mathbf{n}q_{\text{total},n} + \boldsymbol{\tau}q_{\text{total},\tau} + \mathbf{b}q_{\text{total},b} = \\ & -\rho_a U_g^2 \mathbf{n} \left[f \frac{\xi_{,s}^2 (H_{,ss} \xi_{,s} - \xi_{,ss} H_{,s})}{(\xi_{,s}^2 + H_{,s}^2)^{5/2}} + a \frac{(H_{,s} / \xi_{,s})^2 \text{sign}(H_{,s} / \xi_{,s})}{1 + (H_{,s} / \xi_{,s})^2} \right] \\ & + \pi a \rho_a (U_g \tau_\xi - V_\tau)^2 c \left[\frac{2a (U_g \tau_\xi - V_\tau)}{\mathbf{v}_a} \right]^{-0.81} \boldsymbol{\tau} \end{aligned} \quad (6.12)$$

Here U_g is the magnitude of the absolute blowing velocity of gas (air), τ_ξ denote the projection of the blowing velocity onto the local direction of the jet axis, and c is a constant.

Since in the present case of strong stretching the deviatoric stresses satisfy the inequality $\tau_{\tau\tau} \gg \tau_{nn}$, the normal deviatoric stress can be neglected. Then, the longitudinal internal force is determined by the longitudinal deviatoric stress, i.e. $P = f\tau_{\tau\tau}$. The constitutive equation for $\tau_{\tau\tau}$ is obtained from the viscoelastic upper-convected Maxwell model (UCM) in the following Lagrangian form [Yarin 2014, Yarin 1993, Yarin et al. 2010]

$$\frac{\partial \tau_{\tau\tau}}{\partial t} = 2\tau_{\tau\tau} \frac{1}{\lambda} \frac{\partial \lambda}{\partial t} + 2 \frac{\mu}{\Theta} \frac{1}{\lambda} \frac{\partial \lambda}{\partial t} - \frac{\tau_{\tau\tau}}{\Theta} \quad (6.13)$$

6.3. Rate of crystallization and degree of crystallinity

Polymer crystallization kinetics is addressed next to predict the degree of crystallinity and relate the zero-shear viscosity μ and the relaxation time Θ to it. Figure 6.1 introduces the spherical coordinate system used to describe nuclei formation and growth at a certain location of polymer melt in a jet.

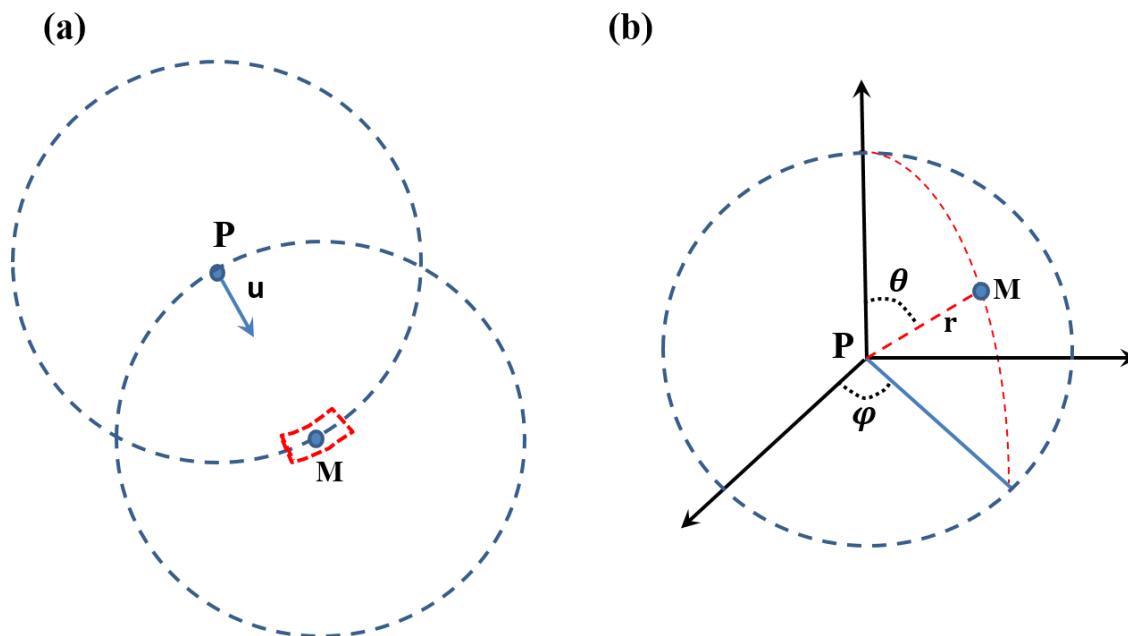


Figure 6.1. Schematic of the spherical coordinate system used to describe crystal nuclei formation and growth.

The origin of the spherical coordinate system is located at point P, while at point M a crystal nucleus is nucleated due to a fluctuation. The radial coordinate of point M is r and a volume element surrounding point M is found, accordingly, as $r^2 \sin \theta d\theta d\varphi dr = r^2 dr d^2\mathbf{u}$, where θ and φ are the angular coordinates, and \mathbf{u} is a randomly oriented unit vector.

Let the nucleation rate is I_* , and the crystal cross-sectional diameter is d , while it is implied that the growing crystals have a cylindrical shape. It should be emphasized that the crystal nucleation rate I_* per unit volume per unit time is determined, as usual, by thermal fluctuations. Assume that from each nucleus in the volume surrounding point M in Fig. 6.1a begins to grow a cylindrical crystal with cross-sectional diameter d . With the probability density $W(\mathbf{u}, t)$ it is directed along the line PM. The probability that point P will be incorporated in this crystal is equal to $2W(\mathbf{u}, t)\left(\pi d^2 / 4r^2\right)$, where $\pi d^2 / 4r^2$ is the solid angle surrounding point P into which the growing crystal is expected to enter. The factor 2 appears due to the fact that not only the crystal growing in the \mathbf{u} direction, but also the one growing in the $-\mathbf{u}$ direction can reach point P, since crystals are supposed to grow from both sides.

The time it takes a crystal to reach point P from point M is r/v , where v is the crystal growth rate. It should be emphasized that v is assumed to be temperature-independent. So, by a time moment t , all crystals which are growing toward the element surrounding point P and were nucleated not later than time r/v before t will reach point P. Accordingly, the number of crystals growing from the element surrounding point M in the \mathbf{u} and $-\mathbf{u}$ directions that will arrive at the element surrounding point P during time t will be

$$dN = \int_0^{t-r/v} I_*(\tau) d\tau W(\mathbf{u}, t) \frac{\pi d^2}{2} dr d^2\mathbf{u} \quad (6.14)$$

In the particular case of an isothermal crystallization the nucleation rate I_* is constant.

Therefore,

$$\int_0^{t-r/v} I_*(\tau) d\tau = I_* \left(t - \frac{r}{v} \right) \quad (6.15)$$

and Eq. (6.11) takes the following form

$$dN = I_* \left(t - \frac{r}{v} \right) W(\mathbf{u}, t) \frac{\pi d^2}{2} dr d^2 \mathbf{u} \quad (6.16)$$

Thus, integrating Eq. (6.13), one obtains the number of crystals from a spherical layer of thickness dr at a distance r from point P that will arrive at point P during time t in the case of the isothermal crystallization

$$\begin{aligned} N(r) &= \int d^2 \mathbf{u} I_* \left(t - \frac{r}{v} \right) W(\mathbf{u}, t) \frac{\pi d^2}{2} dr \\ &= I_* \left(t - \frac{r}{v} \right) \frac{\pi d^2}{2} dr \int W(\mathbf{u}, t) d^2 \mathbf{u} = I_* \left(t - \frac{r}{v} \right) \frac{\pi d^2}{2} dr \end{aligned} \quad (6.17)$$

Note that $\int W(\mathbf{u}, t) d^2 \mathbf{u} = 1$, since $W(\mathbf{u}, t)$ is the probability density function.

Denote by E the average number of crystals which will arrive at point P during time t from the entire space. Then, integrating Eq. (6.17), one obtains in the case of the isothermal crystallization process

$$E(t) = \int_0^{r=vt} I_* \left(t - \frac{r}{v} \right) \frac{\pi d^2}{2} dr = I_* \frac{\pi d^2}{4} v t^2 \quad (6.18)$$

Assume that crystals are nucleated randomly in time as is schematically shown in Fig. 6.2 and calculate the degree of crystallinity η_c . Consider an observer located at point P. Since crystals are nucleated randomly in time in the space surrounding point P, their edges arrive at point P at random time intervals. The mean expected value of the arriving crystals in the isothermal process is given by E from Eq. (6.18), however, due to the random nucleation process there might be deviations from the mean value. To evaluate the probability that during time t the edges of i

growing crystals will reach point P, subdivide this time interval into many equal sub-intervals $\Delta t = t/n$, with n being the number of the sub-intervals. Probability that during a certain time interval one or several crystals have arrived at point P is denoted p_n . Thus, the probability that no crystals have arrived at

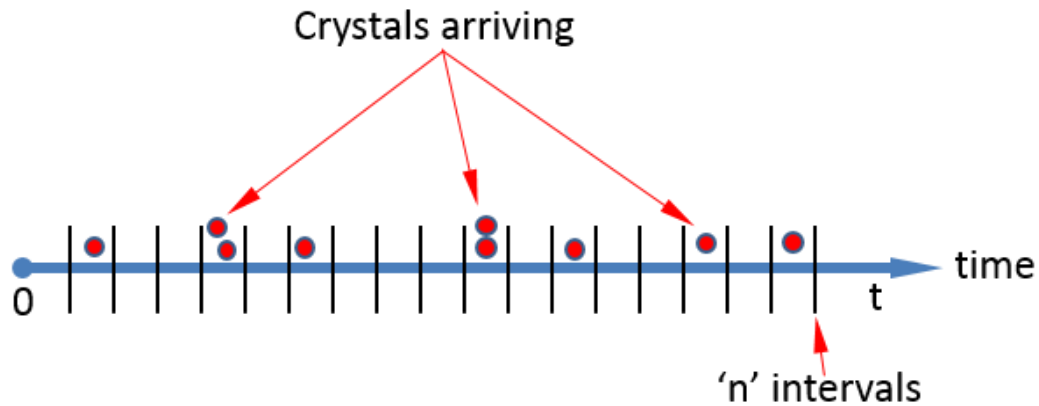


Figure 6.2. Schematic of the random process of crystallinity build-up at point P. The total number of the intervals is n .

point P during a certain time interval is, accordingly, $(1-p_n)$. Then, the probability of a certain realization with i time intervals with crystals arriving at point P and the remaining $(n-i)$ intervals with no crystals arriving at this point is $(p_n)^i(1-p_n)^{n-i}$. The number of such realizations is $n!/[i!(n-i)!]$. Therefore, the probability of i intervals with crystals arriving at point P and $(n-i)$ intervals without crystals during time t is

$$b(i, n, p_n) = \frac{n!}{i!(n-i)!} (p_n)^i (1-p_n)^{n-i} \quad (6.19)$$

It should be emphasized that as $n \rightarrow \infty$, $p_n \rightarrow 0$, while $E = p_n n$ is finite. Equation (6.19) shows that

$$\frac{b(i, n, p_n)}{b(i-1, n, p_n)} = \frac{n-i+1}{i} \frac{p_n}{1-p_n} \rightarrow \frac{E}{i} \quad (6.20)$$

Since according to Eq. (6.19)

$$b(n, 0, p_n) = \frac{n!}{0!(n-0)!} (p_n)^0 (1-p_n)^{n-0} = (1-p_n)^n \quad (6.21)$$

and thus,

$$\begin{aligned} \ln[b(n, 0, p_n)] &= n \ln[(1-p_n)] = n \left(-p_n - \frac{p_n^2}{2} \right) \\ &= -np_n - \frac{np_n^2}{2} = -E(t) - \frac{E^2}{2n} = -E(t) + O\left(\frac{1}{n}\right) \end{aligned} \quad (6.22)$$

i.e. as $n \rightarrow \infty$,

$$b(n, 0, p_n) = \exp(-E) \quad (6.23)$$

Accordingly, using Eq. (6.20) as a recurrent formula starting from Eq. (6.23), it is easy to show that at $n \rightarrow \infty$

$$b(i, n, p_n) = \frac{E^i(t)}{i!} e^{-E(t)} \quad (6.24)$$

Hence, the probability that during time t , i growing crystals will arrive at point P denoted $P_i(t)$ is equal to

$$P_i(t) = \frac{E^i(t)}{i!} e^{-E(t)} \quad (6.25)$$

Note that, as expected, the mean value corresponding to Eq. (6.25), as is easy to see, is nothing but $E(t)$

$$\sum_{i=0}^{\infty} i \frac{E^i(t)}{i!} e^{-E(t)} = E(t) \quad (6.26)$$

It should be emphasized that the probability that no growing crystals will arrive at point P, is equal, according to Eq. (6.25), to

$$P_0 = e^{-E(t)} \quad (6.27)$$

This is the probability that the neighborhood of point P will stay non-crystalline during time t in a random isothermal crystallization process around it. Let V be a total volume of polymer melt during isothermal crystallization. Then, the volume of polymer that will stay non-crystallized during time t is $V \exp[-E(t)]$, while the corresponding volume of the crystallized part of polymer is $V - V \exp[-E(t)] = V \{1 - \exp[-E(t)]\}$. Accordingly, the degree of crystallinity η_c is found as

$$\eta_c = \frac{V[1 - e^{-E(t)}]}{V} = 1 - e^{-E(t)} \quad (6.28)$$

This is essentially the Avrami equation [Yarin et al. 1992, Sinha-Ray et al. 2010, Ziabicki 1976, Avrami et al. 1939, Avrami et al. 1940]. The case of the non-isothermal crystallization, with temperature of an individual material element of polymer jet/fiber varying in time, is considered similarly. In this case Eq. (6.17) is replaced by the following equation

$$N(r) = \int_0^{t-r/v} I_*(\tau) \left[\int W(\mathbf{u}, t) d^2\mathbf{u} \right] \frac{\pi d^2}{2} dr d\tau \quad (6.29)$$

which yields

$$N(r) = \int_0^{t-r/v} I_*(\tau) \frac{\pi d^2}{2} dr d\tau \quad (6.30)$$

Integrating Eq. (6.30), one finds the average number of crystals arriving at point P during time t from the entire space

$$E(t) = \int_0^{r=vt} \int_0^{t-r/v} I_*(\tau) \frac{\pi d^2}{2} dr d\tau = \frac{\pi d^2}{2} \int_0^{vt} \left[\int_0^{t-r/v} I_*(\tau) d\tau \right] dr \quad (6.31)$$

Equation (6.31) is the generalization of Eq. (6.18) for the non-isothermal case.

In the non-isothermal case Eqs. (6.19)-(6.28) still hold. Accordingly, differentiating Eq. (6.28), one arrives at

$$\frac{d\eta_c}{dt} = e^{-E(t)} \frac{dE(t)}{dt} \quad (6.32)$$

On the other hand, according to Eq. (6.28) $\exp[-E(t)] = 1 - \eta_c$, and thus Eq. (6.32) becomes

$$\frac{d\eta_c}{dt} = (1 - \eta_c) \frac{dE(t)}{dt} \quad (6.33)$$

Differentiating Eq. (6.31), one obtains

$$\frac{dE(t)}{dt} = \frac{\pi d^2}{2} \int_0^{vt} I_* \left(t - \frac{r}{v} \right) dr = \frac{\pi d^2}{2} v \int_0^t I_*(\tau) d\tau \quad (6.34)$$

Denote the number of nuclei beginning to grow from a unit volume as $C = \int_0^t I_*(\tau) d\tau$, with the units being $[C] = 1/\text{cm}^3$. Accordingly,

$$\frac{dC}{dt} = I_*(t) \quad (6.35)$$

In addition, Eqs. (6.33) and (6.34) yield

$$\frac{d\eta_c}{dt} = (1 - \eta_c) \frac{\pi d^2}{2} v C \quad (6.36)$$

It should be emphasized that the derivative d/dt in Eqs. (6.35) and (6.36) denotes the material time differentiation, accompanying a material element in the Lagrangian sense.

The initial conditions for the system of equations (6.35) and (6.36) read

$$t = 0: \eta_c = C = 0 \quad (6.37)$$

Equations (6.35) and (6.36) were previously used in [Yarin et al. 1992, Entov et al. 1934]. Note also that Eqs. (6.28) and (6.31) yield the generalized Avrami law in the following form [Yarin et al. 1992, Ziabicki et al. 1988]

$$\eta_c = 1 - \exp \left\{ \frac{\pi d^2}{2} \int_0^{vt} \left[\int_0^{t-\tau/v} I_*(\tau) d\tau \right] d\tau \right\} \quad (6.38)$$

6.4. Thermal balance equation

Crystallization is accompanied by heat release, which contributes to the thermal balance in the cooling polymer jets in flight. Then, with s being the Lagrangian coordinate of a material element, as in the dynamic equations in section 6.2 and in [Yarin 2014, Yarin 1993, Sinha-Ray et al. 2010, Yarin et al. 2010, Yarin et al. 2011, Sinha-Ray et al. 2013, Ghosal et al. 2016], the thermal balance equation accounting for the heat release due to crystallization takes the following form

$$\frac{\partial(\rho c_L T f)}{\partial t} = -q_w 2\pi a + \Delta h^0 \frac{\partial \eta_c}{\partial s} \rho f V_\tau \quad (6.39)$$

where q_w is the heat flux at the lateral surface of the polymer jet and $\Delta h^0 > 0$ is the latent heat of crystallization, c_L is the specific heat of the polymeric liquid, and V_τ is the longitudinal velocity in the jet.

Note that

$$\Delta h^0 \frac{\partial \eta_c}{\partial s} V_\tau = \Delta h^0 \frac{d\eta_c}{dt} \quad (6.40)$$

and thus, Eq. (6.39) can be written as

$$\frac{\partial(\rho c_L T f)}{\partial t} = -q_w 2\pi a + \Delta h^0 \rho f \frac{d\eta_c}{dt} \quad (6.41)$$

which is coupled with Eqs. (6.1), (6.2) and (6.13) and the problem (6.33) and (6.36), and forms the set of the governing equations used for tracking the polymer jet behavior in-flight and on a collector screen. After inclusion of the crystallization term, the thermal profile polymer jets can thus be found using the following equation

$$\frac{\partial \bar{T}}{\partial t} = -2 \frac{\text{Nu}}{(a_0/L)} \left(\frac{\lambda}{\lambda_0} \right) \left(\frac{\rho_{\text{gas}}}{\rho_{\text{polymer}}} \right) \left(\frac{c_{\text{p,g}}}{c_{\text{p,polymer}}} \right) \frac{(\bar{T} - \bar{T}_g)}{\text{Re}_a \cdot \text{Pr}_g} + \frac{\Delta h^0}{c_{\text{p,polymer}}} \frac{1}{T_0} \left(\frac{d\eta_c}{dt} \right) \quad (6.42)$$

The thermal profile dictates the crystallinity along the jet and the degree of crystallinity and temperature together affect the rheological parameters of the upper-convected Maxwell model (UCM) [Sinha-Ray 2012], μ and Θ , as

$$\mu = \mu_0 \exp\left(\frac{U}{RT}\right) \exp(B\eta_c^b) \quad (6.43)$$

and

$$\Theta = \Theta_0 \frac{T_0}{T} \exp\left[\frac{U}{R} \left(\frac{1}{T} - \frac{1}{T_0}\right)\right] \quad (6.44)$$

where T_0 is the temperature of the polymer melt and gas jet at the die exit, μ_0 is the pre-exponential factor, U is the activation energy of viscous flow, R is the absolute gas constant, and B and b are the dimensionless material constants. They are taken as $B=5$ and $b=10$, according to [Yarin 1993, Yarin et al. 1992]. The governing differential equation for the thermally-dictated rheological behavior can be expressed as

$$\frac{\partial \Phi}{\partial t} = \left[\frac{d\eta_c}{dt} \left(\frac{B b \eta_c^{b-1} T}{\lambda^2} + \frac{\Delta h^0}{\lambda^2 T_0 c_{\text{p,polymer}}} \right) + \frac{-2 \text{Nu} \rho_{\text{gas}} c_{\text{p,g}} (\bar{T} - \bar{T}_g)}{\text{Re}_a \text{Pr}_g \lambda \lambda_0 (a_0/L) \rho_{\text{polymer}} c_{\text{p,polymer}}} \right] \frac{\exp(U_A + B\eta_c^b)}{\text{De}_0} - \frac{\bar{T}}{\lambda^2} \frac{\tau_{\tau\tau}}{\text{De}_0} \exp\left[-U_A \left(\frac{1}{\bar{T}} - 1\right)\right] \quad (6.45)$$

where $\Phi = \tau_{\tau\tau} / \lambda^2 + (\bar{T} / \lambda^2) \exp(U_A + B\eta_c^b) / \text{De}_0$, De_0 is the Deborah number, and U_A is the dimensionless form of the activation energy of viscous flow defined as $U_A = U/RT_0$.

The nucleation rate was described following [Yarin et al. 1992, Yarin 1993], in particular, accounting for not only the thermally-induced but also for the flow-induced crystallization as

$$I_* = \frac{K C_m}{2} \frac{k_B T}{h} \exp\left(-\frac{U}{RT}\right) \exp\left[-\frac{U_0}{RT(1-T/T_m^0 \lambda^N)^2}\right] \left(\frac{2\pi RT_0}{U_0 D}\right)^{1/2} \lambda^{-\frac{3}{2}} \quad (6.46)$$

where K is the reciprocal mean number of polymer macromolecules incorporated in a single fibrillary nucleus, C_m is the concentration of the polymer macromolecules, h is Planck's constant, and k_B is Boltzmann's constant. In addition, the following notation is used

$$D = \frac{6n}{[1-T/(T_m^0 \lambda^N)]^3} \frac{1}{T_m^0} \frac{\lambda^3 - 1}{\lambda^{N+3}}, \quad N = \frac{3}{2} n \quad (6.47)$$

where $n = T_m^0 R / \Delta h^0$, with T_m^0 being the melt temperature unaffected by the flow-induced crystallization, and also

$$U_0 = \frac{8\pi\sigma_t^2 \sigma_e N_A}{(\Delta h^0 \rho_{pc})^2} \quad (6.48)$$

In Eq. (6.48) N_A is Avogadro's number, ρ_{pc} is the polymer density, σ_t and σ_e are the lateral and edge surface energies for cylindrical fibrillar crystal nuclei, respectively.

It should be emphasized that the temperature dependence of the nucleation rate I^* in Eq. (43) stems from the probability of the appearance of a critical nucleus. Such a probability is determined by the temperature dependence of the free enthalpy (the Gibbs potential) of the critical nucleus affected by the flow-induced crystallization, as well as by the overall thermal energy, which are the dominant thermal effects.

Note also that in the simulations the values of all the parameters were taken as in [Yarin 1993, Sinha-Ray et al. 2010, Yarin et al. 2010, Yarin et al. 2011] and, in particular, the value of N was taken as 0.1 [5]. In addition, it should be emphasized that the effective melt temperature increases due to the flow-induced crystallization facilitated by stretching material elements ($\lambda \geq 1$) [Wehmann et al. 1999, Yarin 1993, Yarin et al. 1992]

$$T_{m,\text{eff}} = T_m^0 \lambda^N \quad (6.49)$$

and that when $T > T_{m,\text{eff}}$, the rate of nucleation $I_* = 0$.

The complete system of the dynamic and thermal equations is solved numerically using the boundary conditions, as described in detail in the previous works of the present group [Yarin 2014, Sinha-Ray et al. 2010, Yarin et al. 2010, Yarin et al. 2011, Sinha-Ray et al. 2013]. Note also that if it would be assumed that upon touchdown onto a collector screen, an element of a polymer jet immediately attains the screen temperature, a sudden rise in the degree of crystallinity near the touchdown point would appear, as discussed in section 6.5.

6.5. Results and discussion

The numerical results are discussed as follows. First, a brief overview of the numerical simulations of crystallization kinetics are described and compared with the experimental data. Then, the effect of temperature of the collector screen T_{Screen} and melt temperature at the die exit (T_0) on the crystallization kinetics is described. After that, the effects of two additional parameters are studied, namely- of the activation energy of the viscous flow (the material parameter) and of the die-to-collector distance (DCD). At the end, challenges and opportunities related with varying several parameters for obtaining a desired degree of crystallinity in the meltblown laydown are described.

6.5.1. Numerical simulations of meltblowing process accounting for crystallization.

An example of the numerically predicted isometric view of the laydown collected on a collector screen, as well as the overall pattern of molten polymer jets moving from the nosepiece to a collector predicted accounting for crystallization are shown in Fig. 6.3. Figure 6.3a shows the nonwoven laydown formed by deposition of 100 jets on a moving collector screen by a certain time moment. Figure 6.3b depicts the distribution of the degree of crystallinity along a single polymer melt jet in flight at the moment it has just touched the collector screen. Figure 6.3b also shows schematically the forces acting on a polymer jet in flight. The color of sections of the polymer jets in in Fig. 6.3c expresses the degree of crystallinity quantified in the color bar. It is seen that near the die exit, in the relatively straight part of the jets, the degree of crystallinity is very low. Further on, when significant bending perturbations appear, the degree of crystallinity rises abruptly, and after the polymer jets touch the moving screen the crystallinity continues to increase.

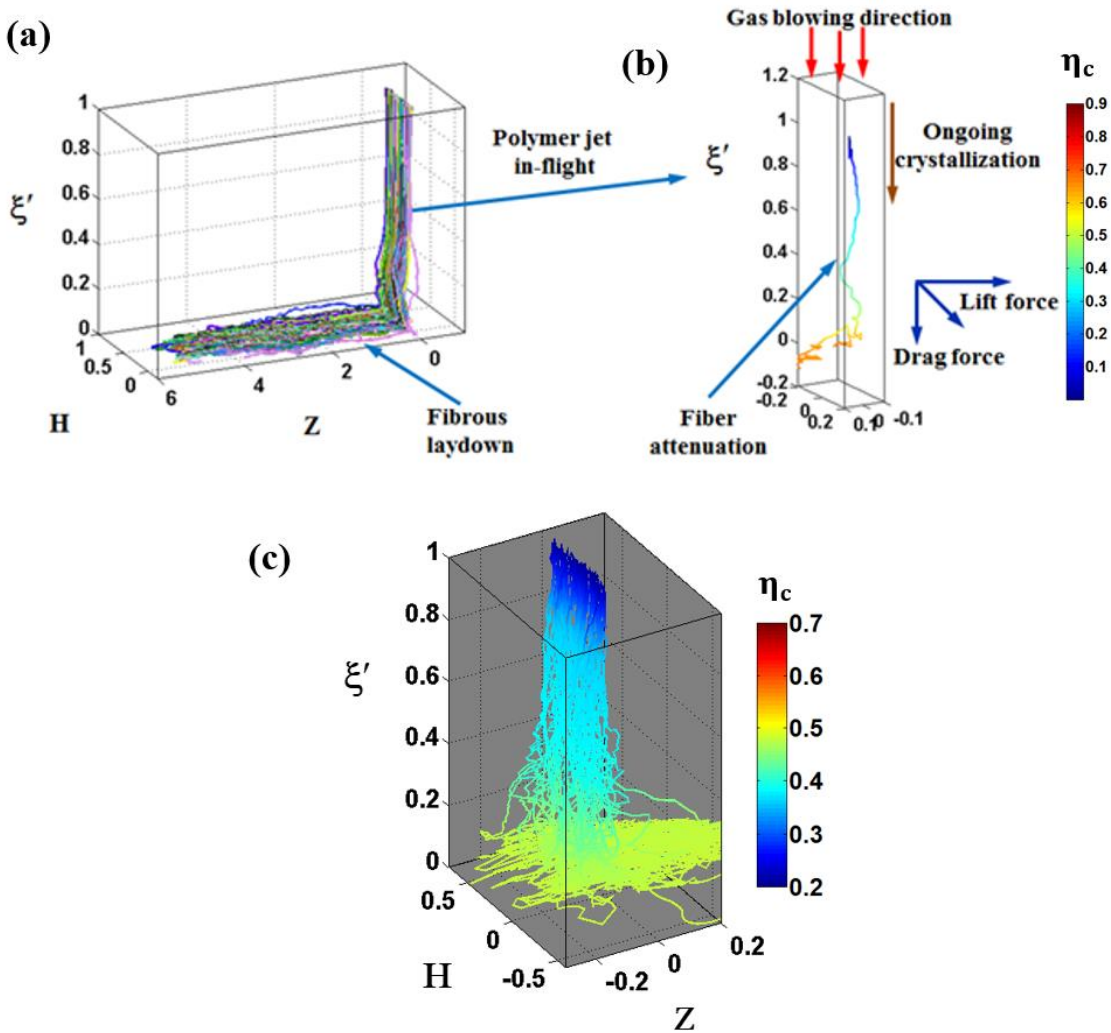


Figure 6.3. Isometric view of the predicted meltblowing process accounting for crystallization. The coordinate across the laydown is denoted as H , and the coordinate spanning the nosepiece and the collector belt, and thus normal to the latter is denoted as ξ . The third Cartesian coordinate is Z . It is orthogonal to ξ and H , and thus, ξ , H , and Z form a Cartesian trihedron. Note that the auxiliary dimensionless axis $\xi' = 1 - \xi$ is used in the images, as a convenient representation for the laydown elevation. Panel (a) is the isometric view of predicted meltblown multiple polymer jets, panel (b) depicts a single jet with the degree of crystallinity increasing along it. Panel (c) shows the degree of crystallinity along multiple polymer jets in meltblowing process.

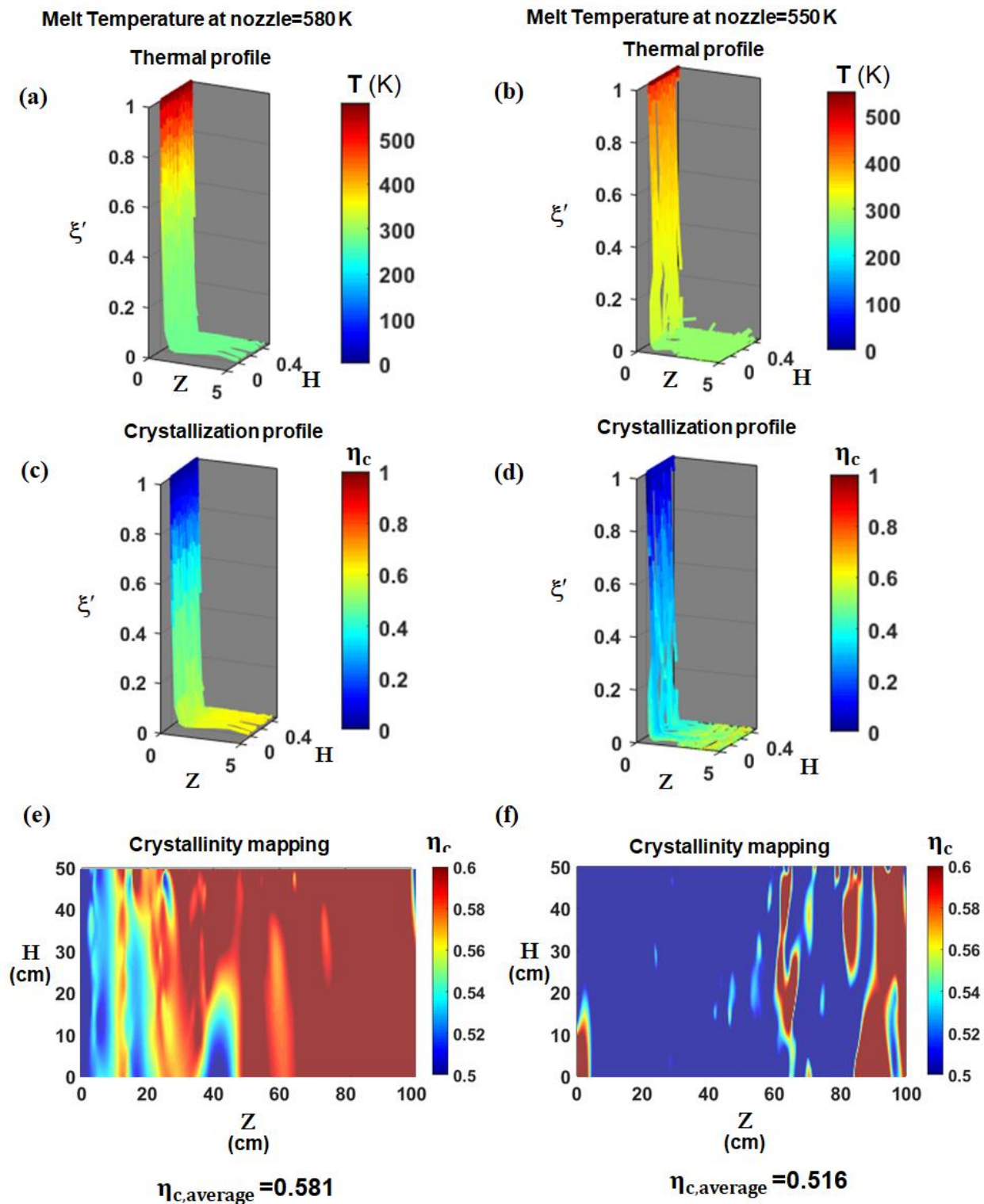


Figure 6.4. Effect of the polymer melt temperature at the die exit T_0 on the overall degree of crystallinity in the meltblown jets and laydown. Panels (a), (c) and (e) are isometric view of the

thermal profile of 100 polymer jets, the degree of crystallinity along the jet path, and the resulting 2-D map of the degree of crystallinity of the nonwoven, respectively. The temperature of the molten polymer at the nozzle exit T_0 is 580 K. The right panels (b), (d) and (f) show the corresponding results for the initial polymer melt temperature of 550 K.

Figure 6.4 shows that the higher temperature (the temperature of the melt at the die exit) of the molten polymer results in a higher degree of crystallinity in the laydown. This can be attributed to the fact that a lower temperature of molten polymer at the die exit reduces the flow-induced crystallization.

6.5.2. Comparison with experimental data.

For the purpose of experimental verification of the predicted degree of crystallinity in meltblown laydown, meltblown polypropylene (PP) samples were obtained from the pilot-scale testing facility of the Nonwoven Institute, North Carolina State University. The processing conditions of these samples are summarized in Table 6.1. It should be emphasized that the current simulations were conducted for 100 polymer jets (lower than in the experiments), albeit under the conditions listed in Table 6.1, since 100 jets provide a statistically sound data set. The Deborah number $De_0=400$ was used in the simulations, which corresponds to the relaxation time of 0.1 s [Yarin 2014, Yarin 1993, Sinha-Ray et al. 2010]. The diameter of the polymer jets at the die exit was taken as 200 μm . The initial gas/melt temperature was in the 528-535 K range. The predicted degree of crystallinity is reported in Table 6.1. It was calculated by averaging over 200 cm of each of the numerically simulated laydowns. It should be emphasized that for the meltblown laydown samples specified in Table 6.1, one should assume that as the meltblown laydown is deposited, the

temperature of the polymer fibers does not immediately attain the temperature of the collector screen, since the lower-located fibers could insulate the oncoming jets. Accordingly, the laydown polymer fibers should dissipate heat by convection/conduction to the surrounding environment before attaining the temperature of the collector screen which is the ambient temperature. Accordingly, (i) for the sake of comparison with such data, in the numerical simulations the temperature field continued to evolve over the laydown, and the nucleation rate was truncated when temperature reached the ambient temperature. (ii) On the other hand, in many other cases discussed below the laydown temperature was forced to become the collector screen temperature on touchdown, which is also feasible technically. Cases (i) and (ii) are compared in Figs. 6.6a and 6.6b, respectively. After that, only the condition (ii) was implemented.

The degree of crystallinity of the samples listed in Table 6.1 was measured using Differential Scanning Calorimetry (DSC) following [Brown 1988, Haines 2012, Menczel 2014, Brown 2011, Hassan et al. 2013, Lee et al. 2002, Franck 2004, Meerveld et al. 2004]. The samples weighing approximately 5 mg were heated at the rate of $10\text{ }^{\circ}\text{C min}^{-1}$ in the 1st heating cycle from room temperature to $100\text{ }^{\circ}\text{C}$ and kept for 5 min. Then, they were heated further up to $200\text{ }^{\circ}\text{C}$ at the rate of $5\text{ }^{\circ}\text{C min}^{-1}$, and after that cooled at the rate of $20\text{ }^{\circ}\text{C min}^{-1}$. The DSC curves of all the nonwoven samples studied are shown in Fig. 6.5a. The results of the thermogravimetric analysis of all the samples are shown in Fig. 6.5b. The zoomed-in views of the DSC thermograms of samples 1 and 2 are shown in Fig. 6.5c and 6.5d, respectively.

PP nonwoven sample No.	DCD (mm)	No. of jets in the simulation	Velocity of planar collector screen (m/min)	η_c (Degree of crystallinity)	
				Measured from DSC	Predicted numerically (Averaged over the length)
1	150	100	13.2	0.41	0.5077
2	300	100	13.2	0.5637	0.70154
3	225	100	39.8	0.5136	0.61414 and 0.5915 from 2 trial runs
4	225	100	13.2	0.484	0.53434 and 0.559 from 2 trial runs

Table 6.1. Numerically predicted and experimentally measured degree of crystallinity for the four meltblown PP samples formed at different values of DCD and the uptake velocity. In particular, the last two columns with the values of the degree of crystallinity η_c are the average values

predicted numerically and measured from the DSC thermograms. The degree of crystallinity is defined as the ratio of the volume of the crystallized part of polymer to the total volume.

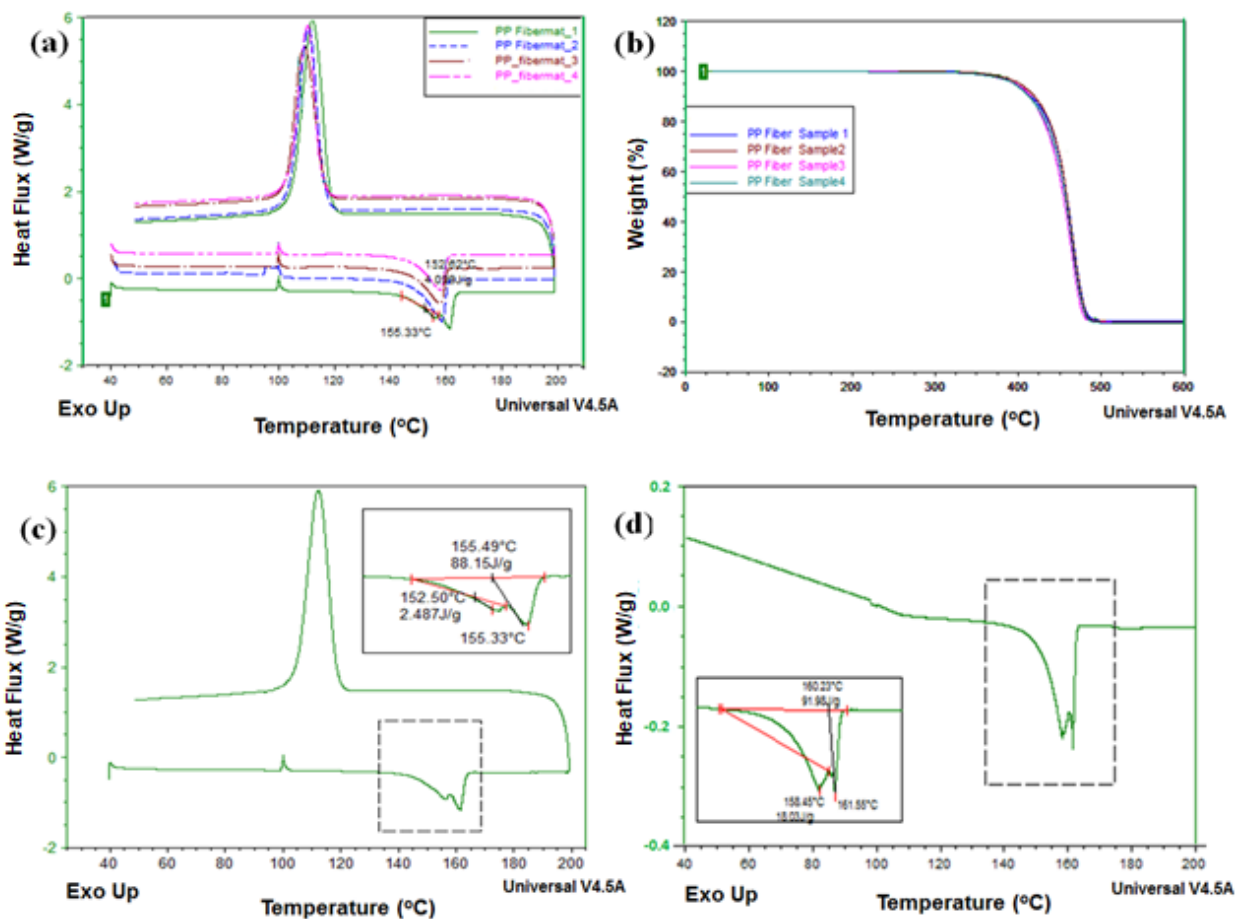


Figure 6.5. DSC thermograms and thermogravimetric plots for samples 1-4 of Table 6.1. Panel (a) shows the first heating and cooling cycles for the four PP nonwoven samples listed in Table 6.1. Panel (b) shows the results of the thermogravimetric analysis of all four samples and suggests that there was no thermal degradation in the samples in the operating temperature range used in DSC. Panel (c) shows only the first heating curve for the nonwoven sample 1 heated at the rate of 10 °C/min. It shows that the melting temperature is approximately 151 °C. Integrating over the peak, the melting enthalpy was found as 88.15 J/g. The latter value corresponds to the degree of

crystallinity of 0.425, or 42.5 %. Panel (d) show the 1st heating/cooling cycle at the rate of 5 °C/min for the sample with a higher DCD (sample 2) with a zoomed-in view of the melting peak in the inset.

The comparison in Table 6.1 reveals that the numerically predicted values of the degree of crystallinity of all four samples closely resemble the corresponding experimental values. It is seen that as DCD increases, there is an increase in the crystallinity (the phenomenon found numerically and experimentally). Overall, the reasonable agreement of the numerically predicted degree of crystallinity with the experimental one validates the predictions of the proposed method. In the following subsections it is used to explore some other effects.

6.5.3. Numerical prediction of the laydown degree of crystallinity

6.5.3.1. Effect of temperature of the collector screen. Technologically it is possible to enforce the laydown temperature near the touchdown point by means of a localized cooling. In the present section we explore the effect of such localized cooling. To study this effect, two cases were considered. In these cases meltblown jets were issued under the same conditions, namely, with the identical DCD, initial temperature (T_0), Deborah number, blowing velocity, the activation energy of viscous flow and the collector speed. The only difference is that in one of the cases the fibers continued to crystallize after touchdown on the collector belt where the fibers, where according to condition (i) discussed above, temperature and the degree of crystallinity continued to evolve (Fig. 6a). On the other hand, in Fig. 6b another case the laydown temperature has been enforced as 280 K according to condition (ii). It can be seen that the average degree of crystallinity ($\eta_{c,avg}$ of the polymer jets at the touchdown point in Fig. 6.6b, $\eta_{c,avg} = 0.594$, is significantly higher than that in

Fig. 6.6a, $\eta_{c,avg} = 0.4476$. In Fig. 6.7 the difference in degree of crystallinity at touchdown caused by the enforced cooling is explored. The value of U_A was taken as 10. Temperature T_0 was equal to 580 K in both cases, while the touchdown temperature T_{Screen} was either 300 K (in Fig. 6.7a) or 280 K (in Fig. 6.7b). It can be seen that at the touchdown point the lower collector screen temperature resulted in a higher average degree of crystallinity, $\eta_{c,avg} = 0.7011$ in comparison to $\eta_{c,avg} = 0.5953$ corresponding to the higher temperature. Figure 6.7 also depicts the close-up view of the degree of crystallinity fields in the two different laydowns. It can be seen that the effect of the collector screen temperature affects the crystallinity field at the dimensionless distance ~ 0.05 - 0.1 from the touchdown point. For the lower touchdown temperature, the degree of crystallinity begins to change drastically practically at the touchdown point.

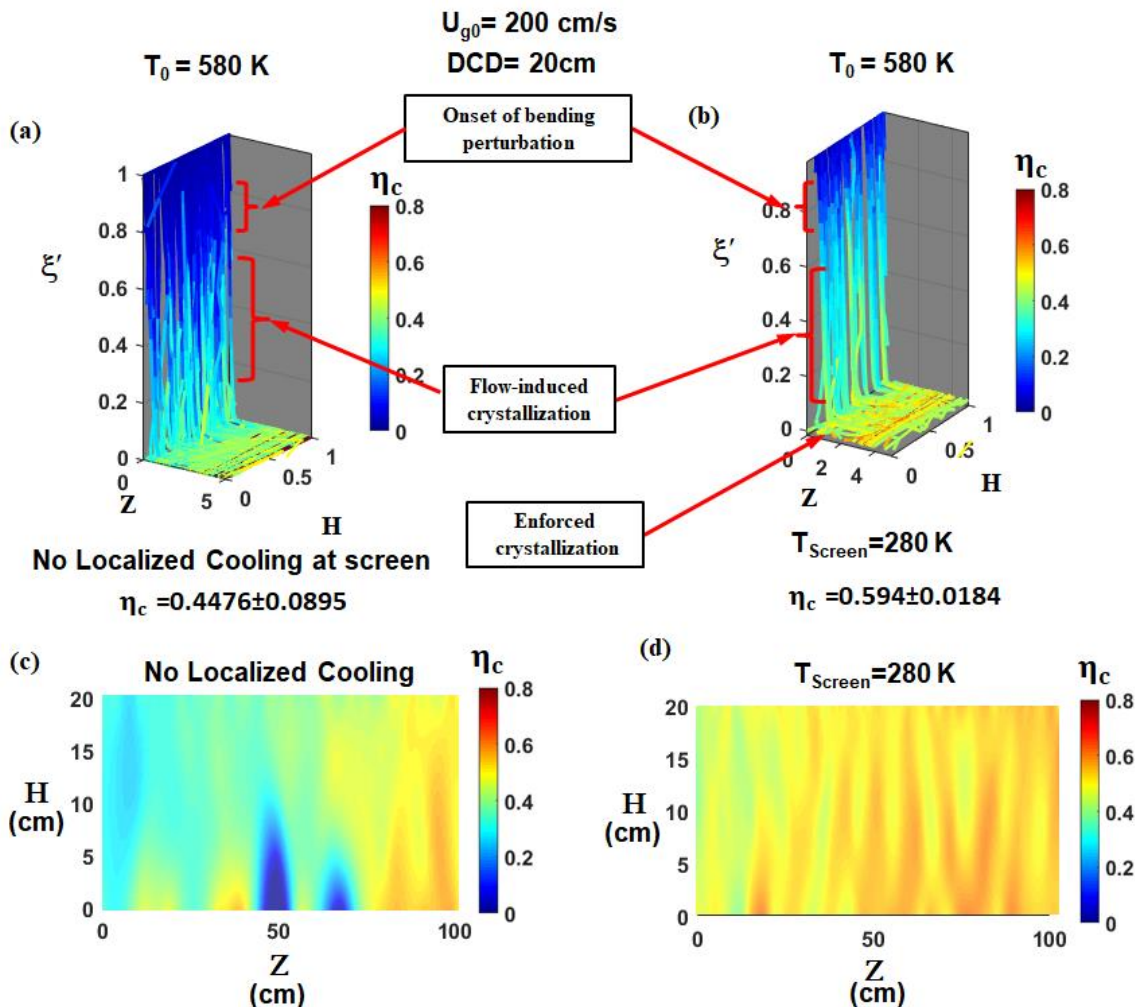


Figure 6.6. The predicted 3D conformations of 100 polymer jets and the corresponding fields of the degree of crystallinity shown by color. (a) No localized cooling and enforcing of the laydown temperature to immediately become equal to the collection screen temperature. (b) The case with localized cooling at the touchdown point enforcing the laydown temperature to become that of the collection screen temperature and causing an enforced crystallization. The initial Deborah number at the nosepiece was $De_0=400$. The diameter of the polymer jets at the nozzle exit was taken as $500 \mu\text{m}$. The gas blowing velocity at the die U_{g0} was 200 m/s , the die-to-collector distance (DCD) was taken as 20 cm , the collector screen velocity was 1 m/s , and the mass flow rate was 0.3 g per

hole per minute (it varies in the 0.25 ghm-0.3 ghm range in several experimental studies in the literature).

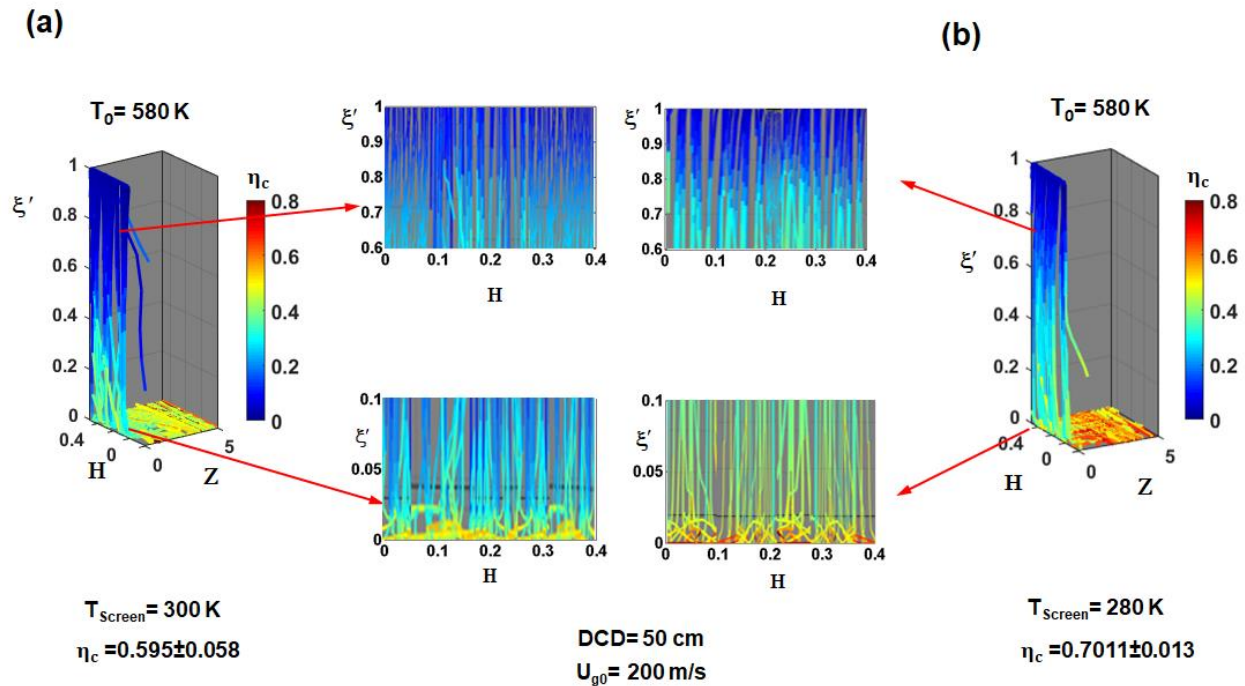


Figure 6.7. Two cases with the enforced temperature of the laydown at the touchdown point. (a) $T_{\text{Screen}} = 300 \text{ K}$, (b) $T_{\text{Screen}} = 280 \text{ K}$. The isometric view of 100 meltblown polymer jets with the field of the degree of crystallinity shown in color. The initial polymer melt temperature at the nosepiece is $T_0 = 580 \text{ K}$. DCD is 50 cm and the gas blowing velocity at the die is 200 m/s; DCD=50 cm. The gas blowing velocity U_{g0} is taken as 200 m/s. The polymer density here is 0.9 g/cm^3 , which is different from the rest of the simulations reported in this work.

To elucidate the effect of the enforced temperature at the touchdown point, the temperature profiles in the jets in flight under different conditions are plotted in Fig. 6.8a. It can be seen that the temperature profile in the jet is affected by the touchdown temperature, since the entire jet

dynamics is affected via changes in the viscoelastic parameters and stresses. Figures 6.8b and 6.8c show the average stretching ratio and the nucleation rate, respectively, for polymer jets subjected to two different touchdown temperatures, $T_{\text{Screen}} = 280 \text{ K}$ and $T_{\text{Screen}} = 300 \text{ K}$. Figures 6.8d and 6.8e show the diameter distributions in the laydowns formed with the enforced touchdown temperatures of $T_{\text{Screen}} = 280 \text{ K}$ and 300 K , respectively. It is seen that for the lower touchdown temperature the diameter distribution becomes wider. The largest fibers origin is explained by the fact that at a lower touchdown temperature, stretching of the polymer jet is significantly diminished and thus, the fibers practically 'freeze' upon touching the collector screen.

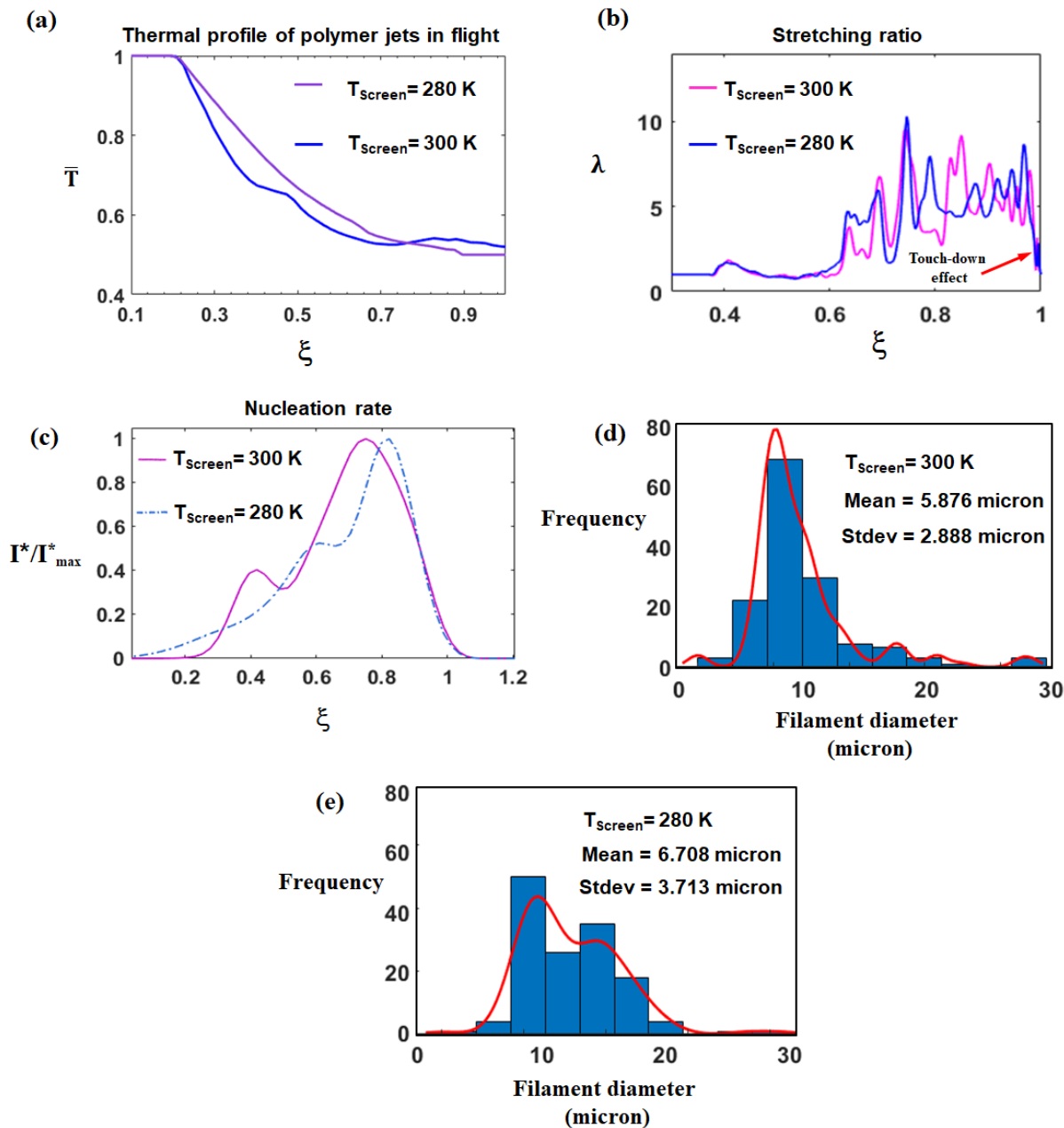


Figure 6.8. The effect of the enforced touchdown temperatures on polymer jets in flight. (a) Temperature profiles along the jets. (b) The stretching ratio distribution. (c) The nucleation rate distribution. (d) Fiber-size distribution in the laydown with $T_{\text{Screen}} = 300 \text{ K}$. (e) Fiber-size distribution in the laydown with $T_{\text{Screen}} = 280 \text{ K}$.

The fluctuating behavior of nucleation rate depends on the polymer jet temperature as well as the effective melting temperature in moving jets in-flight. The rate of crystallization along the jet path from the nozzle reveals an initial increase followed a sudden decrease in its value. However, the diameter of the jet being within the 5-15 μm range makes the heat transfer an immediate process upon touching the moving collector belt. Accordingly, it is expected that a sudden drop in the nucleation rate happens at the lower belt/collector temperature. There the filament attains the temperature of the collector belt, and thus the temperature variation ‘freezes’, and so does the nucleation rate.

6.5.3.2. Effect of DCD (Die-to-collector distance).

DCD (die-to-collector distance) is another important process parameter. To study the effect of DCD, two different DCD values were chosen and the results are reported in Figs. 6.9 and 6.10. Figures 6.9a and 6.9b correspond to the case of DCD = 20 cm, and Figs. 6.9c and 6.9d – to DCD = 50 cm. Figure 6.10 shows the resulting distribution of the degree of crystallinity in the predicted laydowns. For all the results in Fig. 6.9, the gas blowing velocity at the die U_{g0} was kept as 200 m/s. Also, $U_A = 10$ and $De_0 = 400$ were used in the simulations. The other parameters were the same as before. It should be emphasized that in Figs. 6.9a and 6.9c the touchdown temperature was enforced as $T_{\text{Screen}} = 280$ K, whereas in Fig. 6.9b and 6.9d it was enforced as $T_{\text{Screen}} = 300$ K. The average values of the degree of crystallinity at the touchdown point for Figs. 6.9a-6.9d are 0.4676, 0.4761, 0.6567 and 0.650, respectively. It can be seen that irrespective of the touchdown temperature, the average degree of crystallinity in the laydown increases with an increase in DCD, since at larger DCD values polymer jets cooling in flight is more thorough. To elucidate the effect

of DCD on the overall laydown structure, the laydown views for DCD=20 cm are shown in Figs. 6.10a and 6.10b, and for DCD=50 cm - in Figs. 6.10c and 6.10d. Figures 6.10a and 6.10c show the laydowns formed with enforcing the touchdown temperature as $T_{\text{Screen}} = 280$ K, whereas Figs. 6.10b and 6.10d elucidate the cases with the touchdown temperature enforced as $T_{\text{Screen}} = 300$ K. It can be seen that as DCD increases, the overall degree of crystallinity across the laydown increases as well due to a more thorough cooling of polymer jets in flight. Table 6.1 shows that in the experiments as the DCD increased, the degree of crystallinity in the laydown also increased, in agreement with the numerical predictions. A comparison between Figs. 6.10a and 6.10c reveals the following. As DCD was increased from 20 cm up to 50 cm and the value of T_{Screen} was fixed at 280 K, not only the overall degree of crystallinity has increased, but also its variation across the laydown has decreased.

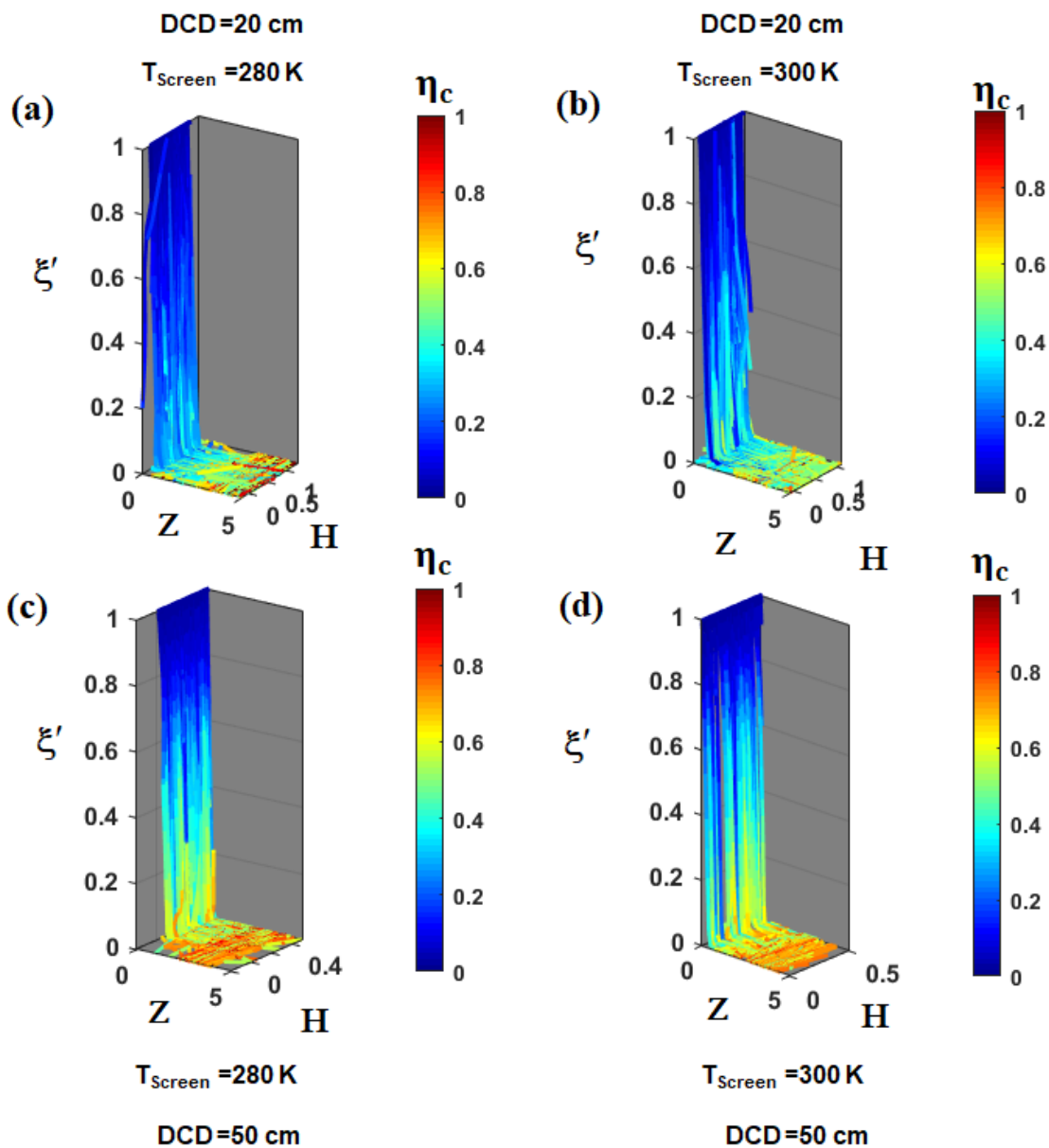


Figure 6.9. Effect of DCD on the degree of crystallinity. The isometric views of 100 meltblown polymer jets. Panels (a) and (b) correspond to DCD of 20 cm. Panels (c) and (d) correspond to DCD of 50 cm. Panels (a) and (c) show the results with the touchdown temperature being enforced as 280 K. Panels (b) and (d) show the results with the touchdown temperature enforced as $T_{\text{Screen}}=300$ K.

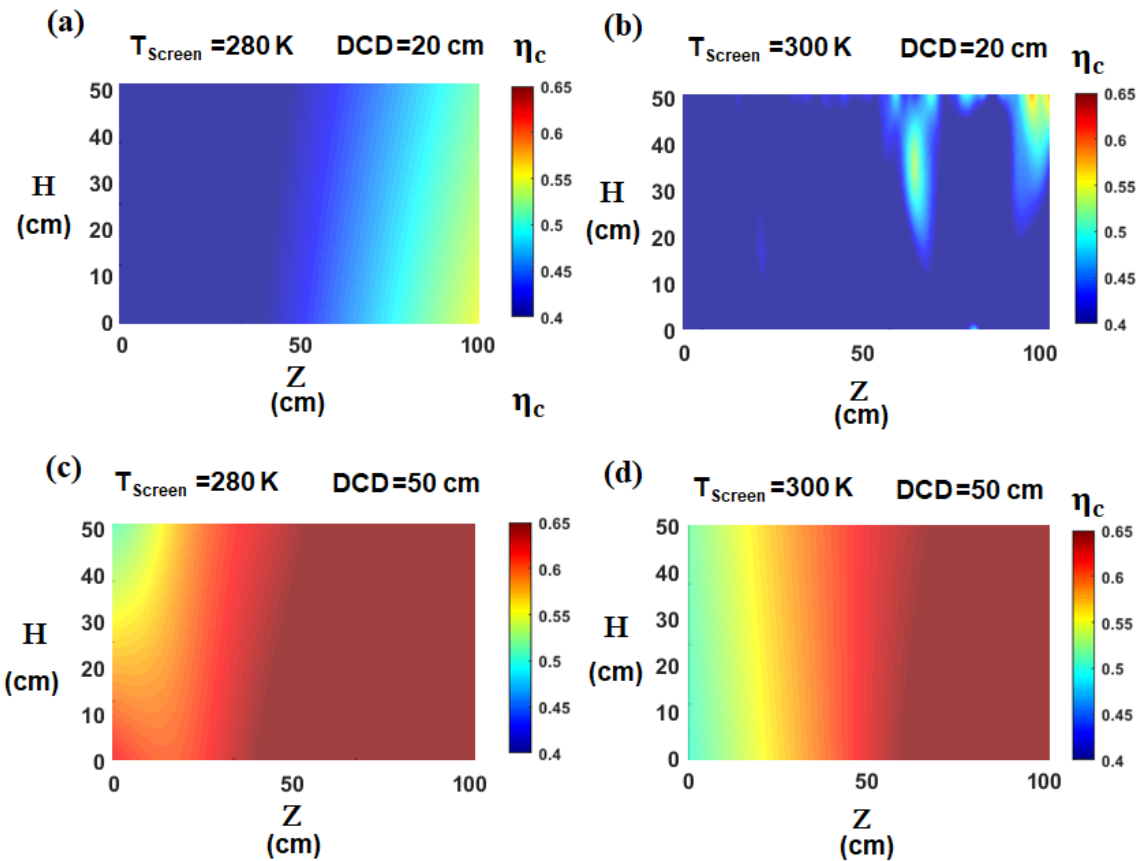


Figure 6.10. Distribution of the degree of crystallinity in laydowns formed with different DCD values corresponding to the panels in Fig. 6.9. The initial melt temperature was kept at 580 K [Wehmann et al. 1999] for all cases. Panels (a) and (c) correspond to DCD of 20 cm and 50 cm, respectively, with the touchdown temperature being enforced as 280 K. Panels (b) and (d) correspond to the touchdown temperature enforced as $T_{\text{Screen}} = 300 \text{ K}$.

6.5.3.3. Crystallization in polymers with different activation energy of viscous flow

The activation energy of viscous flow U is another material parameter of interest for meltblowing process. Here the moderately-high range of the Deborah number between 400 and 600 is chosen, which is insufficiently high for the shish-kabob formation [Braun et al. 2003]. Two different dimensionless values of $U_A = 10$ and 20 were chosen (cf. Fig. 6.11) according to the data in [Balzano et al. 2008, Oleksandr et al. 2008, Luigi et al. 2009, Jarecki et al. 2018, Wang 2004, Toth et al. 2018, Brenn et al. 2000, Baert et al. 2006]. The uptake velocity of the collector screen was kept at 10 m/min, and the initial Deborah number at the die exit $De_0 = 400$ which corresponds to the relaxation time of molten polymer of 0.1 s; the polymer density was taken as 0.99 g/cm³. Fig. 6.11 shows that the degree of crystallinity increases for polymers with higher U_A . It should be emphasized that in the simulations the degree of crystallinity varies at a fixed set of the input parameters due to the randomness implemented to mimic the effect of turbulence.

The effect of gas blowing velocity on the degree of crystallinity, specifically in the case of polymers with higher values of U_A , was investigated as well. The corresponding results are shown in Figs. 6.12 and 6.13. In these cases, the touchdown temperature is enforced as 280 K. Here a higher value of the Deborah number $De_0=600$ is used, because for polymers with a higher activation energy, the relaxation time is higher [Baert et al. 2006]. The polymer jet diameters at the die exit were taken as 500 μm , and the gas blowing velocity was 150 m/s and 200 m/s in Figs. 6.12 and 6.13, respectively.

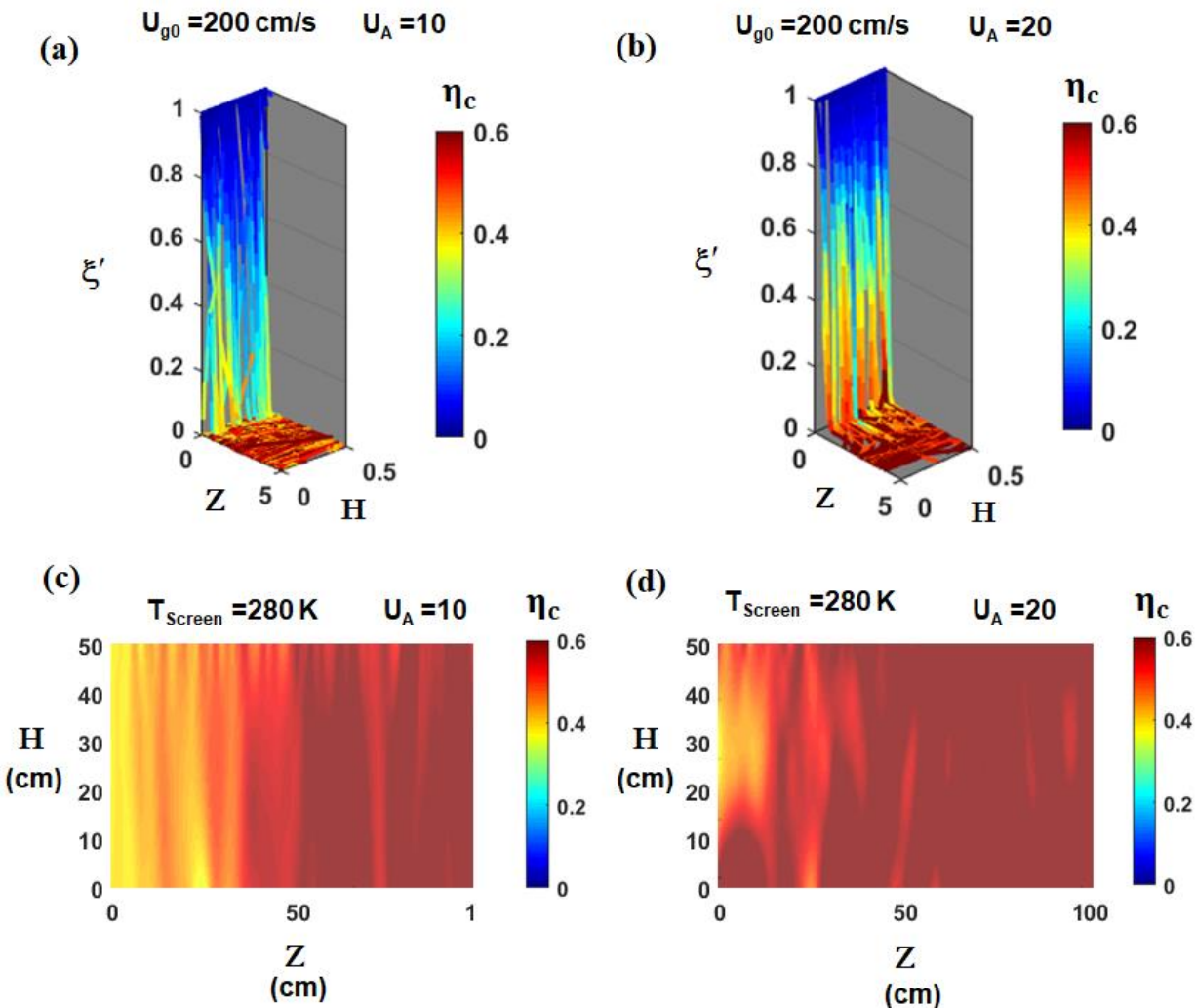


Figure 6.11. Variation of the degree of crystallinity in nonwoven laydown due to variation in the activation energy of viscous flow of the polymer. The isometric view of the in-flight crystallization and the distribution of the overall degree of crystallinity corresponding to different values of the activation energy of viscous flow shown in panels. (a) $U_A=10$, (b) $U_A=20$. The corresponding distribution of the degree of crystallinity for the laydowns formed are shown in panels (c) and (d), respectively. The average degree of crystallinity in the fibrous laydown for panels (a) and (c) varies in the 0.4872-0.514 range in multiple repeated simulations, and the average degree of crystallinity

in the fibrous laydown for panels (b) and (d)- in the 0.501-0.545 range in multiple repeated simulations. The gas blowing velocity at the die is denoted U_{g0}

6.5.3.4. Effect of gas blowing velocity

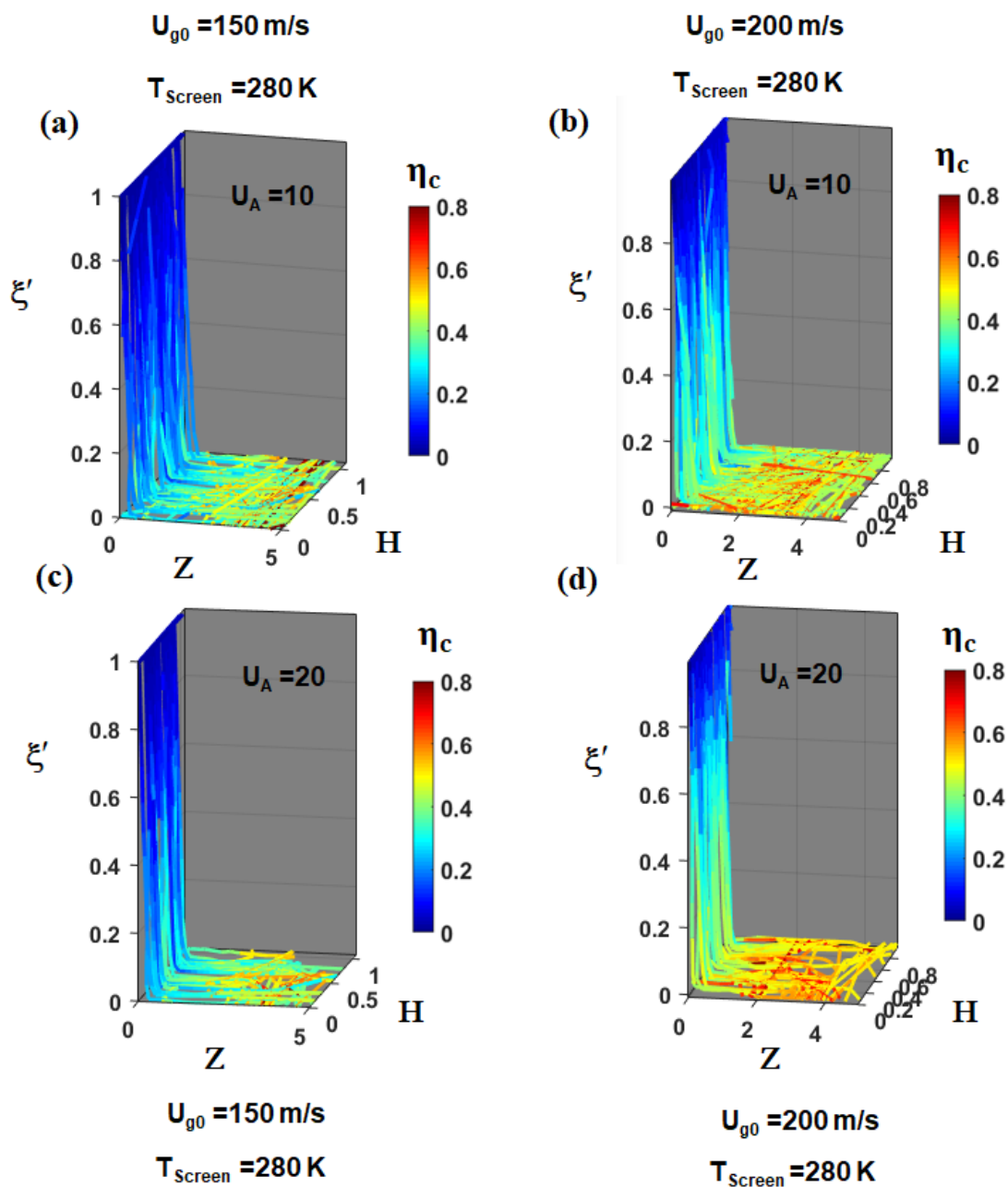


Figure 6.12. Effect of gas blowing velocity U_{g0} on the degree of crystallinity. The isometric views of 100 meltblown polymer jets are shown. Panels (a) and (c) show the results with the gas blowing velocity $U_{g0} = 150 \text{ m/s}$, and panels (b) and (d) show the results with $U_{g0} = 200 \text{ m/s}$. Panels (a) and

(b) correspond to $U_A = 10$. Panels (c) and (d) correspond to $U_A = 20$. All panels show the results with the touchdown temperature being enforced as $T_{\text{Screen}} = 280$ K, and $\text{DCD} = 20$ cm. The average values of the degree of crystallinity of the laydown formed for panels (a), (b), (c) and (d) are 0.471, 0.518, 0.514, 0.589, respectively. The gas blowing velocity at the die is denoted U_{g0} .

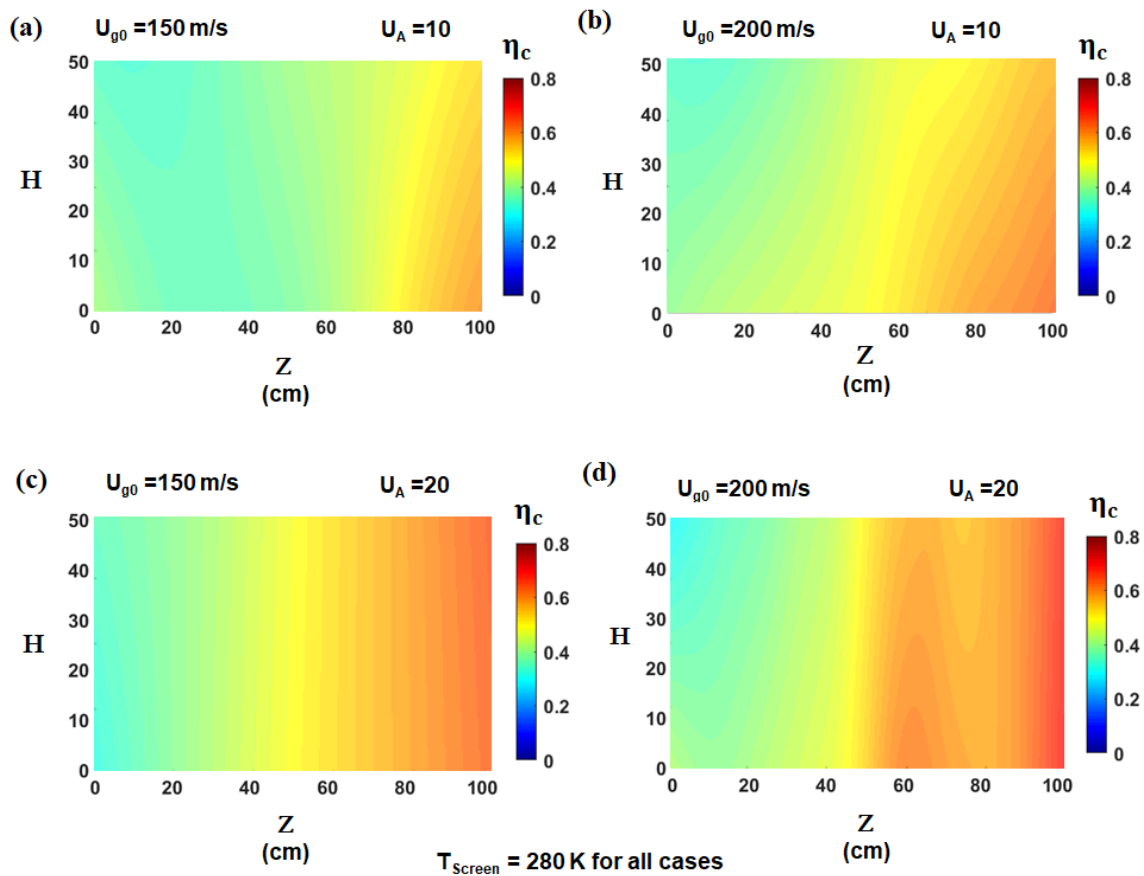


Figure 6.13. The 2-D mapping of the degree of crystallinity in laydowns formed by 100 jets. The results illustrate the effect of the gas blowing velocity U_{g0} on the laydowns formed from polymers with different activation energies of viscous flow. Panels (a) and (c) show the results with the gas blowing velocity $U_{g0} = 150$ m/s, and panels (b) and (d) show the results with $U_{g0} = 200$ m/s. Panels (a) and (b) correspond to $U_A = 10$. Panels (c) and (d) correspond to $U_A = 20$. All panels show the results with the touchdown temperature being enforced as $T_{\text{Screen}} = 280$ K and $\text{DCD} = 20$ cm.

In Fig. 6.13 the 2-D mapping of the predicted degree of crystallinity in laydown reveals the effect of the gas blowing velocity at different values of the activation energy of viscous flow. The operating conditions for Fig. 6.13 are specified in the corresponding panels (a)-(d) in Fig. 6.12. The results elucidate that a higher gas blowing speed results in a higher degree of crystallinity in nonwoven laydown in meltblowing process.

The following three methods of laydown control, i.e., the variation of the screen temperature, DCD and gas blowing velocity deserve an additional discussion. For polymer melts with lower values of the activation energy of viscous flow, as those in Figs. 6.7, 6.9, 6.12(a) and 6.12(b) and lower values of the Deborah number (the lower relaxation time) as in Figs. 6.7 and 6.9, all the three control methods can be applied effectively. However, it should be emphasized that variation of the gas blowing velocity and screen temperature may be less cost-effective than variation of DCD for such polymeric materials from a manufacturing perspective. On the other hand, as it is seen from Figs. 6.11, 6.12(c), 6.12(d), 6.13(c) and 6.13(d), that crystallinity of the laydowns formed from polymer melts with the higher activation energy of viscous flow and higher Deborah number, can only be effectively controlled by the variation of the gas blowing velocity.

The results of sub-sections 6.5.3.3 and 6.5.3.4 revealed no significant variation in the degree of crystallinity for polymers with the higher value of the activation energy ($U_A=20$), and the Deborah number of $De_0=600$ due to an imposed localized cooling, or varying in DCD. Therefore, one can imply that the most effective way to control crystallization is to change the gas blowing velocity rather than in changing the screen temperature or DCD.

6.6. Conclusion

The theoretical model of crystallization kinetics is coupled with the quasi-one-dimensional equations of the dynamics of molten polymer jets in meltblowing process, where the jets experience stretching and bending forces from the surrounding high-speed air flow. As a result, polymer jets experience significant thinning and bending (which also enhances thinning) as well as lose heat to the surrounding air. All these processes affect the rate of nucleation and growth of linear crystals in polymer jets, which ultimately determine the degree of crystallinity in nonwoven meltblown laydown. The numerical predictions for the degree of crystallinity were compared with experimental results, and revealed a reasonable agreement. The numerical model was also used to predict the effect of different process and material parameters on the degree of crystallinity. Two radically different situations were explored. In one of them polymer filaments were essentially thermally insulated from the collector screen due to the low thermal conductivity of the underlying fibers, in another one the low touchdown temperature was enforced, which can be essentially done on the industrial scale. It was found that the latter measure facilitates an increase in the degree of crystallinity in the laydown. It was also found that increasing the die-to-collector distance (DCD) facilitates cooling of polymer jets in flight and results in an increased crystallinity of the nonwoven laydown. On the other hand, the material parameter, the activation energy of viscous flow of polymer melt revealed an insignificant effect on the laydown crystallinity. Overall, the results imply that the most effective way to control crystallization is to change the gas blowing velocity rather than changing the screen temperature or DCD.

It should be emphasized that the crystallization processes are predicted in this work in the framework of a continuum model and the non-equilibrium thermodynamics. In distinction from the analysis based on the equilibrium phase diagrams, the present approach allows one to tackle

transient crystallization processes and the flow-induced crystallization characteristic of meltblowing. In addition, in comparison with atomistic and molecular dynamics simulations, the present approach allows one to tackle realistic spatial and time scales characteristic of meltblowing. The model developed in this work can be used to avoid a trial-and-error stage in search for optimized processing conditions replacing it by numerical experimentation.

CHAPTER 7: SUMMARY AND CONCLUSION

Meltblowing:

The primary objective of this thesis has been to find out optimized processing conditions in nonwoven manufacturing process and propose the most cost-effective way to produce manufactured products as per specified physical characteristics. To achieve that goal, a parametric study was conducted using the developed numerical simulation package by systematically varying air speed, polymer feed and gas and melt temperatures to investigate their effect on specific properties such as fiber diameter distribution, fiber orientation, porosity, tortuosity and degree of crystallinity in fibrous laydowns. The estimation of the thickness distribution and mass distribution of the meltblown fiber mats were carried out using the simulations, and the subsequent comparison with the experimentally measured data produced under similar conditions revealed good agreement. This work provides a unique insight into the sensitivity of the nonwoven production processes by exploring the parametric dependence of the product properties. A micromechanical model is developed incorporating the quasi-one-dimensional dynamics equations of thin polymeric liquid jets which are viscoelastic in nature. It predicts the three-dimensional web structure of the micro-fibrous laydown and the resulting thickness, porosity and permeability. This is the first time such an approach was developed, as to our knowledge. The novelty of this work is in developing the framework and the corresponding algorithm that can predict the touch-down times of fiber elements from the simulations and use that information along with the fiber-size distribution to predict the 3-D conformation of individual fibers in the laydown. Also, the arrangement of continuous filaments in the fibrous structure is predicted, i.e., the three-dimensional architecture of the microfiber web is

revealed numerically. Additionally, the fiber-size distributions, and polymer mass distributions are predicted. The dependence of the cross-sectional and volumetric porosities, as well the corresponding dimensionless permeability on the processing parameters is numerically predicted and validated versus the specimens produced under similar conditions at pilot-scale manufacturing line. It is found that the collector screen velocity (the uptake velocity) is an important parameter to control the product properties and also implement a cost-effective approach via this downstream parameter in a manufacturing setup. The numerical results revealed how porosity and permeability increase with the collector velocity, which is explained by the fact that the material elements touching down at the screen form sparser laydown structures consisting of thinner fibers. The present results for the dependence of the dimensionless permeability on the solid volume fraction of the predicted meltblown laydown are in good agreement with the experimental data and analytical and direct numerical simulations of the pre-determined structures available in the literature. The surface elevations and porosities were measured using the experimentally formed samples and compared with the numerical predictions. The comparison between the simulated and measured data revealed good agreement for volumetric porosity values as well as the elevation. It should be emphasized that the present results point at the change in the collector velocity as a convenient way of changing the laydown porosity, the conclusion, which aims at guiding practical implementations of the meltblowing process. The results are discussed in detail in Chapter 4 for the two limits of a wide range of velocities of the collector screen (0.1 m/s and 10 m/s), albeit the simulations were conducted for the entire range in between. Currently, the collector screen velocities are of the order of 1 m/s in case of meltblowing, whereas there are frequent applications with the screen velocity being lower,

of the order of 0.1 m/s. From the economic viewpoint, an increase in the production rate is feasible with an increase in the collector velocity. In some other processes collector velocities of the order of 10 m/s are not unusual, and can be also sought in meltblowing. The findings of the present section are expected to provide a guideline for the optimization of the collector screen velocity to control properties of meltblown laydown.

Solution blowing:

Solution blowing is treated here as an offshoot of the meltblowing process. The quasi-one-dimensional model of polymeric jets in solution blowing developed earlier extends the inclusion of the 3-D architecture of the fibrous laydown formed under different velocities of rotating drum, expected to be the most sensitive processing tool. The present work provides a predictive platform to estimate the 3-D configurations of the polymer solution jets as they are deposited on a rotating drum. Due to the high potential of solution blowing as a large scale manufacturing process in nonwoven industry, it is imperative to find optimized processing conditions to organize an on-demand, rapid and cost-effective formation of polymeric nanofibers on the industrial scale. The present numerical and experimental investigation provides an insight in the fundamental mechanisms responsible for the laydown formation. It also elucidates the parametric sensitivity of the laydown thickness, porosity and permeability on processing conditions. The results established that the angular velocity of the collecting rotating drum is a significant parameter, which affects these physical characteristics of the laydown. The angular velocity of the rotating drum significantly changes the mass distribution in the laydown, and thus the volumetric porosity and dimensionless permeability without affecting the fiber size. It is observed from the

experimental measurements as well as from the numerical predictions that a higher angular velocity of the collector produces more uniform mass distribution in the laydown, larger inter-fiber distances and thus, higher volumetric porosity and permeability. From the point of view of cost optimization and economic feasibility, it is of immense importance to produce high-end products such as nanofiber webs within a higher range of permeability which can be achieved by operating solution blowing at a higher collection rate. The numerical simulation revealed that the nanofibrous laydown with higher porosity and permeability can be achieved by a higher collector speed. Large-scale manufacturing of micro- and nanofibers using solution blowing promises immense benefits from the economic standpoint. The volumetric porosity as well as thickness of solution-blown laydowns predicted in this work are in a reasonable agreement with the experimentally measured properties of samples produced in a lab-scale setup and with the data available in the literature.

Crystallization kinetics in meltblowing:

A robust numerical code for prediction of meltblowing process and degree of crystallinity is developed by incorporating a model for polymer crystallization kinetics. The meltblowing process, as described in the thesis, has included the flow-induced crystallization and the crystallization kinetics. The effect of multiple processing parameters on the obtained crystallinity along the fiber mat is investigated. Multiple polymer jets are considered simultaneously when they are depositing on a moving screen and forming a joint laydown. The numerical model is used for a wide range of processing parameters such as the initial gas temperature at meltblowing nozzles, the die-to-collector distance (DCD), collector belt

speed, the activation energy of viscous flow, and in addition, gas speed at the nozzle exit. The results reveal that the crystallization kinetics is sensitive to all of the above-mentioned parameters. The results also elucidate a correlation between the onset of bending perturbation and a sudden fluctuation in the predicted crystallinity along the polymer jets. The stiffness matrix representation of the polymeric on-line flow-induced crystallization is shown to depend on these above-mentioned processing conditions.

The parametric study carried out under different conditions of meltblowing process revealed valuable insights into process optimization and control for a value-based manufacturing framework. The code is developed to be user-friendly, fast and it does not require exceptional computational resources contrary to the most of the industrial and commercial software available in the nonwovens industry. The theoretical model for crystallization kinetics coupled with the previously developed model for the three-dimensional dynamics of molten polymeric jets facilitates predictions of the degree of crystallinity achieved in the produced fibrous laydowns. The numerical predictions revealed that the degree of crystallinity of meltblown laydowns is sensitive to multiple operating parameters, specifically to the initial gas temperature, the initial Deborah number of the molten polymer, DCD and especially, to the gas blowing velocity, whereas the uptake collector screen velocity and DCD also affect the laydown morphology. The 2-D mapping of the elevation and the degree of crystallinity reveals an anisotropic nature of such laydowns. The experiments with meltblowing were conducted and samples of nanofiber laydowns were collected on a flat collector plate under fully controlled conditions. The numerical code for prediction of meltblowing was modified to accommodate the flat collector screen. The numerical predictions revealed the surface and volumetric porosities

of the meltblown laydowns, and in particular, that they differ from each other, which signifies an un-isotropic nature of such laydowns. Pilot-scale meltblown fiber mat samples produced under controlled conditions were supplied by industry, and this project used them for experimental verification of the predicted elevation, porosity and degree of crystallinity. The surface elevations and porosities were measured using the experimentally formed samples and compared with the numerical predictions. The first comparisons revealed a reasonable agreement between the trends in the experimental data and the predicted values, albeit the degree of crystallinity seems to have been over-predicted by the numerical code by approximately 10-13%, as it follows from a limited number of measured datasets.

Meltblowing is highly non-isothermal process, and the thermal profile along the jet path not only affects the rheological parameters, but also affects the rate of crystallization, which in turn, affects the viscoelastic behavior of the polymeric jets. The polymer jets experience stretching and bending forces from the surrounding high-speed air flow. As a result, polymer jets experience significant thinning and stretching in bending (which enhances thinning), as well as lose heat to the surrounding air. All these processes affect the rate of nucleation and growth of linear crystals in polymer jets, which ultimately determine the degree of crystallinity in nonwoven meltblown laydowns. The numerical predictions for the degree of crystallinity were compared with the experimental results, and revealed a very good agreement. The processes of formation of polymer crystals amidst the high-speed surrounding hot air flow, are described for both isothermal and non-isothermal cases. The on-line crystallization is studied using numerical solutions of the coupled system of the quasi-one-dimensional equations of dynamics of free liquid polymer jets moving, cooling and solidifying along the travel path when driven by air jet and the kinetics of crystal nuclei

formation and their subsequent growth pattern. The developed code predicts the extent of crystallization of the molten polymer in flight and inside the three-dimensional laydown. The overall crystallinity of fibrous laydowns is presented as a crystallinity map over the surface of the web. Two radically different situations were explored. In one of them polymer filaments were essentially thermally insulated from the collector screen due to the low thermal conductivity of the underlying fibers and the surrounding air. In another one, the low touchdown temperature was enforced, which can be essentially done on the industrial scale. It was found that the latter measure facilitates an increase in the degree of crystallinity in the laydown. It was also found that increasing the die-to-collector distance (DCD) facilitates cooling of polymer jets in flight and results in an increased crystallinity of the nonwoven laydown. On the other hand, such material parameter as the activation energy of viscous flow of polymer melt revealed an insignificant effect on the laydown crystallinity. The model developed in this work can be used to avoid the trial and error stage in search for optimized processing conditions replacing it by numerical experimentation.

BIBLIOGRAPHY

Argentina M, Mahadevan L; Fluid-flow-induced flutter of a flag;; PNAS; 102;1829-34 (2005).

Astarita G, Marrucci G: Principles of non-Newtonian fluid mechanics , McGraw-Hill, New York (1974).

Avrami, M; Kinetics of phase change. I General theory. The Journal of chemical physics, 7(12), pp.1103-1112(1939)

Avrami, M; Kinetics of phase change. II transformation-time relations for random distribution of nuclei. The Journal of chemical physics, 8(2), pp.212-224 (1940).

Baert J, Van Puyvelde P; Effect of molecular and processing parameters on the flow-induced crystallization of poly-1-butene. Part 1: Kinetics and morphology. Polymer, 47(16), 5871-5879 (2006).

Balzano L, Kukalyekar N, Rastogi S, Peters G W, Chadwick J; Crystallization and dissolution of flow-induced precursors. Physical review letters, 100(4): 048302: (2008).

Bansal V, Shambaugh R L; On-Line determination of density and crystallinity during melt spinning. Polymer Engineering & Science, 36(22), 2785-2798 (1996).

Bansal V, Shambaugh R: On-line determination of diameter and temperature during melt blowing of polypropylene. Industrial & engineering chemistry research, 37 (1998) 1799-1806.

Barilovits S. "Experimental Study of a Unique Multi-Row Meltblowing Fiber Formation Process and the Web Structures Produced Thereby." PhD thesis, North Carolina State University, Raleigh, North Carolina (2018).

Batra S K, Pourdeyhimi B: Introduction to nonwovens technology. DEStech Publications, Inc; (2012).

Bazilevsky A V, Yarin A L, Megaridis C M: Pressure-driven fluidic delivery through carbon tube bundle, Lab. Chip 8 (2008) 152-160.

Begenir A, Tafreshi H V, and Pourdeyhimi B: Effect of nozzle geometry on hydroentangling water jets: experimental observations, Textile Research Journal 74, (2004): 178-184.

Bonilla L L, Gotz T, Klar A, Marheineke N, Wegener R; Hydrodynamic limit of a Fokker-Planck equation describing fiber lay-down processes; SIAM J. Appl. Math.;68 :648-65 (2007).

Brenn G, Liu Z, Durst F; Linear analysis of the temporal instability of axisymmetrical non-Newtonian liquid jets. International journal of multiphase flow 26(10): 1621-44 :(2000).

Bresee R R, Ko W C: Fiber formation during melt blowing. International nonwovens journal, 12 (2003) 21-28.

Brown M E, Gallagher P K; Handbook of thermal analysis and calorimetry: recent advances, techniques and applications (Vol. 5). Elsevier, 2011.

Brown M E; Introduction to Thermal Analysis: Techniques and Applications. Chapman and Hall, London, 1988.

Chen X, Papathanasiou T D: The transverse permeability of disordered fiber arrays: a statistical correlation in terms of the mean nearest interfiber spacing. Transport in Porous Media, 71 (2008) 233-251.

Chhabra R, Shambaugh R L: Experimental measurements of fiber threadline vibrations in the melt-blowing process. *Industrial & engineering chemistry research*, 35 (1996) 4366-4374.

Cho K, Li F, Choi J; Crystallization and melting behavior of polypropylene and maleated polypropylene blends. *Polymer*, 40(7): 1719-1729 (1999).

Chun, I, Reneker D H, Fong H, Fang X, Deitzel J, Beck Tan N, Kearns K: Carbon Nanofibers from Polyacrylonitrile and Mesophase Pitch, *Journal of Advanced Materials*, Volume 31, Number 1, January 1999, pages 36 – 41.

Connell BSH, Yue DKP; Flapping dynamics of a flag in a uniform stream; *J. Fluid Mech.* 581; 33-67 (2007).

Davies C N, in: *The separation of airborne dust and particles. Proceedings of the Institution of mechanical engineers B1*, 1953, pp.185-213. London.

Debye, P, Daen, J., Stability considerations on nonviscous jets exhibiting surface or body tension; *Phys. Fluids*; 2; 416-21. (1959)

Doshi J, and Reneker D H, “Electrospinning Process and Applications of Electrospun Fibers”, *Journal of Electrostatics*, Volume 35, 1995, pp. 151-160.

Doufas A K, McHugh A J, Miller C, Immaneni A; Simulation of melt spinning including flow-induced crystallization: Part II. Quantitative comparisons with industrial spinline data. *Journal of non-newtonian fluid mechanics*, 92(1), 81-103, (2000).

Doufas A K, McHugh A J, Miller C; Simulation of melt spinning including flow-induced crystallization: Part I. Model development and predictions. *Journal of Non-Newtonian Fluid Mechanics*, 92(1), 27-66, (2000)a.

Drummond J E, Tahir M I: Laminar viscous flow through regular arrays of parallel solid cylinders. *International Journal of Multiphase Flow*, 10 (1984) 515-540.

Ellis C J, Everett R D, Surge Management Fibrous Nonwoven Web for Personal Care Absorbent Articles and the Like, 1996, US Patent Number 5,490,846.

Entov V M, and Yarin A L: Dynamical equations for a liquid jet, *Fluid Dynamics* 15, (1980): 644-649.

Entov V M, Yarin A L; The dynamics of thin liquid jets in air. *Journal of Fluid Mechanics*, 140, 91-111 (1984).

Fedorova N V: Investigation of the utility of islands-in-the-sea bicomponent fiber technology in the spunbond process. PhD Thesis, Nonwovens Institute, (2017)

Feynman R: There's Plenty of Room at the Bottom: An Invitation to Enter a New Field of Physics *Caltech Engineering and Science*, Volume 23:5, pp 22-36 February 1960

Filatov Y, Budyka A, Kirichenko V; Electrospinning of micro-and nanofibers: fundamentals in separation and filtration processes. *J. Eng. Fibers Fabrics*(3): 488 (2007).

Formhals A, "Process and Apparatus for Preparing Artificial Threads", U.S. Patent 1,975,504, October 2, 1934.

Franck, A., Understanding rheology of thermoplastic polymers. TA Instruments (2004).

Gagliardi M. Global markets and technologies for nanofibers. PR Newswire. 2016.

Gangloff C, Report: U.S. Nonwovens Fabric Demand, Freedonia Group, http://www.nonwovens-industry.com/issues/2013-03/view_features/reportus-nonwovens-fabric-demand/, NonWovens Industry report, (2013).

Ghosal A, Sinha-Ray S, Yarin A L, Pourdeyhimi B; Numerical prediction of the effect of uptake velocity on three-dimensional structure, porosity and permeability of meltblown nonwoven laydown. *Polymer*, 85: 19-27 (2016).

Ghosal A, Sinha-Ray S, Sinha-Ray S, Yarin A L, Pourdeyhimi B; Numerical modeling and experimental study of solution-blown nonwovens formed on a rotating drum. *Polymer*, Nov 22, 105:255-263 (2016a).

Gogins M A; On-line web filtration efficiency test method. Donaldson Co Inc, assignee; United States patent US 5,203,201. Apr 20 (1993).

Gotz T, Klar A, Marheineke N, Wegener R; A stochastic model and associated FokkerPlanck equation for the fiber lay-down process in nonwoven production processes; *SIAM J. Appl. Math.*; 67: 1704-17 (2007).

Grady B P, Pompeo F, Shambaugh R L, Resasco D E; Nucleation of polypropylene crystallization by single-walled carbon nanotubes. *The Journal of Physical Chemistry B*, 106(23), 5852-5858 (2002).

Grafe T, Graham K, Polymeric nanofibers and nanofiber webs: a new class of nonwovens. *International Nonwovens Journal* :1558925003os-200113 March (2003)

Grafe, T.H., Gogins, M., Barris, M.A., Schaefer, J., Canepa, R., "Nanofibers in Filtration Applications in Transportation"; *Filtration 2001 Conference Proceedings*, 2001.

Graham K, Gogins M, Schreuder-Gibson H: Incorporation of electrospun nano fibers into functional structures. INJ, 13 (2): 21-27, summer 2004.

Graham K, Ouyang M, Raether T, Grafe T, McDonald B, Knauf P; "Polymeric Nanofibers in Air Filtration Applications"; American Filtration & Separations Society Proceedings, April 2002.

Greiner A, Wendorff J H, Electrospinning: a fascinating method for the preparation of ultrathin fibers. *Angewandte Chemie International Edition*, 46(30), 5670-5703 (2007).

Haines P J; *Thermal methods of analysis: principles, applications and problems*. Springer Science & Business Media, 2012.

Han W, Wang X, Gajanan S, Nanomater J: Mass production and high photocatalytic activity of ZnS nanoporous nanoparticles. *Angewandte Chemie International Edition*, 2 (2013) 3.

Han W, Wang X, Gajanan S: Modeling permeability of 3-D nanofiber media in slip flow regime. *Nanomater. Mol. Nanotechnol.* 2 (2013) 2-3.

Hassan M A, Yeom B Y, Wilkie A, Pourdeyhimi B, Khan S A; Fabrication of nanofiber meltblown membranes and their filtration properties. *Journal of Membrane Science* ,427: 336-344 (2013).

Hlod A, Aarts A C T, Van de Ven A A F, Peletier M A: Mathematical model of falling of a viscous jet onto a moving surface. *European Journal of Applied Mathematics*, 18 (2007) 659-677.

Hlod A, Aarts A C T, Van de Ven A A F, Peletier M A: Three flow regimes of viscous jet falling onto a moving surface. *IMA Journal of Applied Mathematics*, 77 (2012) 196-219.

Hoferer J, Hardy E H, Meyer J, Kasper G: Measuring particle deposition within fibrous filter media by magnetic resonance imaging. FILTRATION-COALVILLE, 7 (2007) 154-158.

Hosseini S A, Tafreshi H V: Modeling permeability of 3-D nanofiber media in slip flow regime. Chemical Engineering Science, 65 (2010) 2249-2254.

<http://polymerdatabase.com/Fibers/Nonwovens.html>

<http://www.bbafiltration.com/UltraFlo-1.html>

<http://www.tikp.co.uk>

<https://textination.de/>

<https://www.chemical-fibers.com/TextileTechnology>

<https://www.marketwatch.com/press-release/global-spunbond-nonwoven-market-trends-demand-production-sales-supply-analysis-forecast-to-2023-2019-04-04>

<https://www.reuters.com/brandfeatures/venture-capital/article?id=15814>

<https://www.textileschool.com/>

INDA Association of the Nonwoven Fabrics Industry report <http://www.inda.org/> (2002)

Jackson G K , James D F: The permeability of fibrous porous media, Can. J. Chem. Eng. 64 (1986) 364-374.

Jaganathana S, Tafreshi H V, Pourdeyhimi B: Case study of realistic two-scale modeling of water permeability in fibrous media. Separation Science and Technology, 43 (2008) 1901-1916.

Jaganathana S, Tafreshi H V, Pourdeyhimi B: Realistic approach for modeling permeability of fibrous media: 3-D imaging coupled with CFD simulation. *Chemical Engineering Science*, 63 (2008a) 244-252.

Jarecki L, Blonski S, Blim A, Zachara A; Modeling of pneumatic melt spinning processes. *Journal of Applied Polymer Science*, 125, 4402–4415 (2012).

Jarecki L, Pecherski R B; Kinetics of oriented crystallization of polymers in the linear stress-orientation range in the series expansion approach. *eXPRESS Polymer Letters* 12.(4) 330-348: (2018).

Kalayci V E., “Electrostatic Solution Spinning”, MS Thesis, University of Massachusetts, Dartmouth, July, 2002

Khansari S, Duzyer S, Sinha-Ray S, Hockenberger A, Yarin A L: Two-stage desorption-controlled release of fluorescent dye and vitamin from solution-blown and electrospun nanofiber mats containing porogens, Pourdeyhimi B, *Mol. Pharm.* 10 (2013) 4509-4526.

Kim K H, Isayev A I, Kwon K; Flow-induced crystallization in the injection molding of polymers: A thermodynamic approach. *Journal of applied polymer science*, 95(3), 502-523 (2005).

Kirichenko V, Filatov Y, Budyka A. Electrospinning of micro-and nanofibers: fundamentals in separation and filtration processes. *International Journal for Multiscale Computational Engineering*. 2010;8(4).

Kolbasov A, Sinha-Ray S, Joijode A S, Hassan M A, Brown D, Maze B, Pourdeyhimi B, Yarin A L: Industrial-scale solution blowing of soy protein nanofibers. *Industrial & Engineering Chemistry Research*, 55 (2016) 323-333.

Koponen A, Kandhai D, Hellen E, Alava M, Hoekstra A, Kataja M, Niskanen K, Slood P, Timonen J: Permeability of three-dimensional random fiber webs. *Physical Review Letters*, 80 (1998) 716-719.

Kwok K C, E.W. Bolyard, Jr, Riggan L E, Jr: U.S. Patent No. 5,904,298. Washington, DC: U.S. Patent and Trademark Office, May 18, 1999.

Lau C H; Reverse-selective polymeric membranes for gas separations. *Progress in Polymer Science*, 38(5): 740-766 (2013).

Lee K H, Kim H Y, La Y M, Lee D R, Sung N H; Influence of a mixing solvent with tetrahydrofuran and N, N-dimethylformamide on electrospun poly (vinyl chloride) nonwoven mats. *Journal of polymer science part B: polymer physics*, 40(19): 2259-2268 (2002).

Lee M W, An S, Jo HS, Yoon S S , Yarin A L: Self-healing nanofiber-reinforced polymer composites. 2. Delamination/debonding and adhesive and cohesive properties. *ACS applied materials & interfaces*, 7(2015) 19555-19561.

Li Y, Ma T, Yang S T, Kniss D A: Thermal compression and characterization of three-dimensional nonwoven PET matrices as tissue engineering scaffolds. *Biomaterials*, 22 (2001) 609-618.

Liu S L: Recent progress in the design of advanced PEO-containing membranes for CO₂ removal. *Progress in Polymer Science*, 38(7): 1089-1120 (2013).

Loitsyanskiy L G: *Mechanics of liquids and gases*. Edited by Robert H, Pergamon Press, Oxford, (1966)

Luigi B, Rastogi S, Peters G W; Crystallization and precursors during fast short-term shear. *Macromolecules* 42.6 2088-2092: (2009).

Lux J, Ahmadi A, Gobbe C, Delisee C: Macroscopic thermal properties of real fibrous materials: volume averaging method and 3D image analysis. *International Journal of Heat and Mass Transfer*, 49: 1958-1973.(2006)

Luzhansky D M. Quality control in manufacturing of electrospun nanofiber composites. *International Nonwovens Journal*.:1558925003os-200411, Dec 4 (2003)

Marheineke N, Wegener R: Fiber dynamics in turbulent flows: Specific Taylor drag. *SIAM Journal on Applied Mathematics*, 68 (2006) 1-23.

Marla V T, Shambaugh R L: Modeling of the melt blowing performance of slot dies. *Industrial & engineering chemistry research* 43 (2004) 2789-2797.

Marla V T, Shambaugh R L: Three-dimensional model of the melt-blowing process. *Industrial & engineering chemistry research*, 42 (2003) 6993-7005.

Mattheij R M M, Rienstra S W, Thije Boonkkamp J H M: *Partial Differential Equations: Modeling, Analysis, Computation*; SIAM, Philadelphia (2005)

Medeiros E S, Glen G Mn, Klamczynski A P, Orts W J, Mattosom L H: Solution blow spinning A new method to produce micro and nanofibers from polymer solutions. *Journal of applied polymer science*, 113 (2009) 2322-2330.

Meerveld J V, Hütter M, Peters G W; Continuum model for the simulation of fiber spinning, with quiescent and flow-induced crystallization. *Journal of Non-Newtonian Fluid Mechanics*, 150(2), 177-195 (2008).

Meerveld J V, Peters G W M, Hutter M; Towards a Rheological classification of flow induced crystallization experiments of polymer melts”, *M. Rheol Acta* (44): 119 (2004).

Menczel J D, Prime R B; Thermal analysis of polymers: fundamentals and applications. John Wiley & Sons. 2014.

Moharir A V, Vijayraghavan K M, Panda B C, Gupta V B: Dependence of Stiffness and Strength of Cotton Fibers on Crystallite Orientation. Textile Research Journal, 52(12), 756–760. (1982)

Morozova M Y, Artemenko S E, Ustinova T P; Physicochemical principles of technology for modification of polymeric composite materials: A review. Fibre Chemistry, 30(4): 212-225 (1998).

Mukhopadhyay A, Midha V K: A review on designing the waterproof breathable fabrics part I: fundamental principles and designing aspects of breathable fabrics. Journal of industrial textiles, 37 (2008) 225-262.

NAN043E; Global market report for nanofibers; <https://www.bccresearch.com/market-research/nanotechnology/global-markets-and-technologies-for-nanofibers.html> (2019)

Noruzi M, J: Electrospun nanofibres in agriculture and the food industry A review, Sci. Food Agric. (2016)

NSF Media Advisory (National Science Foundation Market Report) 14-004

https://www.nsf.gov/news/news_summ.jsp?cntn_id=130586 (2014)

Okuno TY, Yasuda T, Yasuda H; Effect of crystallinity of PET and nylon 66 fibers on plasma etching and dyeability characteristics. Textile Research Journal, Aug; 62(8):474-480 (1992).

Oleksandr O M, Chambon P, Graham R S, Patrick A, Fairclough A, Olmsted P D, Ryan A J; The specific work of flow as a criterion for orientation in polymer crystallization. Macromolecules 41, no. 6 1901-1904: (2008).

Oliveira JE, Zucolotto V, Mattoso LH, Medeiros ES. Multi-walled carbon nanotubes and poly (lactic acid) nanocomposite fibrous membranes prepared by solution blow spinning. *Journal of nanoscience and nanotechnology*. Mar 1;12(3):2733-41 (2012).

Paidoussis MP, Dynamics of flexible cylinders in axial flow; *J. Fluid Mech.*; 26, 717-51(1966).

Pinchuk L S, Goldade V A, Makarevich A V, Kestelman V N; *Melt Blowing: equipment, technology, and polymer fibrous materials*. Springer Science & Business Media; Dec 6 (2012).

Pradhan A K, Das D, Chattopadhyay R, Singh S N: Effect of 3D fiber orientation distribution on transverse air permeability of fibrous porous media. *Powder Technology*, 221 (2012) 101-104.

Ramakrishna S, Fujihara K K, Teo W E, Lim T C, Ma Z: *An Introduction to Electrospinning and Nanofibers*, World Scientific, Singapore, 2005.

Reid R C, Prausnitz J M, Poling B E: *The Properties of Gases and Liquids*, McGraw- Hill, New-York, 1987.

Reneker D H, Yarin A L, Zussman E, Xu H: Electrospinning of nanofibers from polymer solutions and melts. *Advances in applied mechanics*, 41 (2007), 43-195.

Reneker D H, Chun I, Ertley D: The effects of operating parameters on the fabrication of polyacrylonitrile nanofibers in electro-centrifuge spinning, US Patent 6382526 B1, May 7, 2002.

Reneker D H, Chun I: Nanometre diameter fibres of polymer, produced by electrospinning. *Nanotechnology*, (1996) 216-223.

Reneker D H, Yarin A L: Electrospinning jets and polymer nanofibers, *Polymer* 49 (2008) 2387-2425.

Schaefer J W., and Olson, L.M., “Air Filtration Media for Transportation Applications”, *Filtration & Separation*, March 1998.

Schaefer, J.W., McDonald, B., and Gogins, M., “Nanofibers in Aerosol Filtration”, *Nanotechnology for the Soldier System Conference, (SSCOM-ARO-ARL-NSF)*, Cambridge, MA, July (1998a).

Schladitz K, Peters S, Reinel-Bitzer D, Wiegmann A, Ohser J, *CompuMaTter.Sci.* 38 (2006) 56-66.

Schneider W A, Köppl A, Berger J; Non-isothermal crystallization of polymers: System of rate equations. *International Polymer Processing*, 2(3-4), 151-154 (1988)

Seaver M, Galloway A, Manuccia T J: Acoustic levitation in a free-jet wind tunnel. *Review of Scientific Instruments*, 60 (1989) 3452-3459.

Seongpil An, Changmin Lee, Minho Liou, Hong Seok Jo, Jung Jae Park, Yarin A L, and Sam S: Yoon *ACS Applied Materials & Interfaces* 2014 6 (16), 13657-13666

Shambaugh R L; A macroscopic view of the melt-blowing process for producing microfibers. *Industrial & Engineering Chemistry Research*, 27, 2363-2372, (1988).

Shelley M, Vandenberghe N, Zhang J; Heavy flags undergo spontaneous oscillations in flowing water; *Phys. Rev. Lett.*; 94; 094302 (2005).

Sinha-Ray S, Yarin A L, Pourdeyhimi B; Melt blowing: I-Basic physical mechanisms and threadline model. *Journal of Applied Physics*, 108, 034912 (2010).

Sinha-Ray S, Chando P, Yarin A L: Enhanced release of liquid from carbon nanotubes due to entrainment by an air layer, *Nanotechnology* 20 (2009) 095711.

Sinha-Ray S, Lee MW, Sinha-Ray S, An S, Pourdeyhimi B, Yoon SS, Yarin AL. Supersonic nanoblowing: a new ultra-stiff phase of nylon 6 in 20–50 nm confinement. *Journal of Materials Chemistry C* ;1(21): 3491-8.(2013)

Sinha-Ray S, S. Sinha-Ray, Yarin A L, Pourdeyhimi B: Theoretical and experimental investigation of physical mechanisms responsible for polymer nanofiber formation in solution blowing, *Polymer* 56 (2015 a) 452-463.

Sinha-Ray S, Sinha-Ray S, Yarin A L, Pourdeyhimi B: Application of solution-blown 20–50 nm nanofibers in filtration of nanoparticles: The efficient van der Waals collectors. *Journal of membrane science* 485 (2015) 132-150.

Sinha-Ray S, Sinha-Ray S, Yarin A L, Weickgenannt C M, Emmert J, Tropea C, *Int. J. Heat Mass Transf.* 70 (2014) 1107-1114. 70 (2014) 1107-1114.

Sinha-Ray S, Yarin A L, Pourdeyhimi B: Meltblown fiber mats and their tensile strength, *Polymer* 55 (2014) 4241-4247.

Sinha-Ray S, Yarin A L, Pourdeyhimi B: The production of 100/400 nm inner/outer diameter carbon tubes by solution blowing and carbonization of core–shell nanofibers, *Carbon* 48 (2010a) 3575-3578.

Sinha-Ray S, Yarin A L, Pourdeyhimi B; Prediction of angular and mass distribution in meltblown polymer laydown. *Polymer*, 54, 860-872 (2013).

Sinha-Ray S, Yarin A L: Drop impact cooling enhancement on nano-textured surfaces. Part I: Theory and results of the ground (1 g) experiments, *Int. J. Heat Mass Transf.* 70 (2014) 1095-1106.

Sinha-Ray S, Zhang Y, Yarin A L, Davis S C, Pourdeyhimi B: Solution blowing of soy protein fibers, *Biomacromolecules* 12 (2011) 2357-2363.

Sinha-Ray S, Zhang Y, Yarin A L: Thorny devil nanotextured fibers: the way to cooling rates on the order of 1 kW/cm², *Langmuir* 27 (2010) 215-226.

Sinha-Ray S. "Mechanics of Micro-and Nano-Textured Systems: Nanofibers, Nanochannels, Nanoparticles and Slurries." PhD dissertation., 2012.

Sinha-Ray S: *Spray in Polymer Processing. Droplet and Spray Transport: Paradigms and Applications.* Springer, Singapore, 31-54 (2018)

Spielman L, Goren S L: Model for predicting pressure drop and filtration efficiency in fibrous media. *Environmental Science & Technology*, 2 (1968) 279-287.

Srikar R, Yarin A L, Megaridis C M, Bazilevsky A V, Kelley E: Desorption-limited mechanism of release from polymer nanofibers *Langmuir* 24 (2008) 965-974.

Srikar R, Yarin A L, Megaridis C M: Fluidic delivery of homogeneous solutions through carbon tube bundles, *Nanotechnology* 20 (2009) 275706.

Stachewicz U, Hang F, Barber A H: Adhesion anisotropy between contacting electrospun fibers. *Langmuir*, 30 (2014) 6819-6825.

Subbiah T, Bhat G S, Tock R W, Parameswaran S, Ramkumar S S: Electrospinning of nano fibers. *J. Appl. Polym. Sci.*, 96: 557 -569, 2005.

Sun Z, Zussman E, Yarin A Y, Wendorff J H, Greiner A: Compound core-shell polymer nano fibers by co-electrospinning. *Advanced Materials*, 15(22):1929-1932, 2003.

Tahir M A, Tafreshi H V: Influence of fiber orientation on the transverse permeability of fibrous media. *Physics of Fluids*, 21 (2009) 083604.

Talbott M F, Springer G S, Berglund L A; The effects of crystallinity on the mechanical properties of PEEK polymer and graphite fiber reinforced PEEK. *Journal of Composite Materials*, 21(11):1056-81 (1987).

Tate B D, Shambaugh R L; Modified dual rectangular jets for fiber production. *Industrial & engineering chemistry research*, 37(9):3772-9 (1998).

Tomadakis M M , Robertson J T: In-plane and through-plane gas permeability of carbon fiber electrode backing layers. *Journal of Power Sources*, 39 (2005) 163-188.

Tomadakis M M, Robertson J T: Viscous Permeability of Random Fiber Structures: Comparison of Electrical and Diffusional Estimates with Experimental and Analytical Results, *Journal of Composite Materials* 39 (2005a) 163-188.

Toth G; Determination of polymer melts flow-activation energy a function of wide range shear rate. *Journal of Physics: Conference Series*. Vol. 1045. No. 1. IOP Publishing, (2018).

Tsai P P, Chen W, Roth J R, Investigation of the fiber, bulk, and surface properties of meltblown and electrospun polymeric fabrics. *International Nonwovens Journal*, (3), 1558925004os-1300306 (2004)

Triantafyllou GS; Physical condition for absolute instability in inviscid hydroelastic coupling;; *Phys. Fluids A*; 4; 544-52 (1992).

Tsai P P, Schreuder-Gibson H, Gibson P: Different electrostatic methods for making electret filters, *Journal of Electrostatics*, Volume 54, 2002.

Uyttendaele M A J, Shambaugh R L; Melt blowing: General equation development and experimental verification, *AIChE J.* 36 (1990) 175-186.

Wang J, Langhe D, Ponting M, Wnek G E, Korley LT, Baer E; Manufacturing of polymer continuous nanofibers using a novel co-extrusion and multiplication technique. *Polymer*, 55(2):673-85 (2014).

Wang Y; PHD THESIS , Application of polymer rheology in melt blowing process and online rheological sensor. (2004).

Weber, C; Zum zerfall eines flüssigkeitsstrahles (On the breakdown of a fluid jet), *Zeitschrift für Angewandte Mathematik und Mechanik (Journal of Applied Mathematics and Mechanics)*, 11, 136-154 (1931).

Wehmann M, McCulloch W J G; Melt blowing technology, *Polymer Science and Technology Series*, 2, 415-420 (1999).

Wei Q F, Mather R R, Fotheringham A F, Yang R D: Evaluation of nonwoven polypropylene oil sorbents in marine oil-spill recovery. *Marine Pollution Bulletin*, 46 (2003) 780-783.

Wendorff J H, Agarwal S, Greiner A: *Electrospinning, materials, processing, and applications*, Wiley-VCH, Weinheim, 2012.

Wente VA, Boone EL, Fluharty CD; Manufacture of superfine organic fibers, *Naval Research Laboratory Report No. NRL-4364*, Washington DC (1954).

Wente VA; Superfine thermoplastic fibers, *Industrial & Engineering Chemistry*; 48(8):1342-1346 (1956).

Williamson CHK, Govardhan, R; Vortex-induced vibrations; *Annu. Rev. Fluid Mech.*; 36; 413-55 (2004).

Wnek G E, Carr M E, Simpson D G, Bowlin G L:Electrospinning of nanofiber fibrinogen structures, *Nano Lett.* 3 (2003) 213-216.

Xiang P, Kuznetsov A V, and Seyam A M: Combined numerical and experimental investigation on the effect of jet pressure and forming belt geometry on the hydroentanglement process, *The Journal of the Textile Institute*; 100 (2009): 293-304.

Xiang P: Numerical modelling and experimental investigation of the hydroentanglement process . PhD Thesis, North Carolina State University, 2007.

Xin S, Wang X: Mechanism of Fiber Formation in Melt Blowing. *Industrial & Engineering Chemistry Research*, 51 (2012) 10621-10628.

Xin S, Wang X: Shear flow of molten polymer in melt blowing. *Polymer Engineering & Science* 52 (2012a) 1325-1331.

Yarin A L, Sinha-Ray S, Pourdeyhimi B; Melt blowing: Multiple jets and fiber-size distribution and lay-down patterns. *Polymer*, 52, 2929-2938 (2011).

Yarin A L, Brenn G, O. Kastner, Rensink D, Tropea C: Seaver, M., Galloway, A., & Manuccia, T. J. (1989). Acoustic levitation in a free-jet wind tunnel. *Review of Scientific Instruments*, 399 (1999) 151-204.

Yarin A L, Koombhongse S, Reneker D H: Bending instability in electrospinning of nanofibers. *Journal of applied physics*, 89 (2001) 3018-3026.

Yarin A L, Pourdeyhimi B, Ramakrishna S. *Fundamentals and Applications of Micro- and Nanofibers*. Cambridge University Press, Cambridge, 2014..

Yarin A L, Sinha-Ray S, Pourdeyhimi B; Melt blowing: II-Linear and nonlinear waves on viscoelastic polymer jets. *Journal of Applied Physics*, 108, 034913 (2010).

Yarin A L, Sinha-Ray S, Pourdeyhimi B: Prediction of angular and mass distribution in meltblown polymer lay-down, *Polymer* 52 (2011) 2929-2938.

Yarin A L, Tropea C, Foss J. (Eds.), *Springer Handbook of Experimental Fluid Mechanics*, Springer, Berlin, 2007, pp. 57-82.

Yarin A L; Flow-induced on-line crystallization of rodlike molecules in fiber spinning. *Journal of Applied Polymer Science*, 46: 873–878 (1992).

Yarin A L; *Free Liquid Jets and Films: Hydrodynamics and Rheology*. Longman Scientific & Technical and Wiley & Sons, Harlow, New York, 1993.

Zhang H, Tumarkin E, Peerani R, Nie Z, Sullan R M A, Walker G C, Kumacheva E. Microfluidic production of biopolymer microcapsules with controlled morphology; 2006; *Journal of the American Chemical Society*; 128; 12205-10.

Zhu S R, Pelton H, Collver K: Mechanistic modelling of fluid permeation through compressible fiber beds, 50 : 3557-3572(1995).

Ziabicki A, Kawai H (Eds), *High-speed Fiber Spinning*, John Wiley & Sons, New York, 1985.

Ziabicki A, The mechanisms of 'neck-like' deformation in high-speed melt spinning. 1. Rheological and dynamic factors. *Journal of Non-Newtonian Fluid Mechanics*, 30(2), 141-155 (1988).

Ziabicki A, The mechanisms of 'neck-like' deformation in high-speed melt spinning. 2. Effects of polymer crystallization. *Journal of Non-Newtonian Fluid Mechanics*, 30(2), 157-168 (1988a).

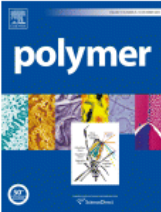
Ziabicki A; *Fundamentals of Fiber Formation*. John Wiley&Sons, New York ,1976.

Zupancic S, Sinha-Ray S, Sinha-Ray S, Kristl J, Yarin A L: Long-term sustained ciprofloxacin release from pmma and hydrophilic polymer blended nanofibers, *Mol. Pharm.* 13: 295-305 (2015).

Zupančič S, Sinha-Ray S, Sinha-Ray S, Kristl J, Yarin AL. Controlled release of ciprofloxacin from core-shell nanofibers with monolithic or blended core. *Molecular Pharmaceutics*. Mar 18;13(4):1393-404. (2016)

Appendix A:- Permission from Elsevier journal for re-usage of chapter 4 in thesis.

HomeHelpEmail SupportArkaprovo Ghosal ▾



Numerical prediction of the effect of uptake velocity on three-dimensional structure, porosity and permeability of meltblown nonwoven laydown

Author: Arkaprovo Ghosal, Suman Sinha-Ray, Alexander L. Yarin, Behnam Pourdeyhimi

Publication: Polymer

Publisher: Elsevier

Date: 24 February 2016

Copyright © 2016 Elsevier Ltd. All rights reserved.

Please note that, as the author of this Elsevier article, you retain the right to include it in a thesis or dissertation, provided it is not published commercially. Permission is not required, but please ensure that you reference the journal as the original source. For more information on this and on your other retained rights, please visit: <https://www.elsevier.com/about/our-business/policies/copyright#Author-rights>

BACK

CLOSE WINDOW

© 2019 Copyright - All Rights Reserved | [Copyright Clearance Center, Inc.](#) | [Privacy statement](#) | [Terms and Conditions](#)
Comments? We would like to hear from you. E-mail us at customer care@copyright.com

Appendix B:- Permission from Elsevier journal for re-usage of chapter 5 in thesis.



Home Help Email Support Sign in Create Account



Numerical modeling and experimental study of solution-blown nonwovens formed on a rotating drum

Author:
Arkaprovo Ghosal, Sumit Sinha-Ray, Suman Sinha-Ray, Alexander L. Yarin, Behnam Pourdeyhimi

Publication: Polymer

Publisher: Elsevier

Date: 22 November 2016

© 2016 Elsevier Ltd. All rights reserved.

Please note that, as the author of this Elsevier article, you retain the right to include it in a thesis or dissertation, provided it is not published commercially. Permission is not required, but please ensure that you reference the journal as the original source. For more information on this and on your other retained rights, please visit: <https://www.elsevier.com/about/our-business/policies/copyright#Author-rights>

[BACK](#) [CLOSE WINDOW](#)

© 2019 Copyright - All Rights Reserved | [Copyright Clearance Center, Inc.](#) | [Privacy statement](#) | [Terms and Conditions](#)
Comments? We would like to hear from you. E-mail us at customercare@copyright.com

ARKAPROVO GHOSAL

Ph.D. Candidate, 2018-19, University of Illinois at Chicago (UIC)

Multiscale Mechanics and Nanotechnology Laboratory (MMNL)
Department of Mechanical and Industrial Engineering

(312) 709-9163
aghos2@uic.edu

EXPERTISE

- Theoretical and **Computational Fluid Dynamics** and Heat Transfer
- Regression Models and Statistical Inference
- **Time Series Analysis** for Weather Forecasting and Turbulence
- **Stochastic Differential Equations** and Statistical Trend Analysis
- Multi-phase and Multi-Component Flow through Porous Media
- Viscoelastic Wave Propagation in Liquid Jets and Films
- Rheological Behavior of Polymeric Liquid Jets and Droplet Dynamics

TOOLS AND TECHNOLOGIES

- **Coding/Programming Language:** C, C++, **MATLAB**, **Simulink**, FORTRAN 77/90/95, **Python 2/3**, R, Peoplecode
- **Commercial Software:** ANSYS CFD/CFX, ANSYS Customization Tool (ACT- Coding Platform), Solidworks
- **Data Analysis and Visualization:** NumPy, Pandas, Matplotlib, Plotly, Seaborn (Statistical plots), Spark (Big Data)
- **Database and Image Processing:** SQL, Origin Pro, ImageJ, MS Office

EDUCATION

- **Ph.D., Mechanical Engineering** **Fall 2019**
University of Illinois at Chicago (**UIC**)
 - **Specialization:** Dynamics of turbulent viscoelastic liquid jets
 - **Ph.D. Thesis Title:** “*Modeling of nonwoven formation processes*”, **Advisor:** Prof. Alexander L. Yarin
- **M.Sc., Water Resource Engineering** **Oct 2009 - Jun 2012**
Institute of Hydrosystems Modeling, Universität Stuttgart, Stuttgart, Germany
 - **Specialization:** Flow of groundwater through subsurface porous media
 - **M.Sc. Thesis Title:** “*A Lagrangian smoothed particle framework to simulate DNAPL contaminant dissolution in the subsurface porous media*”, **Advisor:** Junior Prof. Dr. Wolfgang Nowak
- **B.Eng., Chemical Engineering** **May 2007**
Jadavpur University, Kolkata, India.

EXPERIENCE IN MODELING, STATISTICAL ANALYSIS AND NUMERICAL METHODS

Numerical Simulation and Mathematical Model Development (During Ph.D. Thesis): **Spring 2013 - Spring 2018**

- **MATLAB – (Finite Difference)** Polymeric rheological behavior for nonwoven industry applications.
- **FORTRAN – (Finite Volume)** Simulating turbulent polymer melt jets of **shape memory**.
- **MATLAB – (Post-Processing)** Estimation of architecture, porosity and permeability of fibrous porous media.
- **MATLAB – (Particle Simulation)** **Markovian behavior** of viscoelastic complex fluid-air interactions.
- **ANSYS User defined Function – Random Sampling based** Kinetic model development for thermal effects.
- **FORTRAN/C++** - Simulating high-speed water jet impact on fibrous porous structure.

Numerical Simulation and Modeling (at Universität Stuttgart during M.Sc. Thesis) **Spring 2011 - Spring 2012**

- Smoothed Particle Hydrodynamics (**SPH**) framework.
- Stochastic Finite Element Analysis of Groundwater Contaminant Dissolution Behavior.
- **Random Walk Particle Tracking Algorithm** along with **Monte-Carlo** Simulation.
- Pore-scale Percolation Physics and DNAPL (Dense Non-Aqueous Phase Liquid) Infiltration.

DOMAINS OF INTEREST

- Commercial CFD Software Development and **Data-driven Algorithms**
- Weather Forecasting and **Pattern Recognition**
- Random Sampling and **Hypothesis Testing**
- Turbulence Physics and Smoothed Particle Hydrodynamics
- **Neural Networks**, Decision Trees and **Random Forests**
- Poro-elasticity and Behavior of Deformable Porous Media
- High-efficiency Particle Capture and Filtration Applications

PROFESSIONAL EXPERIENCE

FESII (Foreign Exchange Services of Illinois, Inc.)

July 2019 - Present

- Data Science consultant, Foreign exchange trading platform

IBM Global Services

Sep 2007 - Jun 2009

- Associate System Engineer, PeopleSoft ERP (Enterprise Resource Planning)
- Peoplesoft ERP- **People Code** and **HRMS/HCM** module Implementation and support projects - **ABN AMRO**
- Techno-functional role on **Workflow and CRM modules- Oracle Peoplesoft**

TEACHING/INSTRUCTING EXPERIENCE

University of Illinois at Chicago - Graduate Teaching Assistant

- **Senior Design in Mechanical Engineering, ME397:** Spring 2018
Instructor of ANSYS CFX/CFD modules.
- **Experimental Methods in Mechanical Engineering, ME341:** Fall 2017
Laboratory Instructor
- **Intermediate Thermodynamics, ME205(Theoretical problem solving)** Summer 2017
- **Fluid Mechanics, ME211 Theory:** Transport processes 2014- Fall 2015
Instructor of theoretical fluid dynamics problems and CFD projects
- **Fluid Mechanics, ME211 Lab:** Experimental setups for fluid flow Fall 2016, Spring 2017
Instructor of fluid dynamics laboratory section of the class.

TALKS AND PRESENTATIONS

1. **A. Ghosal**, A. L. Yarin, B. Pourdeyhimi, "**Modeling of meltblowing processing conditions- A framework of turbulent liquid jet dynamics**", Bi-annual industrial board research review meetings at The Nonwoven Institute. Raleigh, North Carolina (2014, November – 2016, November).
2. **A. Ghosal**, "**Modeling of nonwoven formation processes- A framework of turbulent and viscoelastic liquid jet dynamics**", Annual meetings on UIC-KU (Korea University) joint conference on Nano-textured composites, Mechanical Engineering Department, University of Illinois at Chicago (April 2015, April 2016, April 2017).

PUBLICATIONS

1. **A. Ghosal**, S. Sinha-Ray, A. L. Yarin, B. Pourdeyhimi, "Numerical prediction of the effect of uptake velocity on three-dimensional structure, porosity and permeability of meltblown nonwoven laydown." -**Polymer** (2016).
2. **A. Ghosal**, S. Ray, S. Sinha-Ray, A. L. Yarin, B. Pourdeyhimi, "Numerical modeling and experimental study of solution-blown nonwovens formed on a rotating drum." - **Polymer** (2016).
3. K. Chen; **A. Ghosal**, A. Yarin, B. Pourdeyhimi, "Modeling of Spunbond Formation Process of Polymer Nonwovens"- **Polymer** (2019)
4. **A. Ghosal**, S. Sinha-Ray, A. L. Yarin, B. Pourdeyhimi, " Modeling Polymer Crystallization Kinetics in Meltblowing Process." - **Journal of Industrial & Engineering Chemistry Research** (2019)

SCHOLARSHIPS AND AWARDS

1. **University of Stuttgart** - DAAD "Matching Funds" Scholarship to pursue M.Sc. (with research thesis) at TU9 (Cluster of 9 Technical Universities) group of Universities.